Toward an understanding of fundamental mechanisms in transitional and turbulence flow control

Ethan A. Davis
University of Nebreaska-Lincoln, ethan.davis@huskers.unl.edu

TOWARD AN UNDERSTANDING OF FUNDAMENTAL MECHANISMS IN

TRANSITIONAL AND TURBULENCE FLOW CONTROL

by

Ethan Allan Davis

A DISSERTATION

Presented to the Faculty of

The Graduate College at the University of Nebraska

In Partial Fulfilment of Requirements

For the Degree of Doctor of Philosophy

Major: Mechanical Engineering and Applied Mechanics

Under the Supervision of Professor Jae Sung Park

Lincoln, Nebraska

August, 2021

TOWARD AN UNDERSTANDING OF FUNDAMENTAL MECHANISMS IN TRANSITIONAL AND TURBULENCE FLOW CONTROL

Ethan Allan Davis, Ph.D.

University of Nebraska, 2021

Adviser: Jae Sung Park

Turbulence is an emergent phenomenon found throughout nature and engineering, alike. It plays a vital role in the aquatic locomotion of organisms, scalar mixing, fluid transport, shipping and transportation, and even the flow of biological fluids in the human body. Therefore, it is of utmost importance in both a practical and engineering sense to better understand turbulence with the goal of better controlling it. This dissertation focuses broadly on better understanding the underlying mechanisms behind wall-bounded turbulent flows, with an emphasis on exploiting those mechanisms for turbulence flow control.

We developed a numerical simulation to study the effect of slip surfaces on the dynamics of transitional and turbulent flows. Slip surfaces were found to promote the return of a turbulent flow to the laminar state. They also impact the transition to and from turbulence depending upon flow structure. The simulation was extended to study composite drag reduction of slip surfaces and polymer additives. An additive effect was observed due to the distinct drag reduction mechanisms of each individual method.

Using simulations and experiments, intermittent dynamics of turbulent flows were investigated which manifest in the form of low-drag events: events described by low levels of skin friction and three-dimensionality. Because these events exhibit desirable traits, they are targets for flow control techniques, and their characterization will

hopefully inform more efficient flow control methods.

The minimal flow unit (MFU) approach to simulating turbulent flows was first popularized by the seminal 1991 work of Jiménez and Moin. Since then, the technique has become a powerful tool in teasing out underlying mechanisms of turbulent flows due to its ability to resolve the many scales in turbulence. While the technique faithfully captures the dynamics of most flows, there are questions surrounding larger Reynolds numbers. We investigate the efficacy of MFUs in promoting "healthy" turbulence and show that additional criteria should be put in place when simulating higher Reynolds number flows with MFUs.

DEDICATION

To my parents. For cultivating in me a curiosity of the world and all those who inhabit it. For ingraining in me the importance of knowledge. For instilling in me a sense of worth and purpose. For supporting me through all my endeavors. I love you to the moon and back.

ACKNOWLEDGMENTS

To Annie, thank you. That is all I can really say. I would fill another 200 pages with the countless acts of love, kindness, and support you have shown me. You have put up with me and the stresses of my PhD program while dealing with the stresses of your own PhD program. We have had so many amazing adventures over the past three years, and so many more to come. Thank you...Doctor.

Finally, I am forever grateful for my family and friends. Without your continuous love and support, I would not be here. Thank you for keeping me grounded and reminding me what is truly important in life. You have impacted my life more than you will ever know.

GRANT INFORMATION

Table of Contents

List of Figures

List of Tables

Chapter 1

INTRODUCTION

1.1 Turbulence and the dynamical systems approach to fluid dynamics

The application of dynamical systems theory has allowed for significant advancement in turbulence, including the discovery of an underlying ordered structure [119]. While typically analyzed in a statistical manner, turbulence viewed through the lens of dynamical systems theory offers a deterministic description. Specifically, this approach has enabled the discovery of three-dimensional, fully nonlinear, exact solutions to the Navier-Stokes equations that not only describe transition to turbulence but also fully turbulent flow. These exact coherent solutions, specifically nonlinear traveling wave solutions, typically arise in pairs at a saddle-node bifurcation at a critical Reynolds number and consist of an upper branch solution and a lower branch solution. The lower branch solution is a low drag state compared to its corresponding upper branch solution. Dynamical systems theory implies that coherent structures can be considered low-dimensional invariant sets where the system spends a significant amount of time. Spatiotemporally organized structures materialize when a turbulent trajectory is in the neighborhood of these sets [102, 72, 229]. The significance of these invariant solutions lies in their ability to effectively describe the near-wall regeneration cycle
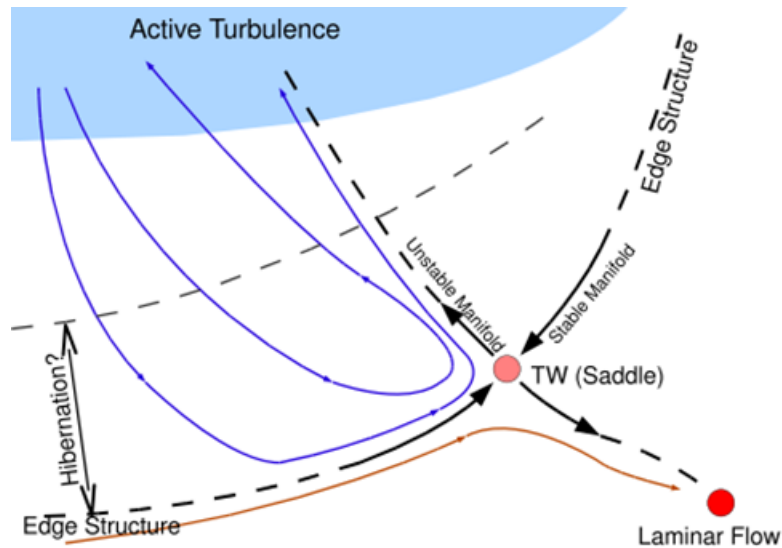
Figure 1.1: State-space depiction of turbulence showing the edge state in relation to the turbulent and laminar states [253].

[231, 259], capturing the dynamics and statistical features of turbulence [72, 233, 182].

Near-wall turbulence is known to oscillate periodically between high- and low-drag states, and the dynamical systems approach to turbulence has offered instructive insight into this behavior with the discovery of the lower- and upper-branch traveling wave solutions [119, 25, 50, 32]. Upper-branch solutions are characterized by large velocity fluctuations and chaotic structures while lower-branch solutions tend to resemble the laminar state more closely with small velocity fluctuations and gentler, streamwise-oriented coherent structures. Thus, invariant solutions have been referred to as the "building blocks" of turbulence [233, 234]. Typical turbulence trajectories are found to closely orbit the upper-branch solution for most of the time, only making infrequent excursions toward the lower-branch solution. While the upper-branch solution can capture the statistical nature of a typical turbulence trajectory, lower-branch solutions lie very close to the laminar state.

There exist distinct lower-branch solutions that are embedded on the boundary

between the laminar and turbulent basins of attraction [238], and are inherently unstable. Exemplifying a separatrix, these solutions separate the two behaviors of a fluid system, namely laminar and turbulent. Initial conditions on the turbulent "side" of the boundary become turbulent, while those on the laminar "side" of the boundary decay and become laminar. Lower-branch solutions on the boundary are significant as they only have one or two unstable eigenvectors and many stable eigenvectors, implying that there are many ways in which to approach these states, but only a few way in which to leave [238]. A state-space schematic illustrating this idea is shown in Figure 1.1 [253]. It is conceivable, then, to imagine control methods in which the trajectory of the system is steered toward these states and, subsequently, not allowed to leave by suppressing the most unstable directions. This has implications in fully turbulent flow control where the idea, generally, is to force the system toward the lower-branch solution, as well as in transition where the idea could be either to keep the system at the lower-branch solution longer (delay transition) or force it to leave sooner (promote transition).

1.2 Flow Control

Within turbulent flow there exist near-wall coherent structures responsible for the production of turbulent kinetic energy production [125, 2]. Near-wall motions result in the formation of structures known as streaks that are inherently unstable due to the spanwise dependence of streamwise velocity. These structures are formed in the laminar sublayer by streamwise vorticity and are slowly lifted upward, or ejected, away from the wall. Once the streaks begin to interact with the buffer layer, they experience more rapid oscillations and a sudden breakdown resulting in a burst of low-speed fluid from the wall into the bulk of the flow. This process is known as a turbulent burst
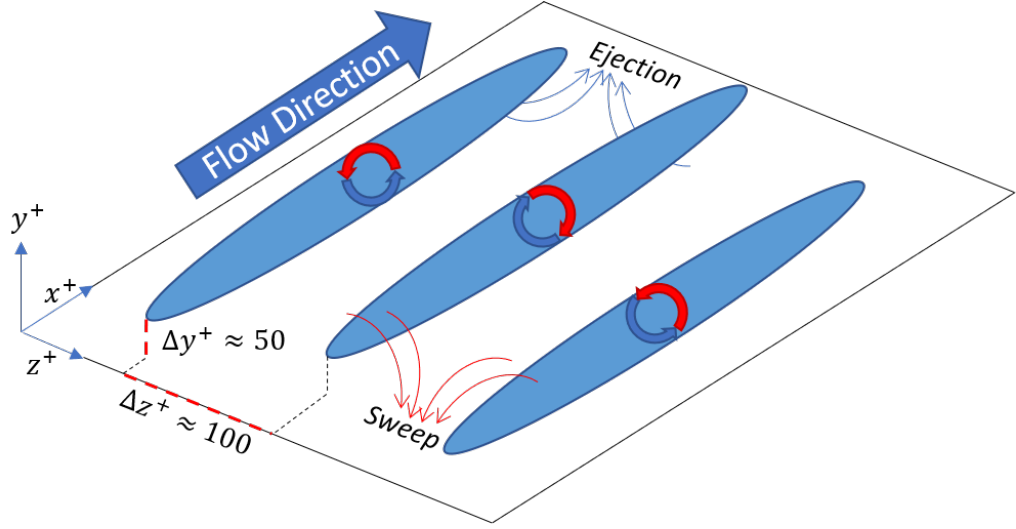
Figure 1.2: Schematic showing the ejection and sweep events associated with vortex structures in the near-wall self-sustaining turbulent process.

and creates finer-scale motions that lead to the formation of new vortices which, in turn, create more streaks. This process is self-sustaining and unaffected by the outer region of the boundary layer at low Reynolds number [231, 234, 125, 107]. As low-speed fluid is forced away from the wall via ejections, it creates areas of low wall shear stress. Simultaneously, high-speed fluid is forced down into the wall via sweeps creating areas of high wall shear stress. An illustration of the process is shown in Figure 1.2.

Thus, the regions of local wall shear stress that are created are highly correlated with these vortex structures – high shear stress under sweeps and low shear stress under the ejections. It becomes apparent, then, that perhaps the most efficient way to control turbulence in the near-wall region (which is responsible for most of the turbulent kinetic energy production in a flow) is to suppress the sweep and ejection events by manipulating the streamwise vortices responsible for their formation. To interrupt the self-sustaining process of turbulence, a multitude of approaches have

been taken in manipulating these structures.

Flow control is typically divided into passive and active control strategies, and meaningful progress has been made both experimentally and numerically using these techniques in furthering our understanding of turbulence. Passive flow control is appealing in that it requires no additional energy input into the system as it does not employ any sensing or actuation. Active control, however, allows for finer control of the system as it employs sensors and actuators that offer time-varying forms of control. As such, additional energy is required in active control. Actuation command may be either pre-determined (open-loop) or dependent on flow state monitoring via sensors (closed-loop). Closed-loop control typically makes the system very complex due to the actuators and sensors. Open-loop has the advantage of being relatively simple as it is predetermined (typically characterized by a harmonic function in space and/or time). The following sections outline notable control strategies used in flow control.

1.2.1 Passive Control

Because of their ease of implementation and lack of additional energy input, much research has been done using passive control methods. It is postulated that their ability to reduce drag in wall-bounded shear flows is due to an introduction of a transverse flow [117] that disrupts the flow structures of equilibrium turbulent flows [112]. In addition to the previously detailed use of superhydrophobic surfaces, a popular technique that has been widely adapted due to its success in drag reduction is directional roughness at the wall. These so-called riblets are streamwise microgrooves with sizes on the order of the viscous sublayer [66] and should be aligned with the local flow direction to achieve maximum drag reduction [117]. Riblets of different geometries have been tested in wind tunnels, achieving drag reductions of $\approx 10\%$ for flow over
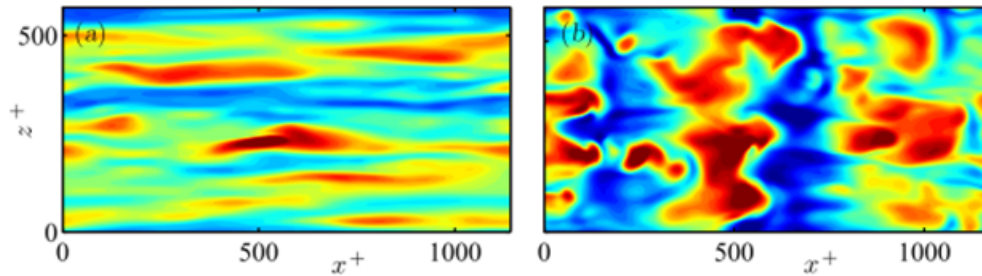
Figure 1.3: Instantaneous wall-normal velocity fluctuations for permeable surfaces with (a) low anisotropy and (b) high anisotropy [77]

.

a flat plate. While this value is smaller than those achieved with superhydrophobic surfaces, riblets have the added advantage of being useful in land and air applications. Riblets have been found to hinder the spanwise movement of the streamwise vortices which prevents their stretching during ejection events, weakening the subsequent sweep events [35]. Much work has been done to identify optimal spacing of riblets as this plays an important role in the drag reduction [66] but streamwise varying riblets, namely sinusoidally varying, have not been fully explored [67]. Kramer et al. [126] studied this type of varying spacing but found that drag reduction was much smaller than that of the wall-oscillation control that their study was based on. This was a result of the inability of the riblet spacing to elicit large enough oscillations in the flow. However, their spacing was based on much larger spacing of wall-oscillations, so sinusoidal riblets could be designed with shorter wavelength on the order of Kelvin-Helmholtz instabilities, or rollers, to inhibit their formation [67].

Anisotropically permeable substrates have also been considered for turbulent flow control. The general idea is to use surfaces which have high permeability in the streamwise direction and low permeability in the spanwise and wall-normal directions. This helps to minimize slip in the spanwise direction and transpiration in the wall-normal direction which are responsible for the formation of Kelvin-Helmholtz rollers.

If a control strategy can reduce the formation of the rollers, drag reduction can be achieved. Gomez-de-Segura and Garcia-Mayoral [77] have done work showing drag reduction of $\approx 25\%$ with the use of anisotropically permeable surfaces for passive flow control. Wall-normal velocity fluctuations using anisotropically permeable surfaces are shown in Figure 1.3.

1.2.1.1 Slip surfaces and their effect on flow behavior

Much work has gone into the design of slip surfaces, with ideas often stemming from a biomimetic point-of-view [48, 75, 147]. When designing slip surfaces, wettability is an important factor that can affect the validity of the no-slip assumption in certain flow systems. The no-slip condition is an assumption made that the velocity of a fluid flowing past a stationary solid surface is so small that its value may be approximated as zero [17]. While this assumption holds for most normal flow configurations, slip surfaces are a class of surfaces that are an overt exception to the rule. These surfaces are of great interest in a multitude of applications as they facilitate a non-zero velocity at the wall that may be formulated as $u_s = b(\partial u/\partial y)_{y=0}$, where the slip velocity u_s is proportional to the shear rate the fluid experiences at the wall, and the proportionality constant b is known as the slip length. The idea of a slip boundary was first introduced by Navier in 1823 [171] and later quantified by Maxwell in 1879 in the flow of rarefied gas [159].

Wettability Wettability is the propensity of a surface to promote liquid spreading, and is characterized by the spreading coefficient, $S = \gamma_{SG} - \gamma_{LG} - \gamma_{LS}$, where γ_{SG}, γ_{LG}, and γ_{LS} are the solid-gas, liquid-gas, and liquid-solid interfacial tensions, respectively [190]. When $S > 0$, a liquid will spread on a surface. Conversely, for $S < 0$, the liquid forms a droplet on top of the surface. Where the droplet meets the surface,

there is a well-defined contact angle θ. Given by a force balance known as Young's equation [265], contact angle of an "ideal", or smooth, surface may be calculated as $\theta = \cos^{-}1[(\gamma_{SG} - \gamma_{LS})/\gamma_{LG}]$. At equilibrium, surfaces with contact angle $\theta \geq 90 \deg$ are considered hydrophobic, while surfaces with contact angle $\theta \leq 90 \deg$ are considered hydrophilic.

Wettability is governed not only by the chemical composition of the surface but also by the topography of the surface. Two important wettability states of "real", rough surfaces are the Wenzel [244] and Cassie [29] states. In the Wenzel state, a liquid fully conforms to the roughness elements, while in the Cassie state, a liquid will rest on top of the roughness elements. There can also exist intermediate wetting states between these two modes. These states are shown in Figure 1.4 [60]. Transition between these two modes is achievable and occurs at a threshold contact angle $\theta_T = (f_s - 1)(r - f_s)$, where f_s is the area fraction of the solid and r is the surface roughness factor. If the Young's contact angle is less than the threshold, the system will assume a fully wetting Wenzel state and if the Young's contact angle is greater than the threshold, the system will assume a non-wetting Cassie state. It is not hard to conceive of methods to exploit this transition contact angle to control the wetting state of the system.

Static contact angle, alone, is insufficient to fully characterize the wettability of a surface. Due to surface roughness or other interfacial heterogeneities, a droplet can exist over a range of contact angles, falling between the advancing contact angle, θ_A, and the receding contact angle, θ_R [48]. The difference between the two is known as contact angle hysteresis [65] and has implications in fluid mobility at the interface. When the contact angle hysteresis is small, a droplet becomes unstable to small perturbations which allows for increased mobility, or less resistance [163]. Conversely, large contact angle hysteresis allows a droplet to become pinned to the surface, in-
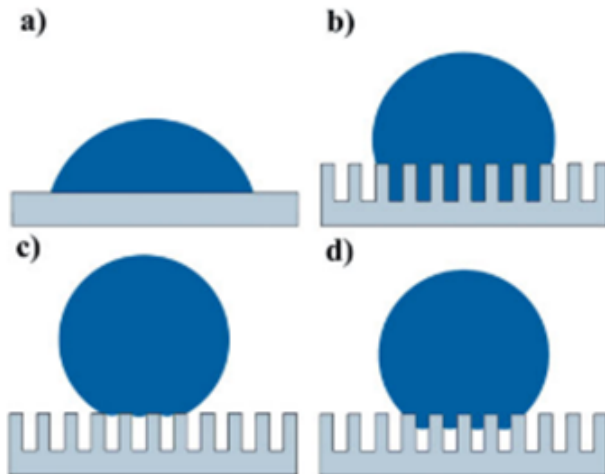
Figure 1.4: Surface structure effects on wettability. A) Liquid on flat substrate (Young's Mode). B) Wenzel's mode on rough surface. C) Cassie's mode on rough surface. D) Intermediate state. [60]

creasing the resistance to motion [190]. Thus, there is a so-called pinning force that must be overcome to initiate droplet motion on a surface, and this force may be related to a system's advancing and receding contact angles by $F = \gamma_{LG}(\cos\theta_R - \cos\theta_A)$ [190].

Certain stimuli-responsive materials can be manipulated using external excitation to reversibly modulate their surface wettability. Exploiting the sensitivity of a material's interfacial energy or morphology to external stimuli, reversible switches between superhydrophobicity and superhydrophilicity may be achieved. Considerable work has been done using micro-rod arrays that allow for directional wetting [40] and reversible switching between superhydrophobicity and superhydrophilicity [210]. Further advancement has been made that allows for the controlled actuation of these surfaces through pH, temperature, and electromagnetic stimuli [123, 89, 140, 88, 260] [39–43]. Notably, complex surfaces have been fabricated that allow for the autonomous reversible actuation of microstructures to maintain a user-defined variable, such as temperature [90]. Particularly relevant in fluid flow systems is a surface that

shows wettability response to applied stress [269].

Effect of slip surfaces on drag reduction In the last few decades, the allure of or slip surfaces for use in a multitude of flow applications has grown [75]. One large reason for the interest in slip surfaces is their demonstrated ability in reducing frictional resistance, or drag, in different flow configurations. Many studies have achieved significant levels of drag reduction via slip by placing hydrophobic surfaces at the walls in both laminar and turbulent flows. Ou et al. [176] were among the first to show experimentally the drag reduction using patterned superhydrophobic surfaces in laminar flow, and found a maximum drag reduction of 40% corresponding to slip lengths on the order of $\approx 25\mu m$. By precisely controlling the topography, the fabricated surfaces were found to operate in the Cassie wetting state, and the drag reduction was attributed to the increased shear-free area at the air-water interface [175]. Lee et al. [132] were able to produce surfaces with giant slip lengths approaching $\approx 200\mu m$ by deep reactive ion etching of silicon to obtain micro posts. These experiments were performed at the limit of where a stable interface can be maintained for a fluid in the Cassie state. As such, the practicality of such a surface for use outside of an ideal system comes into question.

Although new challenges arise, slip surfaces applied in turbulent flows have shown similar success. Absent in laminar flows, secondary flow structures are present in turbulent flows which are responsible for most of the turbulent kinetic energy production [125]. Therefore, possible nonlinear interaction between turbulent flow structures and the texture elements of slip surfaces must be considered. Min & Kim [163] were among the first to perform direct numerical simulations of a turbulent channel flow over slip surfaces, and found that streamwise slip promoted drag reduction while spanwise slip induced drag increase. These results were due to a weakening of the streamwise
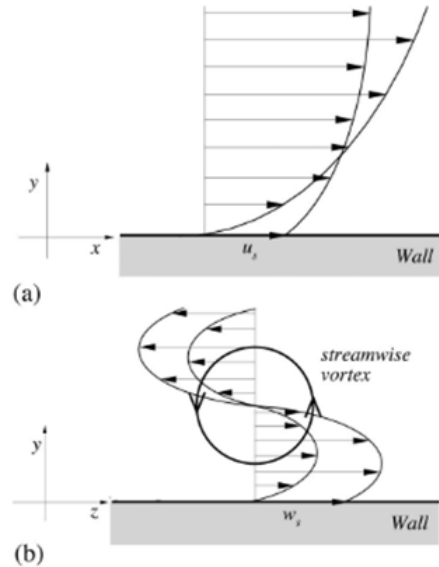
Figure 1.5: Schematic of drag decrease and increase mechanisms in turbulent flow for (a) Streamwise slip velocity and (b) spanwise slip velocity. [163]

vortices from streamwise slip and enhanced strength of the streamwise vortices from spanwise slip. These mechanisms are shown in Figure 1.5 [163]. In their computations, Martell et al. also found similar results in both drag reduction/increase and the responsible mechanisms [157]. Using experimental particle image velocimetry (PIV) methods, Jiang et al. found that the drag reduction in turbulent boundary layers over superhydrophobic surfaces was due to a weakening and shifting of the streamwise vortices away from the wall, resulting in a decrease in coherent structure bursting in the near-wall region [220, 270]. With the spectrum of geometries and Reynolds numbers used, drag behavior for turbulent flows over slip surfaces have ranged anywhere from a 50% increase in drag to as much as 70% decrease in drag [75].

Hydrophilic and hybrid surfaces have also been studied to determine their effectiveness at drag reduction in turbulent flows. Results for a hydrophilic coating for the hulls of marine vessels showed a reduction in friction, resulting in increased fuel efficiency [68]. They attributed the drag reduction to the presence of a water-

water shear area instead of water-surface shear area. A superhydrophilic surface with porous structure was analyzed both experimentally and computationally to elucidate the mechanisms associated with its drag reducing properties [218]. They found that vortices formed in the pores of the surface reduced the frictional drag by lowering the velocity gradient at the wall. However, the pores also introduced a pressure differential between the front and back wall of the pore based on its shape. Therefore, in order to have drag reduction, the friction reduction associated with the spanwise vortices must outweigh the drag introduced by the effect of increased pressure drop across the pores. Similar results were noted by Wang et al. [236]. Additionally, researchers have investigated hybrid surfaces with alternating superhydrophobic and hydrophilic areas [51]. Particularly useful, these surfaces have the ability to pin a layer of air at the boundary between hydrophobic and hydrophilic areas which increases the amount of area water-air interface resulting in skin-friction reduction [95].

Effect of slip surfaces on transition   Another classical problem (that is still not fully understood) in wall-bounded shear flows is the transition to turbulence [9, 13, 196]. The fundamental question of what causes a flow to undergo a change from a highly ordered laminar state in space and time to a chaotic turbulent state in space and time has puzzled the scientific community since its first observation by Osborne Reynolds in 1883 [194]. Several approaches have been developed to study the nature of transition. Directed percolation was proposed to conjecture the spatio-temporal intermittency observed in transitional flow [186, 211, 6, 139] [66–69]. Experimental studies have also been performed based on the observation of puffs and slugs associated with transition in pipe flows [12, 14]. More recently, the dynamical systems theory has provided qualitative and quantitative information on the transition to turbulence [92, 73].
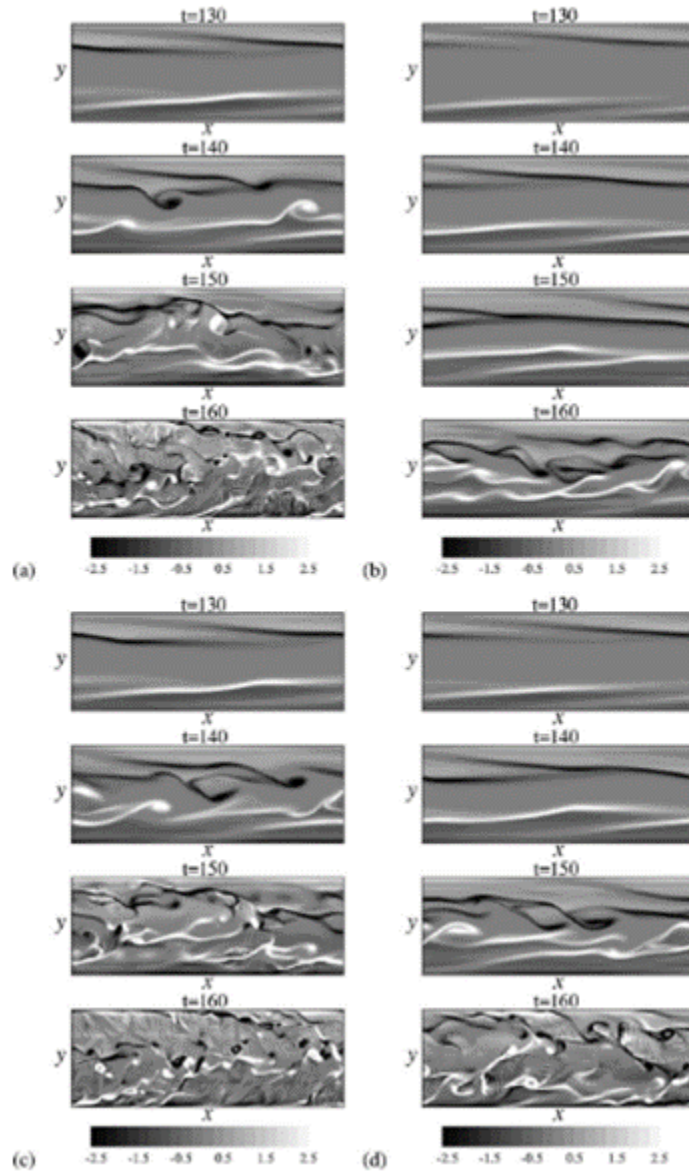
Figure 1.6: Spanwise vorticity at onset of transition for (a) no-slip, (b) streamwise slip, (c) spanwise slip, and (d) combined slip. [164]

While a large amount of effort has been put toward how slip surfaces affect turbulent drag reduction, a much smaller number of studies have been carried out on the effect of slip surfaces on the transition to turbulence. Additionally, most of these studies have concerned themselves with the linear stability analysis of the linearized Navier-Stokes equations. Min and Kim [164] first investigated temporal transition to turbulence over slip surfaces, where the linear stability analysis was applied to the linearized Navier-Stokes equations. They found an increased critical Reynolds number with streamwise slip, which was attributed to stabilizing the Tollmien-Schlichting waves. However, when spanwise slip was applied the critical Reynolds number was decreased, and a combination of the two caused a critical Reynolds number somewhere between the two limiting cases. This is shown in Figure 1.6. Other two-dimensional [214, 266] and three-dimensional [163, 129, 264] analysis on the stability of slip flows has been carried out. Global stability analysis was performed for flow around a superhydrophobic cylinder [8]. While most of studies have shown a stabilizing effect of the slip surfaces, still others have found these surfaces induce or amplify instabilities, triggering an early transition [39, 31]. Furthermore, a recent study by Picella et al. [184] showed that the effectiveness of slip surfaces in transition control may be dependent upon the initial perturbation to the system. They found that slip surfaces are effective at delaying transition initiated by near-wall perturbations but rendered ineffectual for control of transition triggered by free-stream turbulence. As such, there exists no strict consensus on the effects of slip on transition to turbulence, or in which transition scenarios slip surfaces are considered effective.

1.2.2 Active Control

To suppress near-wall vortex structures in a turbulent flow, Choi et al. [36] applied opposition control by using local blowing/suction at the wall. Using direct numerical

simulations, they altered the wall-normal velocity at the wall to be equal and opposite to the wall-normal velocity observed at $y^+ = 10$ to prevent momentum transport away from and toward the wall. This technique results in 30% reduction in drag at a friction Reynolds number of $Re_\tau = 180$. Examining the resultant flow fields, they found the near wall vortices to be weakened substantially. However, this method is impractical as it requires knowledge of the velocity fields at all times. An important result from this work, however, was that streamwise vortex structures could indeed be manipulated, leading to drag reduction. Subsequent work has shown that both the amplitude of blowing/suction and the wall-normal location of the detection plan play a vital role in the efficacy of opposition control [41]. In order to overcome the issues of opposition control, Lee et al. employed an artificial neural network to predict and control actuation in order to achieve a desired behavior, i.e. drag reduction [130]. Wall actuation in this manner resulted in a drag reduction of 20% at lower Reynolds numbers. The flow predicted flow fields from the neural network resembled those observed in the opposition control.

In the opposition control, it was observed that the blowing and suction resulted in an increased spanwise pressure gradient. This result informed Lee et al.'s next study to maximize the spanwise pressure gradient near the wall [131]. Using suboptimal methods, they sought to minimize the objective function over short time horizons $(T \to 0)$. This method resulted in $\approx 20\%$ drag reduction in turbulent channel flow at $Re_\tau = 110$. This new control scheme gave almost identical results to their previous study [130] but the two studies used completely different approaches. This method was then implemented in pipe flow by Xu et al. [258] with similar results. Bewley et al. [19] implemented a control scheme where the objective functions were minimized over a finite time period in turbulent channel flow at $Re_\tau = 100$. They achieved flow laminarization and drag reduction of over 50%. This work illustrated the need to

optimize controls over sufficiently long time periods ($T^+ \geq 25$).

Local wall-deformation has been employed based on the success of opposition control by Kang and Choi [116]. At $Re_\tau = 140$ a drag reduction of $\approx 15\%$ was achieved, which is less than that of the opposition control. The reduced efficiency is attributed to the fact that the area of effect of this method was limited to approximately 5 wall units in the wall-normal direction. Opposition control in channel flow was also implemented by Endo and Kasagi [58] in the form of wall-deformation to attenuate the spanwise motion of low-speed streaks. Drag reduction of 10% was achieved at $Re_\tau = 150$. Direct numerical simulations showed that channel flows with opposition-like control result in nullified wall-normal velocity component and momentum transport due to the appearance of a virtual wall [87] from the interaction between wall-normal velocity of the vortex and wall-normal velocity at the wall.

Pamiés et al. [178] have painfully pointed out that the gains associated with ideal opposition control can be completely nullified when considering realistic sensor and actuator placement. In their simulations, they used finite-sized actuators and found that the form drag resulting from the actuators nullifies any gains from the control. In ideal control, it is assumed that actuators and sensors are infinitely small, infinite in number, and can, subsequently, oppose flow structures at every point. In realistic settings, control is both confined and localized meaning that it can only act in a finite area at finite time intervals.

Studies have explored the possibility of flow control utilizing open-loop control schemes. Mito and Kasagi [166] studied drag reduction in turbulent channel flow with oscillating compliant wall. The deformation, which was comparable to the thickness of the viscous sublayer, is uniform in the streamwise direction and spatio-temporally sinusoidal in the spanwise direction. The skin-friction change is reflected in the vorticity fluctuations, and the receptivity of the induced flow structures changes with

the fluctuating skin-friction.

Similarly, effects of a streamwise traveling wave of blowing/suction [165] and wall-deformation [170] have been studied and found to reduce skin-friction, even leading to complete laminarization under certain parameter sets. The drag reduction is attributed to two factors when using traveling wave-like blowing and suction. The first is called the streaming effect, which results in a net mass flux in the opposite direction to the traveling wave even without a pressure gradient [91]. The control input assists in forcing the flow downstream, thus reducing the required external pressure gradient for a given flow rate. Therefore, properly design upstream traveling wave controls achieved significant drag reduction, and even sub-laminar in turbulent channel flow [165]. Mamori, Fukagata and Hoepffner [156] analyzed the phase relationship between the velocity fluctuations to find that the viscous effect induces near-wall phase shift between the streamwise and wall-normal fluctuations, thus generating Reynolds stresses that were responsible for the streaming effect. Additionally, the varicose mode has been found to be more effect for this than the sinuous mode [250].

The second factor responsible for drag reduction in this control scheme is a stabilizing effect that results from the interaction between the traveling wave-like control and the underlying wall turbulence structures. Lee, Min, and Kim performed stability analysis when an upstream traveling wave control was implemented and found that the resulting turbulent flow is destabilized, and, therefore, the drag reduction by Min et al. was a result of the streaming effect. The stability analysis also showed transient growth of streaks by amplification is significantly suppressed when using a downstream traveling wave control. Significant drag reduction and even relaminarization can be achieved when using downstream traveling wave control when parameters are based on the receptivity analysis. Mamori, Iwamoto, and Murata performed a parametric studying using downstream traveling wave control and were able to re-
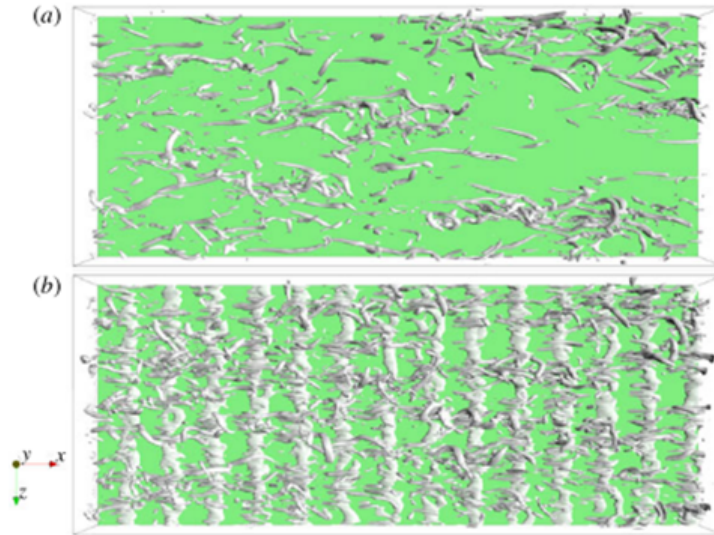
Figure 1.7: Flow structures in turbulent channel flow at $Re_\tau = 150$ for (a) the uncontrolled case and (b) the traveling wave-like control case [115].

laminarize a fully turbulent channel flow at $Re_\tau = 110$ and 300. Globally optimal open-loop control input has been obtained for turbulent channel flow using traveling wave-like blowing and suction to assess the dissimilarity in heat and momentum transport. The effect of this control on the flow structures at $Re_\tau = 150$ is shown in Figure 1.7. While open-loop control strategies are attractive in that they do not require large numbers of sensors, actuation of these controls is still challenging.

1.2.2.1 Polymer Additives

By introducing a small amount of long-chain polymers into a turbulent flow, substantial reduction of friction drag can be achieved, yielding a much higher flow rate at a given pressure drop. Drag reduction percentage up to 80% has been experimentally observed in straight pipe and channel geometries [226] [153] [80]. First discovered in 1940s [222, 223], this polymer-induced drag reduction phenomenon has persisted as an active research field owing to its practical and theoretical significance. Applica-

tions involve enhancing the energy efficiency in various fluid transportation sectors, such as oil-transfer in pipelines, marine propulsion, fire hydrant operations, and heating/cooling systems. On the other hand, the theoretical work lies in two significant research areas: turbulent flows and complex fluids. By understanding the mechanism of polymer-flow interactions and the dynamics of viscoelastic turbulence, we gain insight not only in polymeric fluids but also in turbulence itself, shedding light on another practical area: developing drag reduction schemes without polymer additives [144, 256, 257].

Although polymer drag reduction has been applied in the real world for decades, the underlying mechanisms remain poorly-understood. One most intriguing problem is that an upper limit of drag reduction, called maximum drag reduction (MDR), exists in all drag-reducing polymer systems. For a given Reynolds number, the maximum amount of drag reduction achieved is invariant with changing polymer species, molecular weight, concentration and the characteristic length scale in the flow geometry (pipe diameter or channel height). The universality of MDR and the mechanism whereby turbulence sustained at this regime are two essential questions that needs to be answered.

1.2.2.2 External Applied Body Force

A significant amount of drag-reduction (up to 40%) can be obtained by subjecting a wall flow to high frequency spanwise oscillations [112, 5]. Baron and Quadrio [15] suggested that the disruption of the spatial coherence between the longitudinal vortices and the low-speed streaks by oscillating a wall in the spanwise direction causes the vortices to pump the high-speed fluid away from the wall and low- speed fluid toward the wall, thus reducing the turbulent-energy production. The most widely accepted mechanism is given by Choi [38, 37] who proposed that the log mean

velocity profile is shifted upwards and mean velocity gradient is reduced at the wall due to the creation of a spanwise vorticity near the wall.

Similar results are obtained when an external spanwise force in the form of oscillations or traveling-wave is made to act near the wall. This form of force can be achieved by lining permanent magnets and electrodes alternately in the spanwise direction, and the direction of the spanwise force can be altered periodically by switching the polarity of electric current [97]. Up to 30% drag-reduction can be obtained from the wavy force [52], while the oscillatory form can result up to 40% drag-reduction [18]. However, the efficiency of this technique is usually very low [18, 96, 24] – the energy required to impose the desired force on the flow is more than the energy saved from drag-reduction, and the situation worsens at high Reynolds numbers [24].

1.3   Motivation and contributions

With the varied studies detailed herein, the main motivation behind this work is to elucidate underlying mechanisms associated with wall-bounded laminar and turbulent flows through the implementation of various flow control methods. The hope is that by applying various flow control techniques, which work to alter flow dynamics in distinct manners, the underlying mechanisms responsible for the transition to turbulence and the self-sustaining process of turbulence become clearer and can be used to develop reduced-order models and more informed flow control techniques for more efficient systems in the future.

Along the way, various questions related the efficacy of simulations, data-driven analysis techniques, and application of dynamical systems theory have arisen. These questions have blossomed into their own studies, with the hope that they expand the literature, help lead to answers of long-standing questions about the behavior of

transitional and turbulent flows, and elicit new questions from future researchers.

The major contributions from this work are as follows: (1) the broadening of understanding related to the mechanisms which cause the transition to turbulence via statistical and (newly developed) deterministic methods, (2) new knowledge related to the efficacy of certain simulation methods (i.e. Minimal Flow Units) used in wall-bounded turbulent flows, (3) characterization of intermittent flow dynamics at higher Reynolds number which may be useful in developing reduced-order models of turbulent flows, (4) investigation of combined drag reduction techniques for use in scaled systems, and (5) preliminary investigations into the application of data-driven techniques and dynamical systems theory in the analysis of turbulent systems.

Chapter 2

ON THE TRANSITION TO TURBULENCE AND SLIP SURFACES

[1]

2.1 Dynamics of laminar and transitional flows over slip surfaces

2.2 Introduction

In the last few decades, the allure of slip surfaces for use in a multitude of flow applications has grown [74]. Of particular interest is the demonstrated ability of slip surfaces in reducing frictional resistance, or drag, in many different configurations for both laminar and turbulent flows. Many studies have achieved significant drag reduction via slip by placing hydrophobic surfaces at the walls [152, 242, 163, 176, 224, 44, 21, 205]. However, a smaller number of studies have been performed on the effect of slip surfaces on the transition to turbulence with most limited to linear stability analysis of the linearized Navier-Stokes equations. Two-dimensional [214, 266] and three-dimensional [164, 129, 264] analyses on the stability of flows have been carried

---

[1]A portion of this work was published as Davis, E.A. and Park, J.S., *J. Fluid Mech.*, 894, A16 (2020)

out. While most of these studies have shown a stabilizing effect of slip surfaces leading to a delayed transition, others have found that these surfaces can induce or amplify instabilities and, subsequently, trigger early transition [39, 31]. Studies on a bluff body with a superhydrophobic coating have shown different results on the flow separation – delayed separation [84] and promoted separation [30]. Furthermore, a recent study by Picella et al. [184] found that slip surfaces may be effective at delaying transition for near-wall perturbations similar to ones observed in H-/K-type transition scenarios [124] but are rendered ineffectual for free-stream, or non-modal, perturbations similar to ones observed in a bypass transition scenario [167]. As such, there exists no strict consensus on the effects of slip surfaces on the transition to turbulence, or in which particular transition scenarios slip surfaces may be considered effective.

Interestingly, there have been doubts on the validity of the no-slip boundary conditions at the microscopic scale, showing that under certain circumstances, fluids can slip against solid surfaces [83, 215]. Various factors including wettability, surface roughness, presence of gaseous layers, and impurities can facilitate a non-zero fluid velocity at solid surfaces [47, 189, 172]. The idea of slip was first introduced by Navier, quantifying the slip velocity by the idea of a slip length [171]. The slip length relates the velocity of the fluid at the wall to the wall shear rate as

$$u_s = b \left. \frac{\partial u}{\partial y} \right|_w,$$
(2.1)

where b is the slip length or Navier's slip coefficient. The slip at the solid surface tends to increase the velocity at the wall, leading to skin-friction reduction. [164] investigated temporal transition to turbulence, where the linear stability analysis was applied to the linearized Navier-Stokes equations for a two-dimensional case, showing that the critical Reynolds number increases with the streamwise slip length

and decreases with spanwise slip length. A combination of the two results in a critical Reynolds number between the no-slip and limiting streamwise cases. More recently, superhydrophobic surfaces, which are a combination of surface chemistry and surface roughness at micro- and/or nano-scales, have been introduced for drag reduction [195]. These surfaces appear to lower the free energy of an air-water interface, producing a very high contact angle at the surface. There have been, of course, many studies on the effects of superhydrophobic surfaces on skin-friction reduction in laminar and turbulent flows [181, 134, 111, 133, 146, 78, 205, 59]. Thorough reviews of the effect of slip and superhydrophobic drag reduction on laminar and turbulent flows are given by Rothstein [195], Abdulbari et al. [1], and Lee et al. [133]. It is worth noting that there is a recent study that performs direct numerical simulations of a turbulent channel flow to predict the effective slip length and drag reduction with a lubricated micro-groove surface [33].

In addition to laminar and turbulent flows, a classical problem in wall-bounded shear flows is the transition to turbulence [9, 13, 196]. The fundamental question of what causes a flow to undergo a change from a highly ordered laminar state in space and time to a highly disordered turbulent state in space and time has been puzzled over since Osborne Reynolds in 1883 [194]. There have been several approaches to explore the nature of transition. The directed percolation has been proposed to conjecture the spatiotemporal intermittency observed in a transitional flow [186, 211, 6, 138]. The theoretical and experimental studies based on puffs and slugs have also been explored to study the dynamics of transition to turbulence [252, 173, 12, 14, 208]. Recently, the dynamical systems idea has emerged, enabling computation of non-trivial invariant solutions to the Navier-Stokes equations [119]. These solutions, considered as the building blocks of turbulence, have advanced our understanding of chaotic spatiotemporal flows [217, 221, 182, 183]. These spatially and temporally

well-organized solutions have been observed in all turbulent shear flows, both in experiments and simulations [92, 73], and have been used to help provide qualitative and quantitative information about the transition to turbulence.

We focus here on the dynamical systems approach, which has greatly advanced the understanding of the nature of the transition to turbulence [120, 56, 154]. Specifically, the discovery of three-dimensional fully nonlinear traveling wave (TW) solutions to the Navier-Stokes equations has enabled *a priori* study of the transition to turbulence. These solutions are also denoted as exact coherent states (ECS) since they capture the essential structural and statistical features of a turbulent flow, featuring the near-wall self-sustaining process [233]. They primarily arise in pairs from a saddle-node bifurcation at a particular Reynolds number, consisting of upper- and lower-branch solutions – both of which are unstable. These lower- and upper-branch TW solutions can, thus, be thought of as saddle points in the state-space and turbulent trajectory moves dynamically between these saddle points [182]. More interestingly, the onset Reynolds number for TW solutions to come into existence is quantitatively in good agreement with the Reynolds number for transition to turbulence, corresponding to a spanwise period of 100 wall units [27]. Interestingly, the subcritical nature of these bifurcations of TW solutions has shed light on some features of subcritical turbulent transition such as patterned turbulence [225]. Most of these ECSs have been found in so-called minimal flow units —- they are spatially periodic in the unbounded dimensions of the domain with periods that roughly correspond to the smallest length scales at which turbulence can persist [105]. In addition, localized ECSs in extended domains have also been found to show flow structures resembling the observed spatiotemporal intermittency and the laminar-turbulent patterning that are a common feature of turbulence near transition [11, 23]. [11] found a particular family of localized ECSs for pipe flow that shows features similar to puffs, which

resemble localized turbulent regions in a transitional pipe flow. [267] also found a family of localized ECSs for a plane Poiseuille flow. However, their connections to turbulence transition are still unclear.

Another important issue regarding ECSs is their connection to the laminar-turbulent boundary, or separatrix. This boundary separates the basins of attraction of laminar and turbulent flows [202, 53], and this boundary is inherently unstable. Initial conditions on the turbulent side of the boundary become turbulent, while those on the laminar side laminarize. Initial conditions on this boundary stay on it – they neither become turbulent nor do they relaminarize. There are theoretical arguments that the stable manifold of the lower-branch ECS forms a part of this boundary [237, 118]. If an ECS on the basin boundary has a single unstable eigenvalue and many stable eigenvalues, there are many ways in which trajectories can approach it, but there is only one way to leave. Such ECS has been called an edge state [212]. Some of the lower-branch ECSs are also found to lie on the basin boundary, but they have multiple unstable eigenvalues so are not edge states [182]. The dynamics of trajectories on or near the basin boundary are intermediate between laminar and turbulent flows and thus thought to play an important role in the dynamics of transition to turbulence.

Because of the clear importance of the lower-branch ECSs for the transition to turbulence and proximity to the basin boundary, the present work focuses on the effects of slip surfaces on these ECSs embedded on the laminar-turbulence boundary. It will provide an excellent simplified, yet still exact, model flow for studying the nature of the transition to turbulence. The leading order effect of the slip surfaces on the ECS is one important focus of the present study for identifying dynamics of the transition. The connection between ECSs and slip surfaces has yet to be fully explored and will be investigated in the present study. The nature of turbulence

transition will be identified with respect to ECSs on the laminar-turbulent separatrix found by [182].

We focus here on a channel flow of an incompressible Newtonian fluid with dynamic viscosity μ, density ρ and kinematic viscosity $\nu = \mu/\rho$ in a channel of half-height h. In this geometry, the critical Reynolds numbers are $Re = U_c h/\nu \approx 1000$ and $Re_\tau = u_\tau h/\nu \approx 45$ based on the laminar centerline velocity U_c and friction velocity u_τ, respectively [27, 187]. The laminar and transition flow regimes in a range of $120 < Re < 1800$ ($8 < Re_\tau < 85$) will be considered in the present study. Two lower-branch ECSs (labelled P3 and P4 below) will be considered as they are on the basin boundary – P3 is indeed an edge state as it has only one unstable eigenvalue. It is worth noting that, to our knowledge, there have been only two modes of the exact coherent solutions [233, 73, 229, 169, 70, 182], namely core mode and critical layer mode. P3 and P4 solutions display characteristics of each mode, respectively. Therefore, by examining the P3 and P4 solutions, it is believed that the essential effects of slip surfaces on transition dynamics will be encapsulated.

This paper is organized as follows: Section 2.3 presents the problem formulation for the current study. A validation of the current simulations is given in Section 2.4.1 by comparing drag reduction of laminar flows. To better understand the effect of the slip on the transition, the effect of slip on turbulence lifetimes is presented in Section 2.4.2. Additionally, the effect of slip surfaces on the transition to turbulence is studied using traveling wave solutions to the Navier-Stokes equations in Section 2.4.3. Finally, a summary and implications of the present investigation are given in Section 2.5.

2.3 Problem Formulation

We consider an incompressible Newtonian fluid in the plane Poiseuille (channel) geometry, driven by a constant volumetric flux Q. The x, y, and z coordinates are aligned with the streamwise, wall-normal, and spanwise directions, respectively. Periodic boundary conditions are imposed in the x and z directions with fundamental periods L_x and L_z, and streamwise Navier slip conditions are imposed at the walls $y = \pm h$, where $h = L_y/2$ is the half-channel height. The laminar centerline velocity for a given volumetric flux is given as $U_c = (3/4)Q/h$. Using the half-height h of the channel and the laminar centerline velocity U_c as the characteristic length and velocity scales, respectively, the nondimensionalized Navier-Stokes equations are then given as

$$\nabla \cdot \boldsymbol{u} = 0, \quad \frac{\partial \boldsymbol{u}}{\partial t} + \boldsymbol{u} \cdot \nabla \boldsymbol{u} = -\nabla p + \frac{1}{Re_c}\nabla^2 \boldsymbol{u}. \tag{2.2}$$

Here, we define the Reynolds number for the given laminar centerline velocity as $Re_c = U_c h/\nu$, where ν is the kinematic viscosity of the fluid. Characteristic inner scales are the friction velocity $u_\tau = (\bar{\tau}_w/\rho)^{1/2}$ and the near-wall length scale or wall unit $\delta_\nu = \nu/u_\tau$, where ρ is the fluid density and $\bar{\tau}_w$ is the time- and area-averaged wall shear stress. As usual, quantities nondimensionalized by these inner scales are denoted with a superscript "+". The friction Reynolds number is then defined as $Re_\tau = u_\tau h/\nu = h/\delta_\nu$. Streamwise Navier slip conditions are prescribed as equation (2.1) at both top and bottom walls by an effective homogeneous slip length, $L_s = b/h$. To verify that the slip length can be realistically obtained by practical slip surfaces with roughness features, the length scale L^+ of the micro roughness can be calculated using equation (2.4) of Picella et al. [184], enabling a direct comparison with ones in the literature. Using the largest slip length studied ($L_s = 0.02$) and the solid fraction $\phi_s = 0.25$ used in Min and Kim [164], the largest texture size of the current

study is $L^+ \approx 7$, which ensures that the homogeneous slip surface employed in the present study would provide virtually the same outcomes resulting from employing a heterogeneous microtextured slip surface [262, 206, 184].

Simulations are performed using the open source code *ChannelFlow* written and maintained by [69]. In this study, we focus on the domains of $L_x \times L_y \times L_z = 2\pi \times 2 \times \pi$ and $L_x \times L_y \times L_z = \pi \times 2 \times \pi/2$, which are the same box sizes as the TW solution families dubbed P3 and P4, respectively [182]. A numerical grid system is generated on $N_x \times N_y \times N_z$ (in x, y, and z) meshes, where a Fourier-Chebyshev-Fourier spectral spatial discretization is applied to all variables. A typical resolution used is $(N_x, N_y, N_z) = (48, 81, 48)$. The numerical grid spacing in the streamwise and spanwise direction are $\Delta x^+_{min} \approx 8.2(4.7)$, $\Delta z^+_{min} \approx 4.1(2.3)$ for the P3 and (P4) cases. The nonuniform Chebyshev spacing used in the wall-normal direction results in $\Delta y^+_{min} \approx 0.05$ at the wall and $\Delta y^+_{max} \approx 2.5$ at the channel centre for both P3 and P4 cases. For simulations, a range of $120 < Re < 1800$ ($8 < Re_\tau < 85$) is considered to cover laminar and transition flow regimes. For exact coherent solution, $Re_\tau = 62.52$ and 71.72 are considered for P3 and P4, respectively, as these are the inherent Reynolds numbers at which the P3 and P4 solutions emerge.

2.4 Results and Discussion

2.4.1 Laminar drag reduction: a validation

For the sake of testing the code, the effect of the slip surfaces on laminar flows was investigated. Drag reduction percentage ($DR\%$) was calculated to compare to previous studies and is given by:

$$DR\% = \frac{f_0 - f}{f_0} \times 100, \tag{2.3}$$
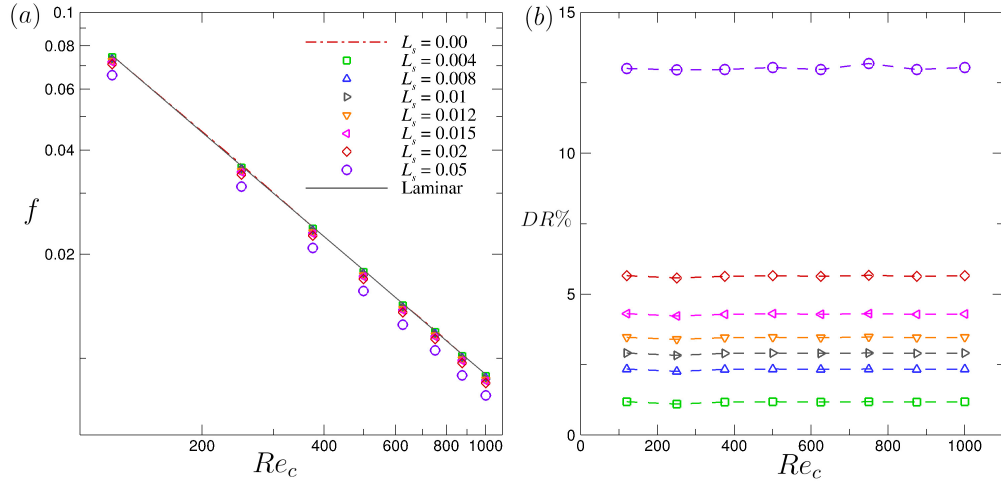
Figure 2.1: (*a*) Friction factor and (*b*) drag reduction percentage as a function of Reynolds number for various L_s values. In (*a*), laminar flow (solid line) corresponds to $f = 9/Re$ [187]. In (*b*), the dashed lines are shown for readability.

where f is the friction factor for the slip surface and f_0 is the friction factor for the no-slip surface at the same Reynolds number: $f = \bar{\tau}_w/(1/2\rho U_b^2)$, where U_b is the bulk velocity. Figures 2.1(*a*) and (*b*) show the friction factor and drag reduction percentage as a function of Reynolds number for various slip lengths, respectively. As seen in figure 2.1(*a*), the friction factor is shifted downward when slip length is increased, while maintaining the same slope as laminar case. Therefore, the relative change in wall shear stress or pressure drop with Reynolds number remains constant and the drag reduction from equation (2.3) is constant for each slip length. Figure 2.1(*b*) confirms that $DR\%$ is almost constant at each slip length regardless of Reynolds number. The same trend of constant drag reduction percentage in the laminar regime has also been observed previously [176], where an increase in drag reduction resulted from increasing slip length, alone, and was not a function of flow rate.

To further validate the present study, drag values (f/f_0) were compared to those of previous studies using superhydrophobic surfaces in laminar flows. Figure 2.2 shows
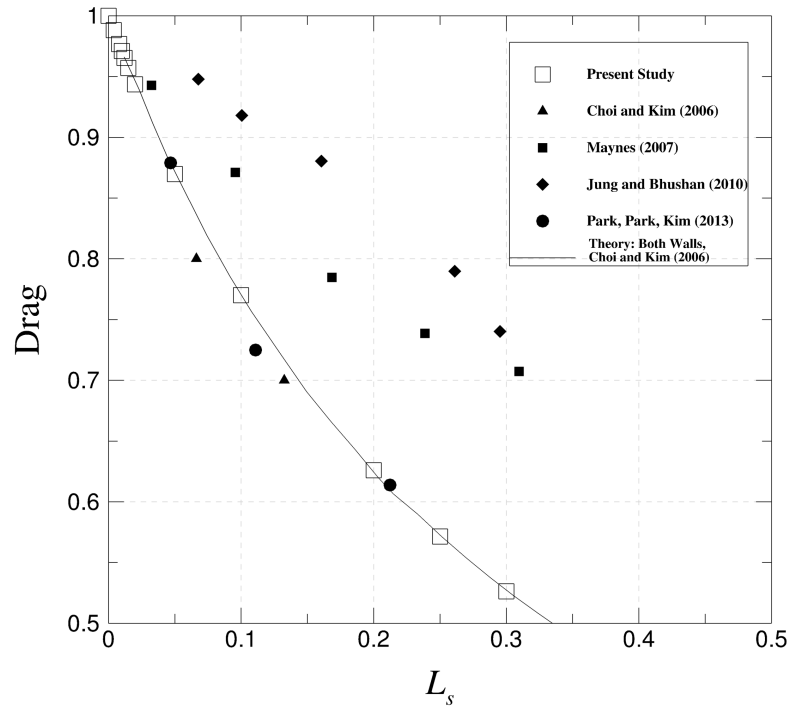
Figure 2.2: Drag (f/f_0) corresponding to the friction factor (f) normalized by that of the no-slip surface (f_0) as a function of slip length L_s normalized by the channel half-height, h: $\square$, present study; $\blacktriangle$, [34]; $\blacksquare$, [160]; $\blacklozenge$,[113]; $\bullet$, [180]; $-$, theory for superhydrophobic surfaces on both walls [34].

the results for the drag value observed in the laminar regime for previous studies (closed symbols) and the current study (open symbols) along with a curve for the theory for the superhydrophobic surfaces on both walls. As expected, the drag values decrease with increasing slip length. Notably, the current study is in great agreement with the theory proposed by Choi and Kim [34] for superhydrophobic surfaces on both channel walls.

2.4.2 Turbulence lifetimes: statistical insight into transition to turbulence over slip surfaces

A common approach used in the study of flow control and its effect on the transition to turbulence is to compute the turbulence lifetime of the flow. This lifetime gives a more physical interpretation of the effects of the flow control on the flow and on the modified distance between the turbulent state and the edge of turbulence in phase space. Ibrahim et al. [100] showed that opposition control in both Couette and Poiseuille flows plays a role in increasing the probability of escaping from the chaotic saddle of turbulence in phase space. In this regard, the effect of slip surfaces on altering turbulence lifetime statistics was investigated. Similar to the procedure used by Ibrahim et al. [100], 100 different turbulent flow fields were created by running simulations at an elevated Reynolds number. These 100 flow fields were then used as the initial conditions for the turbulence lifetime study at the nominal Reynolds number (i.e. flow fields created at $Re_c = 1900$ were used as initial conditions for the turbulence lifetime study at $Re_c = 1800$). The temporal evolution of the wall shear stress was tracked up to $t = 5000$ for four different slip lengths: $L_s = 0.00, 0.008, 0.01$, and 0.02. Note that the slip length for the current study is already in dimensionless form $L_s = b/h$, where h is the channel half-height. If a flow laminarizes, the time it takes for the wall shear stress to reach its laminar value is considered the turbulence lifetime. Probability of turbulence can then be computed as a function of time for each value of L_s by defining it as the fraction of the 100 turbulent flow fields that remain turbulent up to a given time t.

Figure 2.3 shows the probability of turbulence lifetimes for various Reynolds numbers at slip lengths of $L_s = 0.00, 0.01$, and 0.02. The probability is found to approximately follow an exponential distribution that is characteristic of turbulence lifetimes
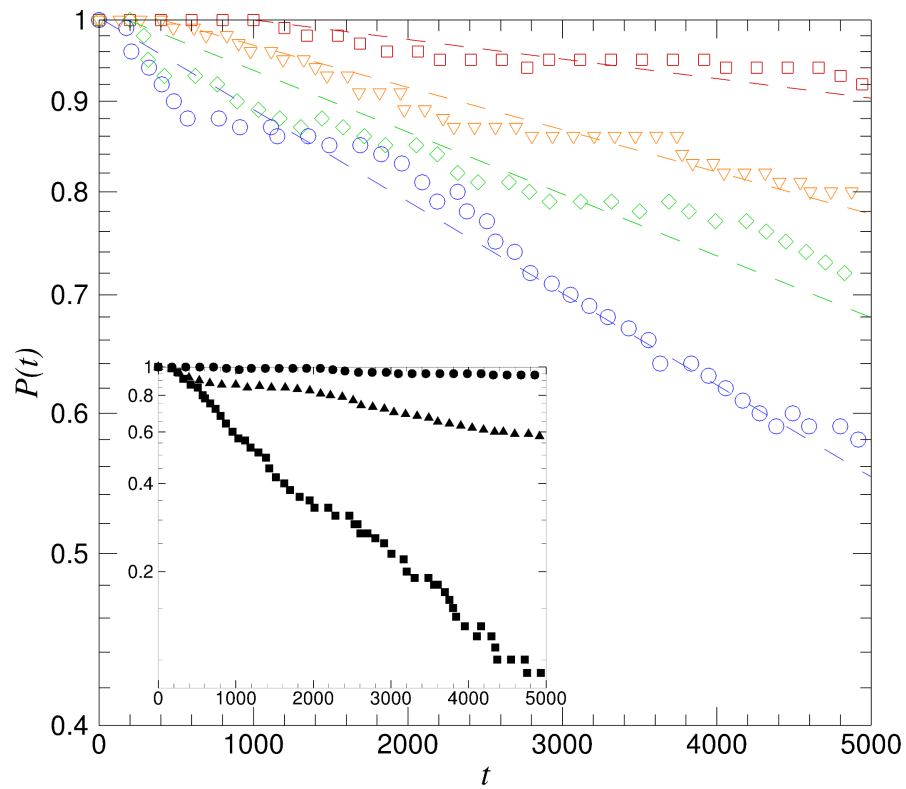
Figure 2.3: Probability of turbulence lifetime for slip lengths $L_s = 0.00$ ($\square$), 0.008 ($\triangledown$), 0.01 ($\diamond$), and 0.02 ($\circ$) at $Re_c = 1800$ on semi-logarithmic axes. The dashed lines are shown for readability to help illustrate the exponentially decaying trend. Inset: Dependence of Reynolds number on turbulence lifetime at $Re_c = 1600$ ($\blacksquare$), 1800 ($\blacktriangle$), and 2000 ($\bullet$) at $L_s = 0.02$.

[57]. It should be noted that the probability of turbulence does decrease for the no-slip case in the transitional flow regime. Given sufficient time and domain size and the nature of initial conditions, it has been shown that there is a tendency for turbulence to decay as a result of a transient process in shear flows [200, 22, 93, 10, 201]. As intuition might suggest, the probability of sustained turbulence at a given time decreases as slip length is increased, indicating a stabilizing effect on the flow. As was investigated by Min and Kim [164], the addition of a streamwise slip velocity stabilizes a flow by which it is likely that the probability of turbulence persisting decreases as streamwise slip length is further increased. While this trend holds for the three Reynolds numbers studied here–$Re_c = 1600, 1800$, and 2000–the effectiveness of a given slip surface decreases with increasing Reynolds number. In other words, as Reynolds number increases, larger slip lengths are needed to obtain the same effect. Notably, the slip lengths studied here have little effect on the flow at $Re_c = 2000$, with a final reduced probability of sustained turbulence of $\sim 94\%$ at the largest slip length examined. Note that the effect of slip surfaces on turbulence lifetime may be interpreted as a reduction of the Reynolds number, which was observed by Min and Kim [163] and Fukagata et al. [64]. These results suggest that the phase space of turbulence may be altered by slip surfaces in such a way to facilitate transition back to the laminar state. This same trend in turbulence lifetime was also observed when using increasing levels of opposition control in channel flow [100].

2.4.3 Exact coherent solutions: a deterministic analysis of the laminar-turbulent separatrix over slip surfaces

We now discuss the effect of slip surfaces on the laminar-turbulent separatrix using exact coherent solutions or travelling-wave solutions to the Navier-Stokes equations. Two travelling-wave solution families, dubbed P3 and P4, were used as the lower-

branch solutions for these two families are embedded in the laminar-turbulent separatrix [182]. The P3 lower-branch solution is indeed an edge state as it has only one unstable eigenvalue in the symmetric subspace, while the P4 lower-branch solution has two unstable eigenvalues in its symmetric subspace (Details of the P3 and P4 solution methods are given in Appendix A.4). The edge state is particularly important because as defined, it implies somehow the weakest, most marginal structure of the basin boundary. In addition, these two solutions were chosen due to their distinct flow structures – the P3 and P4 families are denoted as core and critical layer modes, respectively. This implies that the flow structures for the these solutions propagate in either the core, or bulk, of the flow or centered about the critical layer. As aforementioned, to our best knowledge, the exact coherent solutions that have been found thus far have exhibited flow structures that belong to either the core or critical mode. These modes are also analogous to the modal/non-modal perturbations that have been examined in the classical transition scenarios [251, 184]. Recently, the P4 solution is found to display hairpin-like vortex structures [207]. Additionally, a recent study by Picella et al. [184] found that by using linear stability analysis, slip surfaces have distinct effects on different transition scenarios defined by the initial perturbations applied to the base flow, namely, modal, near-wall perturbations and non-modal, free-stream perturbations. Thus, it is anticipated that the effect of slip surfaces on these solution families exhibit distinct transition dynamics.

Here, we ran simulations using the P3 and P4 lower-branch solutions as initial conditions to investigate the effects of slip surfaces on the separatrix and to elucidate transition dynamics. Using an exact coherent solution (i.e., a traveling-wave solution), a more deterministic approach can be taken in analyzing the effects of slip surfaces. The P3 and P4 lower-branch solutions used are $Re_c = 1760$ ($Re_\tau = 62.52$) and $Re_c = 1800$ ($Re_\tau = 71.72$), respectively. These Reynolds numbers were chosen, in particular,

because it is close to their bifurcation Reynolds numbers but far enough to ensure that they are embedded within the laminar-turbulent boundary.

2.4.3.1 Skin-friction evolution

Figure 2.4 illustrates the temporal behaviours of the skin-friction coefficient $C_f = \bar{\tau}_w/(1/2\rho U_c^2)$ normalized by initial values of each case using various L_s values. Despite their distinct characteristics, the early-time behavior of the skin friction of the P3 and P4 solutions is similar: (1) an initial stable period, (2) a sharp increase, or a strong turbulent burst, following the stable period, and (3) transition to a fully turbulent flow (for P4, a flow is relaminarized beyond $L_s > 0.0105$). This temporal behaviour indeed resembles a typical scenario observed in transition to turbulence [199]. The strong turbulent burst, as it shall be called presently [183], is the process of escape out of the exact coherent solution along its most unstable manifold, comprising of the so-called linearly unstable stage followed by the nonlinear evolution stage [101]. The end of this strong turbulent burst is then defined as the time when the skin friction reaches its maximum. It is evident that distinct transition scenarios are observed between the P3 and P4 solutions by the evolution of the skin friction due to inclusion of the slip surfaces.

Notably, as shown in figure 2.4, the duration of the initial stable period decreases with slip length for the P3 solution, while the duration of this period increases with slip length for the P4 solution. It suggests that the P3 and P4 solutions experience early transition and delayed transition due to slip surfaces, respectively. For the P3 solution, the slip length appears to have a negligible effect on the reduction in maximum skin friction during the strong turbulent burst as the slip length is further increased. However, the behavior of the strong turbulent burst for the P4 solution is quite different. The maximum skin friction reached during the strong turbulent burst
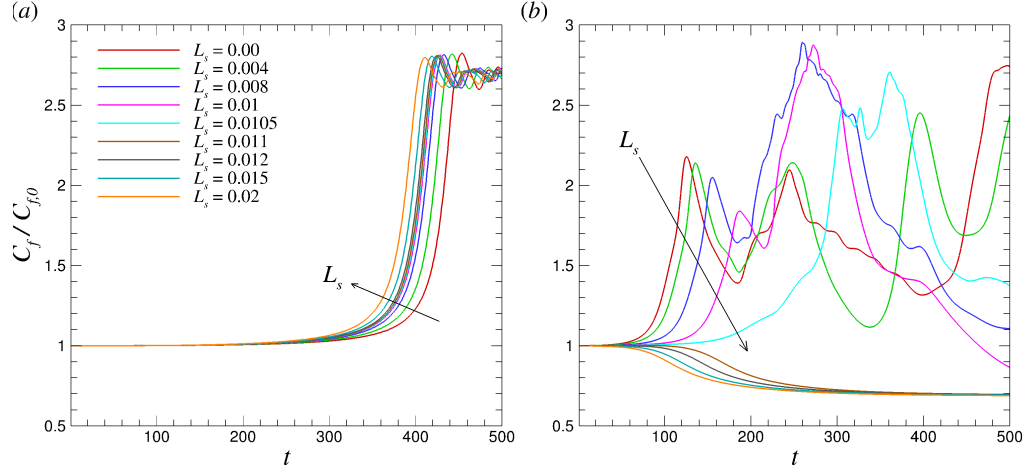
Figure 2.4: Early-time skin-friction coefficient profiles when using the (a) P3 and (b) P4 lower-branch travelling-wave solutions as initial conditions. Profiles are normalized by the initial skin-friction coefficient value for each case. The P3 and P4 lower-branch solutions are on the laminar-turbulent separatrix.

following the initial stable period decreases with increasing slip length. This trend continues until a critical slip length ($L_s = 0.0105$) after which there is no turbulent burst and the flow starts to laminarize after an initial stable period. If slip length is further increased, the initial stable period starts to reduce in duration and eventually the flow immediately laminarizes with negligible initial stable period for very large slip lengths. These observations for the P4 solution suggest that a slip surface appears to stabilize a flow and promote a return to the stable laminar state beyond the critical value ($L_s = 0.0105$). Thus, it is evident that the slip surfaces provide distinct effects on the laminar-turbulent separatrix of the P3 and P4 solutions.

To further characterize the temporal dynamics observed in the behaviors of the skin friction, figures 2.5(a) and (b) show the maximum skin-friction achieved during the turbulent bursting period and the duration of the initial stable period, respectively. Here, we define the bursting skin friction coefficient as $C_{f,b} = C_{f,max} - C_{f,0}$, where $C_{f,max}$ is the maximum skin-friction at the end of the bursting period and $C_{f,0}$

is skin friction at initial time. The stable period, T, is defined as the duration for which skin friction continues to stay between $\pm 10\%$ of the initial skin-friction value depending on the direction of the trajectories: 10% for bursting direction and -10% for laminarization direction. Both quantities are normalized by the associated values of the no-slip case. For the P3 solution, the magnitude of the turbulent burst remains relatively constant with slip length – the slip surface has a negligible effect on skin friction reduction during the strong burst phase of the transition. The stable period slightly decreases with slip length and for a very substantial slip length of $L_s = 0.02$, the stable period is reduced by approximately 10% of the no-slip case. This observation indicates that slip surfaces cause the turbulent burst to occur sooner with almost same magnitude, promoting an early transition to turbulence. For the P4 solution, on the other hand, the magnitude of the turbulent burst decreases almost asymptotically with slip length up to a critical value of $L_s = 0.0105$. After the critical slip length, there are no turbulent burst events because the flow becomes laminarized. Interestingly, the stable period of the P4 solution shows a non-trivial behaviour. It increases until reaching a critical value at $L_s = 0.0105$ and starts to decrease because laminarization occurs sooner with slip length. Before the critical slip length, the slip length appears to play a role in delaying the transition to turbulence, as opposed to the P3 solution. It is worth noting that the dependence of the Reynolds number was tested by using different values of the Reynolds number in the transitional regime, where almost identical trends were produced for the P3 and P4 solutions (not shown).

2.4.3.2 Linear growth rate in transition

We estimate the growth rate of the linearly stable stage along the turbulent burst trajectories for the P3 and P4 solutions by introducing a time-dependent variable $s(t) = ||\boldsymbol{u}(t)|| - ||\boldsymbol{u}(t_0)||$, where $||\boldsymbol{u}(t)||$ and $||\boldsymbol{u}(t_0)||$ are the L^2-norm of the velocity
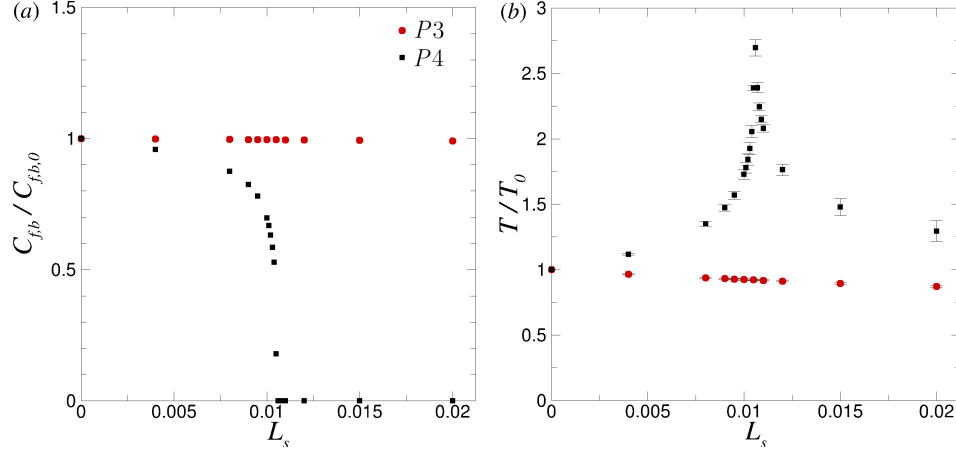
Figure 2.5: (*a*) Maximum skin-friction coefficient C_f in turbulent burst and (*b*) duration of initial stable period. The duration of stable period is defined by the time for which C_f is between $\pm 10\%$ of $C_{f,0}$ and normalized by the duration of the initial stable period for the no-slip case. Lower and upper error bars correspond to values when using $\pm 5\%$ and $\pm 15\%$ of $C_{f,0}$, respectively.

field at time t and initial time t_0, respectively. Given the definition of the turbulent burst as an escape from the exact coherent solutions consisting of linearly unstable and nonlinear unstable stages, the linear growth rate can be estimated by fitting the linear portion of a bursting trajectory observed in $s(t)$ to an exponential function $Ae^{\sigma t}$, where A is a constant related to the magnitude of the unstable eigenvector and σ is the associated growth rate [71].

Figure 2.6 shows the evolution of $s(t)$ and the growth rate of the P3 and P4 solutions for various slip lengths. The growth rate for the P3 solution tends to increase linearly with slip length, which is not all surprising given the trend seen in the skin friction in figure 2.4(*a*). Conversely, the growth rate for the P4 solution decreases almost asymptotically with slip length. This same trend was observed in the turbulent burst value in figure 2.5(*a*). Again, the escape from the P3 solution occurs earlier with increasing slip length, while the escape is delayed for the P4 solution. It should also be noted that the values of the growth rate for the P3 solution are lower than
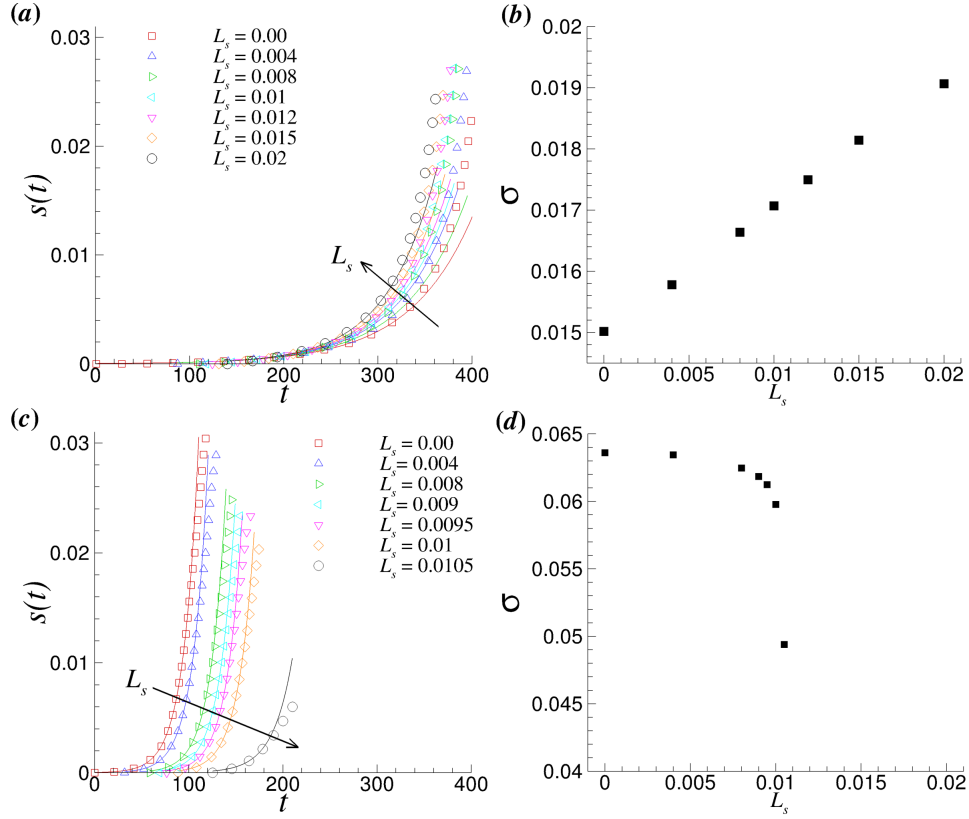
Figure 2.6: Growth rates for the P3 (a, b) and P4 (c, d) solutions for various slip lengths. The growth rate can be approximated for short time during which the system behaves like $\exp(\sigma t)$, where σ s the linear growth rate.

those for the P4 solution as the P3 is believed to be closer to laminar state [182]. In addition, since the escape process from an exact coherent solution follows closely its unstable manifold associated with the most unstable eigenvalue, those growth rate values are comparable to the most unstable eigenvalues of these solutions [182, 183].

2.4.3.3   Phase-space dynamics with slip surfaces

Here, we investigate the phase-space dynamics for the P3 and P4 solutions over slip surfaces by projecting the dynamics onto the I-D space, where I and D are the energy input rate and energy dissipation rate, respectively. For the current study (Poiseuille

flow), the energy input rate is given as

$$I = \frac{1}{2L_z} \int_0^{L_z} \int_{-1}^{1} (pu|_{x=0} - pu|_{x=L_x}) dydz \qquad (2.4)$$

and the energy dissipation rate is given as

$$D = \frac{1}{2L_x L_z} \int_0^{L_z} \int_{-1}^{1} \int_0^{L_x} (|\nabla u|^2 + |\nabla v|^2 + |\nabla w|^2) dxdydz. \qquad (2.5)$$

The total energy of the flow is defined by

$$E = \frac{1}{2L_x L_z} \int_0^{L_z} \int_{-1}^{1} \int_0^{L_x} (u^2 + v^2 + w^2) dxdydz \qquad (2.6)$$

and, thus, the rate of change in energy for the flow is equal to $dE/dt = I - D$. For exact coherent solutions, $D = I$.

Figures 2.7(a) and (b) shows the I-D phase diagrams of transition and turbulent trajectories starting from P3 and P4 lower-branch solutions, respectively, along with their corresponding upper-branch solutions. A joint probability density function (PDF) of turbulent trajectories for no-slip case is also plotted. In figure 2.7(a), all trajectories from the P3 lower-branch solution with different slip lengths exhibit a qualitatively similar trend. Starting from the lower-branch solution, they approach the upper-branch solution, make a turn around the equilibrium line ($D = I$), and move toward a core region of PDF. However, as slip length is increased, the trajectory tends to approach the equilibrium line earlier and then move toward the core region. Therefore, larger slip lengths allow a flow to approach a turbulent state faster, promoting an earlier transition to turbulence, as seen in figure 2.4(a). Figure 2.7(b)
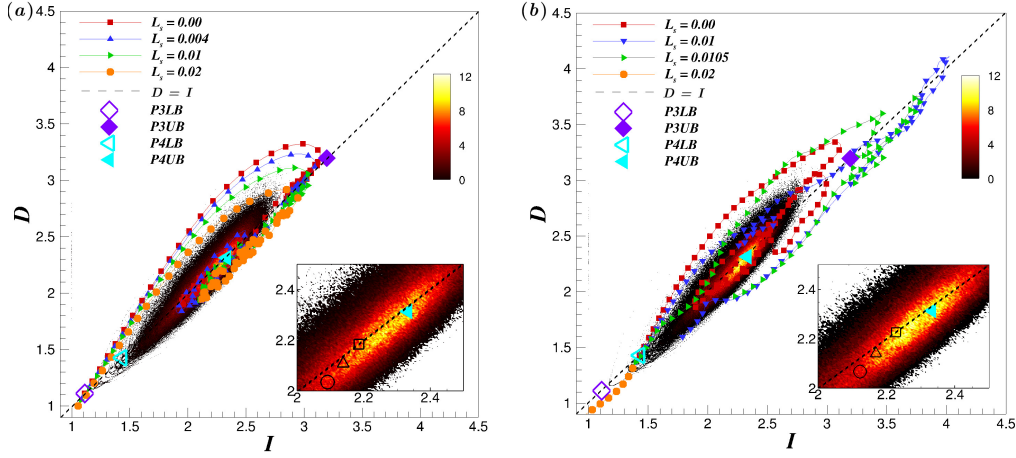
Figure 2.7: The phase space projection of turbulent trajectories onto the energy input rate (I) and energy dissipation rate (D) for various L_s at (a) $Re_c = 1760$ and (b) $Re_c = 1800$. The black dashed line shows an equilibrium line ($D = I$). P3 lower ($\diamond$) and upper ($\blacklozenge$) and P4 lower ($\triangleleft$) and upper ($\blacktriangleleft$) solutions are also shown [182]. The contour shows the probability density function (PDF) of the $I - D$ state for the no-slip case at (a) $Re_c = 1760$ and (b) $Re_c = 1800$. Inset: The mean states of long-time flows at each respective Re_c for $L_s = 0.00$ ($\square$), $L_s = 0.01$ ($\triangle$), and $L_s = 0.02$ ($\circ$) overlaid on the no-slip PDF.

shows the trajectories starting from the P4 lower-branch solution, exhibiting similar trends to those seen in the P3 solution up to the critical slip length $L_s = 0.0105$ – the trajectory gets closer to the equilibrium line as slip length is increased. Around the critical slip length, however, trajectories are altered drastically, bypassing the P4 upper-branch solution and approaching the P3 upper-branch solution before laminarizing. Beyond $L_s = 0.0105$, the trajectories immediately approach the laminar state with no bursting trajectories, as seen in figure 2.4(b).

It is evident that slip surfaces lead to modifications of the turbulent trajectories in the I-D phase-space. The core region of the turbulent trajectories with slip surfaces deviates from that of the no-slip case – it gets closer to the lower-branch solutions. These observations suggest that the distance between the turbulent state and the laminar-turbulent separatrix is reduced with the inclusion of slip surfaces. This is

illustrated by the insets in figure 2.7(a) & (b) showing the mean state of the system for $L_s = 0.00, 0.01$, and 0.02. As slip length is increased, the mean state of the system shifts closer to the lower-branch solutions. This reduced distance indicates a greater likelihood for the flow to approach the separatrix and, thus, a greater likelihood that the flow will laminarize. Similar behavior has also been observed by applying opposition control schemes to wall-bounded turbulent flows [100]. It should be noted that Figure 2.7 shows the locations of the P3 an P4 solutions on the same plane. However, these two solutions were computed using different box sizes and, thus, different dimension. Therefore, the location of these solutions on the plot may differ if a different box size is used to match the box size of the two solutions.

2.4.3.4   Flow structures

We investigate the effects of slip surfaces on flow structures for which the swirling strength λ_{ci}, the imaginary part of the complex conjugate eigenvalues of the velocity gradient tensor [271], are calculated. Figures 2.8 and 2.9 show contours of the swirling strength for the lower half of the channel for the P3 and P4 solutions, respectively, at the end of the turbulent bursting trajectory. The contours represent isosurfaces of 50% of the maximum swirling strength for each solution, which is also given in the figure. The wall-normal velocity is represented by the colour contours flooding the isosurfaces. These colour contours provide insights into the effect of slip surface on the vertical motion of these vortical structures.

As seen in [182], the P3 lower-branch solution displays large vortex cores near the channel centre – this solution is called core mode. As the bursting process proceeds, the large vortices appear to be broken into smaller ones, move toward the wall, and spread across the span of the domain. Eventually, there is a large population of small vortex cores across the channel, as shown in figure 2.8. It appears that the
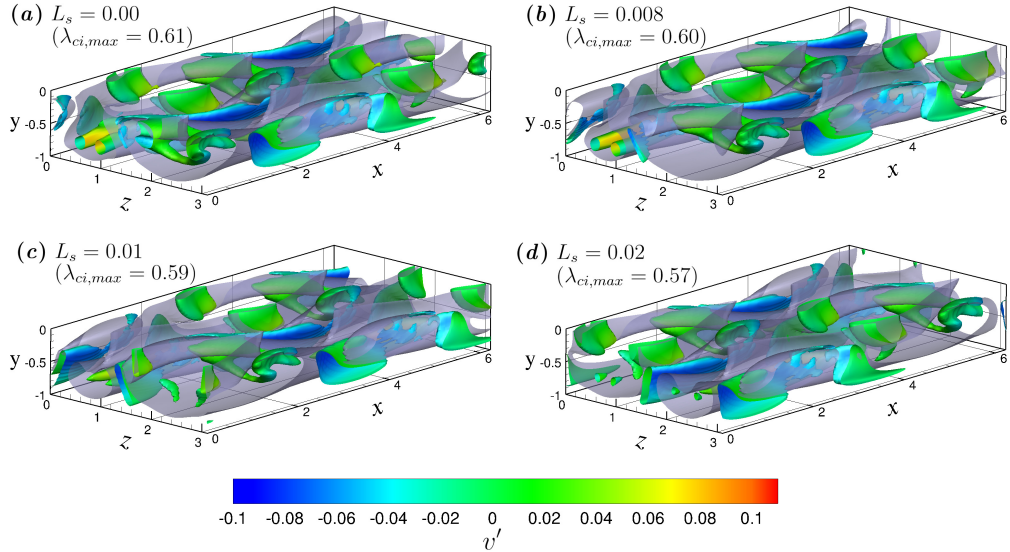
Figure 2.8: Vortical structures of the P3 lower branch solution at $Re_c = 1760$ for slip lengths (a) $L_s = 0.00$, (b) $L_s = 0.008$, (c) $L_s = 0.01$, and (d) $L_s = 0.02$. The maximum swirling strength for each case is presented in parentheses. The multicolored tubes are isosurfaces of $1/2$ of maximum swirling strength. The contours flooding the isosurfaces represent the wall-normal velocity. Minimum and maximum values of wall-normal velocity represented by the contours correspond to -0.1 (blue) and 0.1 (red), respectively. The gray isosurface represents the critical layer, where local streamwise velocity is equal to the wave speed of the traveling wave solution.

general shape and position of the structures is mostly unchanged for all slip lengths studied, while the maximum swirling strength is slightly reduced with slip length. The majority of the wall-normal velocities associated with these vortex structures are close to zero at this instant, while a very strong negative wall-normal velocity is located around vortex structures during bursting trajectories.

In figure 2.9, the vortical structures of the P4 solution are presented. As shown by [182], the P4 lower-branch solution displays vortices of Λ-like structures without a head connecting the legs. The vortex cores are located near the critical layer where the local streamwise velocity matches the wave speed – this solution is called critical-layer mode. Recently, this solution family was continued at higher Reynolds
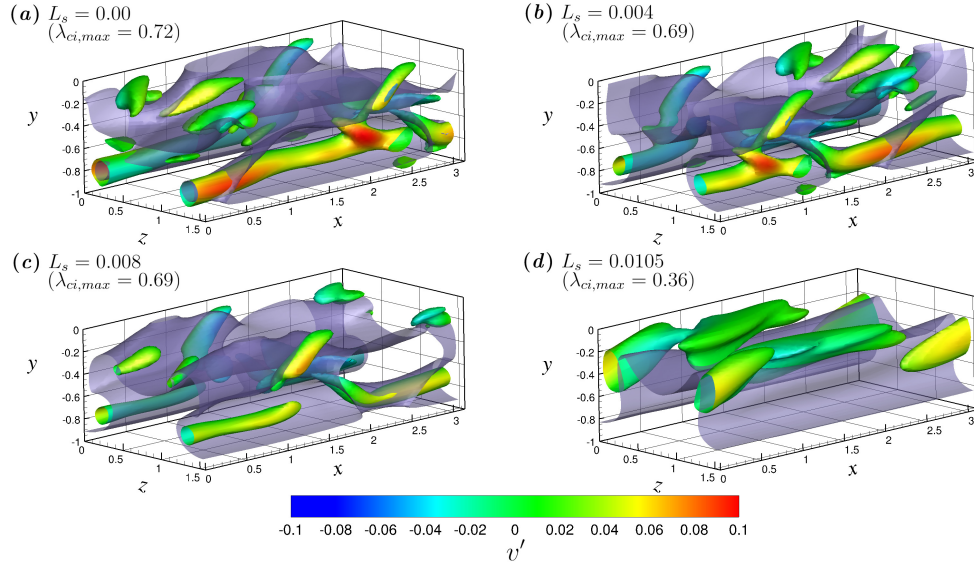
Figure 2.9: Vortical structures of the P4 lower branch solution at $Re_c = 1800$ for slip lengths (a) $L_s = 0.00$, (b) $L_s = 0.004$, (c) $L_s = 0.008$, and (d) $L_s = 0.0105$. The maximum swirling strength for each case is presented in parentheses. The multicolored tubes are isosurfaces of $1/2$ of maximum swirling strength. The contours flooding the isosurfaces represent the wall-normal velocity. Minimum and maximum values of wall-normal velocity represented by the contours correspond to -0.1 and 0.1, respectively. The gray isosurface represents the critical layer, where local streamwise velocity is equal to the wave speed of the traveling wave solution.

numbers, showing hairpin-like vortex structures [207]. With slip surfaces, there still appear to be leg structures with slightly upward side branches, which is also observed in a trajectory along the most unstable manifold of the P4 lower-branch solution [183]. Its structures are significantly longer than ones of the P3 solution and are accompanied by a small number of smaller vortex cores around these long vortex structures. Vortex cores of the P4 solution seem to not extend into the channel centre but remain mostly streamwise-oriented. As slip length is increased, the maximum swirling strength is drastically reduced (i.e. 50% at $L_s = 0.0105$). In particular, from the colour contours of the wall-normal velocity associated with long vortex structures, the vortex structures are shifted upward from the wall as slip length is

increased, leaving a quiescent region near the wall.

To quantitatively investigate the effect of the slip surfaces on the vertical shift-
ing of vortical structures, the wall-normal location for the maximum value of the
area-averaged swirling strength is plotted in figures 2.10(a) and 2.10(c) for P3 and
P4 solutions, respectively. Bulk swirling strength is also shown for the P3 and P4
solutions in figure 2.10(b) and 2.10(d), respectively. The wall-normal location of the
maximum of the average swirling strength for the P3 solution is almost constant for
all slip lengths studied, as shown in figure 2.10(a). Figure 2.10(b) also shows that the
effect of slip length on the bulk swirling strength is minimal, suggesting the slip sur-
faces have a minimal effect on the vortex structures associated with the P3 solution.
However, vortex structure dynamics for the P4 solution are quite different than those
of the P3 solution. There are much larger deviations in height of maximum swirling
strength as slip length is increased. Beyond $L_s = 0.004$, the vortex structures are
significantly shifted upward away from the wall, moving toward the channel centre.
The bulk swirling strength is also significantly decreased as slip length increases as
seen in figure 2.10(d). The trend appears to be asymptotic with slip length. Slip sur-
faces seem to have a profound weakening effect on the P4 vortex structures. These
observations for the P4 solution are in good agreement with the experimental study
[270], where the mechanisms for drag reduction over superhydrophobic surfaces were
investigated for a turbulent boundary layer flow. They performed experiments to
show that the drag reduction is caused by a combination of slip at the surface and
modifications to the turbulent structures – vortices are weakened and lifted away
from the surfaces. The combination of these modifications to the vortical structures
(i.e. weakened and shifted vortices) of the P4 solution help to explain why, beyond
the critical slip length, there is no turbulent burst and flow laminarizes. It appears
that slip surfaces modify the turbulent structures such that the self-sustaining cycle
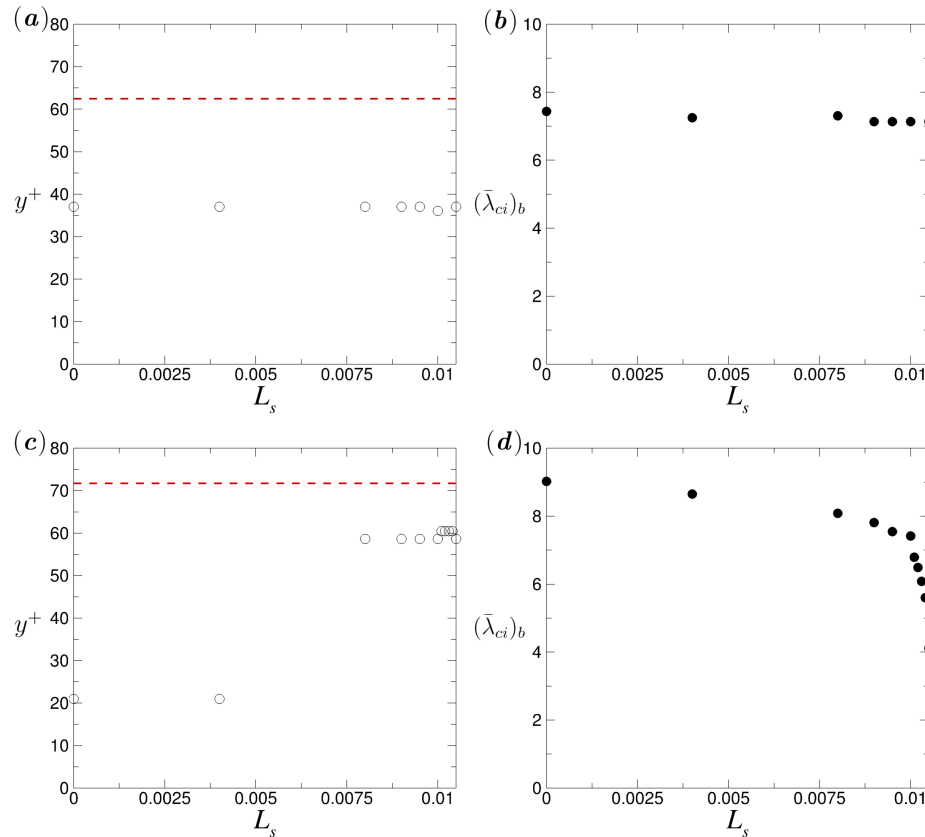
Figure 2.10: (a, c) The wall-normal location corresponding to the maximum of the area-averaged swirling strength for the P3 and P4 solutions, respectively. The dashed line corresponds to the channel centre for the P3 and P4 solutions. (b, d) The bulk swirling strength as a function of slip length for the P3 and P4 solutions, respectively. All values are calculated at the time at which the maximum L^2-norm of velocity is reached.

of near-wall turbulence is disrupted and turbulence can no longer be sustained.

2.4.3.5 Spatiotemporal dynamics

We now attempt to illuminate the mechanisms behind early or delayed transition to turbulence observed in the P3 and P4 solutions. It has been shown that at the onset of turbulence, the spatiotemporal dynamics provides a coherent mechanistic basis for the dynamics of transition to turbulence [9, 208, 14] – puffs and slugs or directed

percolation have been explored in this regard. Similarly, the spatiotemporal dynamics of the exact coherent solutions also appear to provide a coherent mechanistic basis for effects of slip surfaces on the transition observed in the P3 and P4 solutions.

For spatiotemporal dynamics, we incorporate a Fourier decomposition of the velocity field. Similar with [237], the velocity field of the traveling wave solutions can be Fourier decomposed in the x direction as

$$\boldsymbol{u}(x,y,z,t) = \boldsymbol{u}_0(y,z,t) + \sum_{n=1}^{\infty} \left(\mathrm{e}^{in\theta} \boldsymbol{u}_n(y,z) + \mathrm{c.c.} \right), \qquad (2.7)$$

where α is the fundamental wave number in the streamwise direction, $\theta = \alpha(x - ct)$, c is the constant wave speed, and c.c. denotes complex conjugates. For this study, we define the 0-mode as $\boldsymbol{u}_0(y,z,t) = (u_0, v_0, w_0)$. The streamwise fluctuation u' can then be calculated by $u_0(y,z,t) - \overline{u}(y)$, where $\overline{u}(y)$ is the time- and area-averaged mean velocity. Note that the wall-normal velocity fluctuation $v'(y,z,t) = v_0(y,z,t)$ because $\overline{v}(y) = 0$. These 0-mode velocity fluctuations u' and v' provide information about streaky flow and rolls, respectively [237]. Although u' and v' represent streamwise-averaged fluctuations, these quantities still enable identifying the sweep and ejection events based on the quadrant analysis [184].

Figures 2.11 and 2.12 show the spatiotemporal dynamics of streamwise and wall-normal velocity fluctuations at a spanwise location $(z^+ = L_z^+/4)$ for different slip lengths, respectively, along with the dashed line corresponding to time of transition. This spanwise location is chosen because it is the location where the core of vortex structures is located – the other location $(z^+ = 3L_z^+/4)$ where the core of vortex structures is also located was studied, giving essentially identical results.

Both solutions exhibit similar behaviours on the streamwise fluctuations. For the P3 solution, as shown in figures 2.11(a)-(c), the near-wall low-speed streak (negative

u') appears to be enhanced as slip length is increased (u'_{min} decreases from -0.0981 to -0.1223), while for the P4 solutions, the near-wall low-speed streak is slightly extended upward but remains relatively quiescent ($u'_{min} \approx -0.025$ with slip surfaces) compared to the P3, as seen in figures 2.11(d)-(f). Near the channel centre, there are positive streamwise fluctuations for both solutions. In particular, a height of peak streamwise fluctuations for the P3 solution corresponds to the region where the core of vortex structures is localized.

Most interestingly, the wall-normal fluctuations show the opposite behaviours. In figures 2.12(a)-(c), the wall-normal fluctuations of the P3 solution are all negative across the channel height and become more negative in the buffer layer with increasing slip length (v'_{min} decreases from -0.0107 to -0.0158). The combination of increased streamwise velocity near the channel centre and strong negative wall-normal velocity in the buffer layer seems to promote an instability to the vortex structures at the channel centre. Specifically, this instability causes the large vortex structures to propagate toward the wall much sooner where they break up as the slip length is increased. These effects seem to lead to an early transition for the P3 solution. On the other hand, for the P4 solution, figures 2.12(d)-(f) show all positive wall-normal fluctuations across the channel height and peak values are located around $y^+ = 20 - 40$, where the core of the vortex structures is localized. As slip length increases, the peak value decreases as opposed to the P3 solution (from $v'_{max} = 0.0181$ to 0.0147). The combination of the very quiescent flow and positive wall-normal velocity around the vortex structures appears to allow the the vortex structures to be more stable and persist for a longer time before transition to turbulence occurs. Those effects appear to delay the transition. It is interesting to note that based on the quadrant analysis, slip surfaces are likely to promote stronger wall-toward motions (Q4-like) at the channel centre and inward interactions (Q3) in the buffer layer for the

P3 solution, while for the P4 solution, the surfaces tend to promote longer ejection events (Q2) near the critical layer and wall-away motion (Q1-like) at the channel centre. This quadrant analysis may help to elucidate distinct transition dynamics for the P3 and P4 solutions – the combination of the core mode and strong sweep events seems to promote early transition, while the combination of the critical layer mode and extended ejection events seems to delay the transition.

Finally, we can make the link between transition dynamics and flow structures, as the latter can be thought of as different disturbances in a receptivity process of transition [114]. Flow structures associated with the core mode (P3 solution) seem to resemble those found in free-stream turbulence (i.e., more densely located at the centre of the channel or the edge of the boundary layer) as seen in figure 2.8 – it can be called external perturbations. On the other hand, the P4 solution (critical layer mode) exhibits Λ-shaped vortical structures, confined near the wall, resembling three-dimensional flow structures developed from Tollmien-Schlichting waves – it can be called internal perturbations. Depending on different disturbances, transition scenarios appear to be very different. [198] compared the dynamics of different transition scenarios, namely, H-type, K-type, and bypass transition. In the H- and K-type transitions, characterized by Λ-shaped vortical structures, a large overshoot in the skin-friction coefficient was observed when transition starts to occur. However, for the bypass transition, this overshoot was absent, giving a smooth transition to turbulence. This distinct overshoot is present in the skin-friction coefficient profile for the P4 solution and absent in that for the P3 solution as shown in figure 2.4. It is worth noting that, similar to the P3 solution, [251] introduced free-stream turbulence to a boundary layer and showed that the bypass transition was triggered. They showed that the typical near-wall Tollmien-Schlichting waves were not the initiating mechanism for transition and in this case was attributed to a bypass route triggered
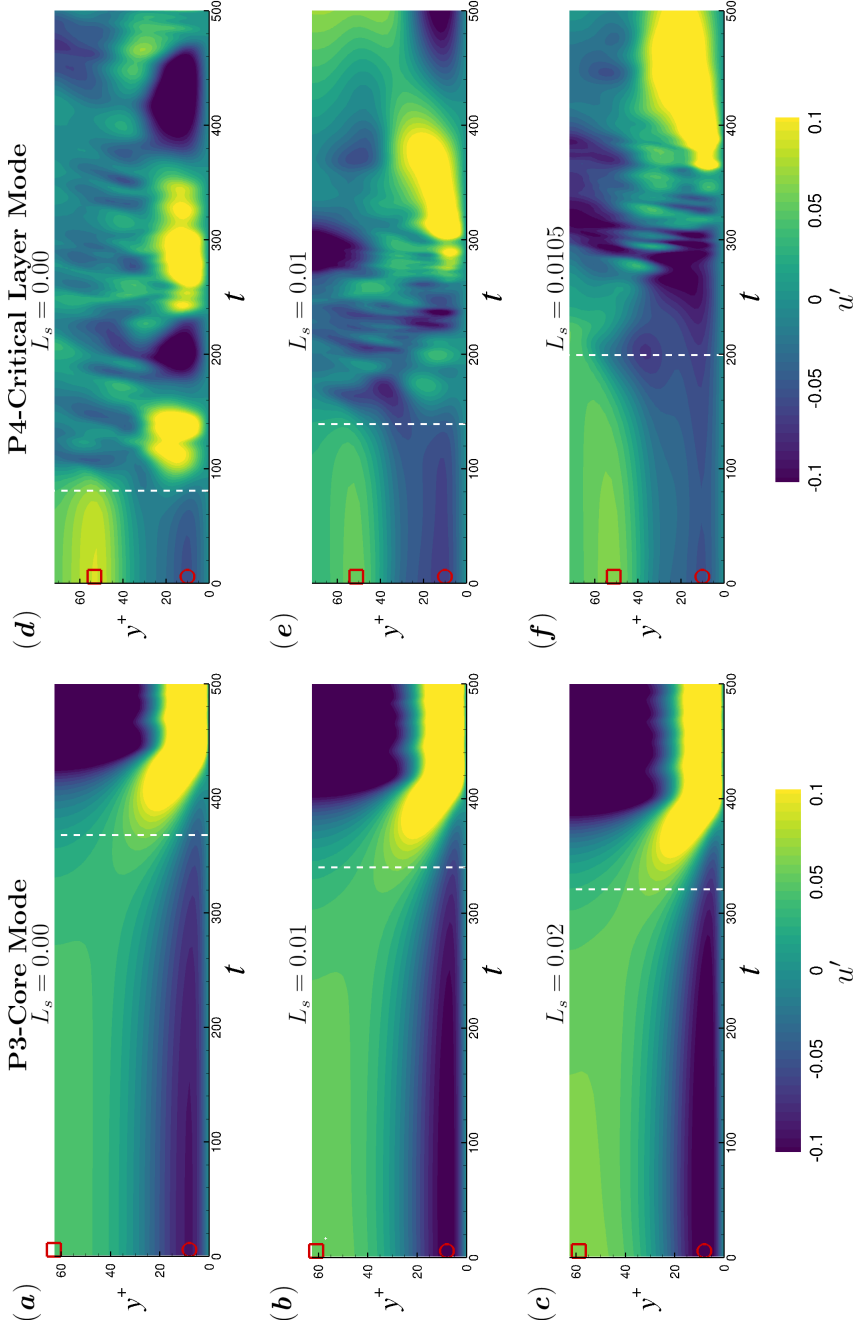
Figure 2.11: The streamwise-averaged streamwise velocity fluctuations u' at $z^+ = L_z^+/4$ as a function of wall-normal distance for the P3 solution (a)-(c) and the P4 solution (d)-(f) for various slip lengths. The dashed white line corresponds to time of transition $(C_f = 1.1 C_{f,0})$. The symbols ($\bigcirc$) and ($\square$) indicate the minimum and maximum u' at their wall-normal locations, respectively. For the P3 solution, $(u'_{min}, u'_{max}) = (-0.0981, 0.0461)$ for (a), $(-0.1110, 0.0569)$ for (b), $(-0.1223, 0.0643)$ for (c). For the P4 solution, $(u'_{min}, u'_{max}) = (-0.0665, 0.1259)$ for (d), $(-0.0248, 0.0917)$ for (e), $(-0.0262, 0.1008)$ for (f). Note that these values remain almost constant before the time of transition.
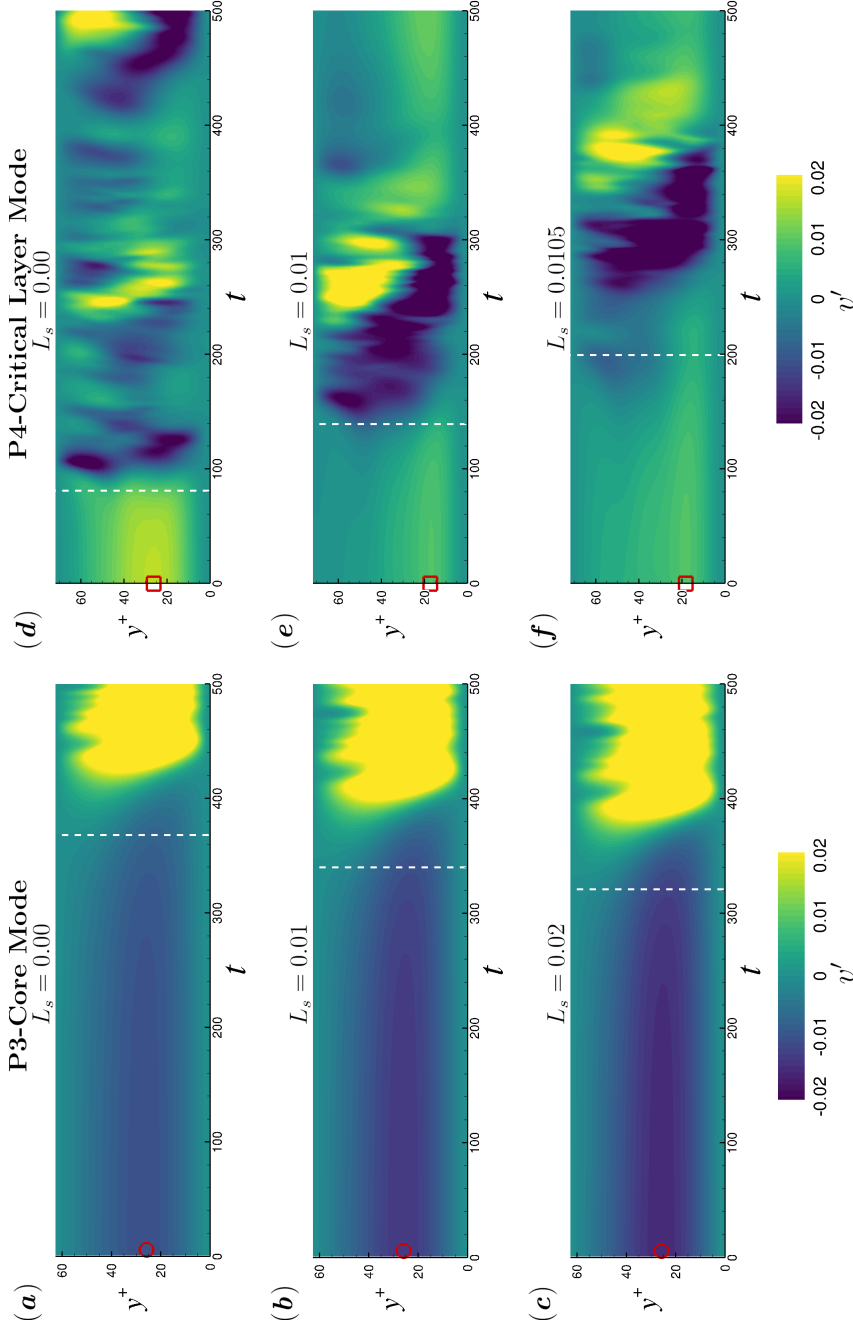
Figure 2.12: The streamwise-averaged wall-normal velocity fluctuations v' at $z^+ = L_z^+/4$ as a function of wall-normal distance for the P3 solution (a)–(c) and the P4 solution (d)–(f) for various slip lengths. The dashed white line corresponds to time of transition $(C_f = 1.1C_{f,0})$. The symbols $(\bigcirc)$ and $(\square)$ are indicated for the minimum and maximum v' at their wall-normal locations, respectively. For the P3 solution, (a) $v'_{min} = -0.0107$, (b) $v'_{min} = -0.0139$, (c) $v'_{min} = -0.0158$. For the P4 solution, (d) $v'_{max} = 0.0181$, (e) $v'_{max} = 0.0131$, (f) $v'_{max} = 0.0147$. Note that these values remain almost constant before the time of transition.

from the free stream. The evolution of the P3 solution is similar in that the structures originate in the centre of the channel (i.e. free-stream) and propagate downward toward the near-wall region before breaking down, subsequently triggering transition. In addition, the shape of the vortical structures for the P4 solution are similar to those found in H- and K-type transitions. A similar observation for the effects of slip surfaces on the H- and K-type transition was also made by Picella et al. [184], where the overshoot in skin-friction was present and transition was delayed by the slip surface with the modal perturbation. However, they also showed that the non-modal perturbation, similar to those perturbations that cause bypass transition, was unaffected by the slip surfaces, contrary to the early transition behavior observed in the P3 solution of the current study. Differences in the transition behavior of the non-modal perturbation of Picella et al. [184] and the P3 solution of the current study could stem from assumptions made in the linearization of the Navier-Stokes equations or, possibly, differences between the non-modal perturbation and the P3 solution. The differences in the skin-friction coefficient and vortical structures between the P3 and P4 solutions may provide clear and plausible mechanisms responsible for early transition for P3 and delayed transition for P4 due to slip surfaces, for which further investigation is yet needed.

2.5   Conclusion

Direct numerical simulations were performed to investigate the effect of slip surfaces on transition in plane Poiseuille (channel) geometry. For the purpose of validations, laminar drag reduction values were calculated and compared to the previous studies. Levels of over 10% drag reduction were observed and in good agreement with previous numerical and experimental studies. The drag reduction percentage remains almost

constant regardless of the Reynolds number. In particular, our results are in great agreement with the theory for drag reduction of superhydrophobic surfaces on both walls in a laminar channel flow.

Turbulence lifetime analysis (i.e. the probability that turbulence will persist) was investigated for transitional flows at $Re_c = 1600, 1800,$ and 2000 ($Re_\tau = 77, 85,$ and 93). Flows with slip surfaces were significantly less likely to maintain turbulence compared to the no-slip case. Additionally, the slip flows were more likely to laminarize at earlier times as slip length is further increased. As Reynolds number is increased, this trend still holds, while a larger slip length is needed to obtain the same likelihood of laminarization found at lower Reynolds numbers. Phase-space projection of transitional trajectories on the energy input and dissipation rates showed a reduced distance between the laminar and turbulent states, which helps explain the increased likelihood of laminarization due to slip surfaces.

Exact coherent solutions, specifically nonlinear travelling wave solutions, to the Navier-Stokes equations were used to investigate the effects of slip surfaces on the laminar-turbulent separatrix. The P3 and P4 solution families were chosen as their lower-branch solutions are shown to lie on the basin boundary between laminar and turbulent flow [182]. The skin-friction evolution and linear growth rate from the lower-branch solutions were calculated. For slip flows, the strong turbulent burst associated with the P3 lower-branch solution was induced at earlier times while the bursting magnitude and growth rate were mostly unaffected. For the P4 solution, however, the strong turbulent burst was delayed with the reduced magnitude and growth rate for slip flows. Beyond a critical slip value, the turbulent burst was completely eliminated as a flow is immediately laminarized after a short stable period. Effects of slip surfaces on vortex structures of the P3 and P4 solutions were examined to elucidate mechanisms responsible for the difference in transition behaviours

between the solutions. It appears that structures associated with the P3 solution were largely unaffected by the slip surfaces. Overall structure and strength remained relatively constant. However, the strength of P4 vortex structures was weakened by ∼ 50%, and they were shifted away from the wall.

Based on the quadrant analysis and spatiotemporal dynamics, it was suggested that slip surfaces promote the prevalence of strong wall-toward motions (Q4-like events) in the area of the P3 vortex cores close to the channel centre. This results in instability, which promotes the propagation of the vortex structures down into the wall where they break up and induce transition, similar to the bypass transition [197]. However, sustained ejection events (Q2) were present in the region of the P4 vortex cores (which resemble the Λ-shaped structures in H- and K-type transitions) resulting in a shift of the vortex structures away from the wall allowing them to remain intact and propagate downstream for a longer time. It can be suggested that the slip surfaces tend to affect core-mode structures (P3 solution) or non-modal perturbations via inward interactions (Q3) near the wall and wall-toward motions (Q4-like events) near the channel centre, subsequently leading to bypass-type early transition. On the other hand, the slip surfaces tend to affect critical-layer structures (P4 solution) or modal perturbations via ejection events (Q2) near the wall and wall-away motions (Q1-like events) near the channel centre, subsequently leading to H- and K-type delayed transition. These distinct transition dynamics of the P3 and P4 solutions due to slip surfaces could suggest that different flow control techniques could be used to delay or promote a transition to turbulence, which will be a subject of interesting future work.

Chapter 3

ON THE DECAY OF TURBULENCE AND SLIP SURFACES

[1]

3.1   Decay of turbulent flows

There is much insight to be gained from the dynamics of a flow decaying from a turbulent state to a laminar state. While the study of transition in fluid systems is largely concerned with the transition from a laminar state to a turbulent state, previous studies have also analyzed the properties of turbulence by performing 'quench' protocols in plane Poiseuille flow (PPF) [22, 179, 209, 49], where quenching involves the the sudden reduction in Reynolds number at some time $t_q > t_0$. One motivation for these studies was to find a threshold Reynolds numberRe_g where turbulence is sustained. They found that below $Re_g \approx 700$, turbulence was not sustainable and the system decayed to the laminar state. Another experimental study by Seki and Matsubara [203] found $Re_g = 1050$ by way of linear extrapolation of the intermittency factor.

One advantage of the quenching protocol is that because the system is initialized

---

[1]This work is in preparation to be submitted to a scientific journal.

from a turbulent state, it is much less sensitive to noise or perturbations in the initial condition. Additionally, this type of study provides insight into mechanisms responsible for the susceptibility of a turbulent flow to laminarization. Subsequently, these mechanisms can be used to inform more efficient flow control techniques.

Recently, Liu et al. [148] visualized the decay of turbulence in a Couette-Poiseuille (CPF) flow using particle image velocimetry (PIV). In this geometry, the flow is driven by the shear due to a moving belt on one wall. The speed of the belt can be adjusted such that the Reynolds number is quenched quickly. The time required for the quenching process is less than 2 time units (h/U_{belt}) They observed distinct decay rates for the streaks and rolls during decay. The decay rates were quantified by comparing the time evolution of turbulent energy in the streamwise and spanwise directions, and the spanwise rolls decay approximately two times faster than the streamwise streaks. These experimental findings provide support for the different decay rates in the self-sustained model put forward by Waleffe [231].

In this section, we study the effect of non-zero wall slip on turbulent decay rates. Taking a similar approach to Liu et al. [148], we analyze the time evolution of turbulent energy associated with the streamwise and spanwise directions using a quench protocol. In addition, we also consider the wall-normal component to further elucidate possible mechanisms responsible for the self-sustaining process. This process is repeated for various final quench Reynolds numbers Re_f to gain insight into the self-sustaining process [231] to contribute to the knowledge base for better-informed flow control methods.

3.2 Problem formulation

The details of the numerical problem formation are the same as those used in Section 2.3. The initial Reynolds number used in the current study is $Re_i = 1800$ and the flow is quenched to $Re_f = 1000, 800, 600$ to study the effect of final Reynolds number on decay characteristics. The initial Reynolds number is chosen such that it is above the transitional Reynolds number $Re \approx 1000$. The final quenched Reynolds numbers are chosen such that they are at or below the critical Reynolds number. To achieve this, a long-time, no-slip simulation $(tU_c/h = 10000)$ is run at $Re = 1800$ to obtain a collection of turbulent fields. A random field is then chosen from these turbulent fields to use as an initial condition for the quenched simulation at the Reynolds numbers and slip lengths of interest. The slip lengths of interest are $L_s = 0.00, 0.01, 0.02$ to illustrate the effect of slip on decay characteristics, where L_s is defined above in Section 2.3. The procedure for the P3 and P4 upper-branch traveling wave solutions is the same, only using the solution velocity fields as the initial conditions. The initial Reynolds numbers for the traveling wave solutions are the inherent Reynolds numbers where the solutions emerge (i.e., $Re = 1800$ and $Re = 1855$ for P3 and P4, respectively).

Simulations are performed in domains of $L_x \times L_y \times L_z = 2\pi \times 2 \times \pi$ for random initial conditions. Domain sizes for the P3 and P4 upper branch solutions are $L_x \times L_y \times L_z = 2\pi \times 2 \times \pi$ and $L_x \times L_y \times L_z = \pi \times 2 \times \pi/2$, respectively. Typical numerical grid spacing in the streamwise and spanwise directions are $\Delta x^+ \approx 6$, $\Delta z^+ \approx 3$. Non-uniform Chebyshev spacing in the wall-normal direction results in $\Delta y^+_{min} \approx 0.05$ at the wall and $\Delta y^+_{max} \approx 3$ at the channel center.

3.3 Results: Decay of turbulence

Shown in 2.3 is the turbulent lifetime of transitional flow over slip surfaces. It can be seen that wall slip decreases the likelihood that a given turbulent trajectory will be sustained. Figure 2.3 inset also shows that a given slip length has less of an impact on a turbulent trajectory as the Reynolds number increases. While there is meaningful statistical information to be gleaned from these results, which were detailed in 2.4.2, we also consider the decay of turbulent trajectories to elucidate possible mechanisms responsible for the decrease in turbulence lifetime with wall slip. In this section, we detail the decay of random turbulent initial conditions, as well as the decay of exact coherent solutions (i.e. P3 and P4 upper-branch traveling wave solutions [182]), to the laminar state.

3.3.1 Decay of random initial conditions

This section details a statistical study on the decay of random initial conditions using a quench protocol. A random turbulent initial condition starting from $Re_i = 1800$ is allowed to decay to various final Reynolds numbers, $Re_f = 600, 800, 1000$, with increasing slip length, $L_s = 0.00, 0.01, 0.02$. This procedure is performed for 10 different initial conditions with varying turbulence intensity. The L_s-norm of disturbance velocity is calculated to observe the decay to the laminar state, where disturbance velocity is defined as

$$\mathbf{u}(x, y, z, t) = \mathbf{U}(x, y, z, t) - U_{base}(y) \tag{3.1}$$

Analysis of the time-evolution of velocity magnitude, flow structures, streamwise variance of velocity fields, and the time-evolution of wall shear rate are all detailed below for the 10 random initial conditions.

3.3.1.1 Time-evolution of L_2-norm of velocity

Figure 3.1 shows the time evolution of the L_2-norm of the disturbance velocity, The decay rate for in all three directions increases for decreasing Re_f. These results are similar to observations made in previous studies [76, 148], and there is no rigorous understanding of the mechanisms behind this behavior. The black diamond correspond the the time when the spanwise perturbation velocity magnitude reaches 5% of its initial value. Shortly after this time, decay rate for the spanwise velocity magnitude reduces. At this point in the streamwise and wall-normal directions, there is an increase in the decay rate, signaling a change in the decay behavior of the flow structures in these directions. These results are consistent with those found previously by Liu et al. [148], where they found that the "waviness", or undulation, of the streamwise streaks reduces initially allowing the rapid decay of the spanwise rolls. Once the rolls have decayed, then the streaks begin to decay more rapidly. These observations are consistent with the self-sustaining process put forward by Waleffe [231], and the present results corroborate these previous findings.

The same procedure is also shown in Figure 3.3 for $Re_f = 1000$ and varying levels of slip at the boundaries to illustrate the effect of slip surfaces on the decay of turbulence. The addition of wall slip appears to increase the decay rate, at least initially, when compared the the no-slip case. After . It should be stated that it is unclear whether the inclusion of slip surfaces has a significant effect on the decay rate, or whether the slip surfaces simply cause the flow to begin the process of laminarization sooner. The effect of wall slip on the decay process for final Reynolds numbers $Re_f < 1000$ studied here is negligible and shown in Figure 3.2. This may be due to the fact that these final Reynolds numbers are close to and below the critical Reynolds number $Re_g \approx 700$ where turbulence cannot persist [179, 209].
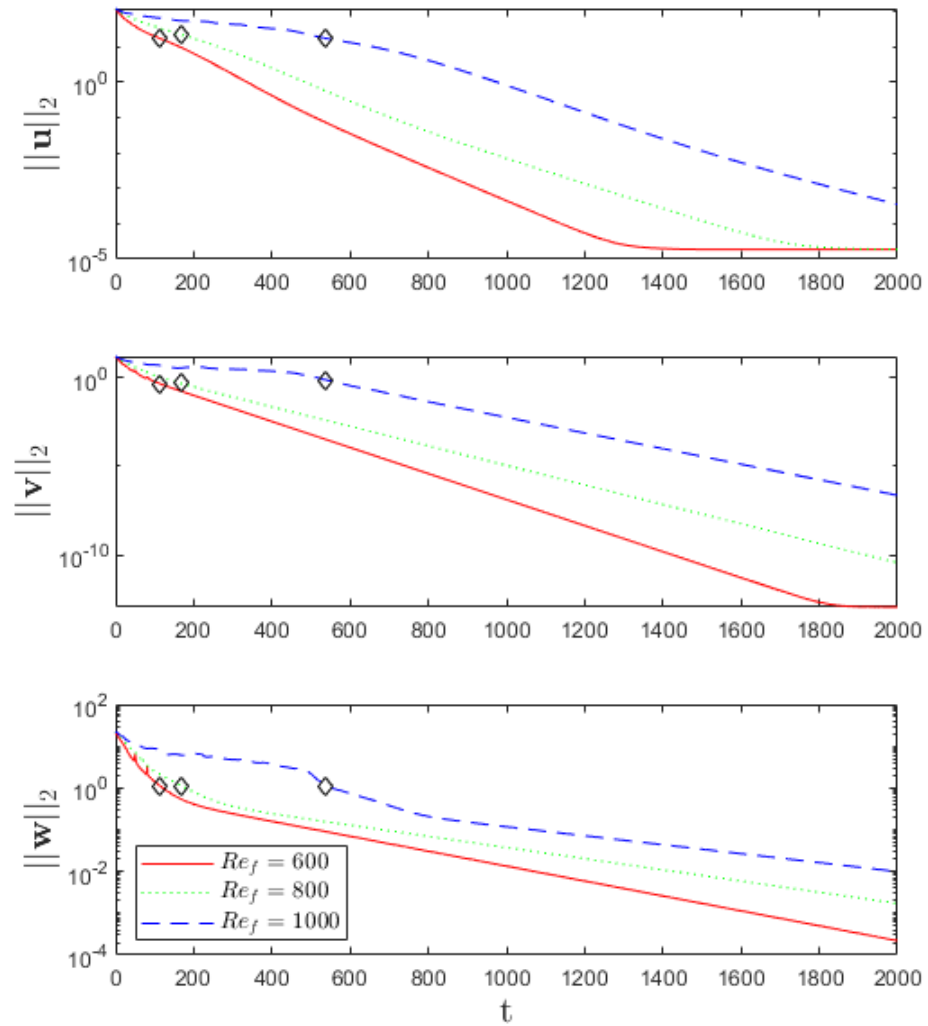
Figure 3.1: Decay of a random initial condition at initial Reynolds number $Re_i = 1800$ for quench Reynolds numbers, $Re_f = 600, 800, 1000$. Black diamond corresponds to the time when the spanwise magnitude reaches 5% of its initial value.
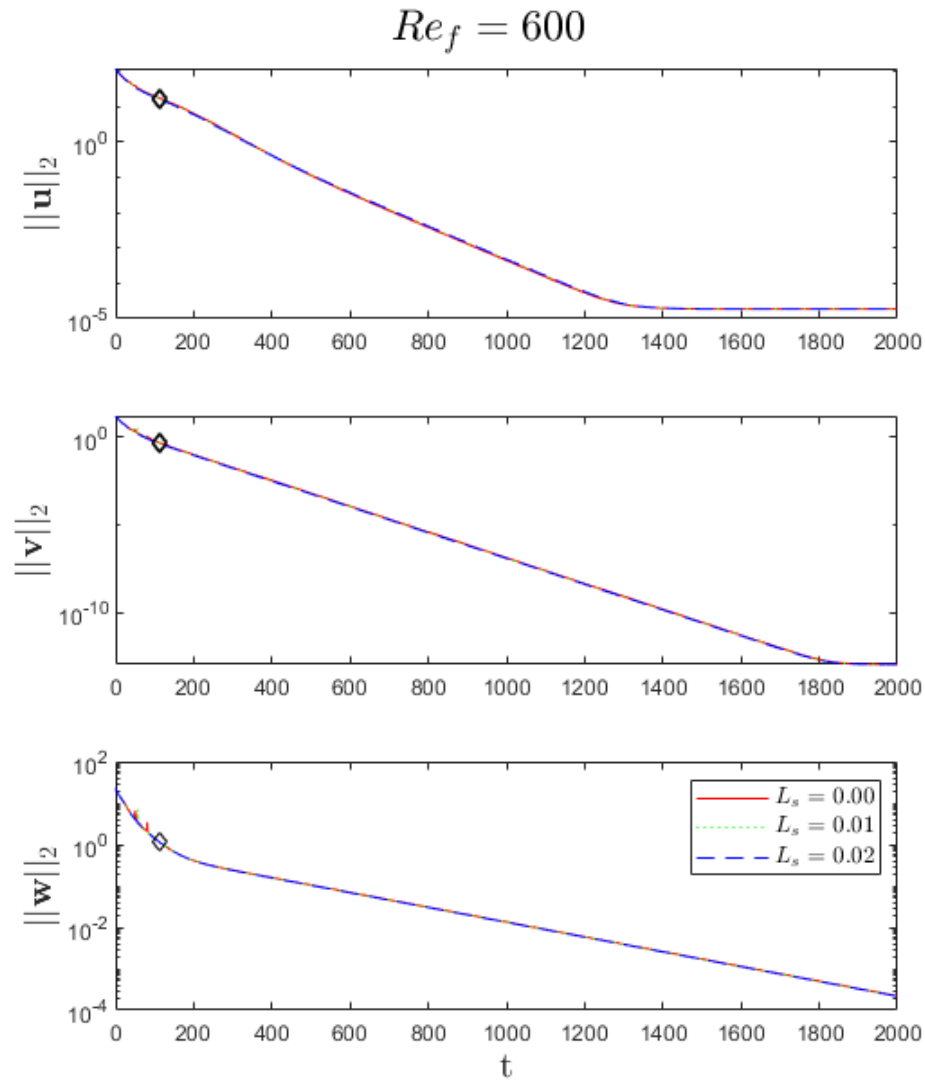
Figure 3.2: Decay of a random initial condition at initial Reynolds number $Re_i = 1800$ for quench Reynolds numbers, $Re_f = 600$, and slip lengths, $L_s = 0.00, 0.01, 0.02$. Black diamond corresponds to the time when the spanwise magnitude reaches 5% of its initial value.

Therefore, the wall slip may have negligible effect on the decay as the system will decay regardless.
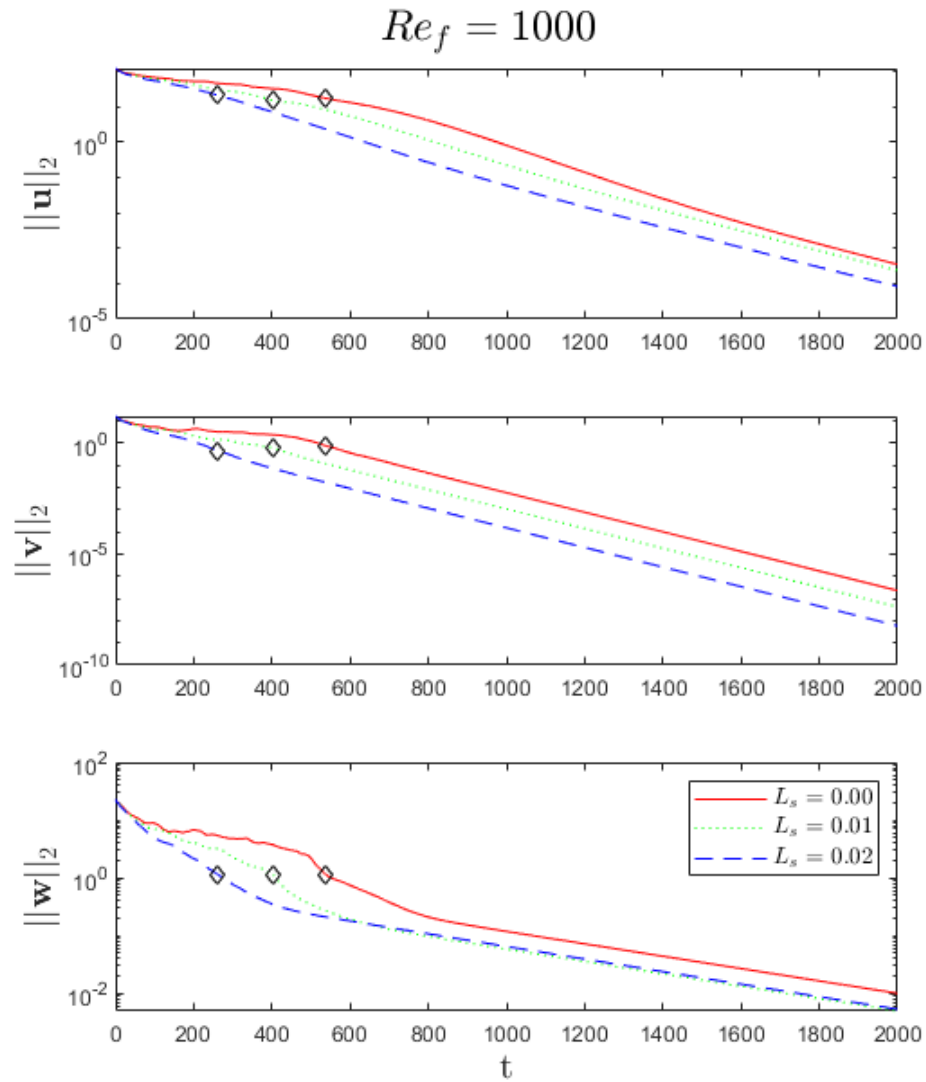
Figure 3.3: Decay of a random initial condition at initial Reynolds number $Re_i = 1800$ for quench Reynolds number, $Re_f = 1000$, and slip lengths, $L_s = 0.00, 0.01, 0.02$. Black diamond corresponds to the time when the spanwise magnitude reaches 5% of its initial value.

3.3.1.2 Flow structures

The following figures show, via disturbance velocity $\mathbf{u}^+$, the flow structures present at a wall-normal plane of $y^+ = 12$ for all three spatial dimensions. This wall-normal distance was chosen as the viscous stress and Reynolds shear stress are equal, resulting in peak production $\mathcal{P}$ at that point [187]. The color axis is such that the absolute values are less than the maximum value of the initial condition of the no-slip case (i.e., $|u| < max(u_{L_s=0,t=0})$).

Figure 3.4 shows the disturbance velocity in the three spatial directions for $Re_f = 600$ and $L_s = 00$. The trend observed in the decay of structures matches that observed in 3.1 showing faster decay of the structures in the wall-normal and spanwise directions when compared to the streamwise direction. This, again, corroborates results seen in [148]. The results for $L_s = 0.01, 0.02$ (not shown) show no significant difference from the no-slip case and match the trend observed in 3.2 showing negligible effect of the wall slip on the decay rates of velocity magnitude. The same trend was observed for the $Re_f = 800$ case which is not shown here.

Figures 3.5 - 3.7 show the disturbance velocities for each spatial dimension for the $Re_f = 1000$ case at each slip length, $L_s = 0.00, 0.01, 0.02$. Unlike the $Re_f = 600$ case, it appears that wall slip has an effect on the rate at which the disturbances decay. The strength of the velocity disturbances is reduced with wall slip as evidenced by the decrease in intensity of the color contours. Additionally, the "waviness" of the streamwise structures appears to be reduced earlier in the slip cases than the no-slip case.

To quantify the decrease in the waviness of the structures, the mean variance of the velocity fields in the streamwise direction was calculated. The time-evolution of this value, normalized by the mean variance at time $t = 0$, is shown in Figures 3.9
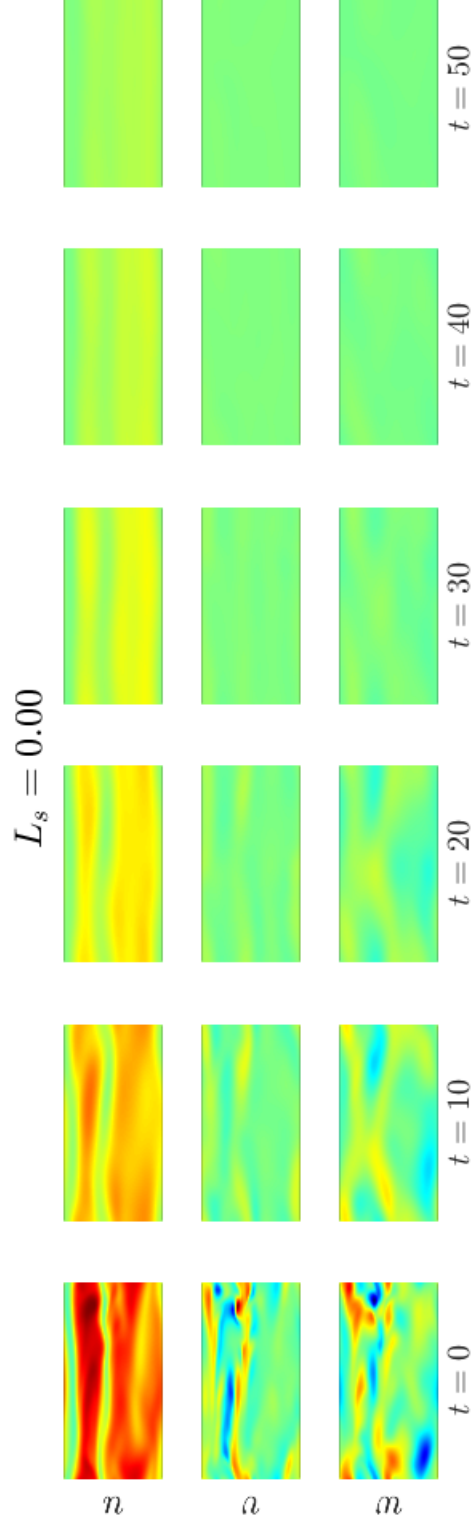
Figure 3.4: Flow structures given by the perturbation velocity in each spatial dimension at $y^+ = 12$ for $L_s = 0.00$ and $Re_f = 600$.
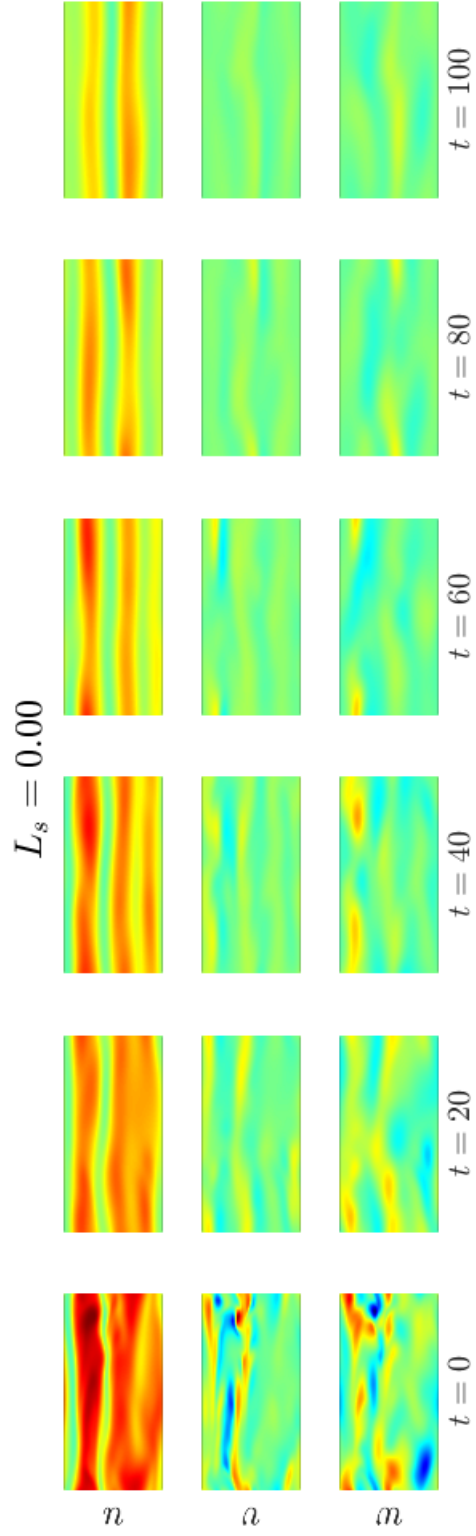
Figure 3.5: Flow structures given by the perturbation velocity in each spatial dimension at $y^+ = 12$ for $L_s = 0.01$ and $Re_f = 600$.
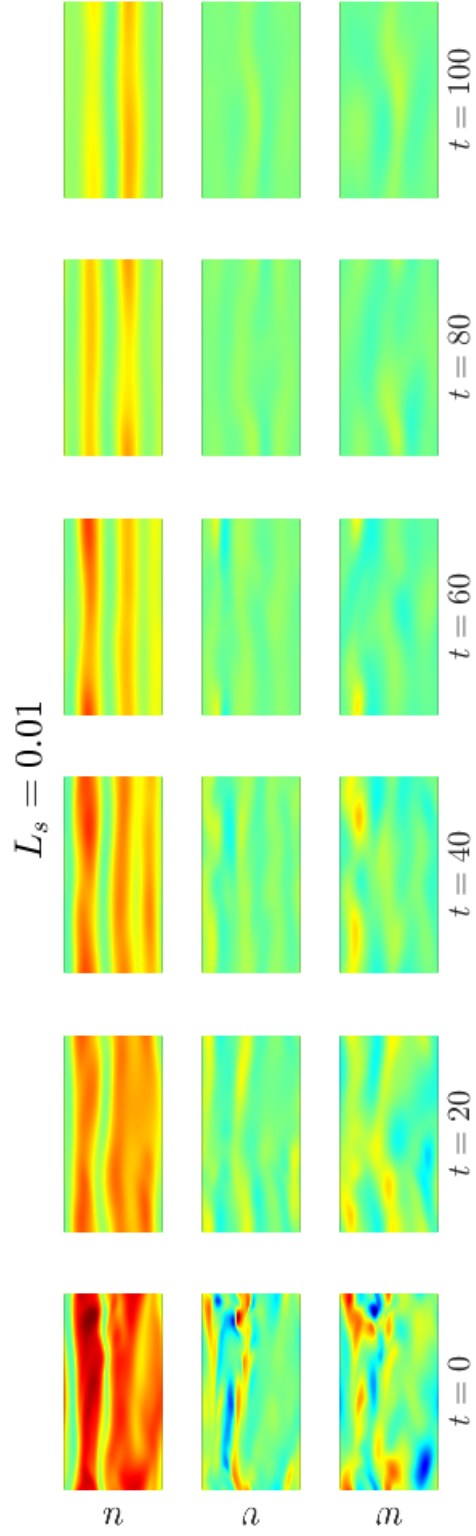
Figure 3.6: Flow structures given by the perturbation velocity in each spatial dimension at $y^+ = 12$ for $L_s = 0.01$ and $Re_f = 1000$.
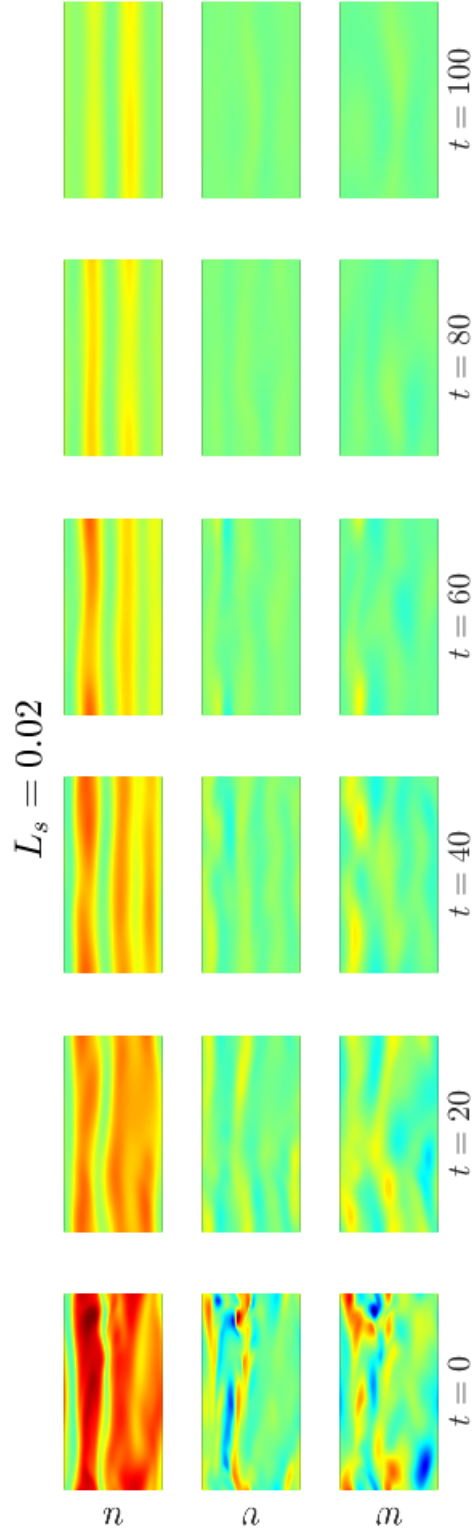
Figure 3.7: Flow structures given by the perturbation velocity in each spatial dimension at $y^+ = 12$ for $L_s = 0.02$ and $Re_f = 1000$.

- 3.11. As Liu et al. [148] put forward, it appears that the streamwise variance, or "waviness", dies out first, indicating that the streamwise streaks first straighten out before allowing the spanwise rolls to decay. After the quick decay of the spanwise rolls, the streamwise streaks are then able to decay. Observed in Figures 3.9 - 3.11, the initial rate at which the variance of the streamwise velocity field decays increases with decreasing final Reynolds number, which would allow the spanwise rolls to decay sooner. This is a possible mechanism for the increased decay rate as final Reynolds number is decreased.

3.3.1.3   Streamwise variance

Liu et al. [148] discuss the process of decay as beginning with the reduction in "waviness" of the streamwise structures before the spanwise rolls can decay. To quantify this, we analyze the streamwise variance of the velocity disturbances in each direction. Figure 3.8 shows the time-evolution of the average streamwise variance as a function of final Reynolds number, where the values are normalized by the average streamwise variance of the initial condition. As the final Reynolds number is decreased, the streamwise variance decreases more rapidly. According to Liu et al. [148], this decrease in waviness allows the spanwise rolls to decay sooner in the evolution of the system, and, ultimately, a faster decay to the laminar state. Figure 3.8 also shows the average streamwise variance for the wall-normal and spanwise perturbation velocities. While the rate at which the streamwise variance of the spanwise velocity appears to remain constant with decreasing final Reynolds number, the time at which this decay begins is earlier. This further corroborates the proposed process that the streamwise streaks first straighten before the spanwise rolls begin to decay quickly, followed by a second stage where the streamwise streaks decay. At lower final Reynolds numbers, this process appears to happen more quickly because the streamwise structures

$$L_s = 0.00$$
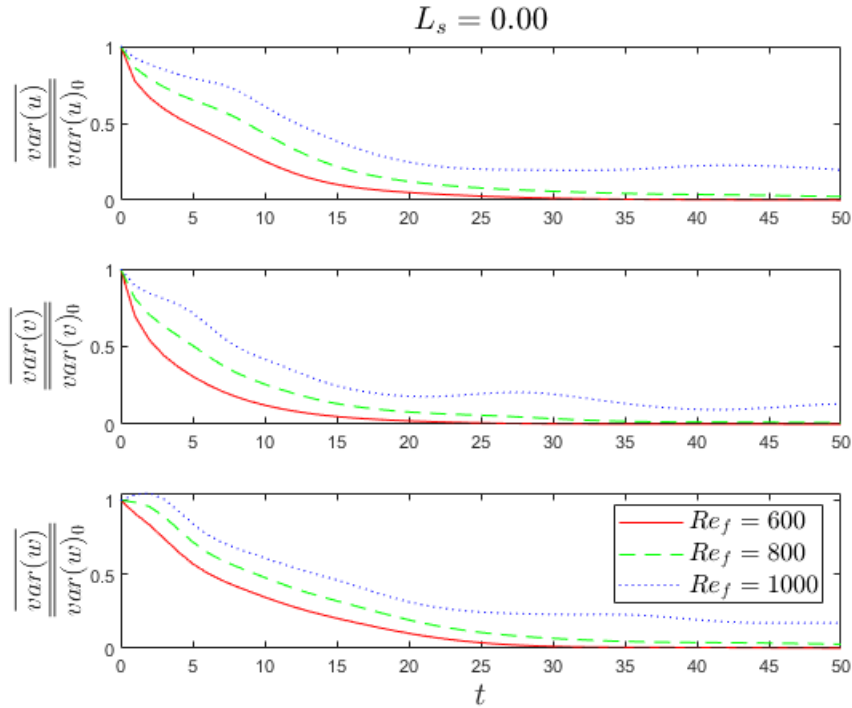
Figure 3.8: Normalized mean streamwise variance for all three velocity fields for the no-slip case at $y^+ = 12$ for $Re_f = 600, 800, 1000$.

become streamwise oriented more quickly.

Figures 3.9 - 3.11 also show the effect of slip on the streamwise variance of the three velocity fields. Similar to the trends observed before in the decay of velocity magnitude, the slip has negligible impact as the final Reynolds number is decreased. However, for $Re_f = 1000$, the slip causes decreased streamwise variance, possibly indicating the mechanism for the increased decay rate with wall slip. For $Re_f = 600, 800$ there is a brief period at $t = 5 \sim 10$ where the slip has a slight effect on the streamwise variance.

3.3.1.4 Wall shear rate

We can compare these results with the decay in the wall shear rate. Figure 3.12 shows the time evolution of a 10-run ensemble average of the area-averaged wall shear rate
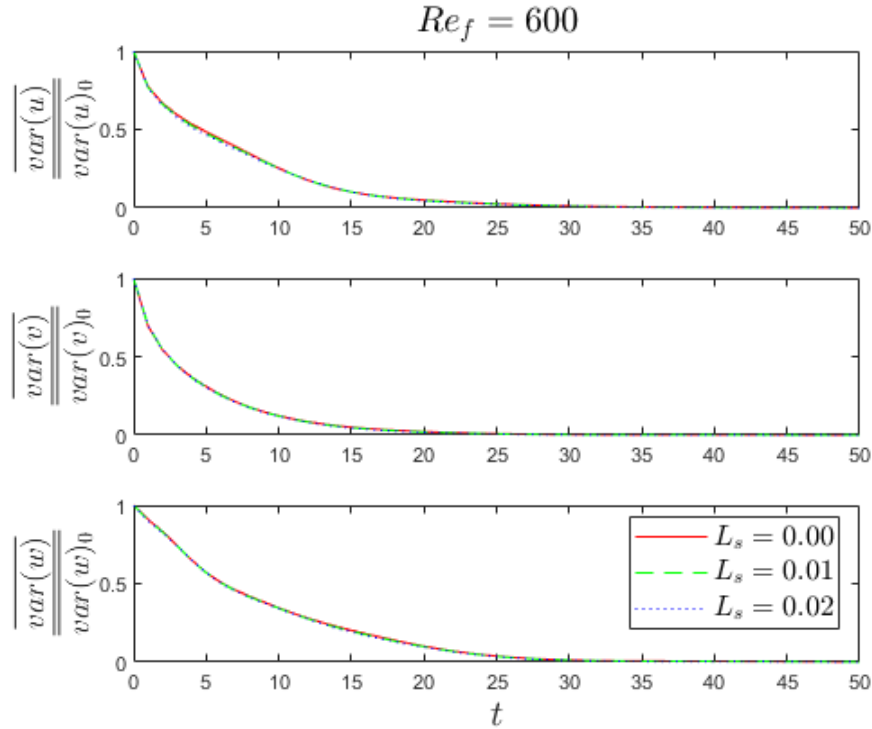
Figure 3.9: Normalized mean streamwise variance for all three velocity fields for the slip and no-slip cases at $y^+ = 12$ for $Re_f = 600$.

for each final Reynolds number and slip length. The vertical dashed lines correspond to the time at which the wall shear rate reaches 101% of the final value. Again, we see that the rate at which the system decays to the laminar state increases with decreasing final Reynolds number. We also see, again, that below $Re_f = 1000$ the slip surfaces have less impact on the decay rate. Slip appears to have no impact for $Re_f = 600$, but a counterintuitive effect for $Re_f = 800$. For this Reynolds number, $L_s = 0.01$ causes the system to decay faster, but $L_s = 0.02$ results in a time to reach the laminar state that is longer than even the no-slip case.
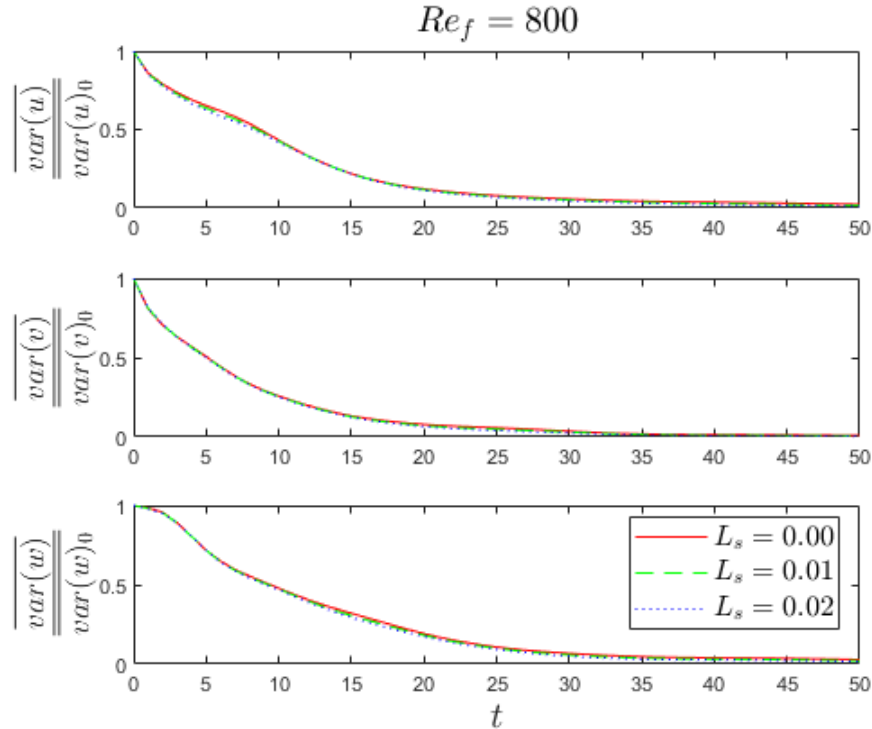
Figure 3.10: Normalized mean streamwise variance for all three velocity fields for the slip and no-slip cases at $y^+ = 12$ for $Re_f = 800$.

3.3.2   Decay of exact coherent solutions

In addition to the decay of random initial conditions, a more deterministic approach can be taken by using exact coherent solutions to the Navier-Stokes equations as the initial conditions. Specifically, the P3 and P4 upper-branch traveling wave solutions to the Navier-Stokes equations are used as initial conditions. These solutions exhibit characteristic short-time behavior. Therefore, any changes associated with this behavior can be attributed to the changes in the system. The upper-branch (UB) solutions are used as they exhibit dynamics similar to those observed in a turbulent channel flows. In fact, a turbulent trajectory at the respective Reynolds number spends most of its time in a region where the UB solution resides. More details of the behavior and characteristics of these solutions can be found in Park and Graham
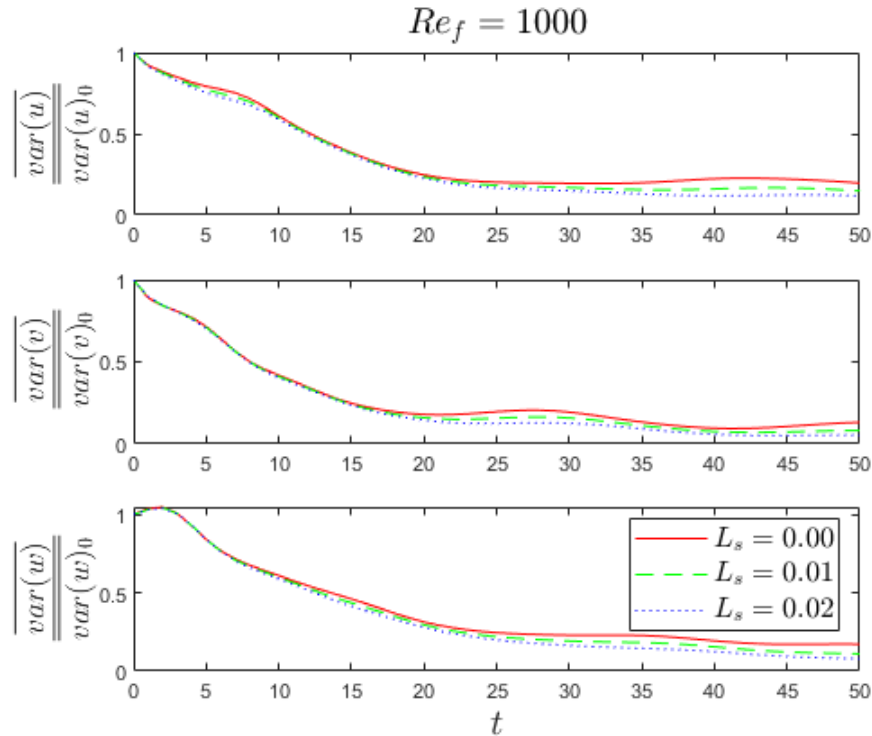
Figure 3.11: Normalized mean streamwise variance for all three velocity fields for the slip and no-slip cases at $y^+ = 12$ for $Re_f = 1000$.

[182].

Analysis of the decay of the P3UB and P4UB solutions via the time-evolution of perturbation velocity magnitude, flow structures, streamwise variance of velocity fields, and the time-evolution of wall shear rate are detailed below.

3.3.2.1   Time-evolution of L_2-norm of velocity

First, the effect of final quench Reynolds number is considered. The time evolution of the L_2-norm of the disturbance velocity in each spatial dimension for the P3 and P4 solutions is shown in Figure 3.13 and Figure 3.14, respectively. The quench protocol is performed for final Reynolds numbers $Re_f = 600, 800, 1000$ for the no-slip case. Unlike the trend observed for random initial conditions in Section 3.3.1 and by Liu
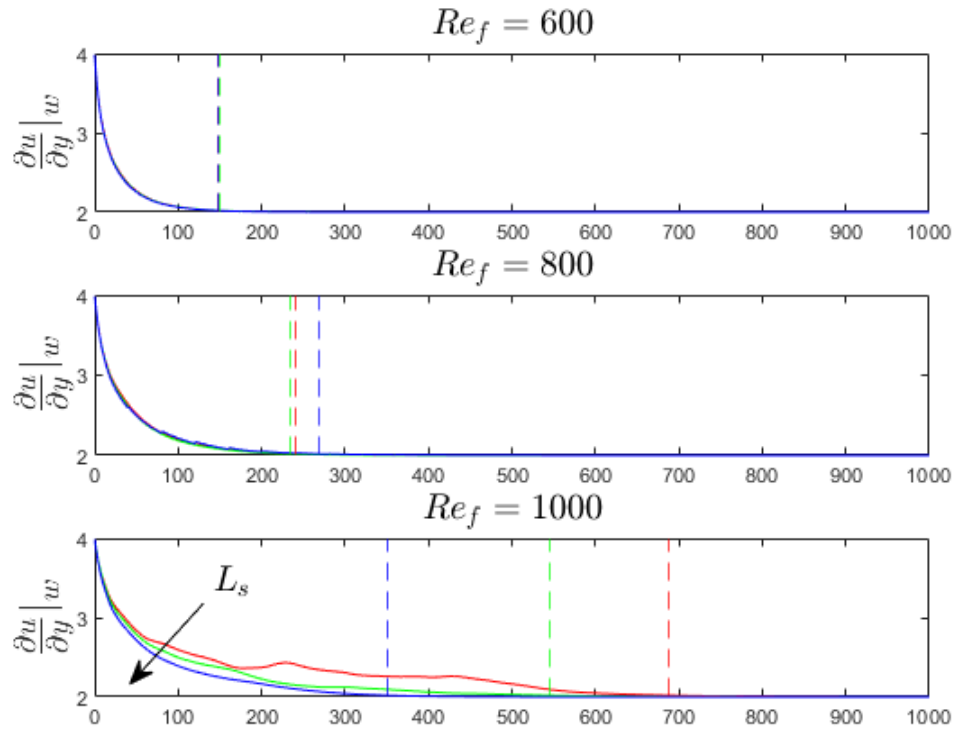
Figure 3.12: Time-evolution of wall shear rate for $L_s = 0.00, 0.01, 0.02$ and for $Re_f = 600, 800, 1000$. Arrow points in the direction of increasing slip length.

et al. [148], the P3 solution appears to have a similar decay rate in the streamwise and spanwise direction during both an initial decay stage and a second decay stage showing an increased rate of decay. This trend is the same for $Re_f = 800, 1000$. For all three Re_f studied, the wall-normal disturbances decay faster than both streamwise and spanwise disturbances. There is an increase in the decay rate as the final Reynolds is decreased. Similar to the behavior observed in 3.3.1 and Liu et al. [148].

Interestingly, similar to the observed behavior in Section 2.4.3, there are distinct decay behaviors between the P3 and P4 upper-branch solutions. The trend seen in the P4 solution is similar to that observed by Gomé et al. [76], Liu et al. [148]: the spanwise disturbances decay faster than the streamwise disturbances for all Re_f studied. The decay rate in all directions increases linearly with decreasing Re_f. For
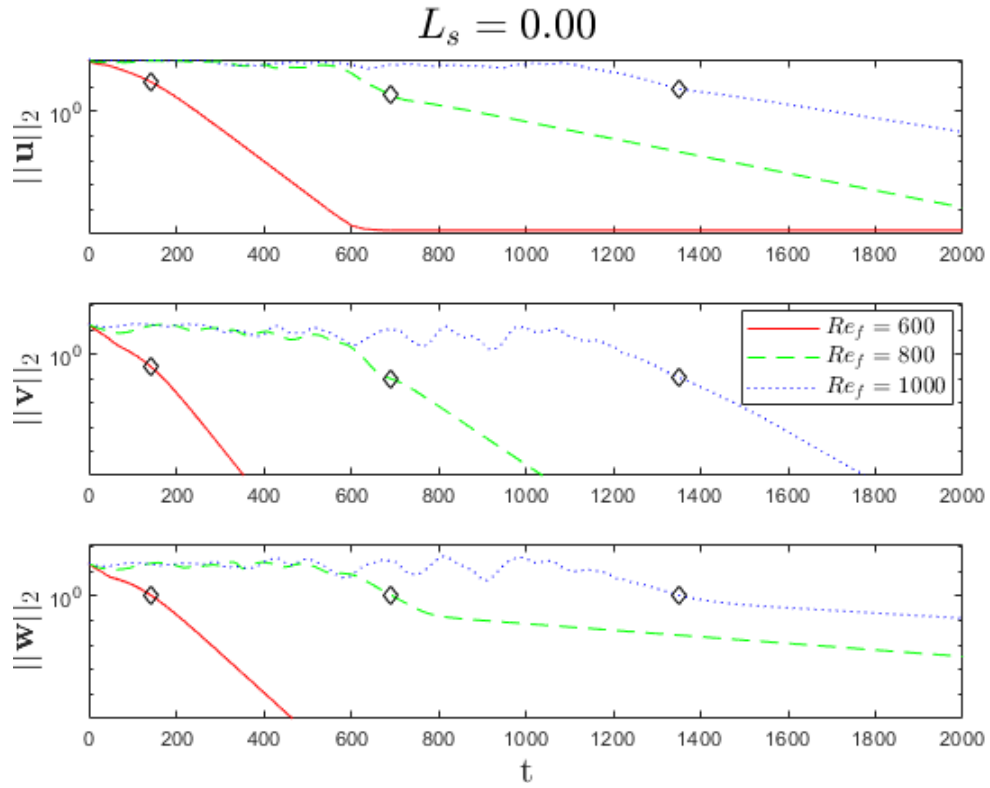
Figure 3.13: Decay of the L_2-norm of x, y, and z velocity disturbances for the P3 upper-branch traveling wave solution at initial Reynolds number $Re_i \approx 1800$ for various quench Reynolds numbers, $Re_f = 600, 800, 1000$, and slip length, $L_s = 0.00$.

the P4 soution, which is characterized by structures localized at the critical layer, the spanwise and wall-normal disturbances are almost identical other than for $Re_f = 600$ where the spanwise disturbances decay with a faster rate during an initial stage before a second slower stage. While the decay rate for the spanwise and wall-normal energy is larger than the streamwise direction, the disturbances in these directions take longer than the streamwise disturbances to decay fully. These may be features associated with the spatial structure of the ECSs.
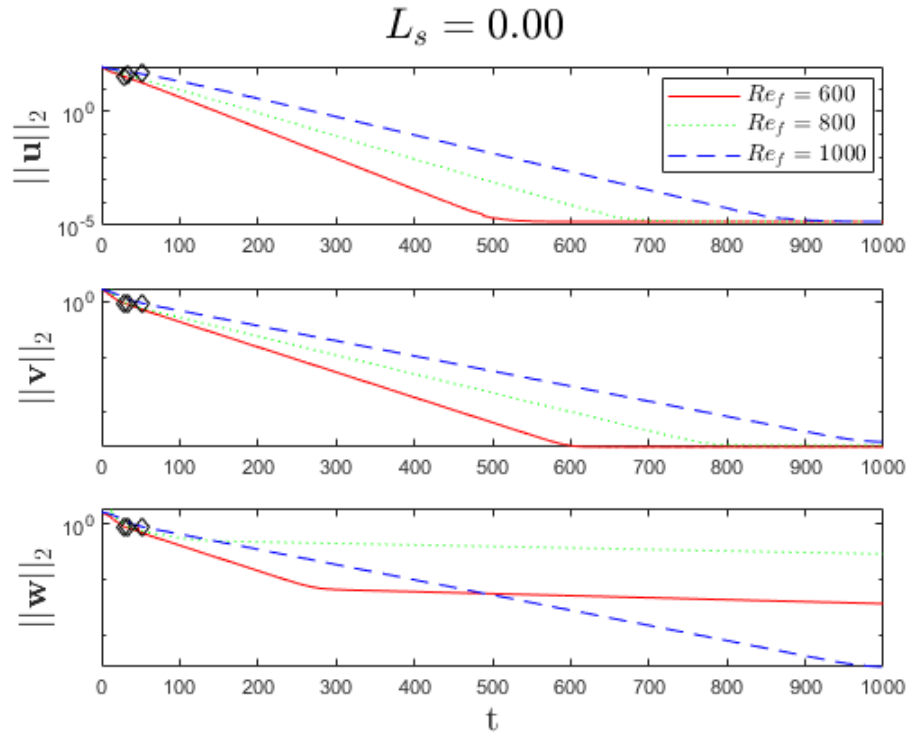
$$L_s = 0.00$$

Figure 3.14: Decay of the L_2-norm of x, y, and z velocity disturbances for the P4 upper-branch traveling wave solution at initial Reynolds number $Re_i \approx 1800$ for various quench Reynolds numbers, $Re_f = 600, 800, 1000$, and slip length, $L_s = 0.00$.

3.3.2.2 Flow structures

Figure 3.17 shows the flow structures at a wall-normal plane at $y^+ = 12$ for the P3 solution at $Re_f = 600$. As observed in the velocity magnitude, the spanwise structures decay faster than the streamwise structures. This same trend is observed in the flow structures for both slip lengths (not shown) studied for this final Reynolds number.

Figures 3.18 - 3.20 show the flow structures at a wall-normal plane at $y^+ = 12$ for the P3 solution at $Re_f = 800$. Spanwise structures decay faster than the streamwise structures. As seen in the velocity magnitude, the system takes longer to decay at this higher final Reynolds number. However, unlike $Re_f = 600$, the slip surfaces have an effect on the dynamics as the P3 solution evolves. Interestingly, the slip
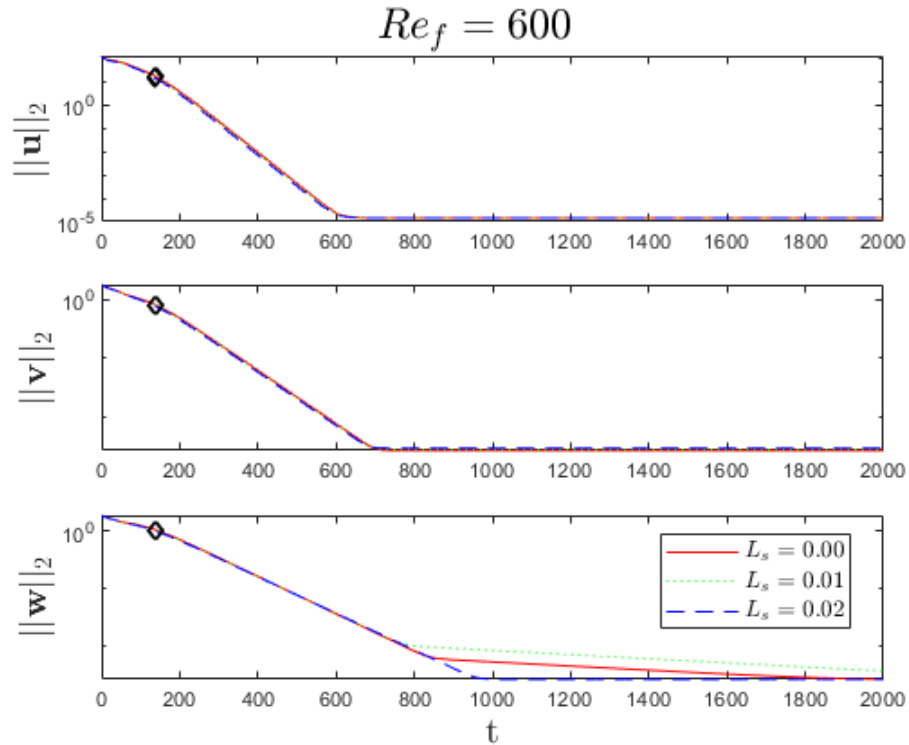
Figure 3.15: Decay of the L_2-norm of x, y, and z velocity disturbances for the P3 upper-branch traveling wave solution at initial Reynolds number $Re_i \approx 1800$ for quench Reynolds number, $Re_f = 600$, and various slip lengths, $L_s = 0.00, 0.01, 0.02$.

prolongs the decay time, with structures still around for twice as long with $L_s = 0.02$ compared with the no-slip case. The spanwise structures still decay more quickly than the streamwise structures.

Figures 3.21 - 3.23 show the flow structures at a wall-normal plane at $y^+ = 12$ for the P3 solution at $Re_f = 1000$. Spanwise structures decay faster than the streamwise structures. As seen in the velocity magnitude, the system takes longer to decay at this higher final Reynolds number. The slip surfaces have an effect on the dynamics as the P3 solution evolves. Again, for this final Reynolds number, the $L_s = 0.02$ case has much stronger fluctuations still present for much longer compared with the no-slip case. The $L_s = 0.01$ case causes the system to decay faster than $L_s = 0.02$
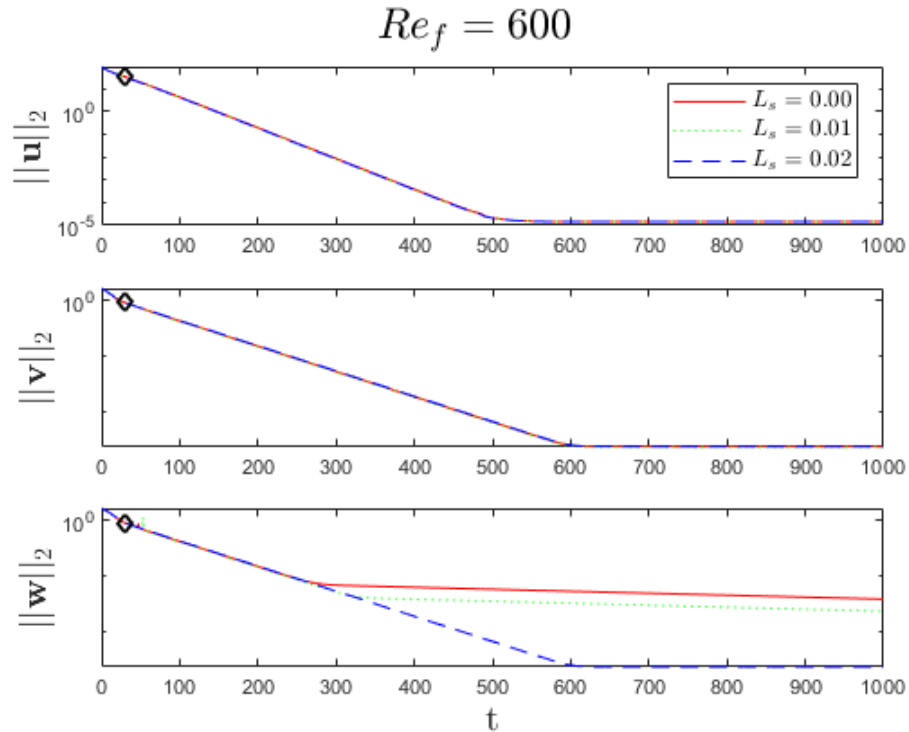
Figure 3.16: Decay of the L_2-norm of x, y, and z velocity disturbances for the P4 upper-branch traveling wave solution at initial Reynolds number $Re_i \approx 1800$ for quench Reynolds number, $Re_f = 600$, and various slip lengths, $L_s = 0.00, 0.01, 0.02$.

but longer than the no-slip case. The slip surfaces appear to have some stabilizing effect on the P3 flow structures.

Figures 3.24 - 3.26 show the flow structures at a wall-normal plane at $y^+ = 12$ for the P3 solution at $Re_f = 600, 800, 1000$, respectively. As observed in the velocity magnitude, the spanwise structures decay faster than the streamwise structures. This same trend is observed in the P4 flow structures for both slip lengths (not shown) studied for this final Reynolds number and is negligible. The flow structures between the three final Reynolds numbers are similar, but appear stronger and take longer to decay in the streamwise direction for $Re_f = 1000$.
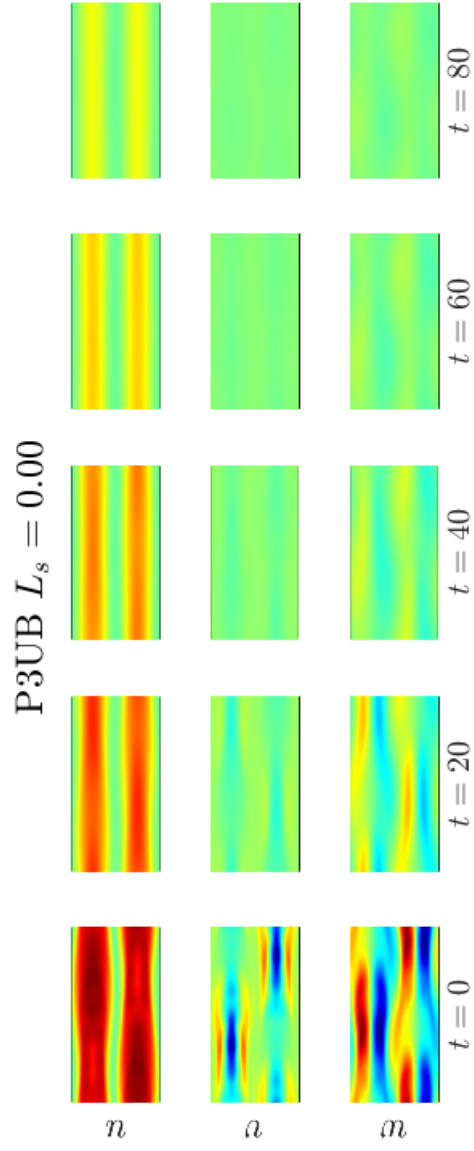
Figure 3.17: Flow structures of the P3 upper-branch solution given by the perturbation velocity in each spatial dimension at $y^+ = 12$ for $L_s = 0.00$ and $Re_f = 600$.
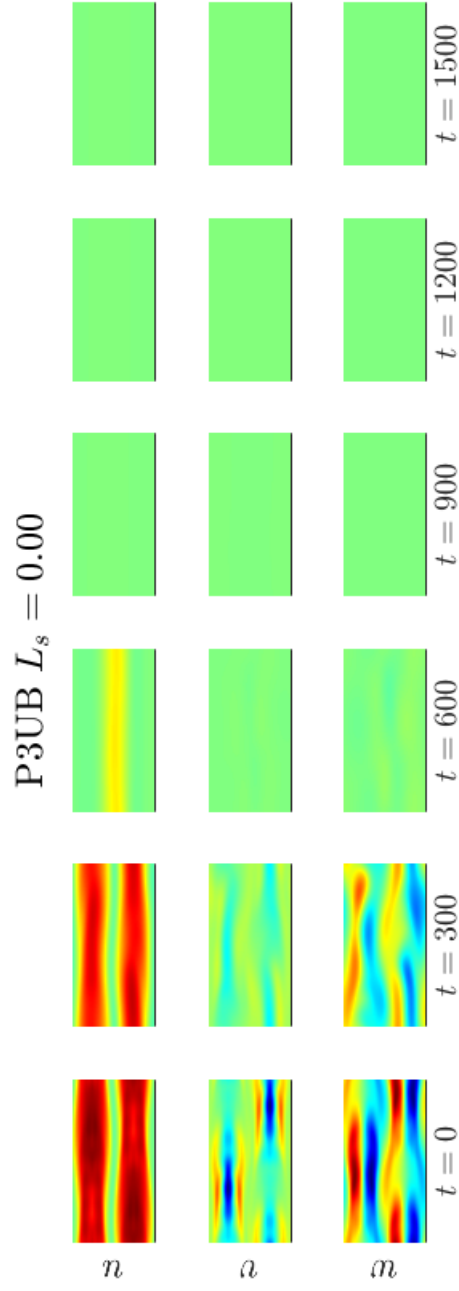
Figure 3.18: Flow structures of the P3 upper-branch solution given by the perturbation velocity in each spatial dimension at $y^+ = 12$ for $L_s = 0.00$ and $Re_f = 800$.
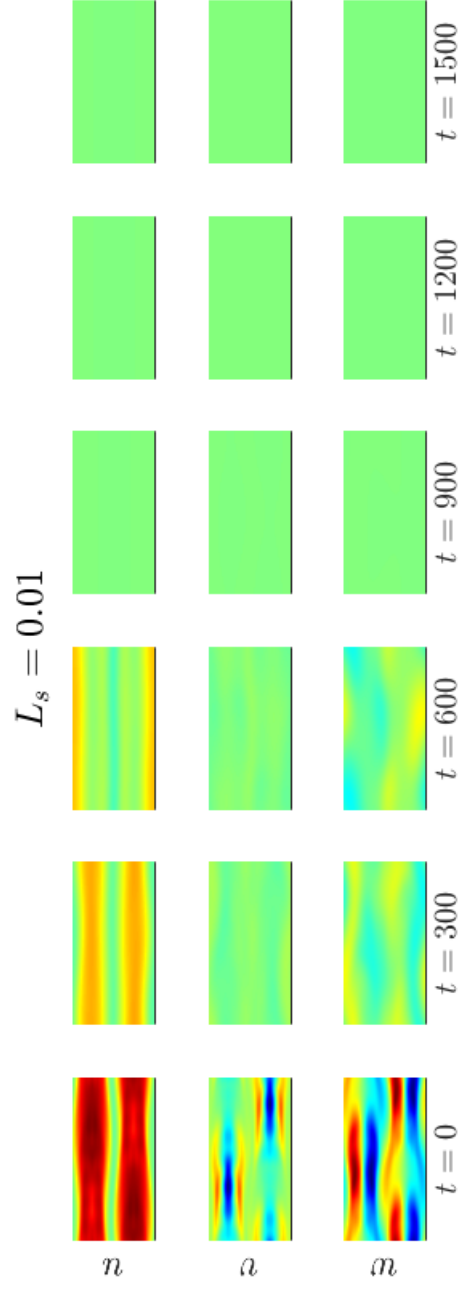
Figure 3.19: Flow structures of the P3 upper-branch solution given by the perturbation velocity in each spatial dimension at $y^+ = 12$ for $L_s = 0.01$ and $Re_f = 800$.
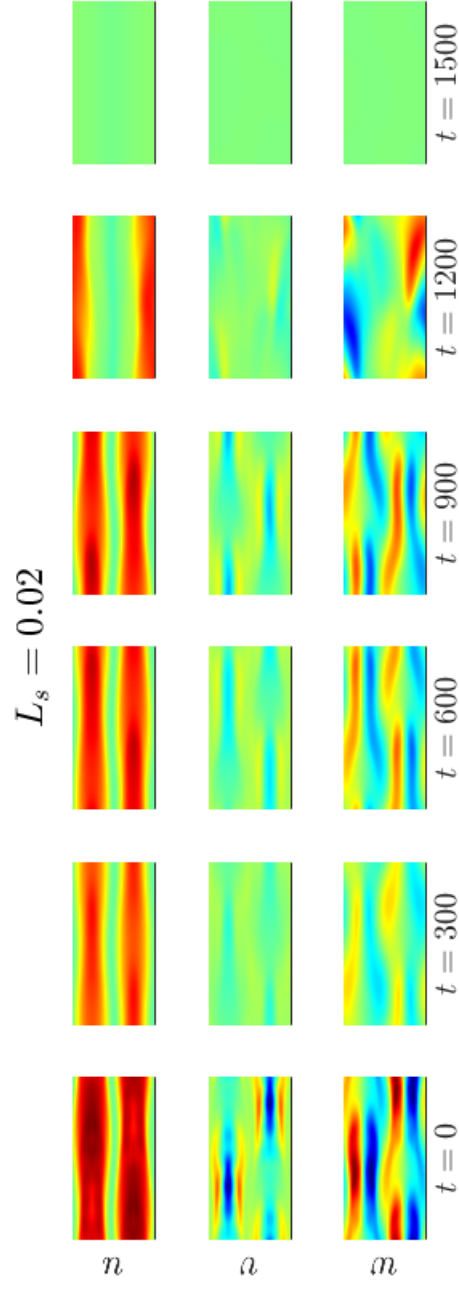
Figure 3.20: Flow structures of the P3 upper-branch solution given by the perturbation velocity in each spatial dimension at $y^+ = 12$ for $L_s = 0.02$ and $Re_f = 800$.
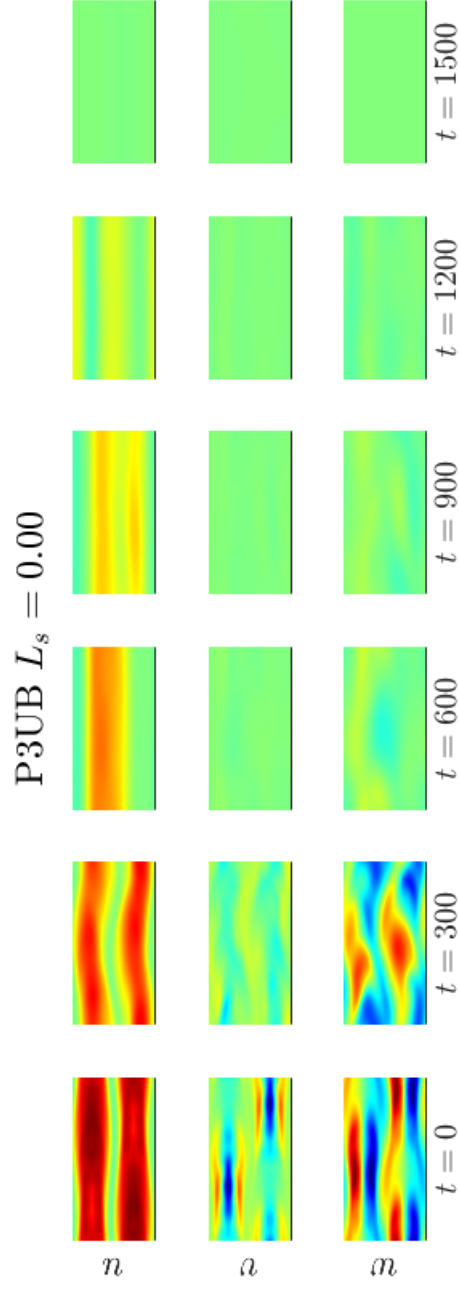
Figure 3.21: Flow structures of the P3 upper-branch solution given by the perturbation velocity in each spatial dimension at $y^+ = 12$ for $L_s = 0.00$ and $Re_f = 1000$.
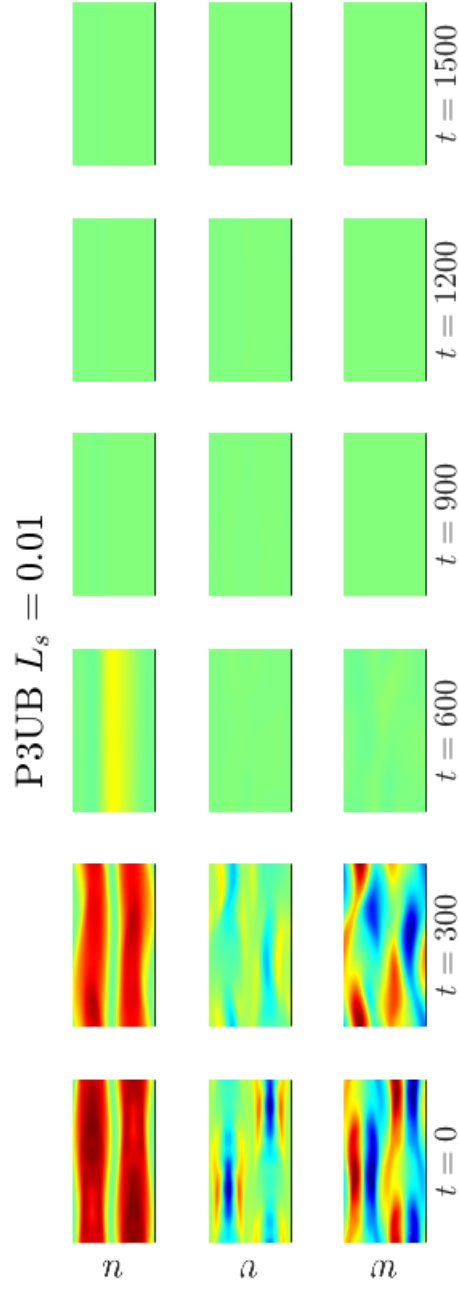
Figure 3.22: Flow structures of the P3 upper-branch solution given by the perturbation velocity in each spatial dimension at $y^+ = 12$ for $L_s = 0.01$ and $Re_f = 1000$.
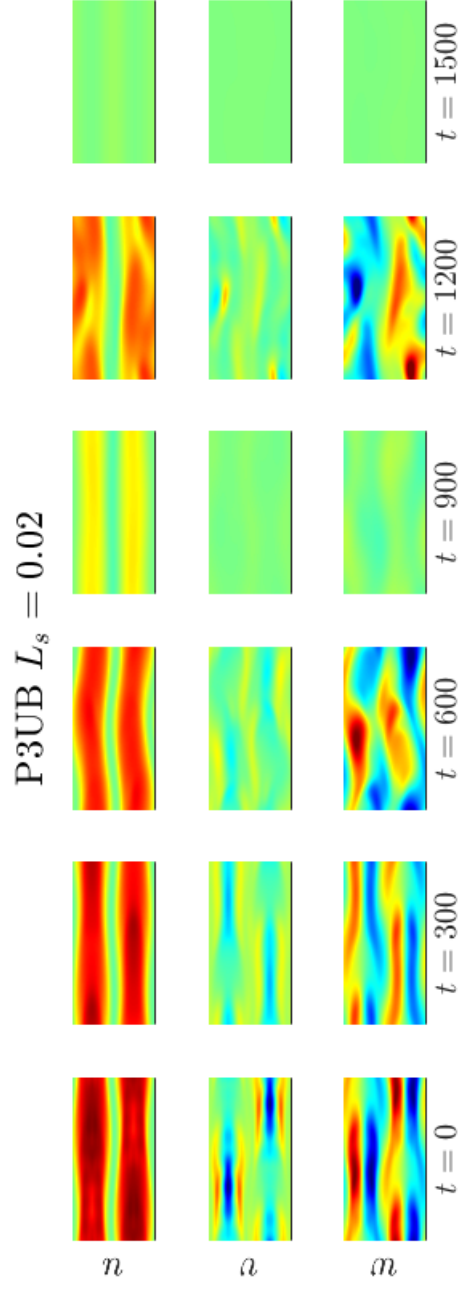
Figure 3.23: Flow structures of the P3 upper-branch solution given by the perturbation velocity in each spatial dimension at $y^+ = 12$ for $L_s = 0.02$ and $Re_f = 1000$.
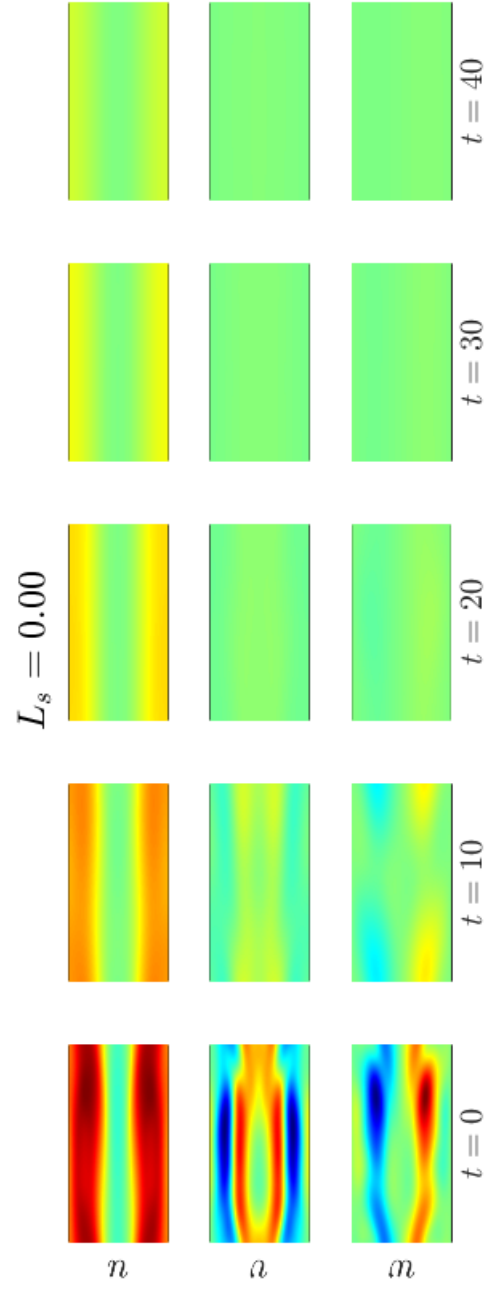
Figure 3.24: Flow structures of the P4 upper-branch solution given by the perturbation velocity in each spatial dimension at $y^+ = 12$ for $L_s = 0.00$ and $Re_f = 600$.

87
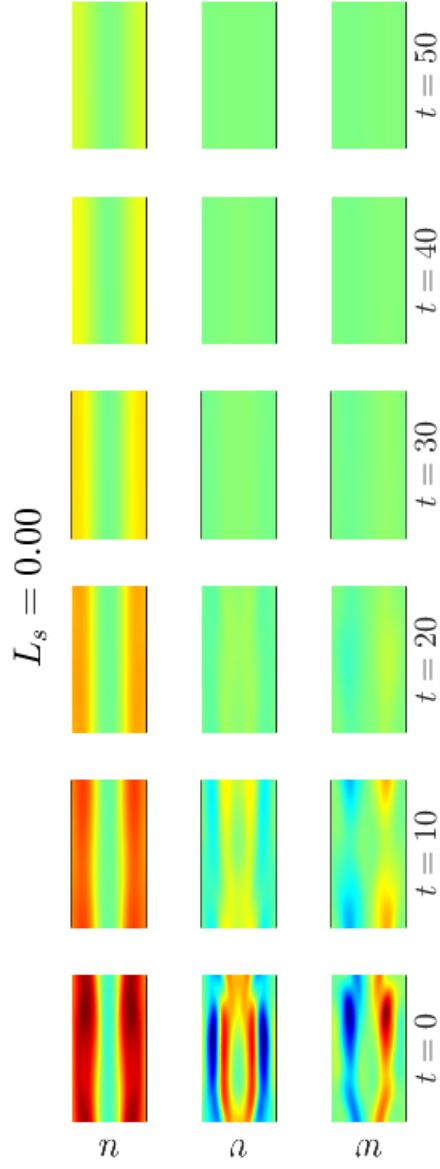
Figure 3.25: Flow structures of the P4 upper-branch solution given by the perturbation velocity in each spatial dimension at $y^+ = 12$ for $L_s = 0.00$ and $Re_f = 800$.
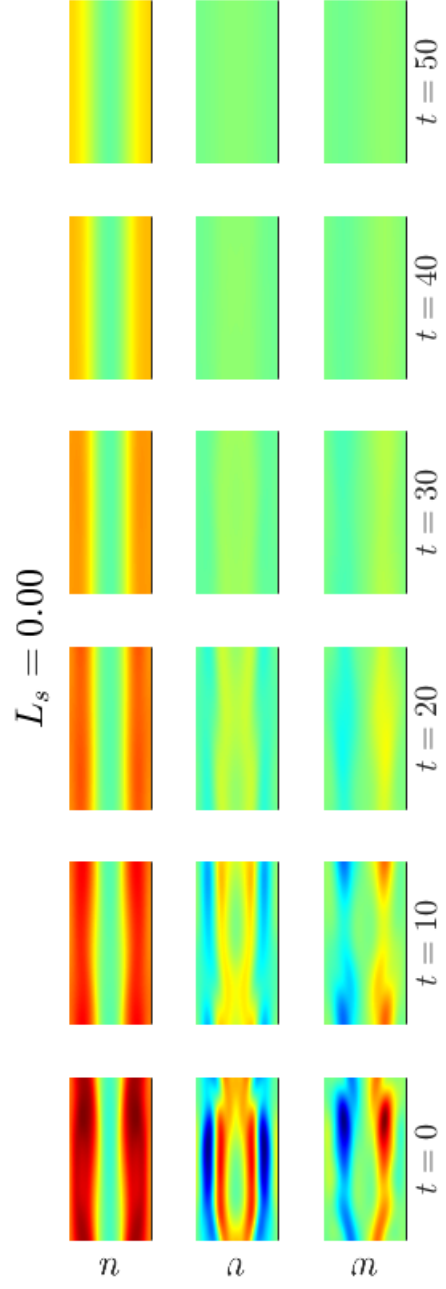
Figure 3.26: Flow structures of the P4 upper-branch solution given by the perturbation velocity in each spatial dimension at $y^+ = 12$ for $L_s = 0.00$ and $Re_f = 1000$.

3.3.2.3 Streamwise variance

Figures 3.27 - 3.29 show the evolution of the average streamwise variance in the perturbation velocity in each spatial dimension for $Re_f = 600, 800, 1000$, respectively. The variance is normalized by the streamwise variance of the initial condition. For $Re_f = 600$, the system decays immediately, so the variance in the streamwise direction also decays immediately. There appear to be three distinct stages in the streamwise and spanwise directions. Initially, the variance decays quickly, before leveling out in the two ensuing stages. The streamwise variance does appear to decay more quickly than the spanwise initially, corroborating observations by [148]. The variance in the wall-normal velocity decays the fastest of the three components, possibly suggesting that the decay first begins in the wall-normal direction before the streamwise streaks straighten. There is a small effect of slip on the streamwise variance of the streamwise perturbation velocity, where the variance is reduced for $t \approx 2.5 \sim 10$.

For the $Re_f = 800$ and $Re_f = 1000$ cases, the variance has more rich dynamics because the system remains turbulent for some time. For $Re_f = 800$, there appears to be some sort of periodic behavior of the system when slip is present at the wall. When the system finally decays, the streamwise variance of the streamwise velocity decays before the streamwise variance of the spanwise velocity. For $Re_f = 1000$, there is no discernible trend in the average streamwise variance of the velocity components. It does appear that the variance in the wall-normal velocity decays first, followed by the spanwise, and then streamwise components.

The average streamwise variance of the perturbation velocity for the P4 solution is shown in Figures 3.30 - 3.32. A similar trend to the P3 solution is observed, other than the system begins to decay immediately compared to the P3 solution. For all three final Reynolds numbers studied, the variance in the wall-normal velocity occurs
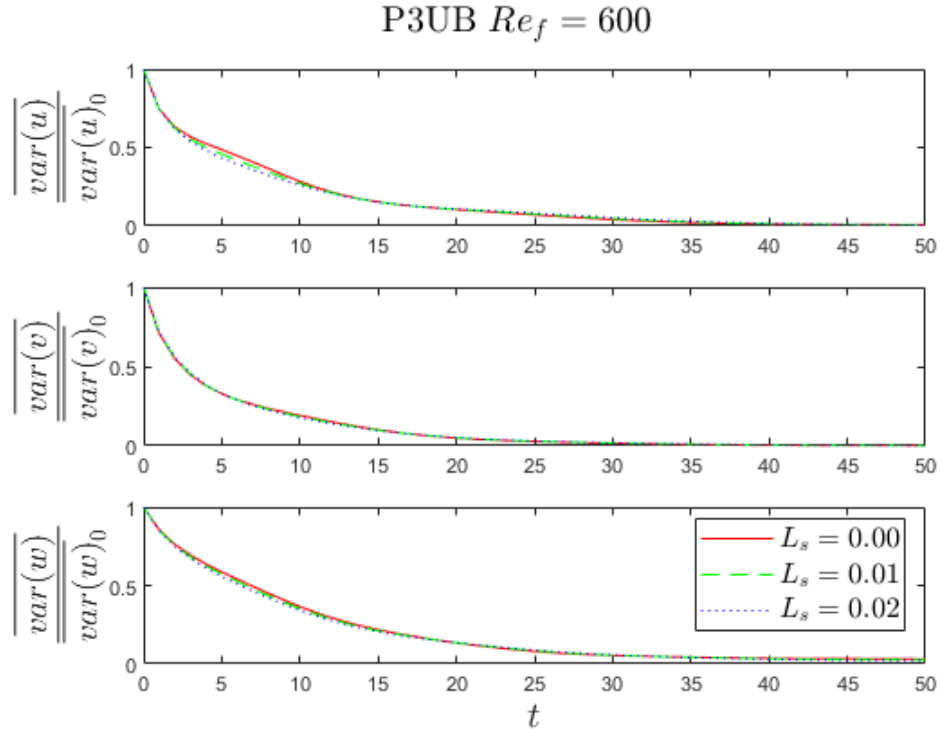
Figure 3.27: Normalized mean streamwise variance of the P3 upper-branch solution for all three velocity fields for the slip and no-slip cases at $y^+ = 12$ for $Re_f = 600$.

first, followed by the streamwise component, and then the spanwise component. Wall slip has negligible effect on the average streamwise variance in the decay of the P4 solution.

3.3.2.4 Wall shear rate

The time-evolution of area-averaged wall shear rate for the P3UB solution is shown in Figure 3.33. The vertical dashed lines correspond to the time at which the value reaches 101% of the final value. There is a counterintuitive behavior of the P3 solution as it decays to the various final Reynolds numbers. While the decay begins immediately, the system takes the longest to decay for the lowest final Reynolds number, $Re_f = 600$. There is no clear trend for the time to decay as a function of final

$$P3UB\ Re_f = 800$$
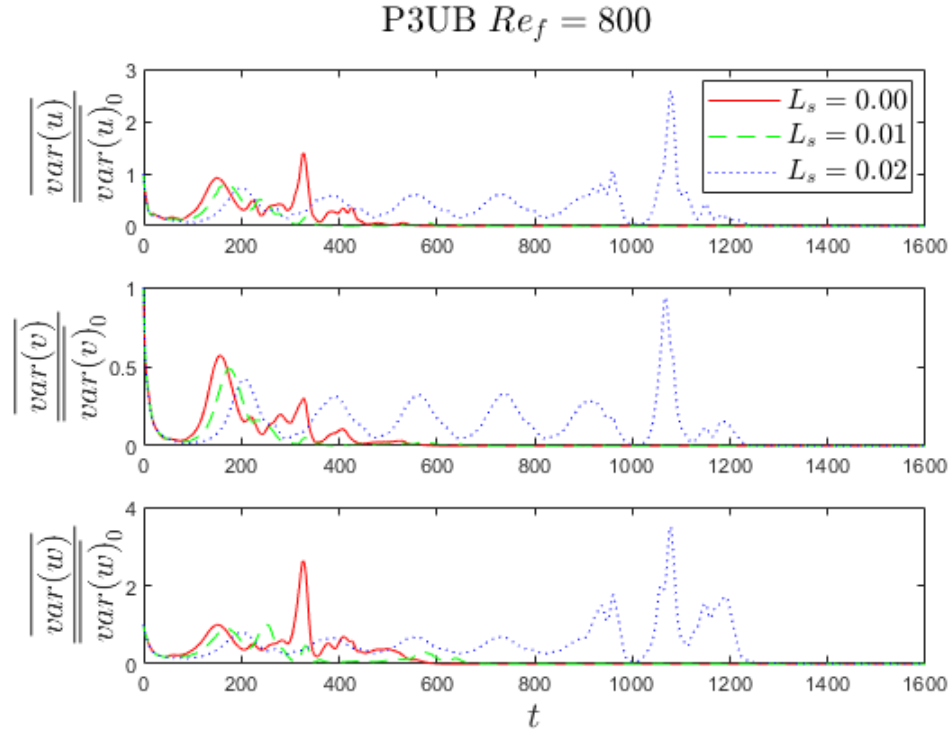
Figure 3.28: Normalized mean streamwise variance of the P3 upper-branch solution for all three velocity fields for the slip and no-slip cases at $y^+ = 12$ for $Re_f = 800$.

Reynolds number.

The effect of wall slip is interesting, as well. Increasing slip decreases the time to decay for $Re_f = 600$. However, for $Re_f = 800$, the time that it takes the system to decay to the laminar state increases for increasing slip length. This trend is not followed for $Re_f = 1000$, where $L_s = 0.01$ causes the system to decay the fastest, followed by $L_s = 0.02$ and then $L_s = 0.00$. There appears to be some critical slip length which causes the fastest decay before causing some interaction with the flow, and increasing the time to reach the laminar state.

The time-evolution of area-averaged wall shear rate for the P4UB solution is shown in Figure 3.34, where the vertical dashed lines correspond to the time at which the value reaches 101% of the final value. Again, the final Reynolds number has a coun-
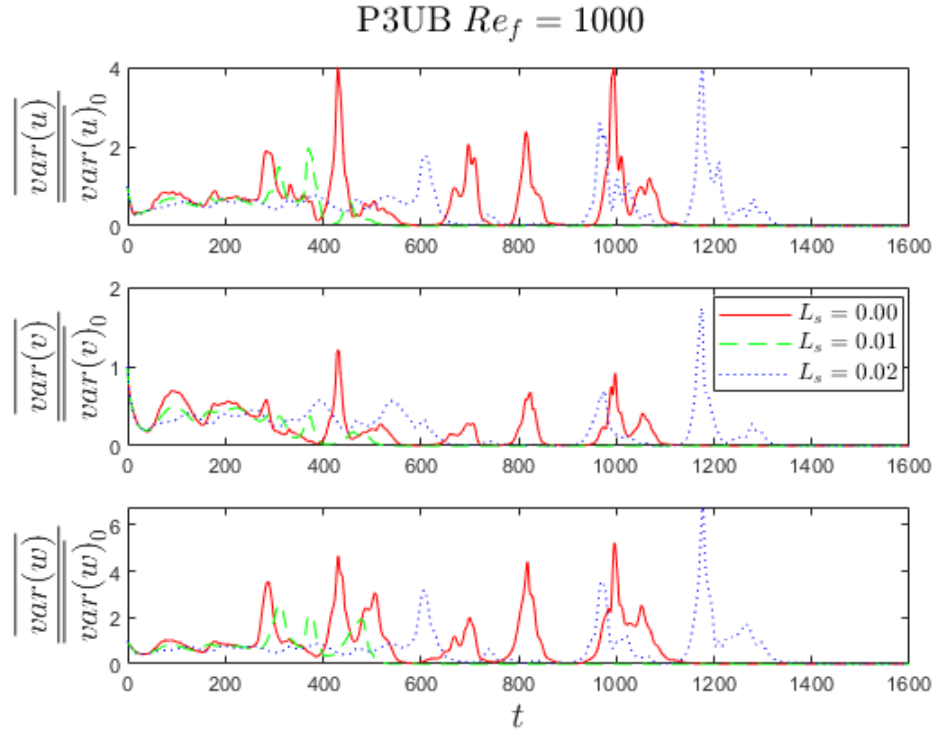
Figure 3.29: Normalized mean streamwise variance of the P3 upper-branch solution for all three velocity fields for the slip and no-slip cases at $y^+ = 12$ for $Re_f = 1000$.

terintuitive effect on the time required to decay to the laminar state. The system takes longest to decay for $Re_f = 600$, reaching the laminar state at $t \approx 875$. The time required to reach the laminar state is then reduced to $t \approx 150$ for $Re_f = 800$ and $t \approx 200$ for $Re_f = 1000$. Wall slip has a negligible effect on the decay time for the P4UB solution. It is interesting to note that the wall shear rate for the P4 solution takes much longer to decay than the time it takes for structures observed at $y^+ = 12$ to decay. While this wall normal distance is away from the wall slightly, it is still approximately the edge of the viscous sublayer. It may be that some structure persists near to the wall that takes longer to decay via viscous dissipation.

The difference in behavior of the P3 and P4 upper-branch solutions most likely stems from the difference in the structure of the solutions. As stated above, the P3 so-
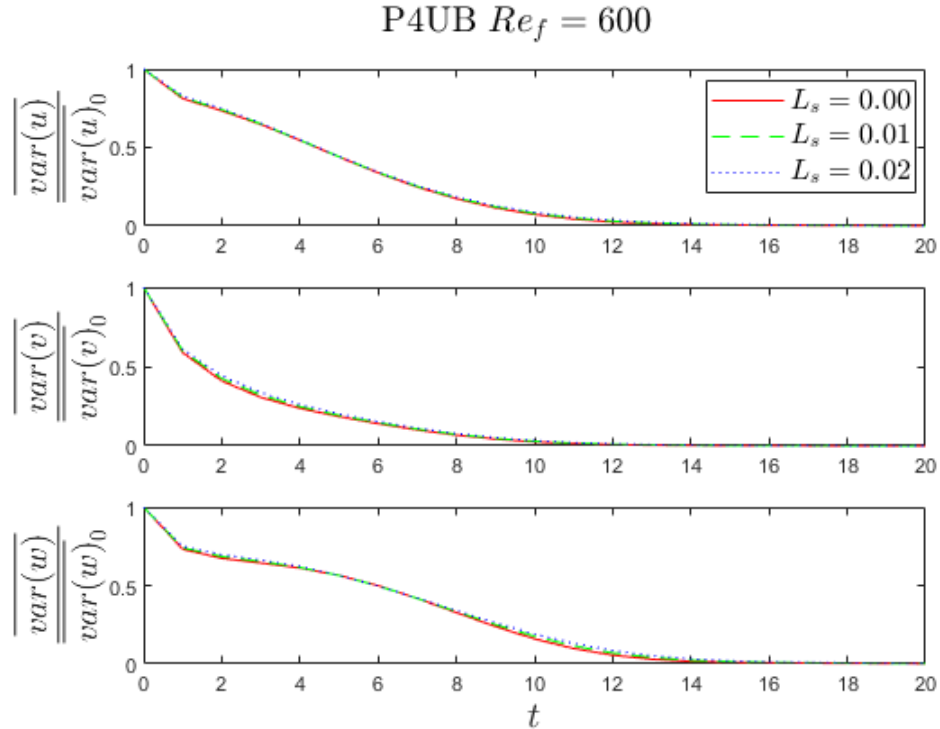
Figure 3.30: Normalized mean streamwise variance of the P4 upper-branch solution for all three velocity fields for the slip and no-slip cases at $y^+ = 12$ for $Re_f = 600$.

lution is characterized by free-stream turbulence, with structures concentrated at the core of the flow. The free-stream structures of the P3 solution may propagate down toward the wall initially to a wall-normal location where the wall slip stabilizes the structures somehow. The P4 solution is characterized by structures centered about the critical layer, closer to the wall. Because these structures are centered about the critical layer, closer to the wall, they may decay faster with the sudden disruption of the critical layer. Further analysis is necessary to elucidate the mechanisms responsible.
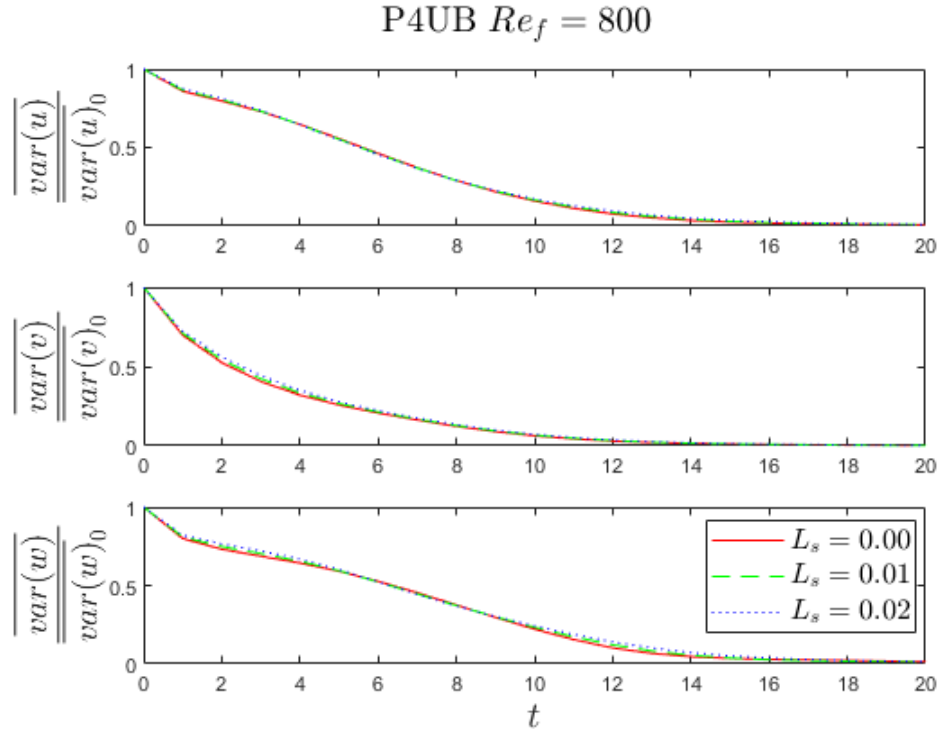
Figure 3.31: Normalized mean streamwise variance of the P4 upper-branch solution for all three velocity fields for the slip and no-slip cases at $y^+ = 12$ for $Re_f = 800$.

3.3.3 Edge states as facilitators to transition

Our fundamental understanding of the transition to turbulence is incomplete. Though there are countless studies on the transition to turbulence, we still have yet to form a full understanding of what causes some perturbations to trigger turbulence and some perturbations to decay due to viscous effects. This spurred a new perspective on the laminar-turbulent transition through the lens of dynamical systems theory. Through this lens, a manifold exists which separates the initial conditions that decay from initial conditions that evolve into turbulence [101, 212, 202]. If a state resides on this stable manifold, meaning that it neither decays nor becomes turbulent, it is attracted to what are known as 'edge states'. The unstable manifold extends from the edge state toward the laminar state and the turbulent attractor.
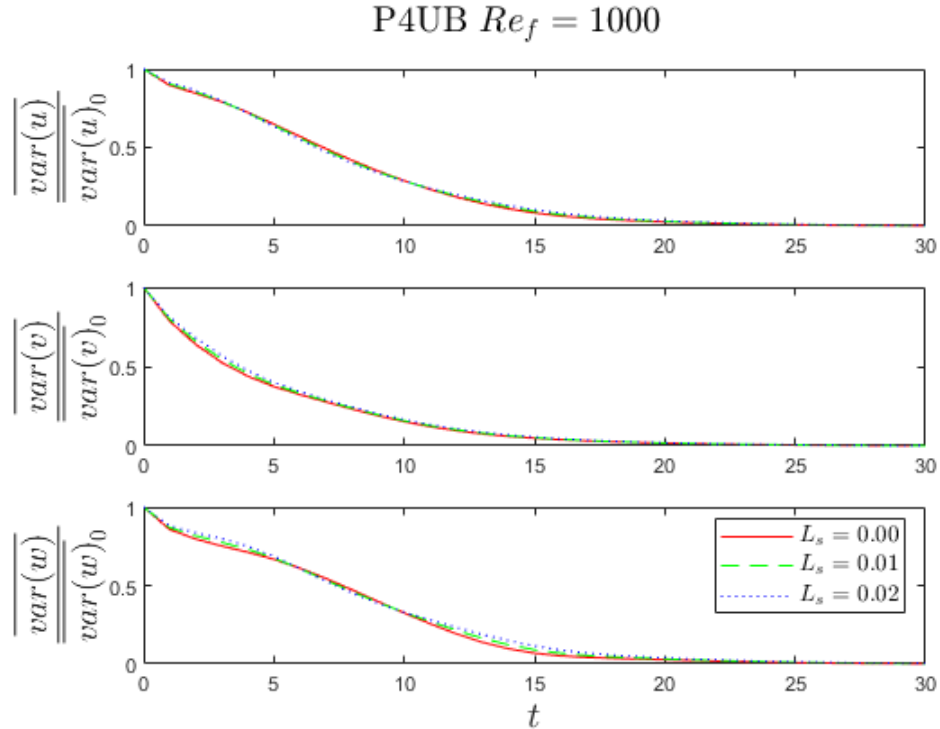
Figure 3.32: Normalized mean streamwise variance of the P4 upper-branch solution for all three velocity fields for the slip and no-slip cases at $y^+ = 12$ for $Re_f = 1000$.

Recently, Khapko et al. [121] investigated the possibility that edge states act as mediators to transition in boundary-layer flows. They studied a set of simulations initialized with non-localized noise and found that a sinuous low-speed streak is observed immediately before transition which is both qualitatively and quantitatively similar to the coherent structure associated with the edge state. What has yet to be studied in depth, and is the goal of this section, is whether these edge states also facilitate the decay to the laminar state. Figure 3.35 shows a schematic of the state space layout for the laminar-turbulent transition with a possible trajectory of the decay from the turbulent attractor, through the edge state, to the laminar state.

The P3 and P4 solution families are of special interest because their lower-branch solutions are embedded in the basin boundary separating the basins of attraction for
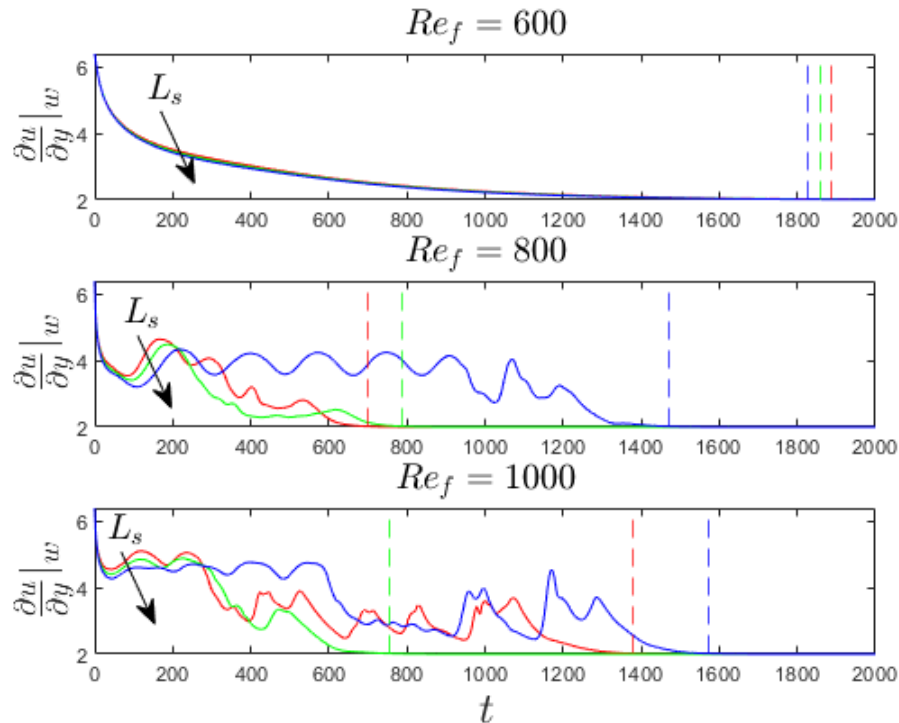
Figure 3.33: Time-evoution of wall shear rate for the P3 upper-branch traveling wave solution at initial Reynolds number $Re_i \approx 1800$ for quench Reynolds numbers, $Re_f = 600, 800, 1000$, and various slip lengths, $L_s = 0.00, 0.01, 0.02$.

the laminar and turbulent states. The P3 lower-branch solution is an edge state as it only has a single unstable direction, while the P4 lower-branch solution has two unstable directions [182]. With these solutions in hand, this section investigates whether the P3 or P4 lower-branch solutions mediate the decay of turbulent trajectories to the laminar state. The goal is to determine whether a turbulent trajectory, when decaying to the laminar state, visits either of these solutions or whether different decay dynamics occur. We use the ensemble averaged values of the 10 decay trajectories from random initial conditions, as well as trajectories from the decay of the P3 and P4 upper-branch solutions. The same final Reynolds number and wall slip lengths are investigated.

A number of state variables can be used to visualize the system in state-space.
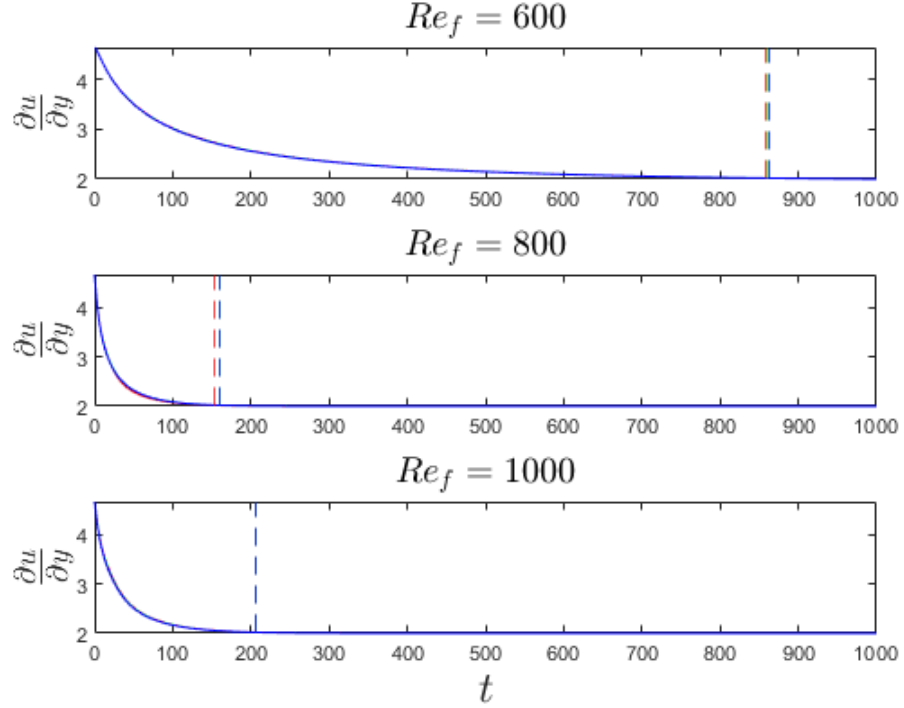
Figure 3.34: Time-evoution of wall shear rate for the P4 upper-branch traveling wave solution at initial Reynolds number $Re_i \approx 1800$ for quench Reynolds numbers, $Re_f = 600, 800, 1000$, and various slip lengths, $L_s = 0.00, 0.01, 0.02$.

Here, we choose to project the infinite dimensional state of the system onto the two-dimensional plane of energy input rate versus energy dissipation rate. Input and dissipation, as they will be referred to, are defined as

$$I = \frac{1}{2L_z} \int_0^{L_z} \int_{-1}^1 (pu|_{x=0} - pu|_{x=L_x}) dy dz \tag{3.2}$$

and the energy dissipation rate is given as

$$D = \frac{1}{2L_x L_z} \int_0^{L_z} \int_{-1}^1 \int_0^{L_x} (|\nabla u|^2 + |\nabla v|^2 + |\nabla w|^2) dx dy dz. \tag{3.3}$$
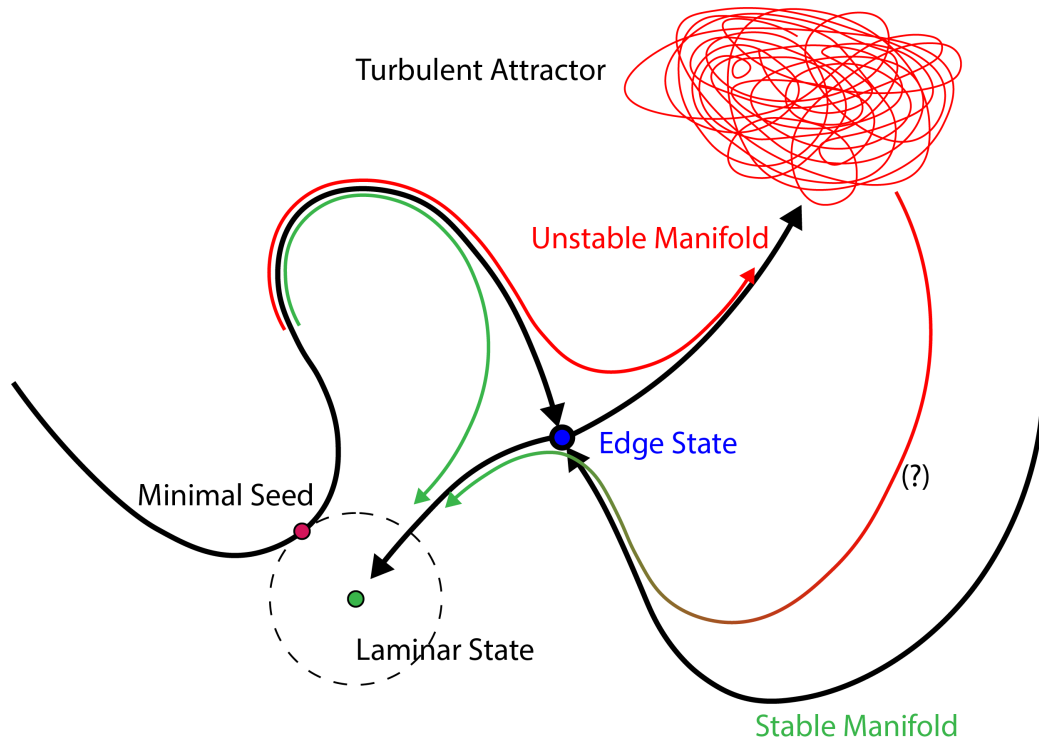
Figure 3.35: State space representation of turbulence and the edge state. The boundary between the the basins of attraction coincides with the stable manifold of the edge state. The edge state's unstable manifold point toward the turbulent attractor or to the laminar state. Minimal seed is the closest point on the edge to the laminar state and corresponds to the minimal energy norm to cause a change from laminar to turbulence. Figure adapted from Khapko et al. [121]

While the total energy of the flow is defined by

$$E = \frac{1}{2L_xL_z} \int_0^{L_z} \int_{-1}^{1} \int_0^{L_x} (u^2 + v^2 + w^2) dx dy dz \qquad (3.4)$$

and, thus, the rate of change in energy for the flow is equal to $dE/dt = I - D$. For exact coherent solutions, $D = I$. Input and dissipation are normalized such that the laminar value corresponds to $I = D = 1$. The P3 and P4 solutions are shown on the same Input-Dissipation plane in the following results. However, the two solutions

were computed using different box sizes and, thus, different dimension. Therefore, it should be noted that it is possible that the position of these solutions on the following figures may be different if they are computed in the same computational domain.

3.3.3.1 Random initial conditions

Figures 3.36 - 3.38 show the ensemble average of the random trajectories in the energy Input-Dissipation plane. The black star represents the mean state of the long-time trajectory at $Re = 1800$, or the average starting point for the decaying trajectories. The trajectories are quite interesting. As final Reynolds number is increased, the system appears to be attracted to the P4 lower-branch solution, as evidenced by the curve in the trajectory when the system nears the solution. It also appears to pass through, or very near to, the P3 lower-branch solution for $Re_f = 1000$. For the $Re_f = 600$ case, the trajectory decays much further away from the P4LB solution, and does not seem to be attracted to it. However, when the system gets close to the P3LB solution, there are large dissipation events, possibly indicating that the system is having some interaction with the P3LB solution. More in-depth analysis is required.

3.3.3.2 Exact coherent solutions

Figures 3.39 - 3.41 show the state-space representation of the decay of the P3 upper-branch solution. Figure 3.39 shows a similar trend to that observed in Figure 3.38, where the system is attracted to the P4 lower-branch solution as it decays, and then goes through, or very near to, the P3 lower-branch solution before reaching the laminar state. As final Reynolds number increases, the dynamics of the system become more complicated. For $Re_f = 800$ the system oscillates between the P4 lower-branch and P4 upper-branch before approaching the P3 lower-branch and then
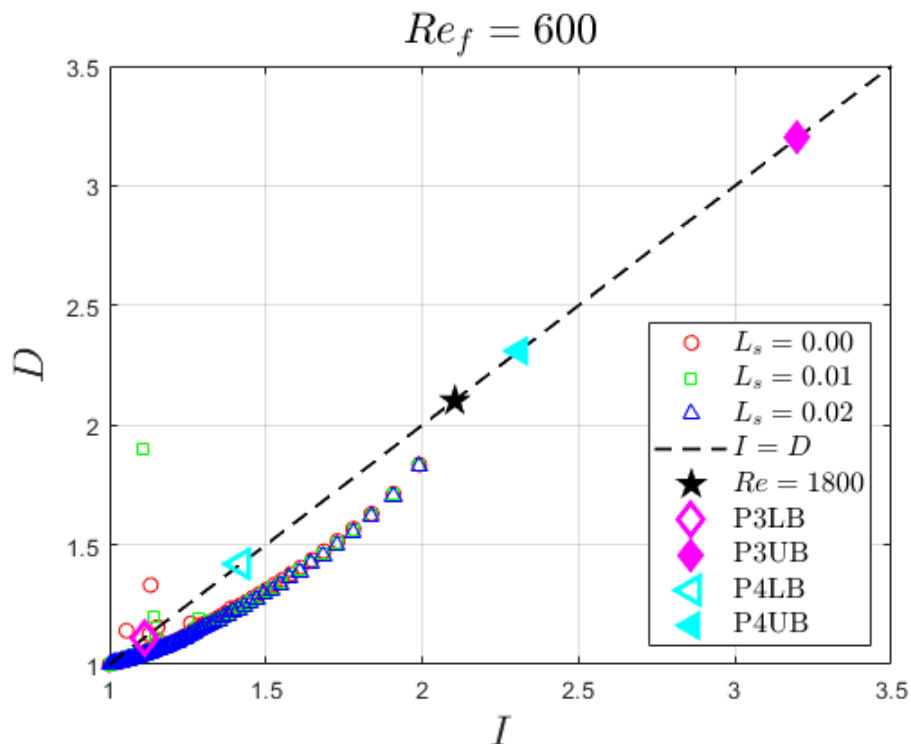
Figure 3.36: Input-Dissipation state space representation of decay of the ensemble averaged random initial conditions at initial Reynolds number $Re_i = 1800$ for quench Reynolds number $Re_f = 600$ and slip lengths $L_s = 0.00, 0.01, 0.02$. Magenta diamonds: P3 lower (open) and upper (closed) solutions. Cyan left triangles: P4 lower (open) and upper (closed) solutions. Black star: long-time mean value for $Re_i = 1800$.

decaying to the laminar state. In fact, this behavior is observed in Figure 3.33 where the wall shear rate oscillates in a periodic fashion for an extended time before finally decaying to the laminar value. This extended periodic behavior is only present for $L_s = 0.02$. For $Re_f = 1000$, there is similar behavior, as there is an interplay between the P4 lower-branch and P4 upper-branch as the system decays. There are much larger 'bursting' trajectories as the Reynolds number is close to the transitional Reynolds number. As the system decays, it orbits the P4 upper-branch solution before approaching and orbiting the P4 lower-branch solution. After some time, the system finally approaches the P3 lower-branch solution and decays to the laminar state. Slip does have a significant effect on the dynamics of the decay of the P3 upper-branch
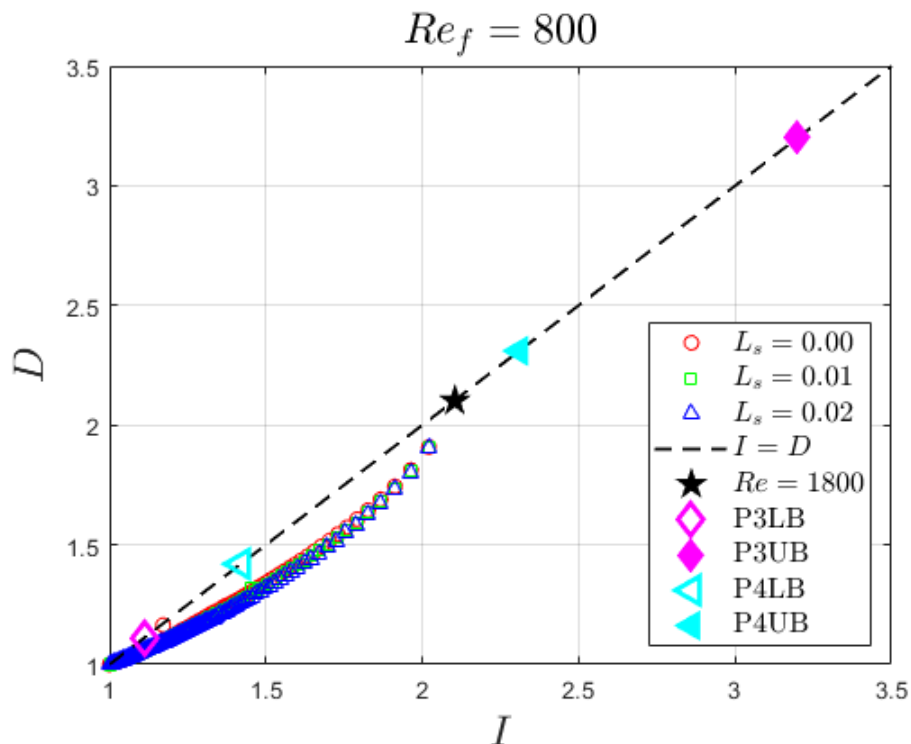
Figure 3.37: Input-Dissipation state space representation of decay of the ensemble averaged random initial conditions at initial Reynolds number $Re_i = 1800$ for quench Reynolds number $Re_f = 1000$ and slip lengths $L_s = 0.00, 0.01, 0.02$. Magenta diamonds: P3 lower (open) and upper (closed) solutions. Cyan left triangles: P4 lower (open) and upper (closed) solutions. Black star: long-time mean value for $Re_i = 1800$.

solution, even stabilizing the system, as evidenced by the emergence of an unstable periodic orbit.

Figures 3.42 - 3.44 show the state-space representation of the decay of the P4 upper-branch solution. The state-space dynamics associated with the P4 upper-branch solution are much simpler. For all three final Reynolds numbers, the system avoids any interaction with either the P4 lower-branch or the P3 lower-branch. It simply approaches the laminar state. For $Re_f = 800$, there is one large-dissipation event for $L_s = 0.00$ as the system nears the P4 lower-branch. However, this is not observed for the slip cases, and slip has negligible effect on the dynamics at any of the final Reynolds numbers studied.
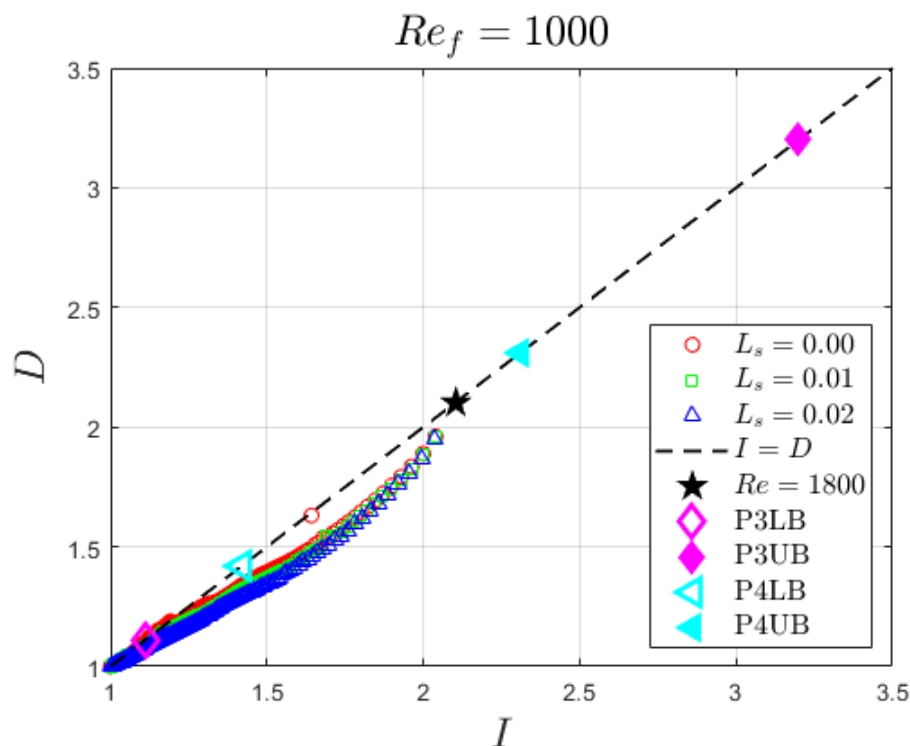
$$Re_f = 1000$$

Figure 3.38: Input-Dissipation state space representation of decay of the ensemble averaged random initial conditions at initial Reynolds number $Re_i = 1800$ for quench Reynolds number $Re_f = 1000$ and slip lengths $L_s = 0.00, 0.01, 0.02$. Magenta diamonds: P3 lower (open) and upper (closed) solutions. Cyan left triangles: P4 lower (open) and upper (closed) solutions. Black star: long-time mean value for $Re_i = 1800$.

3.4 Conclusions and future directions

The decay from turbulence to laminar was studied via the time-evolution of the magnitude of the disturbance velocity in the streamwise, wall-normal, and spanwise directions. Using a quench protocol, where the Reynolds number is suddenly decreased, a turbulent state was allowed to decay to the laminar state. For random turbulent initial conditions, the decay rates increased with decreasing final Reynolds number. As observed in previous plane Poiseuille and Couette-Poiseuille flows [76, 148], the energy in the spanwise direction was found to decay faster than the streamwise energy. This was attributed to differing decay characteristics of streamwise streaks and
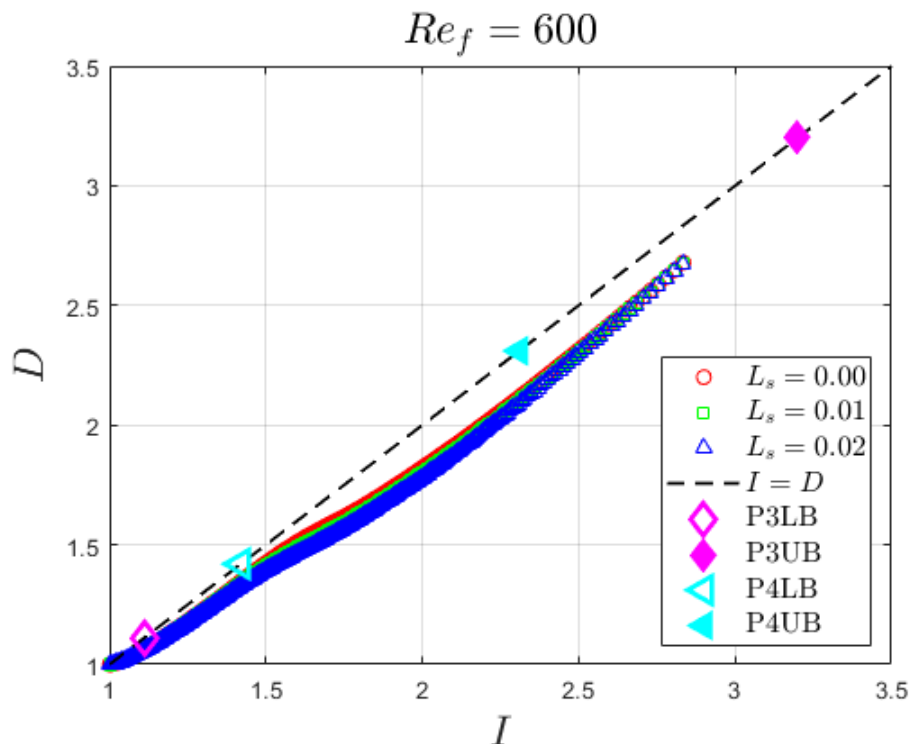
Figure 3.39: Input-Dissipation state space representation of decay of P3 upper-branch solution at initial Reynolds number $Re_i \approx 1800$ for quench Reynolds number $Re_f = 600$ and slip lengths $L_s = 0.00, 0.01, 0.02$. Magenta diamonds: P3 lower (open) and upper (closed) solutions. Cyan left triangles: P4 lower (open) and upper (closed) solutions.

spanwise rolls in the self-sustaining process [231]. Specifically, the waviness of the streaks is reduced initially which causes fast decay of the spanwise rolls followed by a slower decay of the straightened streaks [148]. The results here corroborate those found in previous studies.

The effect of non-zero slip at the wall on the decay of random turbulent initial conditions was also analyzed. The inclusion of slip at the boundaries causes the decay rate to change depending upon the final Reynolds number. For $Re_f = 1000$, the slip surfaces appear to increase the initial decay rate in all three directions. After this initial decay stage, the decay rates saturate and are similar among all slip lengths. For final Reynolds number below $Re_f = 1000$ studied here, the wall slip had no observable

Figure 3.40: Input-Dissipation state space representation of decay of P3 upper-branch solution at initial Reynolds number $Re_i \approx 1800$ for quench Reynolds number $Re_f = 800$ and slip lengths $L_s = 0.00, 0.01, 0.02$. Magenta diamonds: P3 lower (open) and upper (closed) solutions. Cyan left triangles: P4 lower (open) and upper (closed) solutions.

effect on the decay rates. That wall slip is ineffectual at these final Reynolds numbers may be related to the fact that these Reynolds numbers are close to and below the critical Reynolds number $Re_g \approx 700$ where turbulence cannot persist [209, 179]. Flow structures shown via disturbance velocity at a wall-normal plane of $y^+ = 12$ showed the same trends. The streamwise structures persisted for longer than either spanwise or wall-normal directions. One indication as to the mechanism behind the increased decay rate for the slip surfaces may be that, for the slip cases, the "waviness" in the streamwise streaks discussed by Liu et al. [148] appears to be reduced faster. According to the process they put forward, this straightening of the streamwise streaks would allow for an earlier decay of the spanwise rolls. A more detailed investigation

Figure 3.41: Input-Dissipation state space representation of decay of P3 upper-branch solution at initial Reynolds number $Re_i \approx 1800$ for quench Reynolds number $Re_f = 1000$ and slip lengths $L_s = 0.00, 0.01, 0.02$. Magenta diamonds: P3 lower (open) and upper (closed) solutions. Cyan left triangles: P4 lower (open) and upper (closed) solutions.

into the flow structures should be performed.

Additionally, the decay of exact coherent solutions was analyzed. Similar to observations in Section 2.4.3, the P3 and P4 upper-branch solutions were found to display distinct decay characteristics. Unlike the behavior observed in the decay of random initial conditions, the P3 solution exhibited a similar initial decay rate of the streamwise and spanwise velocity perturbation magnitude before entering a second stage where the spanwise decay rate was slower than the streamwise decay rate. This trend held for quench Reynolds number $Re_f = 800, 1000$ but not for $Re_f = 600$. It is interesting as $Re_f = 600$ is below the critical Reynolds number where turbulent spots were found to decay, $Re_g \approx 700$ [22, 179, 209, 49]. However, the decay of the spanwise

Figure 3.42: Input-Dissipation state space representation of decay of P4 upper-branch solution at initial Reynolds number $Re_i \approx 1800$ for quench Reynolds number $Re_f = 600$ and slip lengths $L_s = 0.00, 0.01, 0.02$. Magenta diamonds: P3 lower (open) and upper (closed) solutions. Cyan left triangles: P4 lower (open) and upper (closed) solutions.

disturbances was faster than the streamwise disturbances for the P4 solution at early time, $\mathcal{O}(10tU_c/h)$. Decay rate increased with decreasing Re_f. The addition of wall slip had negligible effect on the decay behavior for both the P3 and P4 solutions.

The decay of the turbulent trajectories and the P3 and P4 solutions was also analyzed using a dynamical systems approach. The dynamics of the high-dimensional system were projected onto the energy input-dissipation plane. Through this lens, the behavior observed in the evolution of these trajectories becomes more understandable. For the random initial conditions, the system is attracted to lower-branch solutions as it decays to the laminar state, even passing through the P3 lower-branch solution in some cases. This is significant, as the P3 lower-branch solution is an edge state,

Figure 3.43: Input-Dissipation state space representation of decay of P4 upper-branch solution at initial Reynolds number $Re_i \approx 1800$ for quench Reynolds number $Re_f = 800$ and slip lengths $L_s = 0.00, 0.01, 0.02$. Magenta diamonds: P3 lower (open) and upper (closed) solutions. Cyan left triangles: P4 lower (open) and upper (closed) solutions.

with only one unstable direction. There was also some interaction with the P4 lower-branch solution. As Reynolds number decreases (i.e., $Re_f < Re_g \approx 700$), the system has almost no interaction with any of the exact coherent solutions, and instead does directly to the laminar state, as it is the global attractor due to the linear instability of other solutions. This behavior is consistent with previous studies done in the plane-Couette and Taylor-Couette geometries [188]. Therefore, one possible explanation for the increase in decay rate with the decrease in final Reynolds number may be that the system has less significant interactions with other solutions, and instead directly approaches the laminar attractor.

For the decay of the P3 and P4 solutions, there were rich and distinct dynamics,

Figure 3.44: Input-Dissipation state space representation of decay of P4 upper-branch solution at initial Reynolds number $Re_i \approx 1800$ for quench Reynolds number $Re_f = 1000$ and slip lengths $L_s = 0.00, 0.01, 0.02$. Magenta diamonds: P3 lower (open) and upper (closed) solutions. Cyan left triangles: P4 lower (open) and upper (closed) solutions.

seemingly orchestrated by the other exact coherent solutions. For the P3 solution at $Re_f = 800$, periodic behavior emerged with the inclusion of wall slip, and the system passed through the P3 lower-branch solution before laminarizing. The P4 solution exhibited much simpler dynamics, mostly avoiding interaction with any of the other exact coherent solutions and directly approaching the laminar state. The dynamical systems perspective gives much insight into the dynamics of the turbulent-to-laminar transition.

While the decay characteristics of the flow in [148] were unaffected by various noise levels, spanwise rolls in the final state after transient decay were found to be susceptible to noise. This type of analysis could be performed in the future using a

more statistically significant amount of initial conditions, ranging in initial turbulence intensity, to analyze the effect of initial condition (i.e. noise) on the decay characteristics of the flow. From the 10 initial conditions studied here, initial turbulence intensity seems to have an effect on the initial behavior of a trajectory, but the decay rates after this transient period appear to be consistent. Additionally, fields from the laminar state could be subjected to perturbations to assess the susceptibility of the final state to noise, and whether the system returns to a transient turbulent state.

Future work should also include further analysis of the mechanisms responsible for the difference in decay rate for varying final Reynolds number, possibly by analyzing the time-evolution of the streamwise and spanwise flow structures during decay. This work contributes to a framework for understanding the transition to and from turbulence, as well as the self-sustaining process of wall-bounded turbulence flow which can be used to inform more efficient future control techniques. Specifically, the use of exact coherent solutions to the Navier-Stokes equations offers a more deterministic view of control methods on the self-sustaining process and transition to turbulent.

Chapter 4

COMPOSITE DRAG REDUCTION OF SLIP SURFACES AND POLYMER ADDITIVES

1

4.1 Introduction

Turbulence is an emergent phenomena found throughout nature. It plays a vital role in the aquatic locomotion of organisms, scalar mixing, the transport of fluid solutions, the resistance experienced by naval watercraft, and the flow of biological fluids in the human body. It is of practical concern, then, to understand and control frictional losses that arise from turbulence to provide energy- and cost-savings. The majority of energy usage in transportation is due to the skin friction drag, and it has been estimated that with a modest reduction of 30% skin friction in ocean-faring vessels, more that $70 billion can be saved annually [122, 162]. Therefore, it is vital to societal sustainability to develop techniques which help mitigate the skin friction drag in turbulent flows.

---

[1]This work is in preparation to be submitted to a scientific journal.

4.1.1 Slip surfaces

Slip surfaces have garnered much attention in the past few decades, owing to their drag reduction capabilities and the countless inspirations for their design found in nature [48, 75, 147]. There is a demonstrated ability of slip surfaces in reducing frictional resistance for both laminar and turbulent flows. Many studies have achieved significant drag reduction via slip with hydrophobic surfaces at the walls [152, 242, 163, 176, 224, 44, 21, 205].

Superhydrophobic surfaces, which are a combination of surface chemistry and surface roughness at micro- and/or nano-scales, have been introduced for drag reduction [195]. These surfaces act to lower the free energy of an air-water interface, producing a very high contact angle at the surface. There have been, of course, many studies on the effects of superhydrophobic surfaces on skin-friction reduction in laminar and turbulent flows [181, 134, 111, 133, 146, 78, 205, 59]. Recently, turbulent drag reductions have been observed of up to 50% on micropattern-arrayed surfaces and up to 30% on randomly textured surfaces, akin to those found in nature [181, 75, 193]. Thorough reviews of the effect of slip and superhydrophobic drag reduction on laminar and turbulent flows are given by Rothstein [195], Abdulbari et al. [1], and Lee et al. [133].

The idea of slip was first introduced by Navier, proposing the existence of a slip velocity at the interface, which is characterized by a virtual distance into the wall, called the slip length [171]. It was later quantified by Maxwell in 1879 in the flow of rarefied gas [159]. The slip length relates the velocity of the fluid at the fluid-solid interface to the shear rate at the interface by

$$u_s = b\dot{\gamma}_w, \tag{4.1}$$

Here, b is the average, or effective, slip length which characterizes the degree of slip at the interface and $\dot{\gamma}_w = \frac{\partial u}{\partial y}|_w$ is the average wall shear rate.

4.1.2 Polymer additives

Dating back to the 1940s[222, 223], it has been understood that the addition of a small amount of long-chain polymer to a liquid results in drastic changes in the behavior of its flow. Of great interest in an engineering and practical sense is the reduction in skin friction at the wall when polymer additives are added to a turbulent flow. By decreasing the strength of streamwise vortices, streaks, and three-dimensionality, the stretching and coiling of the polymer molecules interrupts the self-sustaining process (SSP)[231]. The interruption to the SSP results in drag reductions above 50% by adding a small amount (as little as 10 ppm) of polymer to a fluid [79, 256, 257, 80, 254]. This is especially alluring because frictional resistance in turbulent flows can account for a majority of the energy loss of a system. For instance, a typical ship uses 60% of the propulsive power just to overcome the drag induced by the boundary layer [155]. Others have estimated that if a modest reduction of 30% in skin friction can be achieved for ocean-faring vessels, more than \$70 billion can be saved annually [122].

4.1.3 Combined flow control methods

While most studies focus on a single flow control method, energy demands and the ever-increasing scale of engineered systems is beginning to necessitate the possible use of a combination of various distinct flow control methods. Recently, Yao et al. [261] studied a composite drag control (CDC) scheme which combined opposition control (OC) and spanwise opposed wall-jet forcing (SOJF) in a turbulent channel. The maximum drag reduction of the CDC was 33%, compared with the individual drag reduction levels of 19% and 23% for the SOJF and OC, respectively. This composite

scheme resulted in 32% net power savings. Each individual method targets different scales of the turbulent flow which results in the effective synergistic drag reduction.

While Yao et al. [261], studied active flow control techniques, there is also evidence to support the efficacy of composite drag control using more passive techniques. In a tandem of papers published recently, Rajappan and McKinley used slip-inducing surfaces along with dilute polymer solutions to study drag reduction in a fully turbulent Taylor-Couette flow [192, 191]. They found that the two distinct drag reduction techniques act with synergy, yielding a net drag reduction up to 50% greater than that obtained by either individual method. Again, the synergy comes from the different mechanisms behind the observed drag reduction of each method. While they offer an additive friction law to predict the combined drag reduction, the law overpredicts the total amount of drag reduction compared with the empirical observations. The authors posit that the law provides the maximum theoretical limit of drag reduction, and attribute the difference between the two values to 'non-linear', counteractive interactions between the two drag reduction mechanisms. The experimental study by Rajappan and McKinley and the current numerical work were started in parallel, without the knowledge of either group.

4.1.4 Modeling apparent slip in the turbulent flow of polymer solutions

In recent years, the validity of the no-slip condition has been called into question for the flow of complex fluids [42, 16, 142, 85]. These fluids can create a depletion layer, devoid of polymers, at the wall, resulting in a mismatch in viscosity which facilitates an apparent slip. While the concentration of these complex fluids exhibiting slip is relatively large (typically in the semidilute regime) compared with the concentrations used in turbulent drag reduction, little attention has been paid to the possible effect of slip in the modeling of the flow of dilute polymer solutions.

4.1.5   Goal and motivation of this study

The goal of the current study is to analyze the efficacy of using combined drag re-duction methods. The main advantage of using multiple drag reduction methods is the possible synergistic effect between methods that act to change flow dynamics in distinct manners. The motivation behind this work lies in this cost savings associated with moderate mitigation of skin friction drag. A possible synergistic effect between two distinct flow control methods is alluring, as it could help in the difficult task of scaling drag reduction methods for industrial-scale applications. From analyzing the present data of controlled turbulent flows, it has become apparent that, while the global effect is a reduction in the mean skin friction, there are significant changes to the dynamics of the system compared to the uncontrolled case. A secondary goal of this study, then, is to characterize secondary (possibly adverse) effects of using drag reduction methods in turbulent wall-bounded flows.

This chapter is organized as follows: section 4.2 outlines the numerical procedure used to model combined slip and polymer drag reduction methods, sections 4.3.1.1 and 4.3.1.2 provide results of drag reduction via wall slip and polymer additives, respectively, and section 4.3.2 provides results from the combined drag reduction of wall slip and polymer additives. Finally, section 4.4 gives a brief conclusion and future directions for using combined flow control methods.

4.2   Problem formulation

We consider an incompressible Newtonian fluid in the plane Poiseuille (channel) ge-ometry, driven by a constant volumetric flux Q. The x, y, and z coordinates are aligned with the streamwise, wall-normal, and spanwise directions, respectively. Pe-riodic boundary conditions are imposed in the x and z directions with fundamental

periods L_x and L_z, and streamwise Navier slip conditions are imposed at the walls $y = \pm h$, where $h = L_y/2$ is the half-channel height. The laminar centerline velocity for a given volumetric flux is given as $U_c = (3/4)Q/h$. Using the half-height h of the channel and the laminar centerline velocity U_c as the characteristic length and velocity scales, respectively, the governing equations for mass and momentum conservation are:

$$\nabla \cdot \boldsymbol{u} = 0; \quad \frac{\partial \boldsymbol{u}}{\partial t} + \boldsymbol{u} \cdot \nabla \boldsymbol{u} = -\nabla p + \frac{\beta}{Re_c}\nabla^2 \boldsymbol{u} + \frac{2(1-\beta)}{ReWi}(\nabla \cdot \tau_p) \qquad (4.2)$$

Here, we define the Reynolds number for the given laminar centerline velocity as $Re_c = \rho U_c h / (\eta_s + \eta_p)$, where ρ is the fluid density and η_s and η_p are the dynamic viscosities for the solvent and polymer, respectively. Characteristic inner scales are the friction velocity $u_\tau = (\bar{\tau}_w/\rho)^{1/2}$ and the near-wall length scale or wall unit $\delta_\nu = (\eta_s + \eta_p)/\rho u_\tau$, where $\bar{\tau}_w$ is the time- and area-averaged wall shear stress. As usual, quantities nondimensionalized by these inner scales are denoted with a superscript "+". The friction Reynolds number is then defined as $Re_\tau = \rho u_\tau h/(\eta_s + \eta_p) = h/\delta_\nu$. Streamwise Navier slip conditions are prescribed as equation (4.1) at both top and bottom walls by an effective homogeneous slip length, $L_s = b/h$. The polymer stress tensor $\boldsymbol{\tau}_p$ is governed by a Finitely Extensible Nonlinear Elastic (FENE-P) constitutive model [20, 81]:

$$\frac{\boldsymbol{\alpha}}{1 - \frac{tr(\boldsymbol{\alpha})}{b}} + \frac{Wi}{2}\left(\frac{\partial \boldsymbol{\alpha}}{\partial t} + \boldsymbol{u} \cdot \nabla \boldsymbol{\alpha} - \boldsymbol{\alpha} \cdot \nabla \boldsymbol{u} - (\boldsymbol{\alpha} \cdot \nabla \boldsymbol{u})^T\right) = \left(\frac{b}{b+2}\right)\delta \qquad (4.3)$$

$$\boldsymbol{\tau}_p = \frac{b+5}{b}\left[\frac{\boldsymbol{\alpha}}{1 - \frac{tr(\boldsymbol{\alpha}}{b}} - \left(\frac{b}{b+2}\right)\delta\right] \qquad (4.4)$$

The FENE-P model approximates the polymer molecules as a bead-spring dumbell, where the variable $\boldsymbol{\alpha}$ is the nondimensional polymer conformation tensor $\boldsymbol{\alpha} \equiv$

$\langle \boldsymbol{qq} \rangle$, and $\boldsymbol{q}$ is the nondimensional end-to-end vector of the dumbbells. The maximum extensibility parameter b limits the maximum amount that the polymers are allowed to stretch (i.e., $max(tr(\boldsymbol{\alpha})) < b$). The Weissenberg number $Wi = \lambda \dot{\gamma}$ is the degree of polymer stretching in the flow field. The parameter λ is the relaxation time of the polymer species and $\dot{\gamma}$ is the characteristic shear rate of the system. In wall-bounded turbulent flows, the characteristic shear rate is the shear rate at the wall $\dot{\gamma}_w$, so the Weissenberg number becomes $Wi = \lambda \dot{\gamma}_w = \lambda \partial u / \partial y|_w$. Because the current study employs a constant mass flux driving condition and various slip lengths, there is a change in wall shear rate as a function of slip length. Therefore, Weissenberg numbers differ slightly for each slip length.

The viscosity ratio $\beta = \eta_s / (\eta_s + \eta_p)$ determines the fraction of total shear viscosity that is contributed by the solvent. In most drag reduction applications, a small amount of polymers is necessary to observe significant effects, such that $1 - \beta \ll 1$ is proportional to the polymer concentration and the total viscosity is negligibly affected by the polymers.

Using the FENE-P model, the extensibility number, $Ex = 2b(1 - \beta)/3\beta$, is the maximum value of the ratio between extensional stress due to the polymer and that of the solvent. For the current study, $\beta = 0.97$ and $b = 5000$, thus, $Ex = 103 \gg 1$, implying that the polymers exert a significant amount of stress on the fluid. Simulations for the current study are performed at $Re = 4200$ such that $Re_\tau = 180$ for the Newtonian, no-slip case. The friction Reynolds number will vary depending upon the change in wall shear rate with the inclusion of the flow control methods. To improve numerical stability, an artificial diffusivity term $1/(ScRe)\nabla^2 \boldsymbol{\alpha}$ with $Sc = 0.5$ is added to the FENE-P equation. This value has been shown to be sufficient in previous studies [80]. The numerical algorithm used here was developed by Xi [253] and detailed, therein. The code is developed using spectral Navier-Stokes solver *ChannelFlow*,
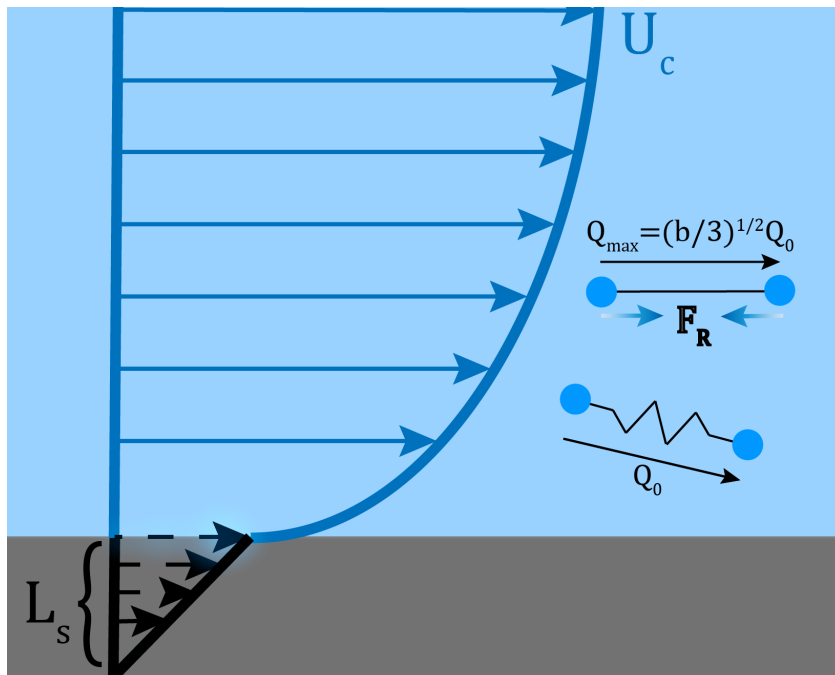
Figure 4.1: A cartoon encapsulating a high-level overview of the current work. The schematic shows the nonzero slip velocity at the wall facilitated by the surface, and the long-chain polymers are shown as two beads attached at either end of a nonlinear spring.

written and maintained by Gibson [69].

Figure 4.1 shows a high-level overview of the current study. The nonzero velocity at the wall is facilitated by the slip surface, where the degree of slip is quantified by the slip length L_s. This slip velocity at the wall is linearly proportional to the shear rate at the wall, and the proportionality constant is the slip length L_s. The polymers are modeled by a bead-spring system with nonlinear elastic behavior. Equilibrium length of the polymer molecules is given by the end-to-end vector of an unstrained molecule, Q_0. Given the maximum extensibility b of the polymer species, the maximum stretching of a polymer is given by $Q_{max} = (b/3)^{1/2} Q_0$. When the polymer molecules are stretched, they exert a retraction force F_R on the fluid, which is proportional to the degree of stretching experienced by the polymer.

A minimal flow unit (MFU)[103, 106] approach was taken in choosing the domain size. The domain size in outer units ($L_x = 2\pi \times L_z = \pi$) was chosen such that turbulence could persist even with the combination of largest slip length and largest Weissenberg number. Box size was based off this particular simulation, as this combination of the two parameters is most likely to lead to laminarization if the box size is too small. This is known from Chapter 1, which showed a higher propensity of the flow to laminarize with increasing slip length due to a weakening of the streamwise vortices. The same trend is observed in viscoelastic flows as Weissenberg number is increased [239, 80], which again has to do with the weakening of streamwise vortices, streaks, and three-dimensionality. Since the box size in inner units scales with τ_w

4.3 Results

We report numerical results for the drag reduction observed in turbulent flow of dilute polymer solutions with and without slip present at the boundaries. The results have been organized into the three sections: Section 4.3.1.1 details the drag reduction observed from slip, Section 4.3.1.2 details the drag reduction resulting from the inclusion of polymer additives, and Section 4.3.2 details the drag reduction observed from the composite drag reduction method, with both slip and polymer additives. For individual and composite drag reduction methods, the drag reduction is computed by

$$\mathcal{DR}(\%) = 100 \times \left(1 - \frac{Re_t au}{Re_{tau,0}} \right) \tag{4.5}$$

where $Re_{\tau,0}$ corresponds to the friction Reynolds number of the Newtonian, no-slip case (i.e., no slip surface and no polymers). In other words, $Re_{\tau,0}$ is the global reference value for all slip, polymer, and composite drag reduction methods.

4.3.1 Drag reduction of individual methods

Before investigating the effect of the composite drag reduction, it is worth detailing the effect of each individual drag reduction technique. We first detail the drag reduction using slip surfaces, followed by the drag reduction using polymer additives.

4.3.1.1 Slip surfaces

Figure 4.2 shows the friction Reynolds number and drag reduction percentage for the three slip lengths studied. There is a linear decrease in the friction Reynolds number, which results in the linear increase in drag reduction. The maximum drag reduction with the inclusion of slip is $\approx 10\%$. This drag reduction percentage is in agreement with previous studies whose surfaces are similar to those modeled here [74]. While the complete understanding of the mechanism behind slip drag reduction still eludes us, there is evidence to suggest that the surfaces weaken and lift the streamwise vortices, responsible for shear-producing sweeps and ejections, away from the wall [270].

The maximum slip length studied here is within the realm of physical realization. Min and Kim [163] first studied the effect of slip surfaces on drag reduction numerically and used similar slip lengths. To further verify that the slip length can be realistically obtained by practical slip surfaces and is not so large as to introduce nonlinear interactions between the surfaces roughness and the flow, the length scale L^+ of the micro roughness can be calculated using Equation (2.4) of Picella et al. [184]:

$$L^+ = \frac{L_s^+ \sqrt{\phi_s}}{0.325 - 0.44\sqrt{\phi_s}} + 0.328 \left(L_s^+ \sqrt{\phi_s} \right)^3 \tag{4.6}$$

where $L^+ = Re_\tau L$ and $L_s^+ = Re_\tau L_s$. This enables a direct comparison of the current surfaces with surfaces found in the literature. Using the largest slip length studied ($L_s = 0.02$) and the solid fraction $\phi_s = 0.25$ used in Min and Kim [164], the largest
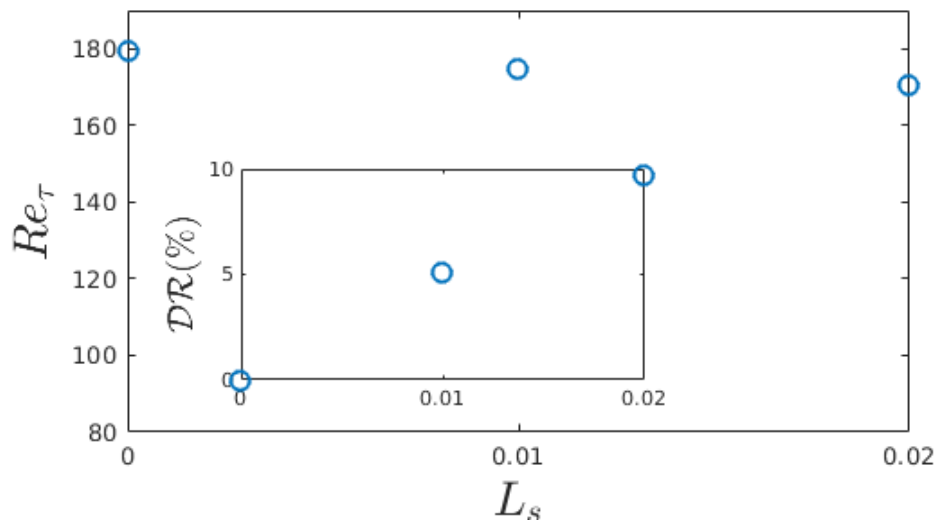
Figure 4.2: Friction Reynolds number and drag reduction resulting from the inclusion of wall slip at the boundaries.

texture size of the current study is $L^+ \approx 19$, which ensures that the homogeneous slip surface employed in the present study would provide virtually the same outcomes resulting from employing a heterogeneous microtextured slip surface [262, 204, 206, 184]. This is also small enough (*i.e.*, $L^+ < 25$) that there would be no nonlinear interactions between the flow and the surface roughness elements [59]. Because $L_s^+ = Re_\tau L_s$, this length scale only decreases in magnitude with a reduction in skin friction.

4.3.1.2 Polymer additives

Friction Reynolds number and drag reduction for the case of only polymer additives are shown in Figure 4.3. We see that the friction Reynolds number decreases, seemingly approaching an asymptote. The inverse trend is observed in the drag reduction, where a value of 33% is reached for $Wi \approx 76$. The asymptote described here likely corresponds to the Maximum Drag Reduction asymptote (MDR) [226], after which, the addition of more polymers or changes in Wi have no additional effect on the flow. Simulations with larger Wi would need to be performed for this to be concluded defi-
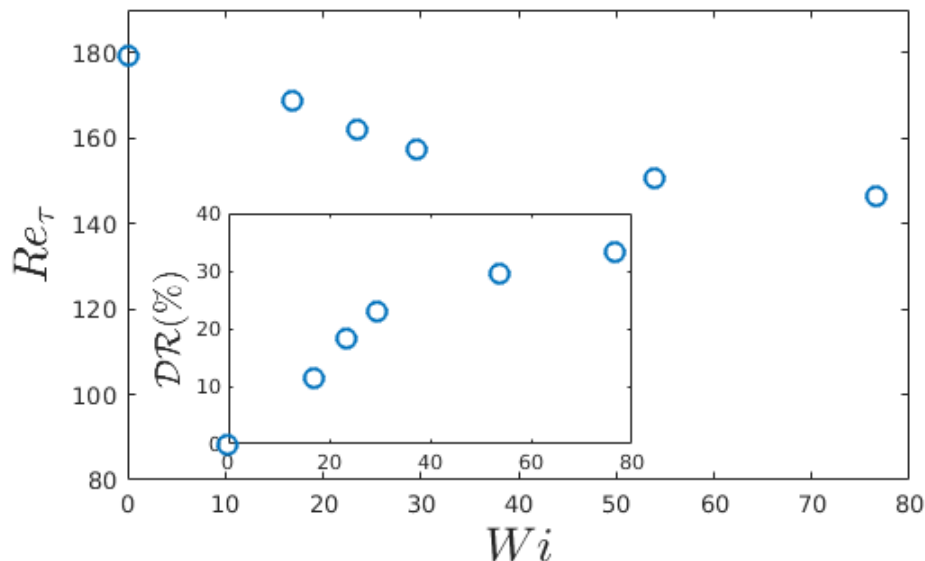
Figure 4.3: Drag reduction resulting from the addition of long-chain polymers.

nitely. The mechanism responsible for the drag reduction observed in dilute polymer solutions is a weakening of near-wall coherent structures by the stretching and coiling of the polymers. The polymers are stretched in the low-speed streaks and relax as they are pulled into the streamwise vortices, which acts to weaken the vortices and suppress turbulence production [80].

The initial behavior observed in the drag reduction is also consistent with previous studies where there is some critical Weissenberg number ($Wi \approx 10$) where the onset of drag reduction occurs [256, 257, 80, 239, 241]. While it does appear that this is the case in the current study, it cannot be confirmed as numerical stability issues prevented the simulation of smaller Wi flows.

4.3.2 Combined drag reduction in turbulent flow of dilute polymer solutions over slip surfaces

We now turn our attention to the drag reduction using the composite approach, incorporating the individual methods of slip surfaces and polymer additives. This
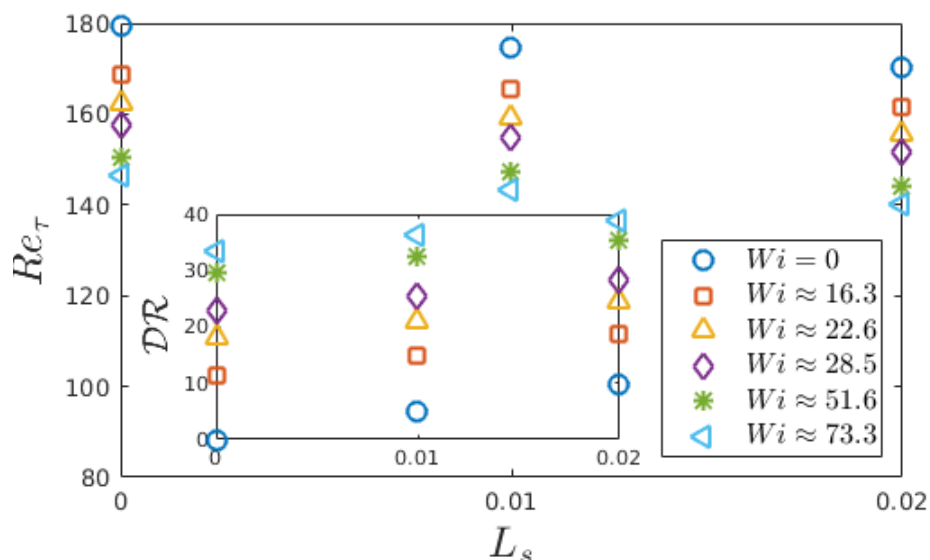
Figure 4.4: Drag reduction resulting from slip and the addition of long-chain polymers.

section first presents the drag reduction observed with the composite drag reduction (CDR) method. Then, average flow variables are investigated to attempt to elucidate the possible mechanisms responsible for any change in behavior.

4.3.2.1 Drag reduction

Shown in Figures 4.4 and 4.5 are the friction Reynolds number and drag reduction as a function of slip length and Weissenberg number, respectively. For Figure 4.4, we again observe a linear decrease in friction Reynolds number which corresponds to a linear increase in drag reduction. The rate at which the drag reduction increases for a given Wi appears to remain relatively constant for the range of Wi studied here, indicating that the two methods work cooperatively via distinct mechanisms.

Figure 4.5 shows the asymptotic reduction in friction Reynolds number, like that observed in Figure 4.3. Again, the curse appear to be shifted down by a constant amount for increasing slip length. These results show a cooperative drag reduction
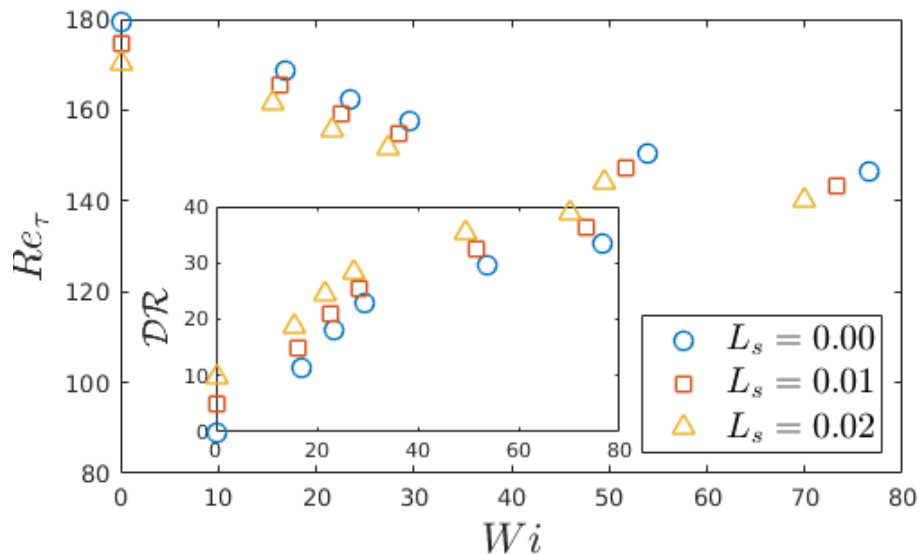
Figure 4.5: Drag reduction resulting from slip and the addition of long-chain polymers.

when these two independent methods are combined, which appears to be somewhat additive. For all slip lengths, it still appears possible that there is constant drag reduction before some critical Weissenberg number. One could deduce, then, that this phenomenon is attributed to the flexibility of the polymers alone. Where that critical Weissenberg number occurs is yet unknown. It may be that increases in Reynolds number reduce the minimal Weissenberg number where there is an onset of drag reduction, but that remains to be seen. The differences in Wi observed in Figure 4.5 are due to the differences in wall shear rate that were mentioned in 4.2. While there are apparent differences, the values are still close to one another.

4.3.2.2 Mean velocity profiles

One common variable that is considered when investigating drag reduction methods is the mean velocity profile [226, 79, 80]. In Figures 4.6 and 4.7 we show the mean velocity profiles for various combinations of slip length and Weissenberg number.

From Figure 4.6(a), we see the effect that Weissenberg number plays on the mean flow for the three slip lengths studied. As typically observed in a polymer drag-reduced flow, there is a characteristic shifting upward of the velocity profile in the low-law region [226]. Otherwise, there is minimal effect on the mean velocity profile in the viscous sublayer and buffer layer. As slip length is increase, this same trend is observed. However, there is a shifting upward of the profile in the viscous sublayer and buffer layer, now, that was not present in the no-slip case. This is to be expected as the effect of a slip surface is to induce non-zero velocity at the wall.

Figure 4.7(a), the effect of slip surfaces on mean velocity profile is illustrated. The degree to which the profile is shifted upward near the wall increases with slip length. In the bulk of the slow, the profile is shifted upward slightly, as well. In Figure 4.7(b) & (c), this trend continues. However, the profile in the log-law region has been significant shifted upward due to the action of the polymers. It does not appear that the slip surfaces have a significant effect in the bulk of the flow, and mainly act at the wall.

4.3.2.3 Reynolds shear stress

Reynolds shear stress $\left(RSS = -\overline{u'v'}\right)$ is another important flow variable to investigate. This is a measure of turbulence intensity in the flow and typically has a peak value around $y^+ \approx 12$ [187]. Figures 4.8 and 4.9 show the RSS for various combinations of slip length and Weissenberg number.

Figure 4.8(a) illustrates the well-known effect that polymers have on the RSS. For increasing Weissenberg number, the peak value is reduced, owing to the polymers weakening of streamwise vortices. The peak is also shifted away from the wall. Figure 4.8(b) & (c) show the effect of slip surfaces in combination with polymers. The trend remains the same as the no-slip case, with negligible effect of the slip surfaces. This
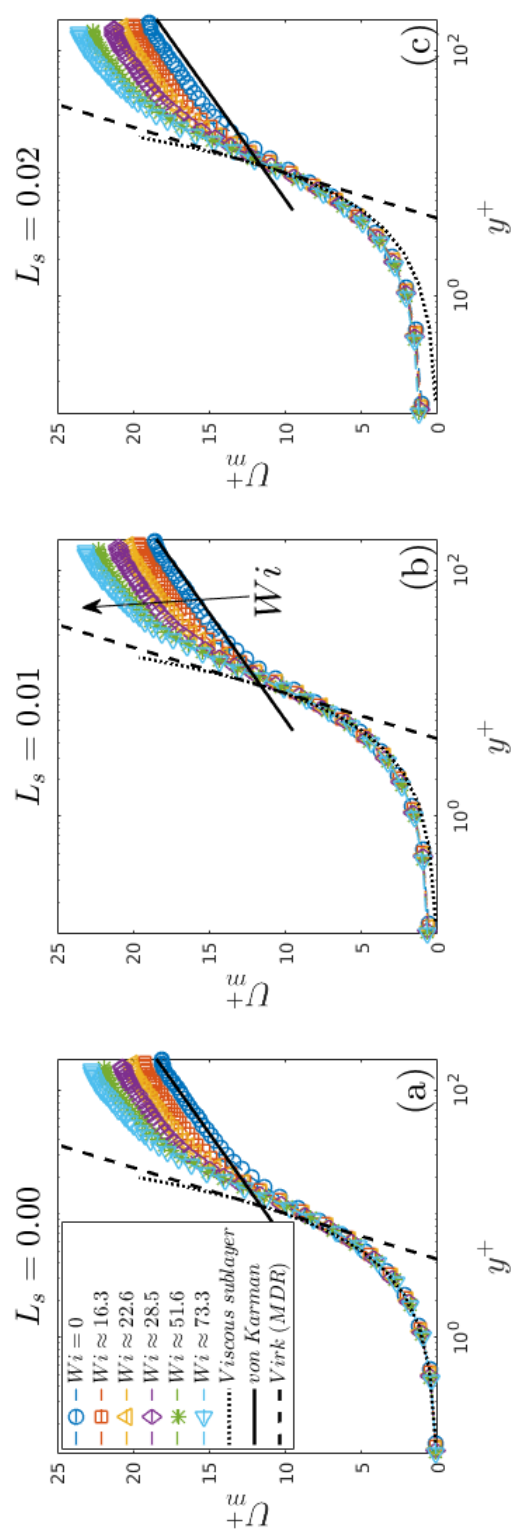
Figure 4.6: Mean velocity profiles for various Weissenberg numbers as a function of slip length.
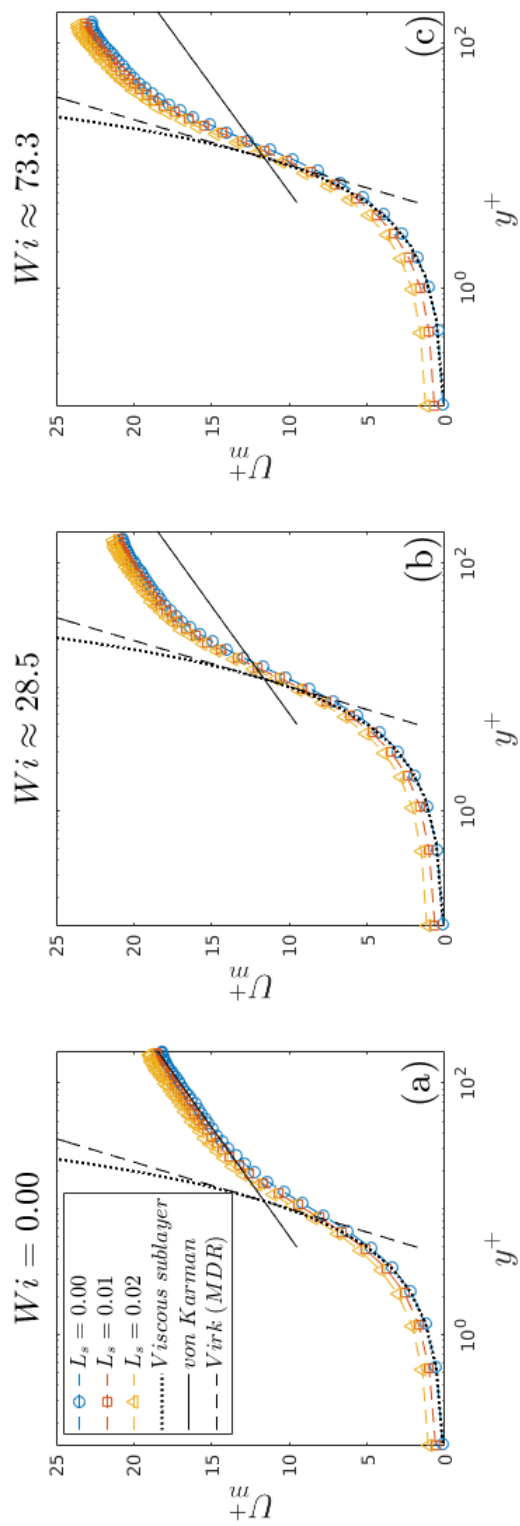
Figure 4.7: Mean velocity profiles for various slip lengths as a function of Weissenberg number.

is further illustrated in Figure 4.9 which shows the effect of slip surfaces for a given Weissenberg number. We see that there is negligible change in the RSS profile with the inclusion of the slip surfaces, indicating that the polymers work, individually, to decrease the RSS.

4.3.2.4   Energy analysis

The time-averaged turbulent kinetic energy (TKE), or the kinetic energy produced by the turbulent velocity fluctuations, is shown as a function of Weissenberg number for the various slip length in Figure 4.10. TKE is defined as

$$TKE = \frac{1}{2L_x L_z} \int_0^{L_x} \int_{-1}^{1} \int_0^{L_z} u^2 + v^2 + w^2 \, dz \, dy \, dx \qquad (4.7)$$

where u, v, w are the velocity fluctuations in the streamwise, wall-normal, and spanwise directions.

For the no-slip case, the TKE increases slightly through $Wi \approx 15$ before the rate increases and TKE reaches a peak value at $Wi \approx 30$. After this peak value, the TKE decreases monotonically with Wi. This same trend holds for the two slip cases, but the initial rate of increase seems to be lower. This is an interesting trend, as the peak value in TKE corresponds to the point in the drag reduction curves where the value begins to level out and approach the asymptote as seen in Figure 4.5. If this is the case, then it appears that the addition of slip causes this peak to occur sooner, and possibly causing the system to reach MDR at a lower Weissenberg number. There is no doubt, however, that the addition of slip surfaces causes a decrease in the amount of TKE for all Weissenberg numbers compared with the no-slip case.

Figure 4.11 shows the average rate at which the kinetic energy is converted to
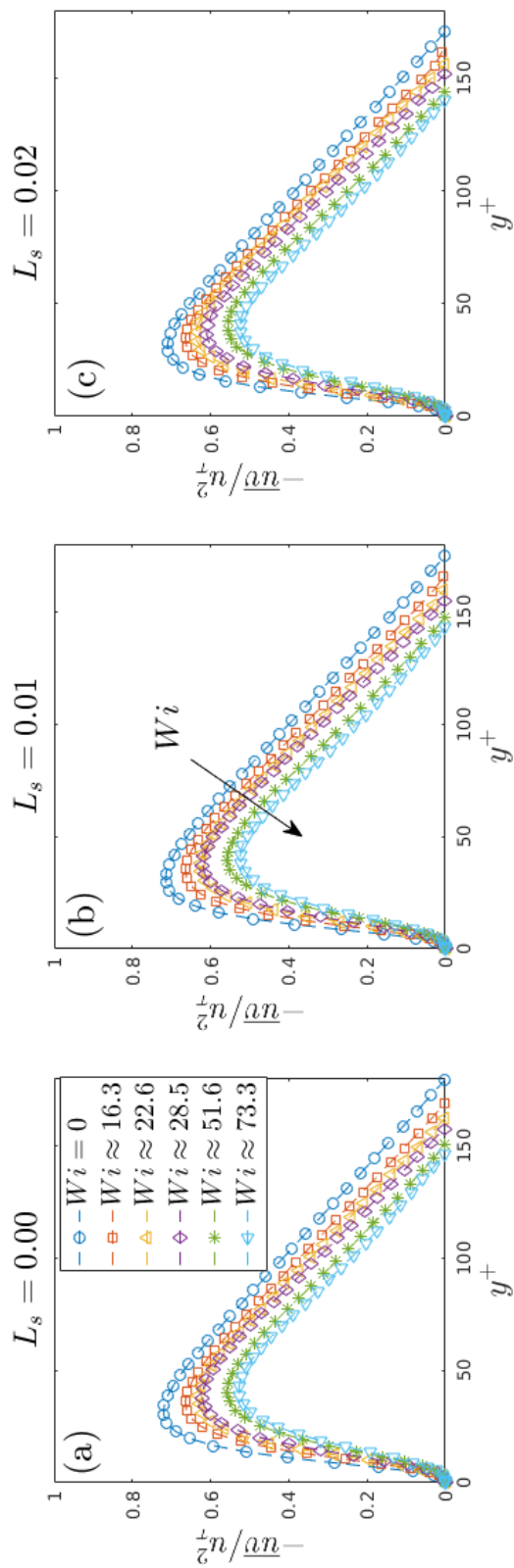
Figure 4.8: Reynolds shear stress profiles for various Weissenberg numbers as a function of slip length.

129
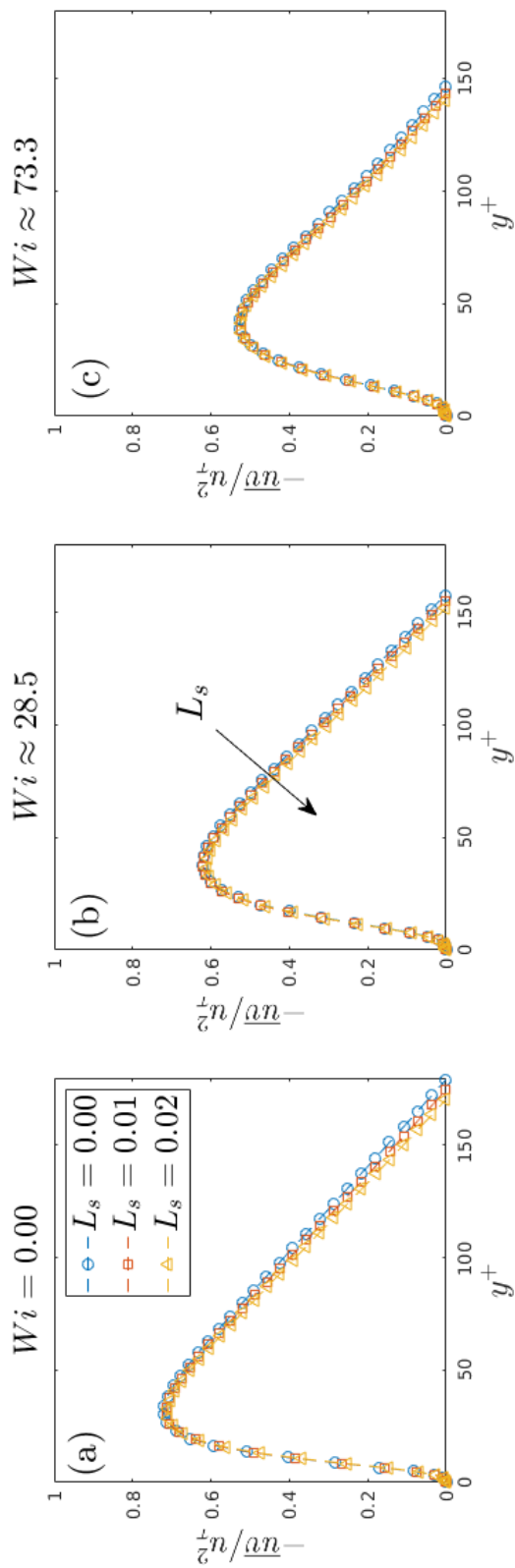
Figure 4.9: Mean velocity profiles for various slip lengths as a function of Weissenberg number.
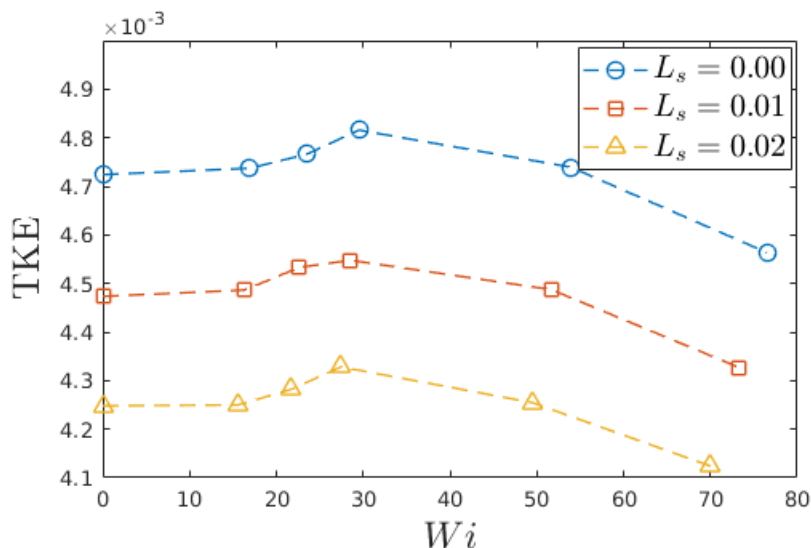
Figure 4.10: Turbulent kinetic energy as a function of Weissenberg number for various slip lengths

elastic energy. This is defined as

$$E = \frac{-1}{L_x L_z} \int_0^{L_x} \int_{-1}^{1} \int_0^{L_z} (\nabla \cdot \boldsymbol{\tau}_p) \, dz \, dy \, dx \qquad (4.8)$$

The kinetic energy converted to elastic energy for the no-slip case follows a quadratic trend with increasing Weissenberg number. The rate of increase of conversion is large at low Weissenberg number, where the polymers are more rigid and unable to deform to siphon energy from the flow. After $Wi \approx 30$, the value begins to level out, which is where we see the drag reduction begin to approach the asymptote. This is also the same Weissenberg number where the TKE reaches its peak value. Slip surfaces cause this leveling out to occur at lower Weissenberg number, as well as a reduction in the asymptotic value. Therefore, with the inclusion of slip surfaces, the rate at which kinetic energy is converted to elastic energy is lower than that of the no-slip case. There is undoubtedly a connection between the trends observed in the drag reduction, TKE, and elastic energy conversion rate. Further analysis into
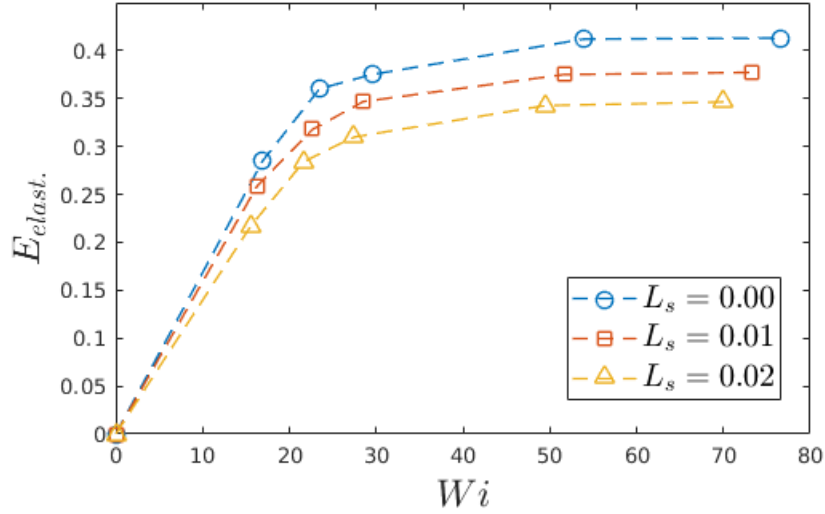
Figure 4.11: Elastic energy of the polymers as a function of Weissenberg number for various slip lengths.

the polymer dynamics is necessary to truly understand the relationship between the observed trends.

4.3.2.5 State-space visualization

The dynamical systems approach to turbulence often has much insight into the behavior of the system. Figure 4.12 shows the mean state of the system projected onto the energy Input-Dissipation plane to help visualize differences in behavior with the composite control method. Energy input rate is defined as

$$I = \frac{1}{2L_z} \int_0^{L_z} \int_{-1}^1 (pu|_{x=0} - pu|_{x=L_x}) dy dz \qquad (4.9)$$

and the energy dissipation rate is given as

$$D = \frac{1}{2L_x L_z} \int_0^{L_z} \int_{-1}^1 \int_0^{L_x} (|\nabla u|^2 + |\nabla v|^2 + |\nabla w|^2) dx dy dz. \qquad (4.10)$$

While the total energy of the flow is defined by

$$E = \frac{1}{2L_x L_z} \int_0^{L_z} \int_{-1}^{1} \int_0^{L_x} (u^2 + v^2 + w^2) dx dy dz \qquad (4.11)$$

and, thus, the rate of change in energy for the flow is equal to $dE/dt = I - D$. For exact coherent solutions, $D = I$. Input and dissipation are normalized such that the laminar value corresponds to $I = D = 1$.

The plot is quite dense, so it is best to go through each detail. The mean state of each Weissenberg number is depicted as a marker shape. The arrow points in the direction of increasing slip length for each marker shape. The magenta and cyan triangles are the P4 upper- and lower-branch exact coherent solutions, which represent high and low drag states in the system, respectively [182]. The contour shows the probability density function for a long-time trajectory of a no-slip, Newtonian simulation. The point (1,1) corresponds to the laminar state.

From this figure, we see that both the polymer additive and the slip surfaces have the effect of forcing the mean state of the flow toward the laminar state at (1,1). Slip surfaces seem to have a more significant effect at lower Weissenberg number, evidenced by the larger distance between the mean states for the $Wi = 0$ case. So, the effect of slip on changing the mean state of the flow is lessened relative to the effect of the polymers at larger Weissenberg number.

The distance between the mean state of the system and the laminar state at (1,1) can be quantified by the norm of the distance between the two points. Here, we define S to be the mean state of the system given by the input-dissipation coordinates, S_0 to be the state of the system for the Newtonian, no-slip case, and S_{lam} to be the laminar
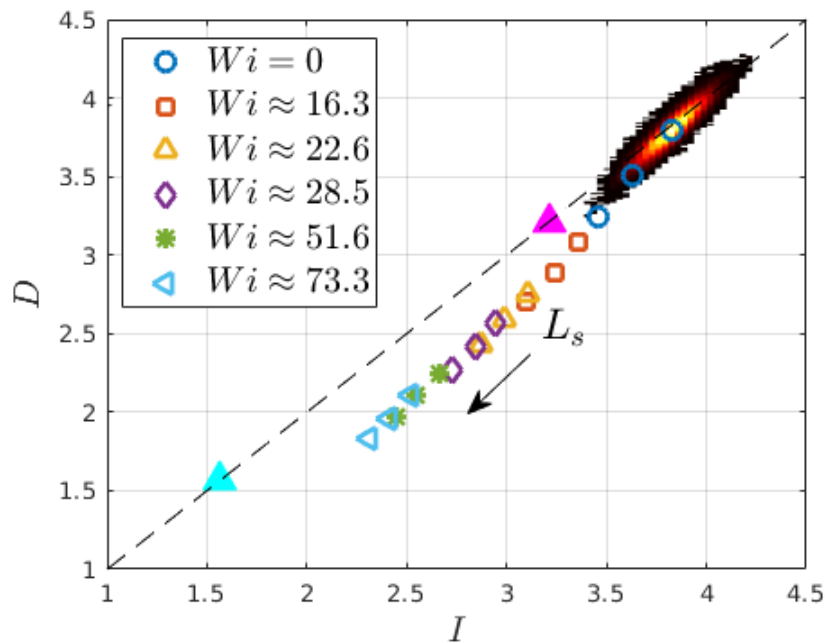
Figure 4.12: State-space visualization of the mean state of the system as a function of Weissenberg number and slip length.

state (i.e., (1,1)). Then we can define the relative distance to the laminar state by

$$d_S = \frac{||S - S_{lam}||_2}{||S_0 - S_{lam}||_2} \tag{4.12}$$

Figure 4.13 shows the distance to the laminar state relative to the distance of the no control case (i.e., Newtonian and no-slip). Under the effect of polymers alone, the relative distance of the system is reduced as Weissenberg number increases. However, it appears to level off and approach an asymptote. This leveling off begins after $Wi \approx 30$. This same trend holds for the slip cases, but the slip surfaces reduce the distance further, relative to the no-slip case. The fact that the distance to the laminar state levels off suggests that the maximum drag reduction asymptote may manifest in state-space as some surface which prevents the state of the system from moving further with the effect of polymers, alone. Though, it seems that slip surfaces affect
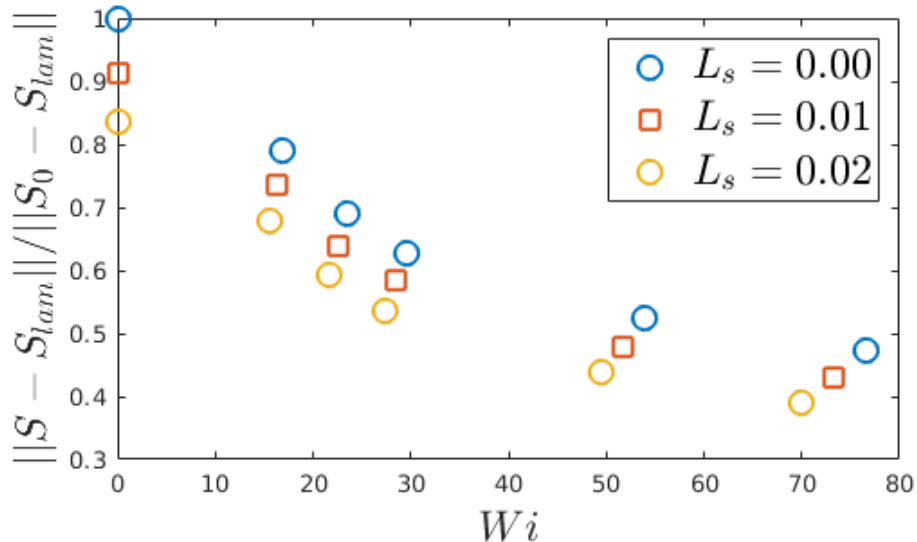
Figure 4.13: State-space visualization of the mean state of the system as a function of Weissenberg number and slip length.

this hypothetical topology in some way to allow the system to become closer to the laminar state. This is corroborates the results found in Chapter 1 and Chapter 2, which showed that slip surfaces facilitate the more frequent return to the laminar state. A "good" choice of state variable to describe the state of the system may provide more insight into the hypothetical MDR surface.

4.4 Conclusions and future directions

We performed direct numerical simulations of channel flows to investigate the composite drag reduction of slip surfaces and dilute polymer solutions. The two individual methods worked in tandem to provide a synergistic, or additive, drag reduction effect. By investigating the mean velocity profiles and Reynolds shear stress profiles, it was determined that the mechanisms responsible for the success of each individual method are distinct and have minimal interaction with each other. While the slip surfaces work to shift the velocity profile upward near the wall, the polymers work

to reduce the Reynolds shear stress in the bulk of the flow. Quadrant analysis [249] should be performed to gain further insight into possible mechanisms responsible for the altered mean behavior of the flow. These control methods undoubtedly have an impact on the self-sustaining process, which would manifest itself as reduced sweep and ejection events that could be observed in quadrant analysis.

An analysis of the the turbulent kinetic energy (TKE) and the rate at which kinetic energy converted to elastic energy (E) was performed. For all slip lengths, the TKE reaches a peak for $Wi \approx 30$ before monotonically decreasing. This Weissenberg number coincides with the Weissenberg number where the drag reduction begins to level off and approach the maximum drag reduction (MDR). The rate at which kinetic energy is converted to elastic energy increases sharply at low Weissenberg numbers, corresponding the increase in flexibility of the polymers. After $Wi \approx 30$ this value levels off and appears to approach some asymptote. Again, this trend and value of Weissenberg number corresponds to that observed in the drag reduction and TKE. A more thorough investigation into the energy budget of the composite drag reduction is necessary. The turbulent kinetic energy in each spatial direction should be analyzed to determine where the reduction in turbulence energy is occurring. Additionally, a similar investigation into the elastic energy associated with with the polymers should be performed. It is believed that further investigation of the polymer dynamics, afforded by the conformation tensor α, would contribute considerable insight into the mechanisms responsible for the observed behavior.

Finally, the mean state of the system was projected onto the energy Input-Dissipation plane. This showed that the control methods reduce the distance between the mean state of the flow and the laminar state. It also showed that this distance appears to reach some asymptote which coincides with the asymptotic approach observed in the drag reduction and rate of conversion into elastic energy. It is possible

that the MDR manifests as some surface in state space which prevents the mean state of the system from being altered any further by the action of polymers, alone. A good choice of state variables may offer a better description of this hypothetical surface.

A limitation of the current study is that only one polymer concentration was considered. Further work should be performed to investigate the effect of polymer concentration on the achievable drag reduction, as it may offer further insights into the mechanisms responsible for the drag reduction and the differences observed by Rajappan and Mckinley [192] between empirically observed and empirically derived drag reduction values. Rajappan and Mckinley [192] also observed that the drag reduction decreased after a critical polymer concentration, resulting from increased shear viscosity and, subsequently, increased viscous dissipation.

An vital study moving forward would be to look into the conditionally sampled flow fields, where the condition admits periods in the turbulent trajectory which are characterized by low wall shear rate. Previous work in this area [80] has gained great insight into the mechanisms behind drag reduction when performing temporal analysis on the turbulent trajectories of polymer drag-reduced turbulent flows.

Future work should also consider the effect of non-ideal slip. The current study considers only a homogeneous, streamwise slip. A more realistic natural surface would, indeed, have slip in both the streamwise and spanwise directions. With advancements in surface fabrication techniques, a multitude of functionalized surfaces can be manufactured which take advantage of various material properties to control surface wetting phenomena [216, 269, 60, 143, 63, 141]. Therefore, modeling of surfaces which display time-varying slip is of much interest for the control of turbulent flows. This is the focus of ongoing and future work.

Chapter 5

CHARACTERIZING LOW-DRAG EVENTS IN WALL-BOUNDED TURBULENT FLOWS AT MODERATE REYNOLDS NUMBERS

[1]

5.1 Introduction

5.1.1 Underlying structure of turbulence

It is human nature to attempt to extract some level of order from chaos; to find patterns in randomness. This human tendency is no different with turbulence, the seemingly chaotic process which is emergent throughout nature. In the past few decades, however, the stochastic shroud surrounding turbulence has slowly been lifted, revealing a more deterministic underlying structure [168, 233, 145, 71, 73, 182, 256, 257, 92, 120, 54]. This structure is made up of fully-nonlinear solutions to the Navier-Stokes equations called "exact coherent states" (ECSs) [233]. With the application of dynamical systems theory to the study of turbulent flows [119], three-dimensional traveling wave solutions (TWSs), have been discovered. These solutions often manifest in the form of streamwise-oriented, counter-rotating vortices which propagate in a

---

[1]This work is in preparation to be submitted to a scientific journal.

coherent manner [182]. Furthermore, these solutions are inherently unstable, emerging in pairs via a saddle-node bifurcation at a finite Reynolds number. Each branch of the solution is referred to as "upper" or "lower", with the lower-branch solutions characterized by lower drag and reduced streamwise variance [233, 71, 256, 182].

A number of studies have successfully identified solutions in the "minimal flow unit" (MFU) [103, 105] in the plane channel geometry, where the temporal behavior qualitatively matches spatio-temporal behavior of near-wall turbulence in extended domains [61, 182, 127]. As $Re \rightarrow 0$, there is evidence to suggest that turbulence is closely organized around the ECSs [119, 71, 182]. While the state space of turbulence is well-mapped at lower (transitional) Reynolds numbers, the landscape is still relatively unknown at high Reynolds numbers due to the existence of an infinitude of solutions that the system can meander between as $Re \rightarrow \infty$ [43, 119].

5.1.2 Low-drag events and their connections to exact coherent solutions

5.1.2.1 Definition of Low-Drag Event

During a typical trajectory of wall-bounded turbulence, the system spends the majority of its time near the upper-branch solution, making infrequent excursions toward the lower-branch solution [182]. When these excursions take place, the wall shear and the streamwise variation of the flow are reduced [230, 107, 256, 182]. This intermittent behavior of alternating between "active" and "hibernating" turbulence (terms coined by Xi and Graham [256]) has been of great interest, in the last two decades [82]. Initially, these events were found in viscoelastic flows in MFU [256]. Later, Xi and Graham [257] showed that these events still occur in the Newtonian limit, and are actually Newtonian structures, simply "unmasked" by the effect of polymers.

Previous studies have shown interesting characteristics of periods of hibernating turbulence, which will herein be referred to as low-drag events (LDEs) [257, 127, 246, 247, 3]. Most notably, these events have been characterized by reduced turbulent fluctuations and quasi-streamwise-invariant structures. Additionally, the conditional mean velocity profiles during hibernating turbulence are shifted upward[256, 257, 80], away from the Newtonian profile [187], and towards the maximum drag reduction asymptote (MDR) [227]. The defining signature of these events, and the signature typically used to detect them, is an uncharacteristically low level of wall shear stress for an extended period of time [256, 257, 80, 182, 127, 246, 247, 3].

5.1.2.2 Identifying low-drag events in turbulence

Previous studies have identified LDEs is various manners but most involve searching for extended periods of uncharacteristically low wall shear behavior in the flow. Initially, in MFUs, Xi and Graham [256] used the criteria that area-averaged wall shear stress must fall below 90% of the time-averaged value for longer than a given number of eddy turnover times, $\Delta t^* = \Delta t u_\tau / h > 1.18$, to identify LDEs. They, later, went on to find that the average duration for these events was $\Delta t^* \approx 5$ for similar Reynolds numbers [257]. Both studies were performed within the transitional regime at $Re_\tau = 85$ and used the mixed time unit duration criterion for conditional event detection. A similar approach has been used by others to identify LDEs in transitional flows.

Kushwaha et al. [127] used mixed time units $\Delta t^* = \Delta t u_\tau / h$ to detect hibernating turbulence in an extended channel geometry. Using point-wise wall shear stress measurements, they detected hibernation at various uncorrelated points in the channel. The definition of hibernation used was that wall shear stress fall below 90% of the mean value for $\Delta t^* > 3$. Using conditional sampling of wall shear stress fields, they

found the spatial patterns around hibernation. Immediately preceding hibernation, there is a large spike in wall shear stress, followed by a low value during hibernation, and a spike again, immediately following. The spatial structure of hibernation found by Kushwaha et al. [127] was consistent with a low-speed streak of approximately 1500 and 50 viscous units in the streamwise and spanwise directions, respectively. This streaky structure was found to result from a pair of counter-rotating vortices, causing the transfer of fluid away from the wall.

Kushwaha et al. [127] also suggest that the temporal intermittency of LDEs in MFUs corresponds to spatio-temporal intermittency observed in extended domains. This lends credence to the idea that LDEs emerge in extended domains, but are both spatially and temporally localized. Therefore, the detection of these events in an extended domain can be difficult when utilizing an area averaged approach. The area which is averaged over may need to correspond to the MFU for that particular Reynolds number.

Whalley et al. [246] studied the intermittency of low-drag events using experimental pointwise measurements in a channel geometry for $Re_\tau = 70 - 130$. They found that the mean velocity profile during these conditional events was shifted away from the Newtonian profile in the log-law region, much like that seen in Xi and Graham [256, 257], Graham [80]. They also found similarities between temporal intermittency in small domains and spatio-temporal intermittency in extended domains, in agreement with [127]. Whalley et al. [247] extended this analysis to further characterize low-drag events in experimental channel flows for $Re_\tau = 70 - 100$. Spatial patterns associated with low-drag events consisted of a low-speed streak flanked by a pair of counter-rotating vortices. In both studies, the criteria used to detect low-drag events was wall shear stress falling below 90% of the mean value for three eddy turnover times, $\Delta t^* > 3$.

Looking to extend the previous analysis to larger Reynolds numbers, Agrawal et al. [3] characterized LDEs for $70 \leq Re_\tau \leq 250$. Using both DNS and experiments, they detected LDEs using conditional sampling of the wall shear stress based on a threshold magnitude criterion and a duration criterion in extended domains. Unlike previous studies, however, they considered three different time scalings for the duration criterion (i.e., outer, inner, and mixed units). Compared with the Reynolds number dependence of LDE frequency found previously when using mixed units [246, 247], Agrawal et al. [3] found invariance in the frequency of LDEs with increasing Reynolds number if the duration criterion is kept constant in inner time units (i.e., $\Delta t^+ = \Delta t u_\tau^2 / \nu = constant$). They also found that the mean velocity profile during these conditional events approached the Virk MDR asymptote for the range of Reynolds number studied.

The previous studies have shown that wall shear stress is useful in identifying LDEs, or hibernating turbulence. As Reynolds number increases, however, wall shear stress can become unreliable for identifying conditional events in experiments. Often, wall shear stress measurements become too noisy, or the accuracy not high enough, to identify these events at high Reynolds number [158]. However, with common flow visualization techniques, other state variables may be viable options for detecting LDEs. Particularly, as observed in previous studies [246, 247, 3], there is a distinct reduction in streamwise velocity that corresponds to the detected LDEs via wall shear stress. Therefore, streamwise velocity may be a more viable option for LDE detection at higher Reynolds number. Additionally, [80] found reduced bulk Reynolds shear stress and increased instantaneous log-law slope during LDEs.

5.1.2.3 Connection between low-drag events and exact coherent solutions

Low-drag events offer an interesting perspective when comparing the characteristics of these conditional events to that observed in ECSs. Given the low levels of drag and the predominantly streamwise nature of LDEs, a stark comparison can be drawn between these events and the behavior seen in TWSs. This is particularly important, as it suggests that during a typical turbulent trajectory, the flow makes infrequent excursions near lower-branch solutions, where the behavior is characterized by reduced turbulent fluctuations and uncharacteristically low drag [80]. Xi and Graham [256] observed this type of behavior in minimal channel flow geometries and later proposed this connection between LDEs and ECSs [257].

Park and Graham [182] found several new families of traveling wave solutions in minimal channel flow and analyzed their connections to flow dynamics in a fully turbulent flow. The state-space dynamics of the fully turbulent flow were found to be closely organized around one of the solution families. While the flow spent most of its time around the upper-branch solution (i.e., "active" turbulence), it would make infrequent excursions toward the lower-branch solution (i.e., "hibernating" turbulence). This temporal intermittency in minimal channels corroborates the observations made in previous studies [256, 257, 80]. Furthermore, mean velocity profiles for the upper-branch and lower-branch solutions resembled the Newtonian log-law profile and Virk MDR asymptote, respectively.

Kushwaha et al. [127] further investigated the relationship between extended domain DNS and ECSs found by Park and Graham [182]. By using wall shear stress values locally averaged over an area corresponding to the size of the minimal channel used for the ECS, they found good agreement between the average bulk velocity of

the ECS and the value found for the ensemble-averaged LDEs. They also found excellent agreement between the mean velocity profiles for the ECSs and the conditionally averaged profiles during LDEs.

5.1.3 Importance of low-drag events

The future of real-time turbulent flow control lies in the synthesis of low-order representations which are robust and parsimonious. The ability to synthesize these models is reliant upon the extraction, and subsequent understanding, of important flow structures and events which emerge in turbulence. In other words, to know which direction to go (i.e. to control the system), we must first know where we are relative to major landmarks (i.e., exact coherent solutions) and become familiar with the roads to travel to get to them (i.e. trajectories). In addition to finding new ECSs, new work on the latter is being done to better understand the "principal" trajectories that are fundamental in a nonlinear system [55].

An image comes to mind of a cartographer filling in the world map as she explores previously unseen territory. In much the same way as traveling in a foreign land without a map, it is easy to get lost in the state space of turbulence without knowing the landscape. However, as we continue to map exact coherent solutions and the flow structures or characteristic events that emerge when the system is near to them, we can begin to form novel flow control methods to force trajectories toward (or away from) these landmarks. The advancements and application of machine learning in fluid dynamics is promising for helping to further reveal the state space of turbulence [177].

Characterization of the temporal and spatial aspects of low-drag events is the first step toward more informed flow control techniques. A better understanding of these events, including when and how they arise, invites the future possibility of their

in situ prediction. Subsequently, an informed flow control method would allow the replacement of "always on" control with "on-off" control, which promotes decreased energy expenditure, as the control is only on when the system is in a more controllable state (e.g., close to an ECS) [43]. Furthermore, low-drag events offer a prudent target for drag reduction. By tailoring techniques to increase the overall frequency of low-drag events or increase the duration of individual events, enhanced drag reduction may be achieved at a lower cost.

Recently, work by Davis and Park [45] showed that the addition of homogeneous slip at the boundaries has a stabilizing effect on certain ECSs, extending the time spent in the quiescent solution state. Conversely, ECSs that manifest different flow structures were coerced to leave the solution state early with the inclusion of slip at the boundaries. It is reasonable to believe, then, that this may be extended to active feedback control to guide the system to a desired state. These advancements in control are preceded, first, by garnering a better understanding of the events themselves and their connections to ECSs.

Given the previous work to characterize LDEs at lower Reynolds numbers, the question naturally arises: what happens as $Re \rightarrow \infty$? Whalley et al. [247] showed that the frequency and fraction of time spent in hibernating turbulence decreases with increasing Reynolds number up to $Re_\tau = 100$ when using mixed units for the time duration criterion ($\Delta t^* = \Delta t u_\tau / h$). However, Agrawal et al. [3] recently found that the fraction of time spent in these low-drag states is constant when using inner units for the time duration for $Re_\tau \leq 250$. Therefore, the goal of this work is to extend the analysis of these previous studies to characterize the intermittent low-drag events at moderate Reynolds numbers (*i.e.*, $200 < Re_\tau < 700$) using temporal and spatial sampling techniques. With insight into the characteristics of these low-frequency events, we can better understand the dynamics of turbulent flows, and exploit these

dynamics to offer more efficient control methods in the future.

Below, we detail the characterization of low-drag events at moderate Reynolds numbers using combined numerical and experimental techniques. This article is organized as follows: Section 5.2 presents the problem formulation and provides numerical details. Section 5.3 provides details on the experimental setup and methods used for data capture of the turbulent boundary layer velocity fields. Comparison of numerical data with experimental data, as well as resulting low-drag event identification and characterization is detailed in 5.4. Finally, a summary and implications of the present investigation are given in Section 5.5.

5.2 Numerical Formulation

We consider an incompressible Newtonian fluid in the plane Poiseuille (channel) geometry, driven by a constant volume flux $\dot{Q}$. The x, y, and z coordinates are aligned with the streamwise, wall-normal, and spanwise directions, respectively. Periodic boundary conditions are imposed in the x and z directions with fundamental periods L_x and L_z, and no-slip conditions are imposed at the walls $y = \pm h$, where $h = L_y/2$ is the channel half-height. Using the half-height h of the channel and the laminar centerline velocity U_c as the characteristic length and velocity scales, respectively, the nondimensionalized Navier-Stokes equations are then given as

$$\nabla \cdot \boldsymbol{u} = 0, \tag{5.1}$$

$$\frac{\partial \boldsymbol{u}}{\partial t} + \boldsymbol{u} \cdot \nabla \boldsymbol{u} = -\nabla p + \frac{1}{Re_c}\nabla^2 \boldsymbol{u}. \tag{5.2}$$

Here, we define the Reynolds number for the given laminar centerline velocity as $Re_c = U_c h/\nu$, where ν is the kinematic viscosity of the fluid. Characteristic inner

scales are the friction velocity $u_\tau = (\bar{\tau}_w/\rho)^{1/2}$ and the near-wall length scale or wall unit $\delta_\nu = \nu/u_\tau$, where ρ is the fluid density and $\bar{\tau}_w$ is the time- and area-averaged wall shear stress. As usual, quantities nondimensionalized by these inner scales are denoted with a superscript "+". The friction Reynolds number is then defined as $Re_\tau = u_\tau h/\nu = h/\delta_\nu$.

Simulations are performed using the open source code *ChannelFlow* written and maintained by Gibson [69]. In this study, we focus on the domains of $L_x^+ \times L_y^+ \times L_z^+ = 1000 \times 1400 \times 600$ to match the SPIV field-of-view. A numerical grid system is generated on $N_x \times N_y \times N_z$ meshes, where a Fourier-Chebyshev-Fourier spectral spatial discretization is applied to all variables. The spatial resolution used is $(N_x, N_y, N_z) = (82, 81, 104)$, resulting in the numerical grid spacing in the streamwise and spanwise direction: $\Delta x^+ \approx 12.2$ and $\Delta z^+ \approx 5.8$. The non-uniform Chebyshev spacing used in the wall-normal direction results in $\Delta y_{min}^+ \approx 0.54$ at the wall and $\Delta y_{max}^+ \approx 27.5$ at the channel center. The DNS spatial resolution is greater than that of the SPIV to ensure the simulations accurately capture the dynamics of the flow.

5.3 Details of the Experiments

The experiments were conducted in a recirculating water channel facility in the Department of Aerospace Engineering and Mechanics at the University of Minnesota. The channel test section is 8 m long and 1.12 m wide. In order to trigger the development of a turbulent boundary layer, a 3 mm diameter cylindrical trip-wire was located at the entrance of the test section. The experiments were performed at an approximate streamwise location of 4 m from the trip wire location. The water depth in the channel was maintained at 0.394 m. The boundary layer thickness was estimated as $\delta = 73$ mm (based on the the location where the mean streamwise velocity
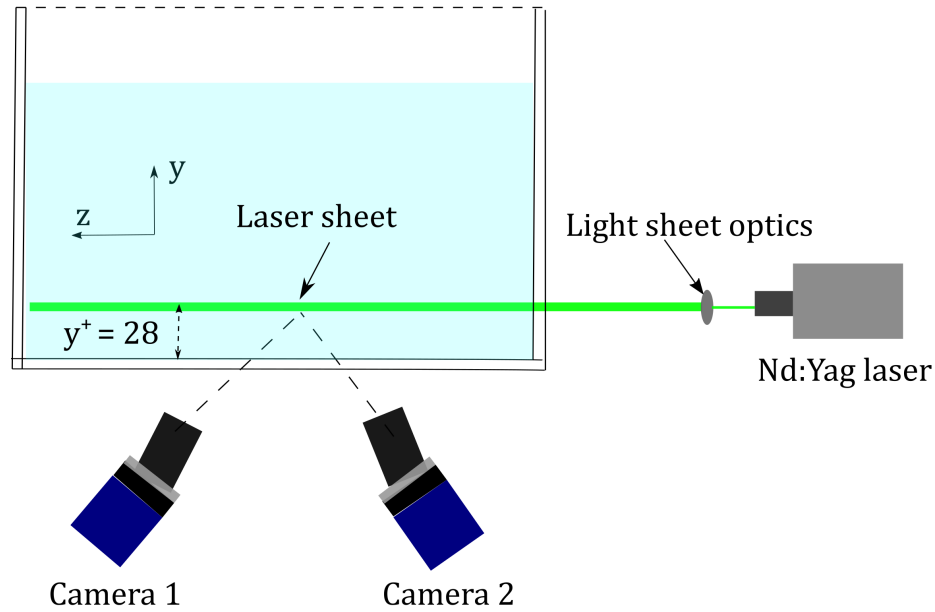
Figure 5.1: Schematic of the Stereoscopic Particle Image Velocimetry setup for the current experiments. x, y and z represent the streamwise, wall-normal, and spanwise directions, respectively.

reaches 99% of the free stream value). The free stream velocity was 0.215 m s^{-1}, and the corresponding frictional Reynolds number was $Re_\tau = u_\tau \delta / \nu = 680$. Here, the frictional velocity, u_τ, was estimated by fitting the logarithmic law of the wall to the boundary layer profile obtained experimentally.

In order to characterise hibernation events close to the wall, Stereoscopic Particle Image Velocimetry (SPIV) was employed at a distance of $y^+ = 28$ from the wall. The flow was seeded with silver-coated hollow glass spheres from Potters Industries LLC with an average diameter and density of 13 μ m and 1600 kg m^{-3}, respectively. a New Wave Solo II Nd:Yag 532 nm double-pulsed laser system with a pulse energy of 30 mJ was employed to illuminate a 1 mm thick plane parallel to the wall at a location of $y^+ = 28$. Two Phantom Miro high-speed cameras with a resolution of 1280 × 800 pixels^2 were arranged in a Stereoscopic configuration, giving a field of view of 951.4 × 613.4 wall units (1.4δ × 0.8δ) in the streamwise and spanwise directions, respectively.
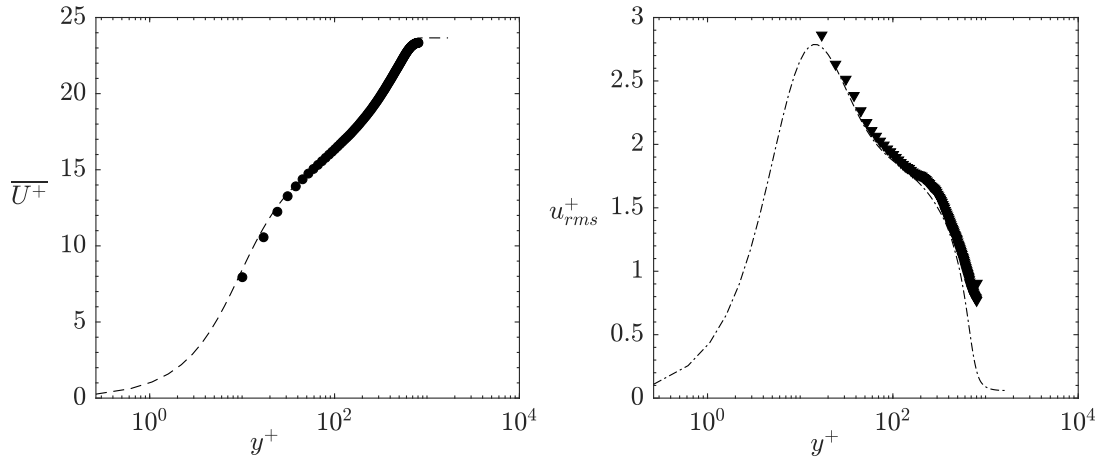
Figure 5.2: (a) Mean streamwise fluid velocity profile (shown as circles) and (b) r.m.s of the streamwise velocity fluctuations (shown as triangles) for the current experiments at $Re_\tau = 680$, compared to the DNS data from [109] (shown in dashed lines) for $Re_\tau = 690$.

The cameras were fitted with Scheimpflug mounts and 105 mm Nikon Micro-Nikkor lenses, giving a magnification factor of 11.76 pixels/mm. The Scheimpflug mounts were added to achieve a uniform focus across the field of view. The system was calibrated by imaging a 3D calibration plate with a high precision dot pattern (Type 22) from LaVision. The mapping function for the calibration was generated in DaVis 8.4 (LaVision) by fitting a third order polynomial function onto the marked planes. The r.m.s error in the estimated dot position varied from 0.05 to 0.1 pixels indicating an optimal fit. The schematic for the SPIV setup for the current experiments is shown in figure 5.1.

Velocity fields were deduced using DaVis 8.4, with an overlap of 50% over initial interrogation window sizes of 64 by 64 pixels followed by three passes of 32 by 32 pixels. The spatial resolutions of the computed velocity vectors was 25 wall units. The obtained velocity fields were post-processed with the universal outlier detection criterion [245] to remove spurious vectors. In order to obtain time-resolved velocity fields, 20 data sets containing 4117 images from each camera were acquired at 200

Re_τ	U_∞ [m s^{-1}]	u_τ [m s^{-1}]	δ [mm]
680 ± 20	0.215	0.0092 ± 0.0001	73 ± 2

Table 5.1: Boundary layer properties in the current study.

Hz. For time-averaged statistics, 2 data sets containing 4117 images from each camera were acquired at 2 Hz.

The mean flow statistics of the turbulent boundary layer was determined from planar PIV measurements. A streamwise wall-normal plane of thickness 1 mm was illuminated using the same laser system as mentioned above for the SPIV. A high speed camera (TSI Powerview Plus 4MP 16-bit) with an image resolution of 2048 by 2048 pixels was used to acquire 2000 image pairs at a sampling frequency of 1.81 Hz. The boundary layer properties are summarised in table 5.1. Further details can be found in Tee et al. [219]. In figure 5.2, the flow statistics from the current experiments are compared with the DNS results reported by Jiménez et al. [109]. The streamwise velocity statistics from PIV shows very good agreement with the DNS results.

5.4 Results and Discussion

5.4.1 Comparison of DNS and SPIV data

It is important to compare the DNS data to the SPIV data to ensure good statistical agreement before moving forward. The three plots in Figure 5.3 show the probability density functions for the streamwise, wall-normal, and spanwise velocity fluctuations normalized by the friction velocity. The streamwise velocity fluctuation distribution for both the DNS and SPIV data are negatively skewed, but match quite well. However, the peak of the wall-normal velocity fluctuation distribution is slightly negative, possibly due to insufficient resolution in the y-direction. There appear to be larger

Table 5.2: Time-averaged statistics

$y^+ \approx 28$	Re_τ	u_τ	$\langle U \rangle / u_\tau$	$\langle u_{rms} \rangle / u_\tau$	$\langle v_{rms} \rangle / u_\tau$	$\langle w_{rms} \rangle / u_\tau$
DNS	700	0.0355	12.960	2.571	0.791	1.310
SPIV	700	0.0093	14.920	2.100	1.020	1.203
Database	690	0.0422	13.020	2.531	0.866	1.440

spanwise velocity fluctuations in the DNS as evidenced by the slightly wider distribution and smaller peak. Overall, there good agreement between the numerical and experimental data.

Additionally, both DNS and SPIV statistics were found to be in good agreement with values from a database of turbulent boundary layer DNS data at a Reynolds number of $Re_\tau = 690$ [110]. A comparison of time-averaged statistics is shown in Table 5.2.

5.4.2 Correlation of wall shear and streamwise velocity

Previously, low-drag events have been identified using observed trends in the wall shear stress or wall shear rate [256, 247]. Due to limitations in the current experimental setup, there is no access to experimental wall shear information, so low-drag events cannot be identified in this manner. However, Whalley et al. [247] also showed a characteristic reduction of streamwise velocity during the low-drag events that were identified using wall shear stress. While the coherence between wall shear stress and streamwise velocity is lost as wall-normal distance is increased, they show the significant deviation from the mean streamwise velocity behavior during low-drag events persists up to a wall-normal distance of $y^+ \approx 30$. However, this result is only for $Re_\tau \approx 100$. With $Re_\tau = 700$ and wall-normal location of the SPIV plane at $y^+ \approx 28$, we now verify whether the wall shear and streamwise velocity are correlated for the current study.
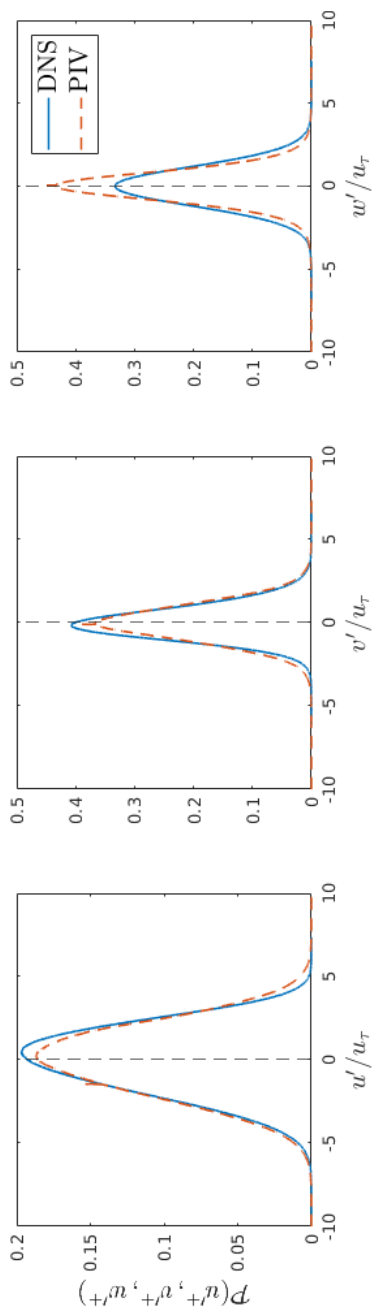
Figure 5.3: Probability density function for (a) streamwise, (b) wall-normal, and (c) spanwise velocity fluctuations. All values are normalized by the friction velocity u_τ.

We consider the correlation coefficient, which is the linear relationship between the two area-averaged signals, and is given by

$$r(\tau_w, u) = \frac{1}{N-1} \sum_{i=1}^{N} \left(\frac{\tau_{w,i} - \langle \tau_w \rangle}{\sigma_{\tau_w}} \right) \left(\frac{u_i - \langle u \rangle}{\sigma_u} \right) \qquad (5.3)$$

and can be more compactly written using the covariance of the two signals.

$$r(\tau_w, u) = \frac{cov(\tau_w, u)}{\sigma_{\tau_w} \sigma_u} \qquad (5.4)$$

The correlation coefficient ranges from 1 for positively correlated entities to -1 for negatively correlated entities. A correlation close to zero signifies negligible correlation and the two entities are incoherent. If two signals trend in the same direction, they are positively correlated, if they trend in opposite directions, they are negatively correlated, and if the relationship between two signals is incoherent, they are said to be uncorrelated.

Figure 5.4 shows the correlation coefficient as a function of wall-normal distance during "nominal" turbulence, as well as during conditionally sampled data from detected LDEs. As expected, very near the wall, the two values are almost perfectly correlated, and become less correlated as wall-normal distance is increased. However, the correlation between the two signals remains significant up to $y^+ \approx 28$, corresponding to the location of the SPIV plane. Additionally, the two signals are more correlated during the LDEs than during nominal turbulence. Therefore, it appears that the streamwise velocity at $y^+ \approx 28$ may be used as a proxy for wall shear to detect low-drag events.
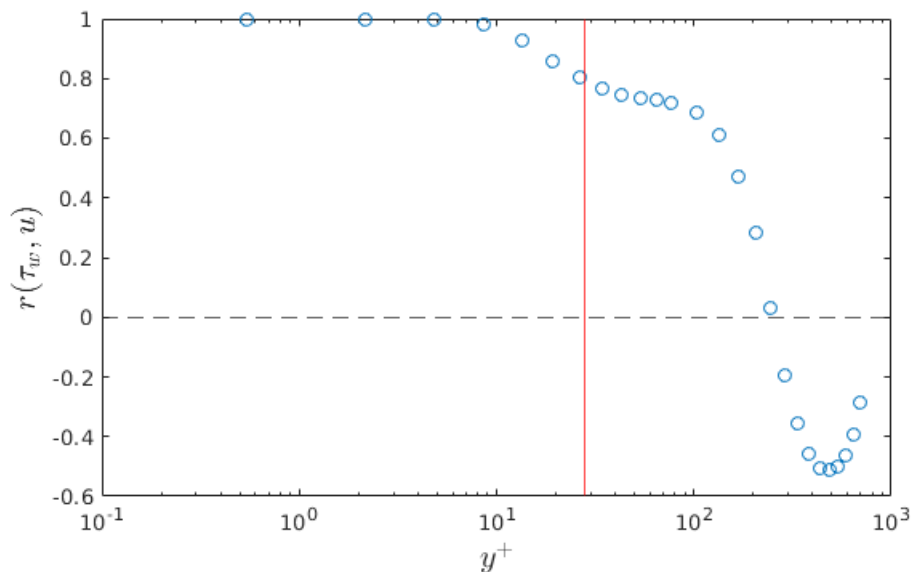
Figure 5.4: Correlation coefficient between the two DNS signals of area-averaged wall shear stress and area-averaged streamwise velocity as a function of wall-normal distance. The vertical red line corresponds to $y^+ = 28$

5.4.3 Detection of low-drag events

We now consider the detection of low-drag events for the DNS and SPIV data and compare their characteristics. We utilize the time series of the area-averaged the wall shear and the streamwise velocity at $y^+ \approx 28$ for the DNS fields and time series of the area-averaged streamwise velocity at $y^+ \approx 28$ for the SPIV fields. For the current study, the quantities are averaged over the entire field of view (i.e., $L_x = 1000 \times L_z = 600$).

5.4.3.1 DNS

We now consider the distribution of the duration of LDEs found via wall shear information from DNS. We use the detection criterion that the wall shear must fall below 95% of the mean value for any amount of time. From this, the probability density function for the duration of these events can be found. A duration criterion
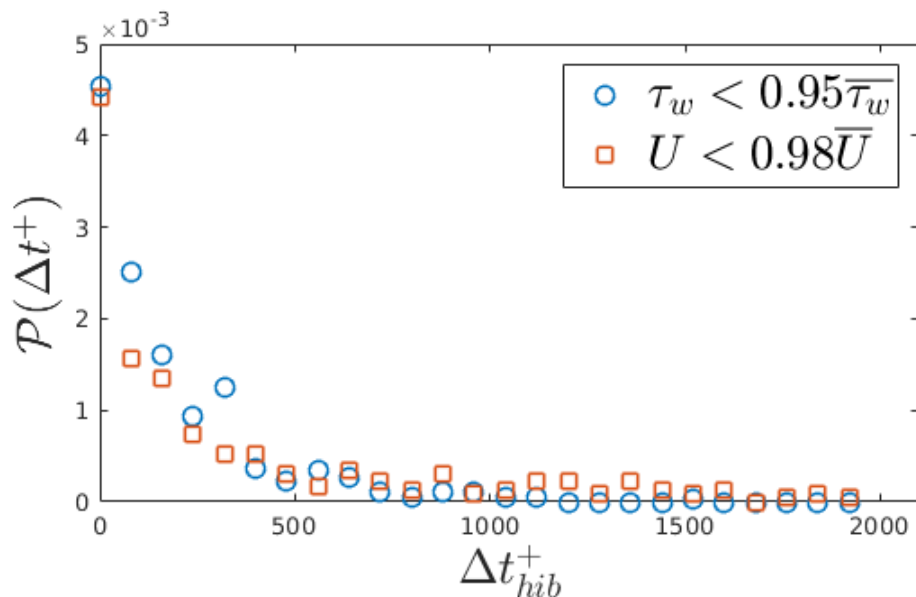
Figure 5.5: Probability density function for the duration of low-drag events using τ_w and $u(y^+ \approx 28)$.

can, then, be determined based on the average duration plus some value to take into account only significant events. The same analysis is done to find the distribution of detected events using streamwise velocity at $y^+ \approx 28$. However, the criterion is now that the area-averaged streamwise velocity must fall below 98% of the mean value for any amount of time. These probability density function are shown in Figure 5.5.

While there is good agreement between the distribution of LDE duration using the two quantities, the question remains whether the events detected via streamwise velocity away from the wall are the same events detected via wall shear. Furthermore, if the events detected are the same between the two cases, what is the relationship between them? Namely, do the events coincide with one another or does the event detected with one signal lag the same event detected with the other signal? Is it possible that some events are detected in one signal that go undetected in the other? To investigate this relationship, area-averaged time series data for a detected LDE are shown in Figure 5.6.
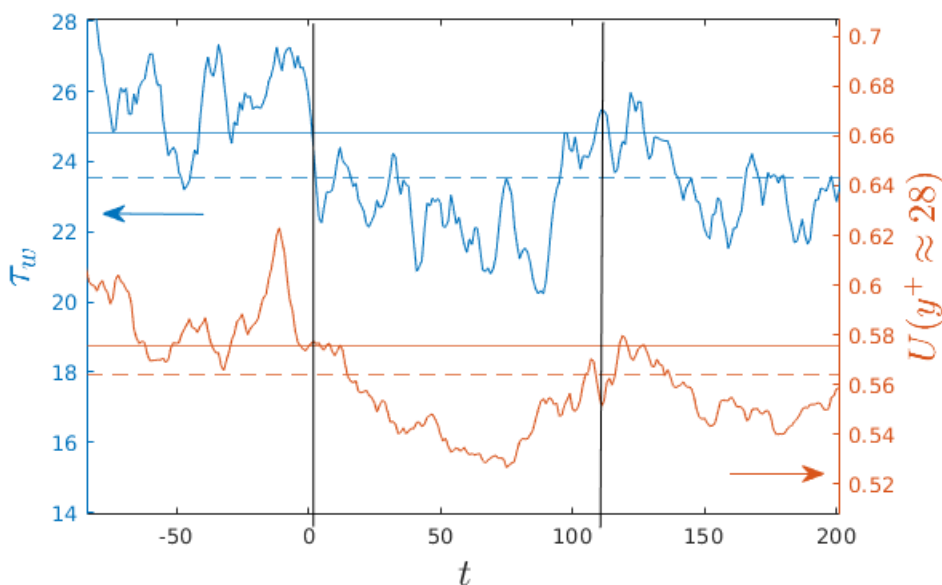
Figure 5.6: Time series data for a detected LDE using wall shear and the same event detected using streamwise velocity at $y^+ \approx 28$. Solid horizontal lines correspond to a signal's mean value. Dashed horizontal lines correspond to a signal's event detection criterion. Vertical lines are visual guides to highlight the low-drag event.

As shown in the figure, the two signals display similar behavior during a significant LDE detected via wall shear rate. The solid horizontal lines correspond to the mean value of each signal and the dashed lines correspond to the detection threshold value for each signal. Detection thresholds shown correspond to $0.95\bar{\tau}_w$ and $0.98U(y \bar{\approx} 28)$ for each respective signal. Overall, the two signals agree with one another during an LDE.

We now consider the joint probability density function of wall shear and velocity fluctuations for the nominal, or unsampled, data and the conditionally sampled data for the DNS, with the condition being $\tau_w < 0.95\langle\tau_w\rangle$ for $\Delta t^+ > 300$. As shown in Figure 5.7, the fluctuations in all three directions are reduced during the detected LDEs relative to the unsampled turbulence, and is quantified by the reduction in the standard deviations for each component. This is in agreement with the calm,

quasi-streamwise-invariant behavior seen in traveling wave solutions [182]. While both positive and negative fluctuations for the wall-normal and spanwise directions are reduced, only the positive fluctuations are reduced for the streamwise direction. This further suggests that streamwise velocity may be a good candidate for LDE detection where wall shear data is not available.

The same procedure is performed as before for LDEs detected via wall shear, except now we attempt to detect events via streamwise velocity at $y^+ \approx 28$. The condition for LDE now is $u < 0.98\langle u \rangle$ for $\Delta t^+ > 300$. The joint probability functions for wall shear and streamwise velocity at $y^+ \approx 28$ are shown in Figure 5.8. Once again, there is a reduction in the velocity fluctuations during LDEs detected via streamwise velocity which is quantified by the reduction in standard deviation of the fluctuations. While the extent to which they are reduced is less than that seen when using wall shear to detect LDEs, the trend is qualitatively the same. If a stricter criterion were set for the threshold value of streamwise velocity, these fluctuations may be reduced further. More importantly, however, is the trend see in the wall shear distribution for the conditionally sampled case. The wall shear is reduced during these events when they are detected using streamwise velocity. This suggests that streamwise velocity may be a good proxy for wall shear when attempting to detect LDEs. Therefore, we propose it is reasonable to apply the same methodology to the velocity planes from the SPIV data to detect LDEs.

5.4.3.2 SPIV

Now that streamwise velocity at $y^+ \approx 28$ has been shown to provide qualitatively similar results to those found using wall shear information, we consider the SPIV data. Shown in Figure 5.9 is the probability density function for the duration of detected LDEs using $U < 0.98\bar{U}$ for any amount of time. From this distribution, a
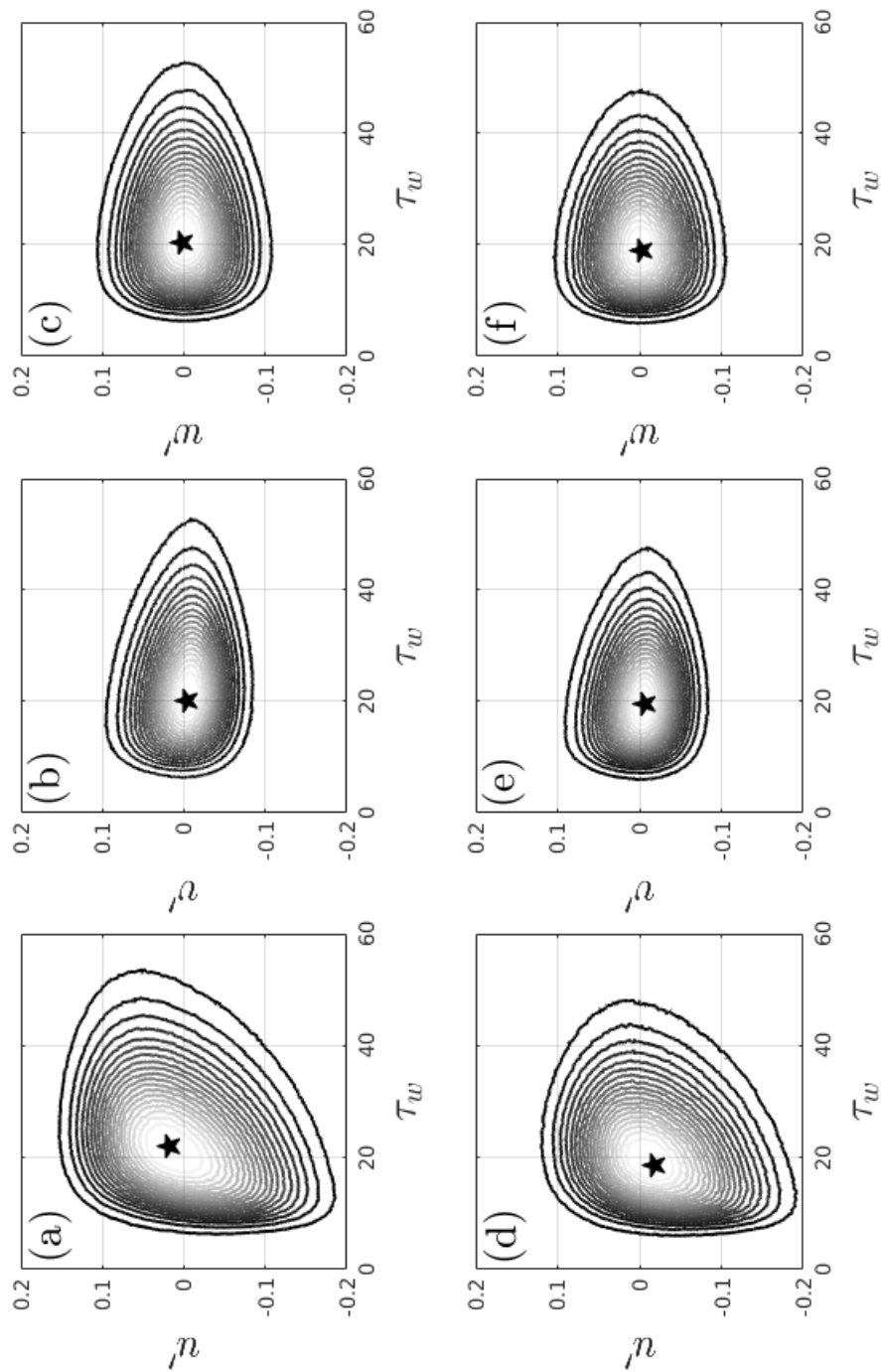
Figure 5.7: Joint probability density function for velocity fluctuations during low-drag events detected in DNS via wall shear, $\tau_w < 0.95\bar{\tau}_w$.
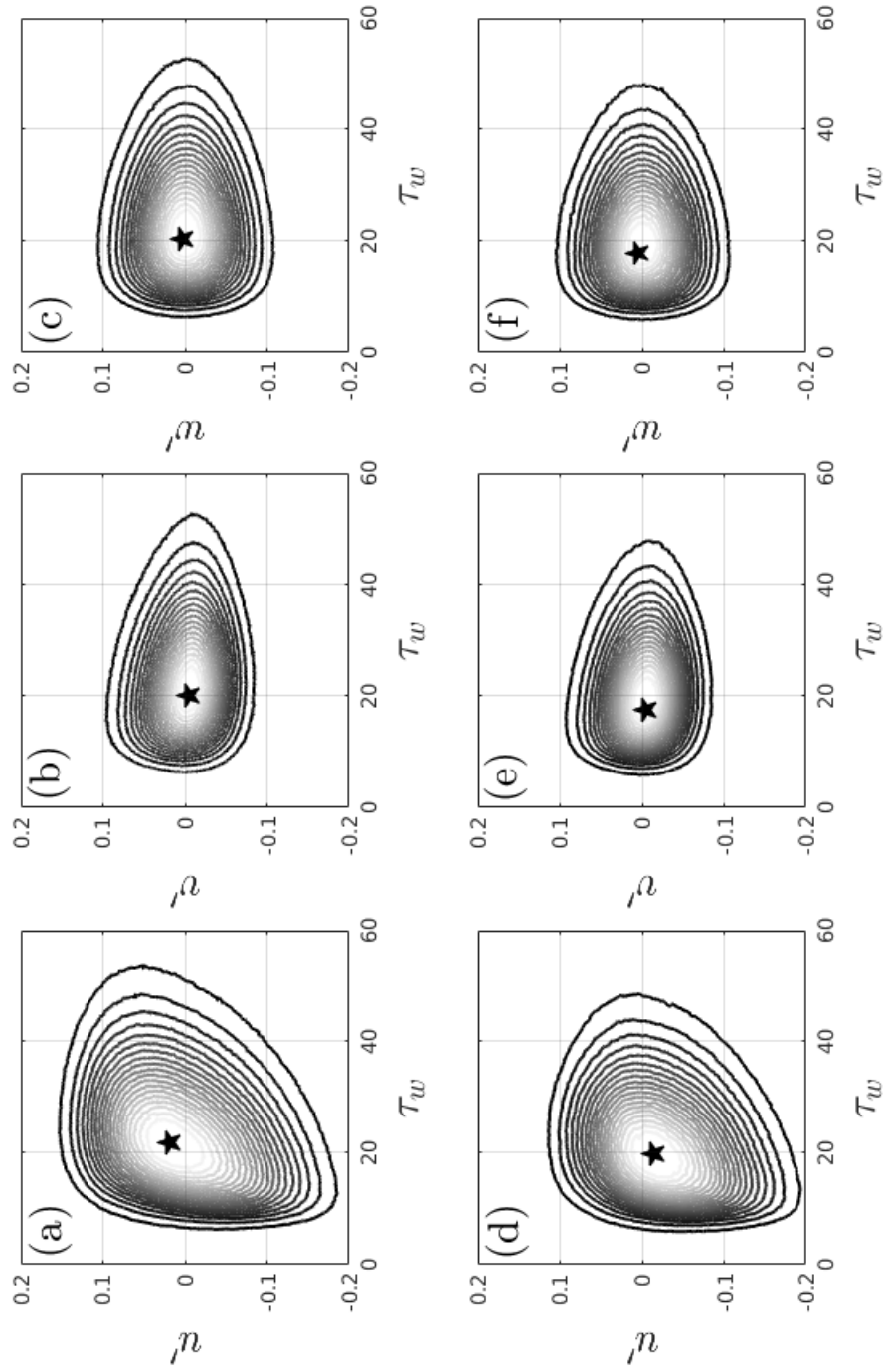
Figure 5.8: Joint probability density function for velocity fluctuations during low-drag events detected in DNS via streamwise velocity at $y^+ \approx 28$, $U < 0.98\bar{U}$.
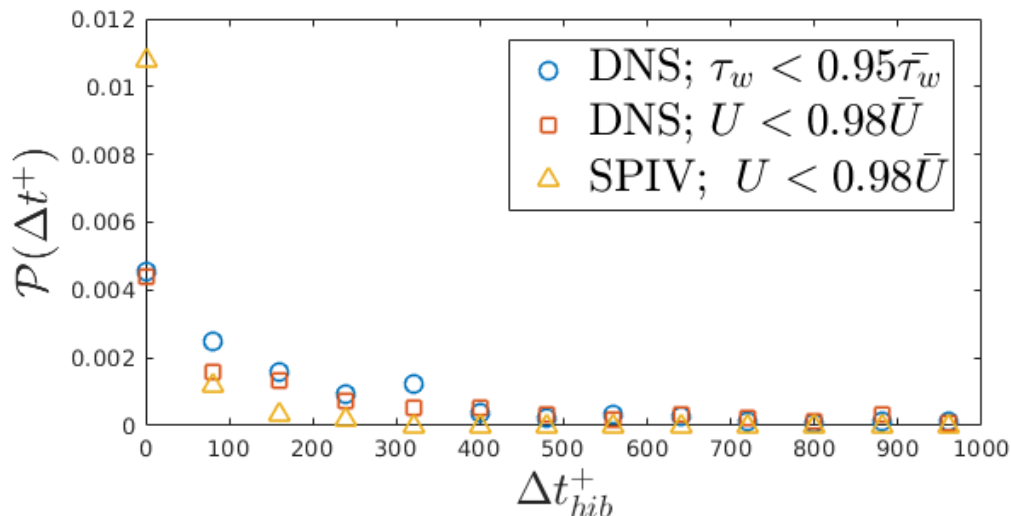
Figure 5.9: Probability density function for the duration of low-drag events detected via streamwise velocity at $y^+ \approx 28$ from turbulent boundary layer SPIV data compared with the probability density functions from DNS data.

critical duration criterion can be deduced to only take into account significant events. Overall, there is still good agreement between the distribution of LDE durations for the SPIV and DNS data. The shape and trend are qualitatively the same as that seen in the distribution of LDE duration of the DNS data. However, the number of significant LDEs detected is lower than that seen in the DNS data. This is illustrated by the rate at which the PDF decays with increasing LDE duration. This is most likely because the number of independent fields for the SPIV data is much less than that of the DNS data (i.e., there are fewer significant events because there are fewer SPIV fields to sample from). Therefore, the majority of the events detected in the SPIV data are short in duration causing the PDF to be much greater close to $\Delta t^+ = 0$. The duration of the longest event detected in the SPIV data is $\Delta t^+ \approx 275$ while the duration of the longest event detected in the DNS data is approximately an order of magnitude larger.

The distribution of velocity fluctuations for the unsampled and conditionally sam-

Table 5.3: Maximum LDE duration for each Reynolds number

Re_τ	$max\left(\Delta t^+_{LDE}\right)$
200	371.8 $\pm$4.3
500	978.0 $\pm$9.4
700	1983.3 $\pm$12.4
1000	4790.4 $\pm$17.1

pled data are shown in Figure 5.10. The LDE detection criteria in this case is $u < 0.98\langle U \rangle$ for $\Delta t^+ > 100$. Similar to the behavior seen in the DNS data, the fluctuations during the detected events are reduced compared to the unsampled case. Again, only the positive streamwise fluctuations are reduced during these events while both the positive and negative wall-normal fluctuations are reduced slightly. These reductions in the cross-flow fluctuations are, again, similar to the quasi-streamwise-invariant behavior seen in traveling wave solutions of Park and Graham [182]. The qualitative agreement between the DNS and SPIV data is promising for using streamwise, or possibly spanwise or wall-normal, velocity to detect LDEs.

5.4.4 Reynolds number dependence of low-drag events

A brief analysis of the effect of Reynolds number on the characteristics of LDEs has been performed. LDEs were detected using criteria that area-averaged wall shear τ_w must fall below 95% of the time-averaged value for any amount of time, i.e., $\Delta t^+ > 0$. The window size that the values are averaged over is $L^+_x = 1000 \times L^+_z = 600$. Probability density functions for the duration of these events are shown in Figure 5.11. Interestingly, the probability density functions are reduced at $\Delta t^+ = 0$ as Reynolds number is increased, suggesting more long-duration events are present at higher Reynolds numbers. This is observed in the non-zero PDF at larger duration. The largest LDE for each Reynolds number is shown below in Table 5.3. Interestingly, the duration of the longest LDE increases with Reynolds number.

161
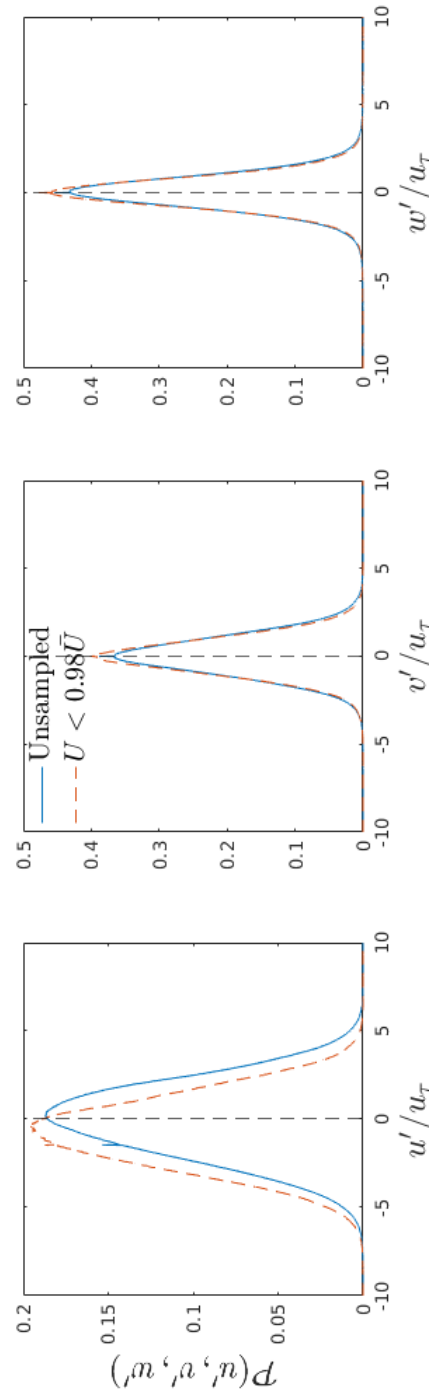
Figure 5.10: Probability density functions for the velocity fluctuations at $y^+ \approx 28$ during LDEs from the turbulent boundary layer SPIV data.
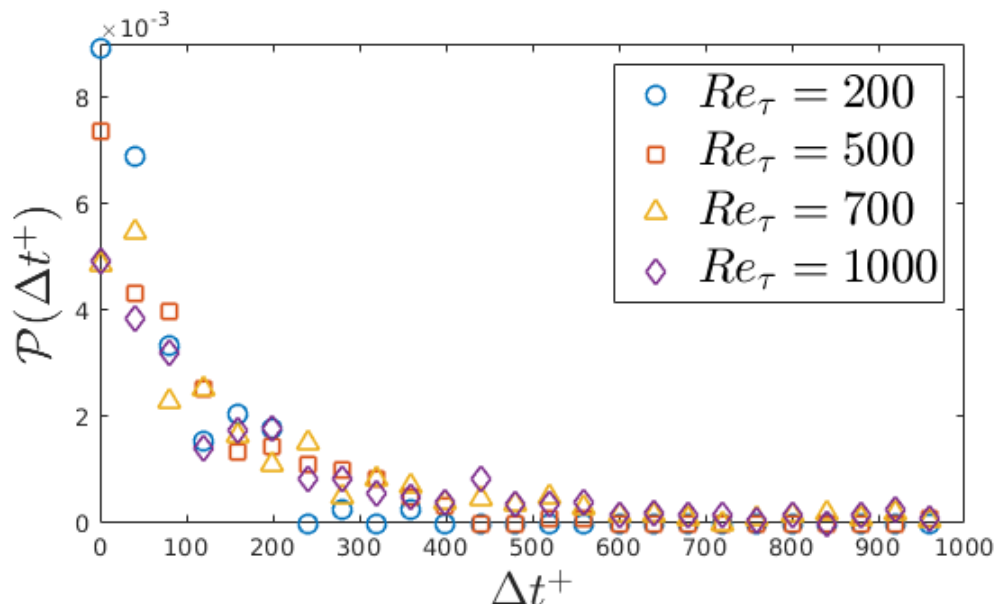
Figure 5.11: Probability density function of low-drag event duration for various Reynolds numbers.

The fraction of time spent in LDE for $\tau_w < 0.95\langle\tau_w\rangle$ and $\Delta t^+ > 100, 200$, and 300 is shown in Figure 5.12. Unlike the trend observe in Agrawal et al. [3], the fraction of time spent in LDE increases with Reynolds number. Previously, they observed that the fraction of time spent in these events remained constant with Reynolds number when inner units were used in the duration criterion to detect events. Similar to previous results, the fraction decreases with stricter duration criteria. This is due to the lower number of events with longer duration. The trend in the LDE fraction appears to be approaching an asymptote above $Re_\tau = 1000$, but more work is necessary to determine if this is the case.

Similarly, the fraction of time spent in LDE when using mixed scaling $(\Delta t u_\tau/h)$ for the duration criterion is shown in Figure 5.13. The trend is different from that seen in Figure 5.12. The fraction seems to stay relatively constant until $Re_\tau = 500$ before increasing for the rest of the Reynolds numbers studied here. Again, the fraction of time spent in LDEs is reduced for stricter duration criteria owing to the
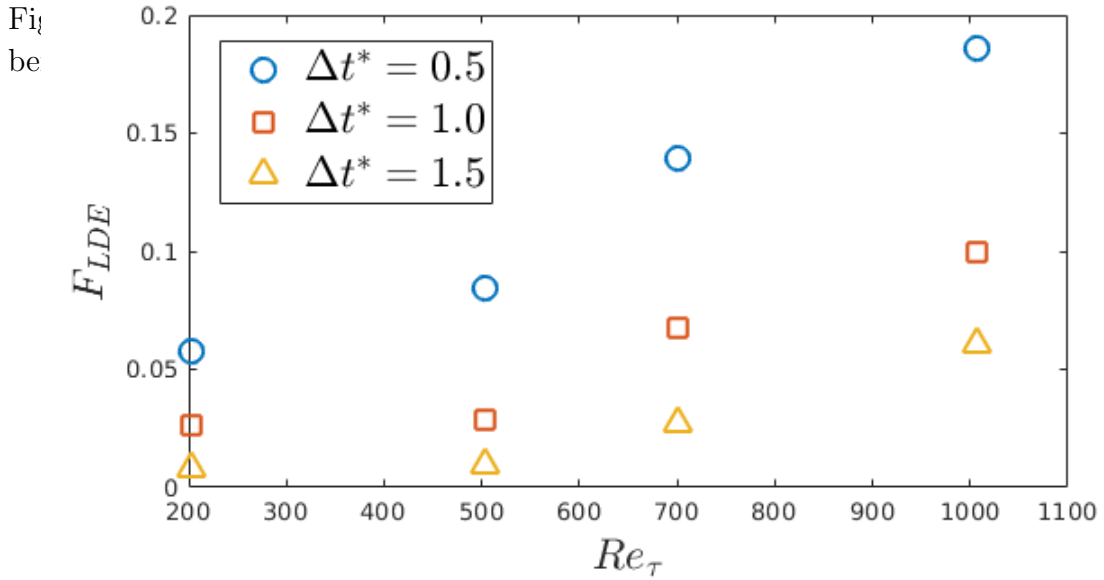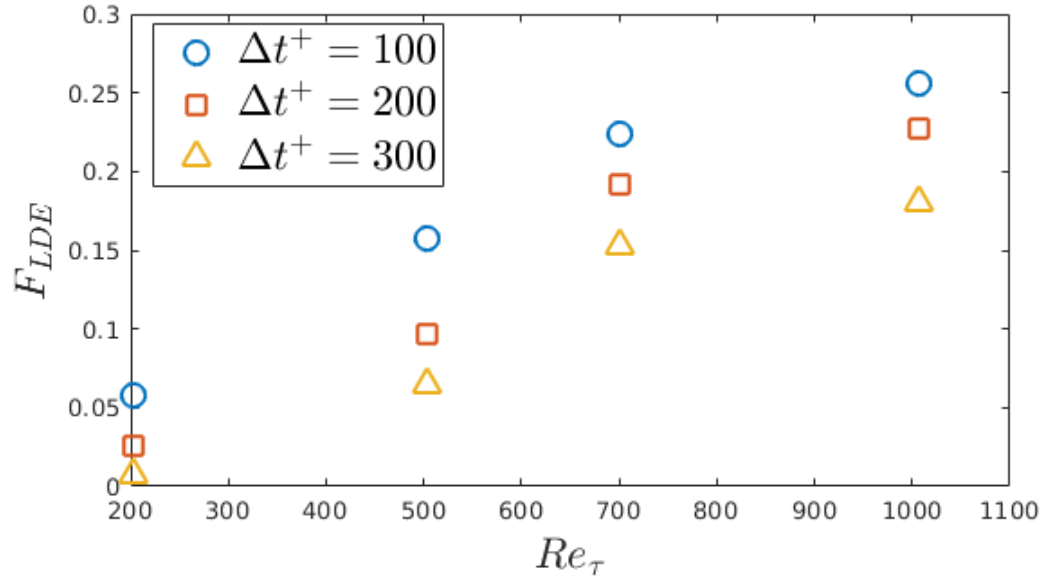
Figure 5.13: Fraction of time spent in low-drag state as a function of Reynolds number. Mixed scaling used for LDE detection duration criterion ($\Delta t^* = \Delta t \frac{u_\tau}{h}$).

decreased number of longer events. This, again, is different from the trend observed by both Whalley et al. [247] and Agrawal et al. [3], where the fraction of time spent in LDEs decreased with increasing Reynolds number when using mixed units for the duration criteria. While the difference is possible because the current study extends the Reynolds number quite considerably (the previous studies only investigated up to $Re_\tau = 250$), more work is necessary to determine if this is accurate.

5.5 Conclusion

This work sought to characterize the intermittent phenomena known as low-drag events (LDEs) for moderate Reynolds number. While this has been studied for transitional Reynolds numbers, $Re_\tau < 250$, the analysis has not been extended to higher Reynolds number flows. Using both direct numerical simulations (DNS) and stereoscopic particle image velocimetry (SPIV), we compared the temporal characteristics of LDEs at $Re_\tau = 700$.

Because wall shear stress measurements were unavailable with the current experimental setup, a relationship between the wall shear stress and streamwise velocity at some wall-normal distance had to be probed. It was found that the signals of area-averaged streamwise velocity at $y^+ \approx 28$ and area-average wall shear rate from the DNS data are highly correlated, with a correlation coefficient of ~ 0.8. Exploiting this relationship, the characteristics of LDEs were compared for those events found via wall shear rate and those found via streamwise velocity. Overall, the distributions of the LDE duration were in good agreement. The velocity-wall shear relationship was also compared by conditionally sampling the two fields using LDE detection criteria. Joint probability density functions for the wall shear rate and streamwise velocity of the DNS data show the reduction in streamwise velocity during LDEs detected using wall shear rate. The reciprocal behavior is observed when LDEs are detected using streamwise velocity. Velocity fluctuations in all three directions are reduced slightly during LDEs.

The distribution of LDE duration was compared for the DNS and SPIV data. While the DNS data admitted much longer events, as evidenced by the probability density function, the trend between the DNS and SPIV data was still consistent. Overall, there is good agreement between the two data sets when considering dis-

tribution of LDE duration. The discrepancy between the two data sets most likely manifests due to the much smaller sample size for the SPIV data. The longest event detected in the SPIV data is $\Delta t^+ \approx 275$ while the longest event detected for the streamwise velocity DNS data is an order of magnitude larger, $\Delta t^+ \approx 2900$. If a larger sample size were obtained for the SPIV data, it is believed that the two distributions would match more closely. It is also possible that the lower resolution and accuracy of the SPIV data plays some role in the lower detection rate.

Preliminary results on Reynolds number scaling of the duration of LDEs show that the fraction of time spent in LDEs increases with respect to Reynolds number using both inner units and mixed units. This result is reflected in the probability density function of the duration of LDEs for the various Reynolds numbers studied here. These results disagree with those observed by Whalley et al. [247] and Agrawal et al. [3], previously. The current results would suggest that there are more frequent LDEs and longer LDEs as Reynolds number is increased. There is also the possibility, evidenced by Figure 5.12, that the fraction of time spent in LDEs approaches some asymptote with increasing Reynolds number. These trends must be verified, and the Reynolds number scaling on the temporal characteristics of low-drag events is the focus of ongoing research.

The spatial locality of these events requires further investigation, as well. The interrogation window for the current study in inner units was 1000×600 for the streamwise and spanwise directions, respectively. The size of this area affects the ability to detect LDEs, as the detection method uses area-averaged wall shear rate, based on the assumption from previous studies that the entire domain should be experiencing the event. However, as domain sizes are extended, these events become spatially-localized. Therefore, area-averaged values mix information from areas of the domain that may be experiencing distinct spatially-localized dynamics. Future

work aims to more accurately describe the spatial characteristics of these events by identifying individual events in extended flow fields and investigating the efficacy minimal flow units at moderate Reynolds numbers. Chapter 3 suggests that certain constraints must be placed on the smallest domain size to ensure valid dynamics. Reynolds number scaling on the spatial characteristic of these events is also ongoing.

In turbulent flow control, a challenge lies in finding descriptive state variables for the system. This study shows that other variables (i.e., streamwise velocity) may be used as proxies for wall shear stress, which is a commonly used state variable in wall-bounded turbulent flows. These proxies may then be used for state estimation and control. This has important implications for high Reynolds number, industrial-scale flows where wall shear stress measurements are inaccurate or altogether unavailable.

Chapter 6

THE EFFICACY OF THE MINIMAL FLOW UNIT FOR HEALTHY TURBULENCE

[1]

6.1 Introduction

Embedded in a turbulent flow is inherent intermittency. The dynamics of wall-bounded turbulence fluctuate between high, intermediate, and low-drag states in a stochastic fashion, which illuminates the self-sustaining process in shear flows [256, 86, 232, 4]. The most straightforward simulation approach to identify the intermittency and self-sustaining structures is the so-called minimal flow unit (MFU) approach [106]. A minimal flow unit is the smallest simulation domain for a given set of parameters, such as Reynolds numbers, containing the essential self-sustaining elements for which turbulence persists. In MFUs, turbulent statistics are spatially correlated, indicating that the entire domain completely experiences the same dynamics. Accordingly, temporally intermittent phenomena can be readily identified by spatial averaging. Thus, the MFU dynamics allow one to concentrate only on the temporal intermittency of turbulence. However, it should be noted that an MFU should

---

[1]This work was published as Davis, E.A., Mirfendereski, S. and Park, J.S., *Fluids*, **6**, 5 (2021)

at least maintain "healthy" near-wall turbulence that reproduces the self-sustaining process and statistical characteristics of full turbulence [62, 158, 98, 99]. In particular, an MFU should be able to contain a single ejection and sweep event by which streamwise streaks and vortices are sustained [161].

In an extended domain, turbulent statistics become less correlated in space and the intermittency becomes both spatial and temporal in nature. In this situation, spatially-averaged statistics could mix information together from different regions, which makes identification of spatiotemporal intermittency difficult to recognize. Moreover, the effects of the computational domain size on turbulent dynamics could be profound [149]. In addition, as the Reynolds number increases, the spatiotemporal intermittency becomes more noticeable [94, 135, 136]. A natural question is how closely the MFU dynamics are related to the spatiotemporal intermittency in a spatially extended domain. This extended domain can be thought of as a more experimentally realizable flow for which no artificial periodicities are imposed [128]. There have been studies to draw the links between minimal-domain temporal intermittency and extended-domain spatiotemporal intermittency for the transitional Reynolds number regime [128, 241], but it has yet to be explored for higher Reynolds numbers until now, which is a focus of the present work.

Prior to proceeding to the present work, we aim to provide a brief description of the minimal flow unit and its potential connection to William W. Willmarth's legacy in turbulent flows. Direct numerical simulations (DNSs) based on minimum flow units have been extensively performed for a variety of purposes, including understanding near-wall turbulent dynamics [185, 174, 182, 263] and flow control [28, 257, 46]. A minimum flow unit involves the periodic computational domain, which has the minimum spanwise length of approximately 100 wall units and the minimum streamwise length of approximately 250–350 wall units [106]. Interestingly, an MFU with the

minimum lengths could capture the turbulence intensity at the near-wall in a turbulent channel experiment performed by Wei and Willmarth [243]. However, lengths too small to accommodate the large-scale structure are likely to result in a statistical abnormality and minimal log layer in a mean velocity [106]. Although the outer portion of the boundary layer might not significantly influence the inner-layer statistics to some extent [108], the influence of the outer layer flow on near-wall flow structures becomes important when there is a significant cancellation in the logarithmic layer. Thus, it is worth noting that the deterioration of near-wall turbulence with narrow MFU domains for higher Reynold numbers could result in the disappearance of the logarithmic region in the mean velocity profile. This situation can be referred to as "unhealthy" turbulence. As mentioned above, ejection and sweep events should be accommodated for valid MFU dynamics. These events could be related to Reynolds stress and coherent structures by means of the so-called quadrant analysis. This approach was advanced by Willmarth and Lu [249, 150, 151, 248]. This quadrant analysis will be employed in the current study to draw connections between MFU dynamics and extended-domain dynamics.

This paper is organized as follows. Section 6.2 presents the problem formulation and numerical details for the current study. In Section 6.3, we present the size of minimal flow units and compare MFU statistics and dynamics to ones for a subdomain of the same size embedded in an extended domain, for which quadrant analysis was employed. Finally, a summary and implications of the present investigation are given in Section 6.4.

6.2   Problem Formulation

We consider a direct numerical simulation (DNS) of an incompressible Newtonian fluid in the plane Poiseuille (channel) geometry, driven by constant volumetric flux Q. The domain was aligned such that the x, y, and z coordinates corresponded to the streamwise, wall-normal, and spanwise directions, respectively. For all DNSs, periodic boundary conditions were imposed in the x and z directions with the maximum wavelengths of L_x and L_z, and a no-slip boundary condition was imposed at the top and bottom walls $y = \pm h$, where $h = L_y/2$ is the channel half-height. However, data analyzed from the extended domain DNS were taken from a sub-domain (SD) which matches the fundamental periods of the MFU, namely, L_x and L_z. An SD was located in the middle of the extended domain to minimize any potential artificial effects of periodic boundaries. The laminar centerline velocity for a given volumetric flux is given by $U_{cl} = (3/4)Q/h$. Using the channel half-height h and the laminar centerline velocity U_{cl} as the characteristic length and velocity scales, the non-dimensionalized continuity and Navier-Stokes equations are given as

$$\nabla \cdot \boldsymbol{u} = 0, \tag{6.1}$$

$$\frac{\partial \boldsymbol{u}}{\partial t} + \boldsymbol{u} \cdot \nabla \boldsymbol{u} = -\nabla p + \frac{1}{Re_c}\nabla^2 \boldsymbol{u}. \tag{6.2}$$

The Reynolds number for the given centerline velocity is defined as $Re_c = U_{cl}h/\nu$, where ν is the kinematic viscosity of the fluid. Inner scales used to non-dimensionalize quantities are the friction velocity $u_\tau = \sqrt{\overline{\tau_w}/\rho}$ and the wall unit $\delta_\nu = \nu/u_\tau$, where ρ is the fluid density and $\overline{\tau_w}$ is the time- and area-averaged wall shear stress. Quantities non-dimensionalized by the inner scales are denoted with the usual superscript "+". The friction Reynolds number is then defined by $Re_\tau = u_\tau h/\nu = h/\delta_\nu$. For the

current simulations, friction Reynolds numbers of $Re_\tau \approx 200, 500, 700,$ and 1000 were considered. For this range of Reynolds numbers, the size of MFUs was $L_x \approx h$ and $L_z \approx 0.75h$, whereas for a typical extended domain, $L_x = 5h$ and $L_z = 3h$ were used. Simulations were performed using the opensource code Channelflow [69].

A numerical grid system was generated on $N_x \times N_y \times N_z$ (in x, y, and z) meshes, where a Fourier–Chebyshev–Fourier spectral discretization was applied to all field variables. The domain sizes used varied depending on the friction Reynolds number, but typical grid spacings used in the streamwise and spanwise directions were $\Delta x^+ \approx 7.5$ and $\Delta z^+ \approx 5$, respectively, for the range of Reynolds numbers studied in the MFUs. The nonuniform Chebyshev spacing used in the wall-normal direction of MFUs resulted in $\Delta y^+_{min} \approx 0.25$ at the wall and $\Delta y^+_{max} \approx 12$ at the channel center for the various Reynolds numbers studied. For the extended domains, streamwise and spanwise grid spacings were close to ones in MFUs. Grid system and resolution parameters are provided in Table 6.1. Note that the wall-normal spacing in the extended domains seems coarser, but it is still the same order as that used in the MFUs and other studies found in high-Reynolds-number literature [149, 135]. A convergence check was also done—spatial resolution was increased and all the quantities reported in the current study were recalculated, yielding negligible changes from the results reported here. Each simulation run is sufficiently long (more than 20,000 h/U_{cl} time units) to ensure meaningful spatiotemporal averages.

The present study provides statistical information about the flow at increasing Reynolds numbers, with the goal of offering insights into the effect of periodic boundary conditions used in minimal flow units on MFU statistics and their connections to statistics of a sub-domain embedded within an extended domain. The sizes of the MFU domain were selected such that "healthy" turbulence was sustained. Healthy turbulence refers to the notion that the statistical properties of a flow are maintained

Table 6.1: A summary of grid systems and resolutions for extended domain and minimal flow unit (MFU) simulations.

Re_τ	N_x	N_y	N_z	Δx^+	$\Delta y^+_{\min}$	$\Delta y^+_{\max}$	Δz^+
200 (MFU)	256 (64)	81 (121)	256 (84)	7.8 (6.2)	0.33 (0.13)	7.8 (6.4)	4.7 (2.2)
500 (MFU)	256 (86)	125 (161)	256 (84)	7.8 (5.2)	0.32 (0.17)	12.6 (8.8)	4.7 (4.0)
700 (MFU)	256 (86)	151 (181)	256 (102)	7.8 (6.9)	0.15 (0.24)	14.7 (12.0)	4.7 (4.7)
1000 (MFU)	256 (96)	191 (181)	256 (140)	7.8 (7.5)	0.14 (0.33)	16.5 (16.9)	6.3 (4.8)

and well represented by fundamental turbulent characteristics, even when using an MFU. Specifically, besides Jiménez and Moin [106], we also refer to healthy turbulence as when the friction Reynolds number saturates to its empirically predicted value and when flow statistics such as mean and fluctuating characteristics agree with those from extended domain simulations and experiments. Overly small domains can cause loss of fidelity in velocity fluctuations that may cause significant differences in flow structures, and subsequently, the statistical behavior of a flow, leading to unhealthy turbulence (see Section 6.3.2 for unhealthy cases).

6.3   Results

6.3.1   Minimal Flow Units up to $Re_\tau = 1000$

In adopting a similar approach to the MFU methodology [255, 240], we fixed the domain length L_x and found the minimal domain width L_z that could sustain the turbulence. However, a larger L_x was sometimes needed if the flow relaminarized even with increasing L_z. As reported in the previous works [106, 149], the minimum spanwise length that sustains turbulence may be associated with an abnormality or unhealthy characteristics in mean velocity profiles, especially for higher Reynolds numbers (see Section 6.3.2 for details). To produce healthy turbulence in an MFU, the minimum domain size, especially in the spanwise direction, is chosen to ensure

that the mean velocity profile collapses reasonably well with the logarithmic profile and that the wall shear stress agrees well with that of the extended domain. Figure 6.1 shows the MFU sizes for each Reynolds number studied. Figure 6.1a shows the maximum streamwise and spanwise wavelengths for each Reynolds number. The wavelengths in both streamwise and spanwise directions appear to increase linearly with Reynolds number. While these values are close to minimal values for sustaining healthy turbulence at these Reynolds numbers, it is possible to use smaller domains. For instance, while not explicitly enforced, the streamwise wavelength for all Reynolds numbers was larger than the spanwise wavelength for all cases. For a range of Reynolds numbers studied, smaller streamwise wavelengths could still allow for sustained healthy turbulence. Moreover, unlike the spanwise wavelength, changing the streamwise wavelength with the spanwise wavelength fixed seems to barely affect the healthiness of the turbulence. However, it should be noted that when the spanwise length $L_z^+ < 0.75 Re_\tau$, it caused MFU dynamics to become unhealthy for the Reynolds numbers studied (see Section 6.3.2 for details). Figure 6.1b shows the resultant area of the domain for each Reynolds number. Since both streamwise and spanwise wavelengths increase approximately linearly with Reynolds number, it is readily seen that the area increases in an approximately quadratic manner.

To ensure the healthiness of turbulent dynamics in MFU and sub-domain (SD) in an extended domain, Figure 6.2 shows a time series of area-averaged wall shear rates for both MFU and SD at each Reynolds number. It is clearly observed that there is good agreement between the two simulations for all Reynolds numbers, as the time series for the MFU and SD are nearly indistinguishable. As such, both mean and fluctuation characteristics agree quite well. To quantify this, the percent difference of the root-mean-square wall shear rates between MFU and SD was calculated. It is shown on the right of Figure 6.2 that for all Reynolds numbers, the percent difference
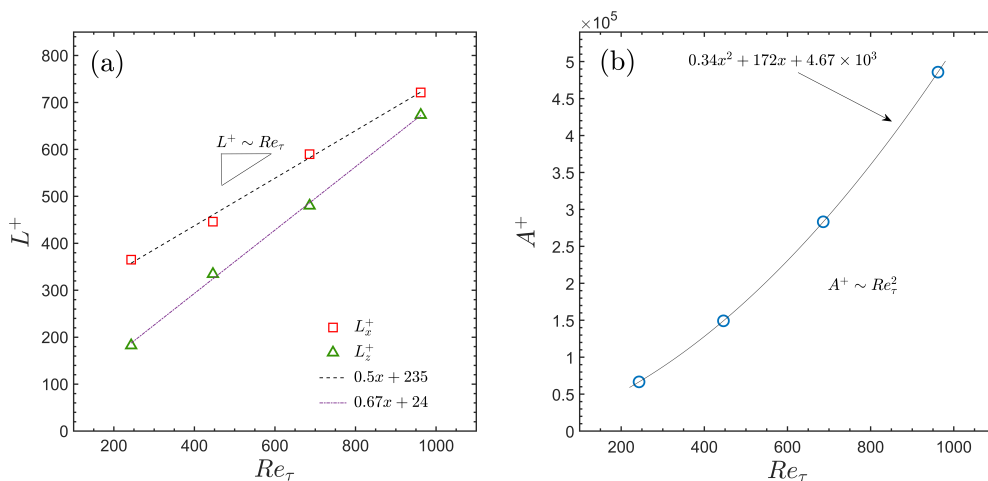
Figure 6.1: (**a**) The maximum streamwise and spanwise wavelengths for minimal flow units as functions of Reynolds number. Lines correspond to a linear fit. (**b**) Corresponding area $A^+ = L_x^+ \times L_z^+$ for each MFU as a function of Reynolds number. As expected, the solid line corresponds to a quadratic fit.
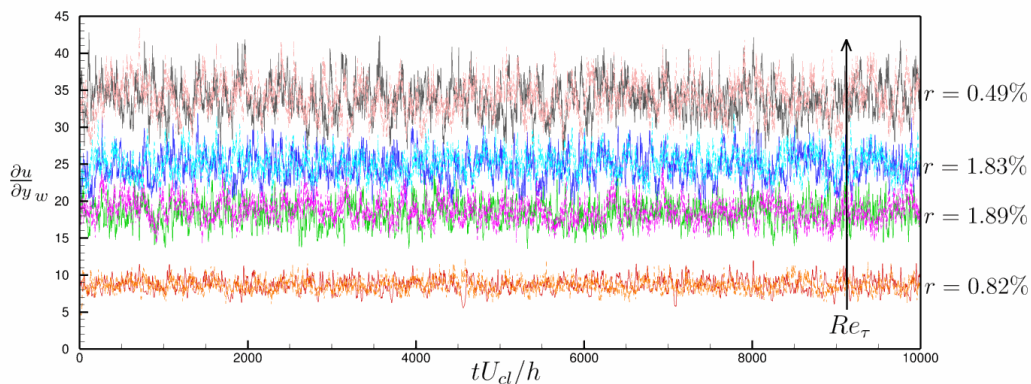
Figure 6.2: Time series of area-averaged wall shear rates for MFU (solid lines) and SD (dashed lines) in an extended domain at $Re_\tau = 200, 500, 700, 1000$. Both time series are nearly indistinguishable, indicating that mean and fluctuation characteristics agree quite well. Note that r is the percent difference of the root-mean-square wall shear rates between MFU and SD.

(r) is less than 2%. It is also shown by power spectral density (not shown) that the most dominant frequencies of the wall shear stress are in good agreement between the MFUs and SDs.
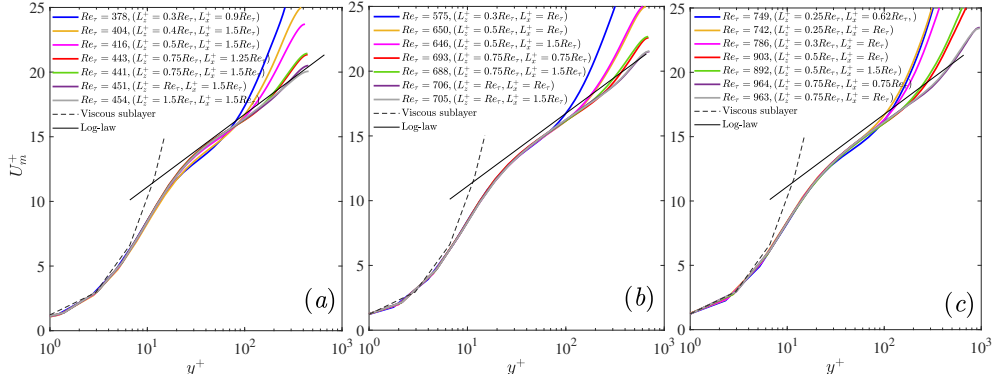
Figure 6.3: Healthy and unhealthy streamwise mean-velocity profiles for MFUs with various values of L_x^+ and L_z^+ at (**a**) $Re_c = 12{,}000$, (**b**) $Re_c = 19{,}800$, and (**c**) $Re_c = 28{,}800$. For these Reynolds numbers, when $L_z^+ < 0.75Re_\tau$, the mean velocity profiles appear to become unhealthy in regard to the logarithmic law.

6.3.2   Healthiness of Minimal Flow Units

For the current MFU simulations, we used the minimum domain size that would sustain healthy turbulence. Figure 6.3 shows the effects of the streamwise and spanwise lengths on mean velocity profiles at $Re_c = 12{,}000$, $Re_c = 19{,}800$, and $Re_c = 28{,}800$. As seen in the figure, the streamwise length did not have a noticeable effect on the mean velocity profile at each Reynolds number. However, the spanwise length did have a significant effect when $L_z^+ < 0.75Re_\tau$. For $L_z^+ \approx 0.75Re_\tau$ at each Reynolds number, the mean velocity profile follows the Prandtl-von Kármán log law and shows a small deviation from the logarithmic profile around the channel center. Thus, it can still refer to healthy turbulence for this spanwise length. Note that for $L_z^+ > 0.75Re_\tau$, a slightly healthier mean velocity is visible around the channel center. It appears to suggest that it is reasonable to choose $L_z^+ \approx 0.75Re_\tau$ as an MFU spanwise length for the Reynolds numbers shown in Figure 6.3 when focusing on near-wall turbulence.

For a decrease in the spanwise length from $L_z^+ \approx 0.75Re_\tau$, however, the MFU turbulence becomes unhealthy, as evidenced by a significant deviation of mean velocity profiles from the log law starting at $y^+ \sim O(100)$. As the spanwise length gets

smaller, a deviation from the logarithmic law gets more severe. This unhealthy turbulence might stem from the fact that the small domain, particularly in the spanwise direction, fails to represent the large-scale coherent structures [149], which results in deteriorated turbulent characteristics despite no sign of relaminarization. However, it is worth mentioning that for Reynolds numbers as small as $Re_c = 6000$ ($Re_\tau \approx 245$), reducing the domain size, particularly in the spanwise direction, is more likely to cause relaminarization [106]. In addition, a smaller domain size also causes an unrealistic reduction of wall shear stress and thus a smaller value of Re_τ for a fixed value of Re_c, as seen in Figure 6.3. By increasing the domain size, especially in the spanwise direction, the unrealistic reduction of wall shear stress can be avoided, which in turn increases Re_τ. Note that a further increase in a domain size from MFU size at a fixed Re_c does not lead to any noticeable change in Re_τ, which confirms the capability of the current MFU domain sizes to produce healthy turbulence. Nevertheless, unhealthy turbulence might be still observed for such small Reynolds numbers within tiny ranges of the spanwise length even with a saturated or correct Re_τ.

6.3.3   Mean Flow Properties

Figure 6.4 compares the mean streamwise velocity profiles for MFUs and SDs from different simulations at various Reynolds numbers. Regardless of Reynolds number or domain size, the profiles collapse agreeably onto the viscous sublayer and logarithmic profiles. Slight bumps are shown at the channel center for all simulations, which are reasonable [149]. One observation to note is the profile for the MFU at $Re_\tau = 200$ within the buffer region ($y^+ \approx 10$–30). It is slightly elevated not only compared to its SD counterpart, but also compared with all larger Reynolds number simulations. While the MFU profile for the rest of the channel agrees reasonably well with its SD counterpart and the log-law profile, similar anomalous behavior has been observed

before in MFUs. It was found that for too small a domain size at $Re_\tau = 950$, a bump in a mean velocity profile was present near the channel center [104], and statistics above $y \approx L_z/3 \approx 0.25h$ were incorrect [62]. This resulted in an accelerated flow near the core of the flow. As the weak anomalous behavior in the present study was observed in the buffer layer at $Re_\tau = 200$, it may suggest that the domain size was too small to capture dynamics reliably. Additionally, the observed anomaly in the previous study was at a significantly larger Reynolds number [149]. To further test the log-law behavior, the inset in Figure 6.4 shows the diagnostic function of Ξ^+:

$$\Xi^+ = y^+ \frac{\partial U_m^+}{\partial y^+},\tag{6.3}$$

which becomes constant and equal to the inverse of the von Kármán constant κ if the mean velocity profile displays a logarithmic layer. Aside from the obvious $Re_\tau = 200$ case, there are plateaus over a range within the log-law region, exhibiting logarithmic behavior. While the MFU diagnostic function near the core deviates from the SD values, there is good agreement between the two in the logarithmic region of the flow, suggesting MFU captures the mean behavior of the flow reasonably well. It should also be noted that despite a slight discrepancy in the log-law slope of $1/\kappa$, the von Kármán constant values are still within the reported range of 0.38–0.41 [213, 149, 135].

Figure 6.5 presents the mean-squared velocity fluctuations at the channel center. This quantity gives statistical information on the strength of velocity fluctuations at the core of the flow, which can also be used to compare differences in behavior between MFU and SD. The fluctuations at the centerline for MFU and SD are in good agreement for all Reynolds numbers. These values are also in good agreement with values shown by Lozano-Durán and Jiménez [149]. However, differences between MFU and SD are seen at low Reynolds numbers again, perhaps because the smaller
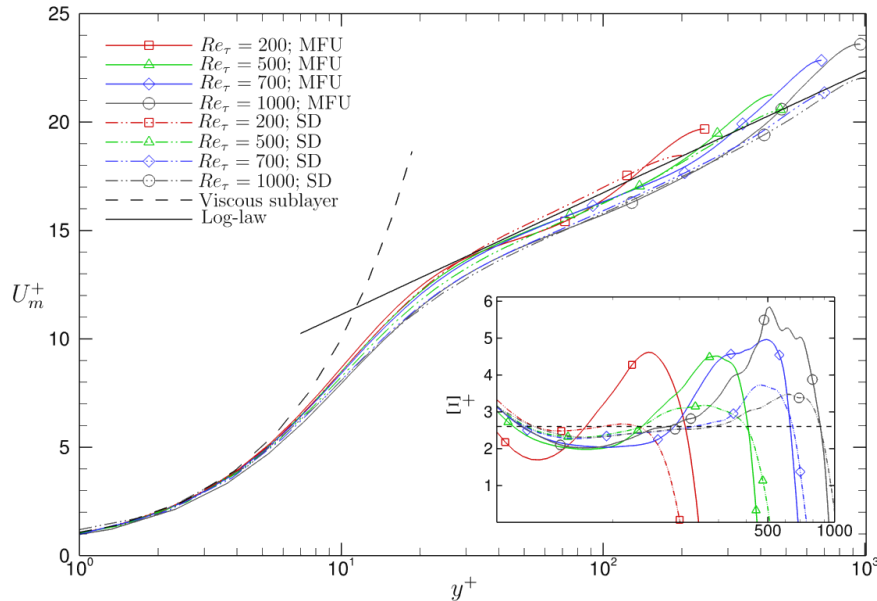
Figure 6.4: Mean velocity profiles for minimal flow units (MFU) and sub-domains (SD) for various Reynolds numbers along with the viscous sublayer and logarithmic law. Inset: Log-law diagnostic function Ξ^+. The dashed horizontal line is $1/\kappa$, where κ is the von Kármán constant and $\kappa = 0.384$.

domain size is too small to capture dynamics reliably. In addition, differences between the current study and Lozano-Durán and Jiménez (2014) could result from the same reason.

6.3.4   Quadrant Analysis

Willmarth and Lu pioneered the use of Reynolds shear stress to describe the structure of turbulence in wall-bounded flows [249]. They utilized the so-called u'-v' plane to shed light on the notion of turbulent bursts, or short, infrequent spikes in turbulent kinetic energy observed in turbulent flows. This same style of analysis was applied here using joint probability density functions (JPDF) of the distributions of streamwise and wall-normal velocity fluctuations. Shown in Figure 6.6 are the JPDFs for the MFU and SD at each Reynolds number. These values were taken at a wall-normal
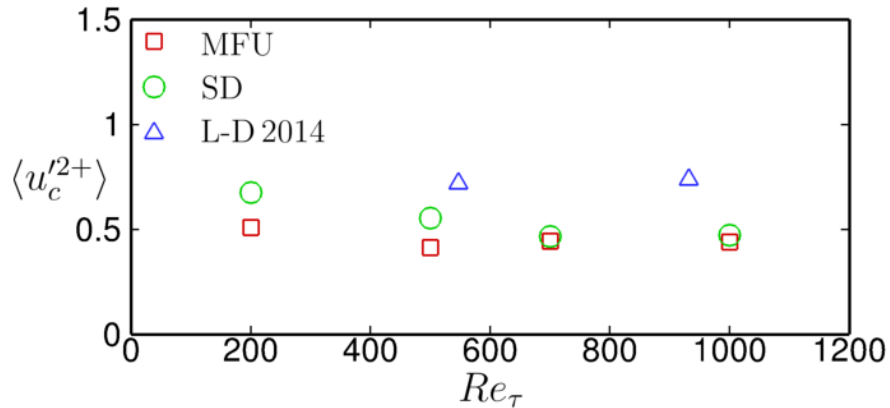
Figure 6.5: Mean-squared velocity fluctuations of minimal flow units (MFU) and sub-domains (SD) at the channel center for various Reynolds numbers. $\triangle$ are values obtained from Lozano-Durán and Jiménez [149] for larger domain simulations (L-D 2014).

plane at $y^+ \approx 30$.

Overall, the shapes and levels of the distributions are in good agreement among the MFUs and SDs for all Reynolds numbers, showing almost no differences. This strongly suggests that MFU near-wall dynamics capture SD near-wall dynamics quite well. The majority of events occurred in quadrants Q2 and Q4, corresponding to ejections and sweeps, respectively, as was to be expected [7, 235]. As the Reynolds number was increased, the distribution spread outward, and larger fluctuations were observed, which was also to be expected. For lower Reynolds numbers, it appears that the flow experienced more frequent and larger fluctuations along the negative u'-axis for MFU simulations. This is especially apparent for the MFU case at $Re_\tau = 200$, as there is a "tail" that formed in the Q2 quadrant corresponding to large negative u' fluctuations and small positive v' fluctuations. This same structure is not present in the JPDF in the SD data at $Re_\tau = 200$. This is in agreement with the trend seen in Figure 6.4 for the MFU at $Re_\tau = 200$, which resulted in a larger mean velocity. This discrepancy at $Re_\tau = 200$ could be explained by the fact that as the length scale of small-scale motions was found to be about 1000 wall units, an

Figure legend values (panel a):

14	0.14
13	0.13
12	0.12
11	0.11
10	0.1
9	0.09
8	0.08
7	0.07
6	0.06

MFU
SD
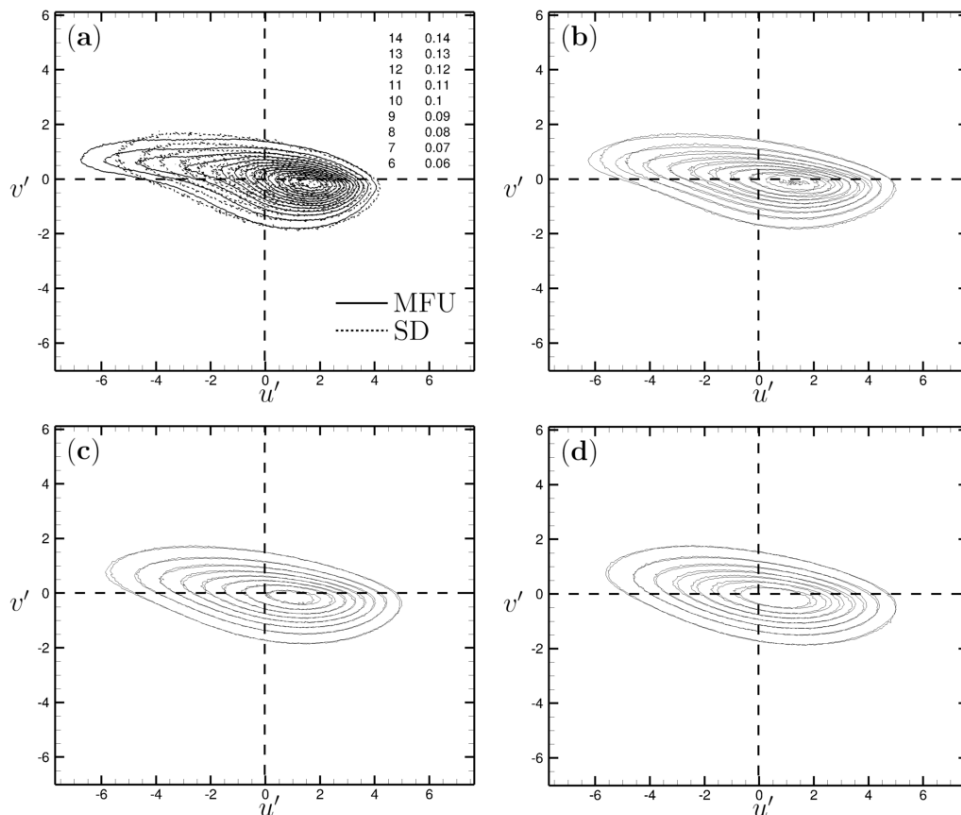
Figure 6.6: Contours of joint probability density functions for streamwise and wall-normal velocity fluctuations in a wall-normal plane at $y^+ \approx 30$ for MFUs (solid lines) and SDs (dashed lines) in an extended domain. Values were normalized by their respective friction velocities. $Re_\tau =$ (**a**) 200, (**b**) 500, (**c**) 700, and (**d**) 1000.

MFU domain was not sufficiently large to capture these small-scale motions at this Reynolds number [137]. For $Re_\tau = 700$ and 1000, however, the difference between the distributions of MFUs and SDs is negligible, as seen in Figure 6.6c,d, suggesting that MFU dynamics represent large-domain dynamics well up to $Re_\tau = 1000$.

6.4 Discussion

In this study, the effect of domain size on statistical behavior in a minimal flow unit (MFU) with periodic boundary conditions was investigated by direct numerical simulations up to $Re_\tau = 1000$. To accomplish this, the statistics from the MFU were

compared with statistics from a sub-domain (SD) of the same dimensions as the MFU in an extended domain simulation. MFU dimensions were found by increasing the streamwise and spanwise dimensions until turbulence was maintained and Re_τ saturated to its empirically predicted value. As one might expect, the minimal domain size necessary to meet these conditions increases with Reynolds number. Both streamwise and spanwise dimensions increase linearly with Reynolds number, and thus, the planar area increases in a quadratic manner. It was also found that when the spanwise length $L_z^+ < 0.75 Re_\tau$, MFU dynamics tended to become unhealthy for Reynolds numbers studied (see Figure 6.3).

Overall, there was good agreement between the wall shear rate dynamics and mean velocity profiles of MFU and SD simulations. Both MFU and SD profiles collapsed well onto the viscous sublayer and log-law profiles. These findings suggest that healthy MFU dynamics could represent more realistic extended-domain dynamics. The mean-squared streamwise velocity fluctuations at the centerline were also in good agreement, with MFU values slightly lower than their SD counterparts at lower Reynolds numbers. The values are slightly lower than those observed in previous extended domain simulations but are still agreeable [149].

A non-trivial finding was an observation that despite meeting these criteria for MFU (i.e., sustained turbulence and saturation of Re_τ), a simulation may still offer incorrect statistics in the bulk of the flow. While the behavior of the area-averaged wall shear rate was in great agreement for both MFU and SD, the mean velocity profile could still be incorrect. At $Re_\tau = 200$, this could be observed by the increase in the mean velocity profile in the buffer region of the MFU compared with all other simulations. There was also a distinct "tail" in the Q2 quadrant of the u'-v' JPDF, which was absent in the SD of extended domain simulations. This suggests that some additional criteria should be put in place to ensure healthy flow statistics when using

MFUs. A detailed analysis should be a subject of future work.

Another future direction of the current work should consider the effect of turbulent flow control methods on the allowable MFU. These methods are known to reduce the wall shear stress, and increase the probability of laminarization. Therefore, it is most likely that the MFU for these simulations would be larger than that of uncontrolled simulations. Different criteria may be needed to ensure healthy turbulence is achieved.

Chapter 7

CONCLUDING REMARKS AND FUTURE DIRECTIONS

7.1 Concluding remarks

This dissertation focused broadly on understanding underlying mechanisms behind wall-bounded turbulent flows, with an emphasis on exploiting those mechanisms for turbulence flow control. This chapter recapitulates the main findings and future directions from each research chapter.

7.1.1 On the transition to turbulence and slip surfaces

Via direct numerical simulations, the effect of slip surfaces (i.e., surfaces facilitating a nonzero velocity at the fluid-surface interface) on the laminar-turbulent transition was investigated. Turbulence lifetime analysis (i.e. the probability that turbulence will persist) was investigated for transitional flows at $Re_c = 1600, 1800,$ and 2000 ($Re_\tau = 77$, 85, and 93). Flows with slip surfaces were significantly less likely to maintain turbulence compared to the no-slip case. Additionally, the slip flows were more likely to laminarize at earlier times as slip length is further increased. As Reynolds number is increased, this trend still holds, while a larger slip length is needed to obtain the same likelihood of laminarization found at lower Reynolds numbers. Phase-space projection of transitional trajectories on the energy input and dissipation

rates showed a reduced distance between the laminar and turbulent states, which helps explain the increased likelihood of laminarization due to slip surfaces.

Exact coherent solutions, specifically nonlinear travelling wave solutions, to the Navier-Stokes equations were used to investigate the effects of slip surfaces on the laminar-turbulent separatrix. The P3 and P4 solution families were chosen as their lower-branch solutions are shown to lie on the basin boundary between laminar and turbulent flow [182]. The skin-friction evolution and linear growth rate from the lower-branch solutions were calculated. For slip flows, the strong turbulent burst associated with the P3 lower-branch solution was induced at earlier times while the bursting magnitude and growth rate were mostly unaffected. For the P4 solution, however, the strong turbulent burst was delayed with the reduced magnitude and growth rate for slip flows. Beyond a critical slip value, the turbulent burst was completely eliminated as a flow is immediately laminarized after a short stable period. Effects of slip surfaces on vortex structures of the P3 and P4 solutions were examined to elucidate mechanisms responsible for the difference in transition behaviours between the solutions. It appears that structures associated with the P3 solution were largely unaffected by the slip surfaces. Overall structure and strength remained relatively constant. However, the strength of P4 vortex structures was weakened by $\sim 50\%$, and they were shifted away from the wall.

Based on the quadrant analysis and spatiotemporal dynamics, it was suggested that slip surfaces promote the prevalence of strong wall-toward motions (Q4-like events) in the area of the P3 vortex cores close to the channel centre. This results in instability, which promotes the propagation of the vortex structures down into the wall where they break up and induce transition, similar to the bypass transition [197]. However, sustained ejection events (Q2) were present in the region of the P4 vortex cores (which resemble the Λ-shaped structures in H- and K-type transitions) resulting

in a shift of the vortex structures away from the wall allowing them to remain intact and propagate downstream for a longer time. It can be suggested that the slip surfaces tend to affect core-mode structures (P3 solution) or non-modal perturbations via inward interactions (Q3) near the wall and wall-toward motions (Q4-like events) near the channel centre, subsequently leading to bypass-type early transition. On the other hand, the slip surfaces tend to affect critical-layer structures (P4 solution) or modal perturbations via ejection events (Q2) near the wall and wall-away motions (Q1-like events) near the channel centre, subsequently leading to H- and K-type delayed transition. These distinct transition dynamics of the P3 and P4 solutions due to slip surfaces could suggest that different flow control techniques could be used to delay or promote a transition to turbulence, which will be a subject of interesting future work.

7.1.2   On the decay of turbulence and slip surfaces

The decay from turbulence to laminar was studied via the time-evolution of the magnitude of the disturbance velocity in the streamwise, wall-normal, and spanwise directions. Using a quench protocol, where the Reynolds number is suddenly decreased, a turbulent state was allowed to decay to the laminar state. For random turbulent initial conditions, the decay rates increased with decreasing final Reynolds number. As observed in previous plane Poiseuille and Couette-Poiseuille flows [76, 148], the energy in the spanwise direction was found to decay faster than the streamwise energy. This was attributed to differing decay characteristics of streamwise streaks and spanwise rolls in the self-sustaining process [231]. Specifically, the waviness of the streaks is reduced initially which causes fast decay of the spanwise rolls followed by a slower decay of the straightened streaks [148]. The results here corroborate those found in previous studies.

The effect of non-zero slip at the wall on the decay of random turbulent initial conditions was also analyzed. The inclusion of slip at the boundaries causes the decay rate to change depending upon the final Reynolds number. For $Re_f = 1000$, the slip surfaces appear to increase the initial decay rate in all three directions. After this initial decay stage, the decay rates saturate and are similar among all slip lengths. For final Reynolds number below $Re_f = 1000$ studied here, the wall slip had no observable effect on the decay rates. That wall slip is ineffectual at these final Reynolds numbers may be related to the fact that these Reynolds numbers are close to and below the critical Reynolds number $Re_g \approx 700$ where turbulence cannot persist [209, 179]. Flow structures shown via disturbance velocity at a wall-normal plane of $y^+ = 12$ showed the same trends. The streamwise structures persisted for longer than either spanwise or wall-normal directions. One indication as to the mechanism behind the increased decay rate for the slip surfaces may be that, for the slip cases, the "waviness" in the streamwise streaks discussed by Liu et al. [148] appears to be reduced faster. According to the process they put forward, this straightening of the streamwise streaks would allow for an earlier decay of the spanwise rolls. A more detailed investigation into the flow structures should be performed.

Additionally, the decay of exact coherent solutions was analyzed. Similar to observations in Section 2.4.3, the P3 and P4 upper-branch solutions were found to display distinct decay characteristics. Unlike the behavior observed in the decay of random initial conditions, the P3 solution exhibited a similar initial decay rate of the streamwise and spanwise velocity perturbation magnitude before entering a second stage where the spanwise decay rate was slower than the streamwise decay rate. This trend held for quench Reynolds number $Re_f = 800, 1000$ but not for $Re_f = 600$. It is interesting as $Re_f = 600$ is below the critical Reynolds number where turbulent spots were found to decay, $Re_g \approx 700$ [22, 179, 209, 49]. However, the decay of the spanwise

disturbances was faster than the streamwise disturbances for the P4 solution at early time, $\mathcal{O}(10tU_c/h)$. Decay rate increased with decreasing Re_f. The addition of wall slip had negligible effect on the decay behavior for both the P3 and P4 solutions.

The decay of the turbulent trajectories and the P3 and P4 solutions was also analyzed using a dynamical systems approach. The dynamics of the high-dimensional system were projected onto the energy input-dissipation plane. Through this lens, the behavior observed in the evolution of these trajectories becomes more understandable. For the random initial conditions, the system is attracted to lower-branch solutions as it decays to the laminar state, even passing through the P3 lower-branch solution in some cases. This is significant, as the P3 lower-branch solution is an edge state, with only one unstable direction. There was also some interaction with the P4 lower-branch solution. As Reynolds number decreases (i.e., $Re_f < Re_g \approx 700$), the system has almost no interaction with any of the exact coherent solutions, and instead does directly to the laminar state, as it is the global attractor due to the linear instability of other solutions. This behavior is consistent with previous studies done in the plane-Couette and Taylor-Couette geometries [188]. Therefore, one possible explanation for the increase in decay rate with the decrease in final Reynolds number may be that the system has less significant interactions with other solutions, and instead directly approaches the laminar attractor.

For the decay of the P3 and P4 solutions, there were rich and distinct dynamics, seemingly orchestrated by the other exact coherent solutions. For the P3 solution at $Re_f = 800$, periodic behavior emerged with the inclusion of wall slip, and the system passed through the P3 lower-branch solution before laminarizing. The P4 solution exhibited much simpler dynamics, mostly avoiding interaction with any of the other exact coherent solutions and directly approaching the laminar state. The dynamical systems perspective gives much insight into the dynamics of the turbulent-to-laminar

transition.

While the decay characteristics of the flow in [148] were unaffected by various noise levels, spanwise rolls in the final state after transient decay were found to be susceptible to noise. This type of analysis could be performed in the future using a more statistically significant amount of initial conditions, ranging in initial turbulence intensity, to analyze the effect of initial condition (i.e. noise) on the decay characteristics of the flow. From the 10 initial conditions studied here, initial turbulence intensity seems to have an effect on the initial behavior of a trajectory, but the decay rates after this transient period appear to be consistent. Additionally, fields from the laminar state could be subjected to perturbations to assess the susceptibility of the final state to noise, and whether the system returns to a transient turbulent state.

Future work should also include further analysis of the mechanisms responsible for the difference in decay rate for varying final Reynolds number, possibly by analyzing the time-evolution of the streamwise and spanwise flow structures during decay. This work contributes to a framework for understanding the transition to and from turbulence, as well as the self-sustaining process of wall-bounded turbulence flow which can be used to inform more efficient future control techniques. Specifically, the use of exact coherent solutions to the Navier-Stokes equations offers a more deterministic view of control methods on the self-sustaining process and transition to turbulent.

7.1.3 Composite drag reduction of slip surfaces and polymer additives

We performed direct numerical simulations of channel flows to investigate the composite drag reduction of slip surfaces and dilute polymer solutions. The two individual methods worked in tandem to provide a synergistic, or additive, drag reduction effect. By investigating the mean velocity profiles and Reynolds shear stress profiles, it was determined that the mechanisms responsible for the success of each individual

method are distinct and have minimal interaction with each other. While the slip surfaces work to shift the velocity profile upward near the wall, the polymers work to reduce the Reynolds shear stress in the bulk of the flow. Quadrant analysis [249] should be performed to gain further insight into possible mechanisms responsible for the altered mean behavior of the flow. These control methods undoubtedly have an impact on the self-sustaining process, which would manifest itself as reduced sweep and ejection events that could be observed in quadrant analysis.

An analysis of the the turbulent kinetic energy (TKE) and the rate at which kinetic energy converted to elastic energy (E) was performed. For all slip lengths, the TKE reaches a peak for $Wi \approx 30$ before monotonically decreasing. This Weissenberg number coincides with the Weissenberg number where the drag reduction begins to level off and approach the maximum drag reduction (MDR). The rate at which kinetic energy is converted to elastic energy increases sharply at low Weissenberg numbers, corresponding the increase in flexibility of the polymers. After $Wi \approx 30$ this value levels off and appears to approach some asymptote. Again, this trend and value of Weissenberg number corresponds to that observed in the drag reduction and TKE. A more thorough investigation into the energy budget of the composite drag reduction is necessary. The turbulent kinetic energy in each spatial direction should be analyzed to determine where the reduction in turbulence energy is occurring. Additionally, a similar investigation into the elastic energy associated with with the polymers should be performed. It is believed that further investigation of the polymer dynamics, afforded by the conformation tensor α, would contribute considerable insight into the mechanisms responsible for the observed behavior.

Finally, the mean state of the system was projected onto the energy Input-Dissipation plane. This showed that the control methods reduce the distance between the mean state of the flow and the laminar state. It also showed that this distance

appears to reach some asymptote which coincides with the asymptotic approach observed in the drag reduction and rate of conversion into elastic energy. It is possible that the MDR manifests as some surface in state space which prevents the mean state of the system from being altered any further by the action of polymers, alone. A good choice of state variables may offer a better description of this hypothetical surface.

A limitation of the current study is that only one polymer concentration was considered. Further work should be performed to investigate the effect of polymer concentration on the achievable drag reduction, as it may offer further insights into the mechanisms responsible for the drag reduction and the differences observed by Rajappan and Mckinley [192] between empirically observed and empirically derived drag reduction values. Rajappan and Mckinley [192] also observed that the drag reduction decreased after a critical polymer concentration, resulting from increased shear viscosity and, subsequently, increased viscous dissipation.

An vital study moving forward would be to look into the conditionally sampled flow fields, where the condition admits periods in the turbulent trajectory which are characterized by low wall shear rate. Previous work in this area [80] has gained great insight into the mechanisms behind drag reduction when performing temporal analysis on the turbulent trajectories of polymer drag-reduced turbulent flows.

Future work should also consider the effect of non-ideal slip. The current study considers only a homogeneous, streamwise slip. A more realistic natural surface would, indeed, have slip in both the streamwise and spanwise directions. With advancements in surface fabrication techniques, a multitude of functionalized surfaces can be manufactured which take advantage of various material properties to control surface wetting phenomena [216, 269, 60, 143, 63, 141]. Therefore, modeling of surfaces which display time-varying slip is of much interest for the control of turbulent flows. This is the focus of ongoing and future work.

7.1.4 Characterizing low-drag events in wall-bounded turbulent flows

This work sought to characterize the intermittent phenomena known as low-drag events (LDEs) for moderate Reynolds number. While this has been studied for transitional Reynolds numbers, $Re_\tau < 250$, the analysis has not been extended to higher Reynolds number flows. Using both direct numerical simulations (DNS) and stereoscopic particle image velocimetry (SPIV), we compared the temporal characteristics of LDEs at $Re_\tau = 700$.

Because wall shear stress measurements were unavailable with the current experimental setup, a relationship between the wall shear stress and streamwise velocity at some wall-normal distance had to be probed. It was found that the signals of area-averaged streamwise velocity at $y^+ \approx 28$ and area-average wall shear rate from the DNS data are highly correlated, with a correlation coefficient of ~ 0.8. Exploiting this relationship, the characteristics of LDEs were compared for those events found via wall shear rate and those found via streamwise velocity. Overall, the distributions of the LDE duration were in good agreement. The velocity-wall shear relationship was also compared by conditionally sampling the two fields using LDE detection criteria. Joint probability density functions for the wall shear rate and streamwise velocity of the DNS data show the reduction in streamwise velocity during LDEs detected using wall shear rate. The reciprocal behavior is observed when LDEs are detected using streamwise velocity. Velocity fluctuations in all three directions are reduced slightly during LDEs.

The distribution of LDE duration was compared for the DNS and SPIV data. While the DNS data admitted much longer events, as evidenced by the probability density function, the trend between the DNS and SPIV data was still consistent. Overall, there is good agreement between the two data sets when considering dis-

tribution of LDE duration. The discrepancy between the two data sets most likely manifests due to the much smaller sample size for the SPIV data. The longest event detected in the SPIV data is $\Delta t^+ \approx 275$ while the longest event detected for the streamwise velocity DNS data is an order of magnitude larger, $\Delta t^+ \approx 2900$. If a larger sample size were obtained for the SPIV data, it is believed that the two distributions would match more closely. It is also possible that the lower resolution and accuracy of the SPIV data plays some role in the lower detection rate.

Preliminary results on Reynolds number scaling of the duration of LDEs show that the fraction of time spent in LDEs increases with respect to Reynolds number using both inner units and mixed units. This result is reflected in the probability density function of the duration of LDEs for the various Reynolds numbers studied here. These results disagree with those observed by Whalley et al. [247] and Agrawal et al. [3], previously. The current results would suggest that there are more frequent LDEs and longer LDEs as Reynolds number is increased. There is also the possibility, evidenced by Figure 5.12, that the fraction of time spent in LDEs approaches some asymptote with increasing Reynolds number. These trends must be verified, and the Reynolds number scaling on the temporal characteristics of low-drag events is the focus of ongoing research.

The spatial locality of these events requires further investigation, as well. The interrogation window for the current study in inner units was 1000×600 for the streamwise and spanwise directions, respectively. The size of this area affects the ability to detect LDEs, as the detection method uses area-averaged wall shear rate, based on the assumption from previous studies that the entire domain should be experiencing the event. However, as domain sizes are extended, these events become spatially-localized. Therefore, area-averaged values mix information from areas of the domain that may be experiencing distinct spatially-localized dynamics. Future

work aims to more accurately describe the spatial characteristics of these events by identifying individual events in extended flow fields and investigating the efficacy minimal flow units at moderate Reynolds numbers. Chapter 3 suggests that certain constraints must be placed on the smallest domain size to ensure valid dynamics. Reynolds number scaling on the spatial characteristic of these events is also ongoing.

In turbulent flow control, a challenge lies in finding descriptive state variables for the system. This study shows that other variables (i.e., streamwise velocity) may be used as proxies for wall shear stress, which is a commonly used state variable in wall-bounded turbulent flows. These proxies may then be used for state estimation and control. This has important implications for high Reynolds number, industrial-scale flows where wall shear stress measurements are inaccurate or altogether unavailable.

7.1.5 The efficacy of minimal flow units for "healthy" turbulence

In this study, the effect of domain size on statistical behavior in a minimal flow unit (MFU) with periodic boundary conditions was investigated by direct numerical simulations up to $Re_\tau = 1000$. To accomplish this, the statistics from the MFU were compared with statistics from a sub-domain (SD) of the same dimensions as the MFU in an extended domain simulation. MFU dimensions were found by increasing the streamwise and spanwise dimensions until turbulence was maintained and Re_τ saturated to its empirically predicted value. As one might expect, the minimal domain size necessary to meet these conditions increases with Reynolds number. Both streamwise and spanwise dimensions increase linearly with Reynolds number, and thus, the planar area increases in a quadratic manner. It was also found that when the spanwise length $L_z^+ < 0.75 Re_\tau$, MFU dynamics tended to become unhealthy for Reynolds numbers studied (see Figure 6.3).

Overall, there was good agreement between the wall shear rate dynamics and

mean velocity profiles of MFU and SD simulations. Both MFU and SD profiles collapsed well onto the viscous sublayer and log-law profiles. These findings suggest that healthy MFU dynamics could represent more realistic extended-domain dynamics. The mean-squared streamwise velocity fluctuations at the centerline were also in good agreement, with MFU values slightly lower than their SD counterparts at lower Reynolds numbers. The values are slightly lower than those observed in previous extended domain simulations but are still agreeable [149].

A non-trivial finding was an observation that despite meeting these criteria for MFU (i.e., sustained turbulence and saturation of Re_τ), a simulation may still offer incorrect statistics in the bulk of the flow. While the behavior of the area-averaged wall shear rate was in great agreement for both MFU and SD, the mean velocity profile could still be incorrect. At $Re_\tau = 200$, this could be observed by the increase in the mean velocity profile in the buffer region of the MFU compared with all other simulations. There was also a distinct "tail" in the Q2 quadrant of the u'-v' JPDF, which was absent in the SD of extended domain simulations. This suggests that some additional criteria should be put in place to ensure healthy flow statistics when using MFUs. A detailed analysis should be a subject of future work.

Another future direction of the current work should consider the effect of turbulent flow control methods on the allowable MFU. These methods are known to reduce the wall shear stress, and increase the probability of laminarization. Therefore, it is most likely that the MFU for these simulations would be larger than that of uncontrolled simulations. Different criteria may be needed to ensure healthy turbulence is achieved.

7.2   Significance of the dissertation

With the varied studies detailed herein, the main motivation behind this work was to better understand the underlying mechanisms of wall-bounded transitional and turbulent flows through the implementation of various flow control methods. The hope is that by applying various flow control techniques, which work to alter flow dynamics in distinct manners, the underlying mechanisms responsible for the transition to turbulence and the self-sustaining process of turbulence become clearer and can be used to develop reduced-order models and more informed flow control techniques for more efficient systems in the future.

Along the way, various questions related the efficacy of simulations, data-driven analysis techniques, and application of dynamical systems theory arose. These questions have blossomed into their own studies, with the hope that they expand the literature, help lead to answers of long-standing questions about the behavior of transitional and turbulent flows, and elicit new questions from future researchers.

The major contributions from this work are as follows: (1) the broadening of understanding related to the mechanisms which cause the transition to and decay from turbulence via statistical and (newly developed) deterministic methods, (2) new knowledge related to the efficacy of certain simulation methods (i.e. Minimal Flow Units) used in wall-bounded turbulent flows, (3) characterization of intermittent flow dynamics at higher Reynolds number which may be useful in developing better-informed drag reduction methods and reduced-order models of turbulent flows, and (4) the efficacy of composite drag reduction techniques to overcome the difficult task of drag reduction in large-scale systems.

Appendix A

Details of the numerical procedure

This appendix provides details of the direct numerical simulation (DNS) of flow over slip surfaces and viscoelastic flows using the *ChanneFlow* package, developed and maintained by Gibson [69]. This C++ code uses spectral spatial discretization (Fourier × Chebyshev × Fourier), finite-differencing in time, and primitive variables (i.e., velocity and pressure) to integrate the incompressible Navier-Stokes equations forward in time. This is performed in periodic, rectangular, wall-bounded domain (i.e., channel geometry). The mathematics are derived from the Section 7.3 of *Spectral Methods in Fluid Dynamics* [26]. For complete details and a guide, see Gibson [69].

A.1 Incompressible Navier-Stokes equations

The governing equations for mass and momentum conservation are restated below:

$$\nabla \cdot \boldsymbol{u} = 0, \tag{A.1}$$

$$\frac{\partial \boldsymbol{u}}{\partial t} + \boldsymbol{u} \cdot \nabla \boldsymbol{u} = -\nabla p + \nu \nabla^2 \boldsymbol{u}. \tag{A.2}$$

Here, the numerical algorithm used to solve the Navier-Stokes equations A.1 &

A.2 is discussed. The primitive variables, velocity and pressure, can be decomposed into the sum of a base and fluctuating component:

$$\mathbf{u}(\mathbf{x}, t) = U(y)\mathbf{e}_x + \mathbf{u}'(\mathbf{x}, t) \tag{A.3}$$

$$p(\mathbf{x}, t) = \Pi_x(t)x + p'(\mathbf{x}, t) \tag{A.4}$$

$$\nabla p(\mathbf{x}, t) = \Pi_x(t)\mathbf{e}_x + \nabla p(\mathbf{x}, t) \tag{A.5}$$

where the base velocity profile $U = U(y)$ is chosen as that of the laminar plane Poiseuille flow – $U(y) = 1 - y^2$ – and the walls are located at $y = \pm 1$. Equations A.3 and A.5 can then be substituted into A.2 to yield

$$\frac{\partial \boldsymbol{u}}{\partial t} + \nabla p = \nu \nabla^2 \mathbf{u}. - \mathbf{u} \cdot \nabla \mathbf{u} + \left[\nu \frac{\partial^2 U}{\partial y^2} - \Pi_x \right] \mathbf{e}_x \tag{A.6}$$

ChannelFlow has the option to implement the nonlinear term $\mathbf{u} \cdot \nabla \mathbf{u}$ using the convection form, divergence form, skew-symmetric form, rotational form, and alternating form. The current work used the alternating form, which alternates between the convection form $\mathbf{u} \cdot \nabla \mathbf{u}$ and divergence form $\nabla \cdot (\mathbf{u}\mathbf{u})$ on successive timesteps. This acts to simulate the skew-symmetric form, which is more robust against errors in the high spatial frequencies. Alternating form is as well-behaved at the skew-symmetric and almost as fast as the rotational form, the least expensive of the forms. For more details on the form of the nonlinear term, see [268].

We can simplify Equation A.6 by defining new notation:

$$\mathbf{N} \equiv \mathbf{u} \cdot \nabla \mathbf{u} \tag{A.7}$$

$$\mathbf{Lu} \equiv \nu \nabla^2 \mathbf{u} \tag{A.8}$$

$$\mathbf{C} \equiv \left[\nu \frac{\partial^2 U}{\partial y^2} - \Pi_x \right] \mathbf{e}_x \tag{A.9}$$

Then, Equation A.6 becomes

$$\frac{\partial \mathbf{u}}{\partial t} + \nabla p = \mathbf{L}\mathbf{u} - \mathbf{N} + C \tag{A.10}$$

This equation is then Fourier-transformed. The Fourier-transformed operators are

$$\tilde{\nabla}_{k_x k_z} \triangleq 2\pi i \frac{k_x}{L_x} \mathbf{e}_x + \frac{\partial}{\partial y} \mathbf{e}_y + 2\pi i \frac{k_z}{L_z} \mathbf{e}_z, \tag{A.11}$$

$$\tilde{\nabla}^2_{k_x k_z} \triangleq \frac{\partial^2}{\partial y^2} - 4\pi^2 \left(\frac{k_x^2}{L_x^2} + \frac{k_z^2}{L_z^2} \right) \tag{A.12}$$

$$\tilde{L}_{k_x k_z} \triangleq \nu \tilde{\nabla}^2_{k_x k_z} \tag{A.13}$$

resulting in the Fourier-transform of Equation A.6

$$\frac{\partial \tilde{\mathbf{u}}}{\partial t} + \tilde{\nabla}\tilde{p} = \tilde{\mathbf{L}}\tilde{\mathbf{u}} - \tilde{\mathbf{N}} + \tilde{\mathbf{C}} \tag{A.14}$$

where $\sim$ denotes variables in Fourier space in the x and z directions, and in physical space in the y direction.

A 3rd-order semi-implicit Adams-Bashforth/backward-differentiation scheme is used for temporal discretization. Linear terms, $\tilde{\mathbf{L}}\tilde{\mathbf{u}}$ and $\tilde{\nabla}\tilde{p}$, are discretized using the implicit backward-differentiation method, while the nonlinear term, $-\tilde{\mathbf{N}}$ is discretized with the explicit Adams-Bashforth method. The discretized time-stepping equation is given by:

$$\frac{1}{\Delta t} \left(\eta \tilde{\mathbf{u}}'^{,n+1} + \sum_{j=0}^{k-1} a_j \tilde{\mathbf{u}}'^{n-j} \right) = \sum_{j=0}^{k-1} b_j \left(-\tilde{\mathbf{N}}^{n-j} \right) + \tilde{\mathbf{L}}\tilde{\mathbf{u}}'^{,n+1} + \tilde{\mathbf{C}} - \tilde{\nabla}\tilde{p}'^{,n+1} \tag{A.15}$$

Table A.1: Coefficients for the Adams-Bashforth/Backward-differentiation temporal discretization scheme for various orders-of-accuracy.

Order	η	a_0	a_1	a_2	a_3	b_0	b_1	b_2	b_3
1	1	-1				1			
2	3/2	-2	1/2			2	-1		
3	11/6	-3	3/2	-1/3		3	-3	1	
4	25/12	-4	3	-4/3	1/4	4	-6	4	-1

where n is the index of the current time step and $n+1$ is the index of the next time step to be solved. For the k-th order accuracy algorithm in time, the previous k time step are necessary at each time step. The coefficients for the k-th order algorithm are given in Table A.1.

A.2 Flow over slip surfaces

The DNS of flow over slip surfaces is an extension of the *ChannelFlow* code and the numerical schemes presented for the incompressible Navier-Stokes equations given above in Section A.1. The previous section used the no-slip boundary equations at the top and bottom walls (i.e., $u|_{y=\pm1} = 0$) and the base profile to be $U(y) = 1 - y^2$. Slip surfaces, however, facilitate a non-zero velocity at the wall which can be modeled by the Navier slip condition [171]

$$u|_{y=\pm1} = L_s \frac{\partial u}{\partial y}|_{y=\pm1} \tag{A.16}$$

where L_s is the slip length, a measure of the amount of slip at the wall. If we assume the shape of the base profile to be parabolic, $U(y) = ay^2 + by + c$, we can solve for the new base profile, given our assumption of the boundary condition in Equation A.16. We also know the bulk velocity, or the integral of the velocity profile, should be equal

to 2/3.

$$u_b = \frac{1}{2} \int_{-1}^{1} u \, dy$$

$$= \frac{1}{2} \left[\frac{a}{3} y^3 + \frac{b}{2} y^2 + cy \right]_{-1}^{1}$$

$$= \frac{1}{2} \left(\frac{2}{3} a + 2c \right) \tag{A.17}$$

$$= \frac{a}{3} + c = \frac{2}{3}$$

The y-derivative of the velocity profile is given by:

$$\frac{\partial u}{\partial y} = 2ay + b. \tag{A.18}$$

Substituting Equation A.18 into Equation A.16 for $y = \pm 1$, we obtain equations for the velocity at the top and bottom walls in terms of the velocity profile:

$$u_s|_{y=-1} = L_s \left(2a(-1) + b \right)$$

$$= a - b + c = L_s \left(-2a + b \right) \tag{A.19}$$

$$u_s|_{y=1} = -L_s \left(2a(1) + b \right)$$

$$= a + b + c = -L_s \left(2a + b \right) \tag{A.20}$$

If we then add Equations A.19 and A.20, we obtain

$$2a + 2c = -4aL_s \Rightarrow a + c = -2aL_s. \tag{A.21}$$

Then, subtracting Equation A.18 from Equation A.19, we obtain

$$\frac{2}{3} a = -2aL_s - \frac{2}{3} \Rightarrow \frac{a}{3} (1 + 3L_s) = -\frac{1}{3} \tag{A.22}$$

and, therefore,

$$a = \frac{-1}{3L_s + 1} \tag{A.23}$$

Then, plugging the constant a into Equation A.21, we obtain

$$a + c = -2aL_s$$

$$\Rightarrow c = a\left(1 + 2L_s\right) \tag{A.24}$$

$$\therefore c = \frac{2L_s + 1}{3L_s + 1}; b = 0$$

Finally, we obtain the new base profile as a function of the slip length, L_s:

$$U(y) = \frac{-y^2}{3L_s + 1} + \frac{2L_s + 1}{3L_s + 1}. \tag{A.25}$$

Therefore, given a slip length, L_s, the base profile can be calculated and used to decompose the streamwise velocity into the base and fluctuating components, as discussed in Section A.1.

A.3   Viscoelastic flows

General details of the numerical methods used to solve the flow of dilute polymer solutions using the FENE-P model are given below. Overall, the procedure is similar to that given above for the incompressible Navier-Stokes equations, with the added complexity of considering the effect of the polymer additives on the flow. The variables and parameters are discussed in Chapter 3. The system of equations to be solved for the flow of dilute polymer solutions is listed below:

$$\frac{\partial u}{\partial t} + u \cdot \nabla u = -\nabla p + \frac{\beta}{Re}\nabla^2 u + \frac{2\left(1 - \beta\right)}{ReWi}\nabla \cdot \tau_p, \tag{A.26}$$

$$\nabla \cdot u = 0, \tag{A.27}$$

$$\frac{\alpha}{1 - tr\left(\alpha\right)/b} + \frac{Wi}{2}\left(\frac{\partial \alpha}{\partial t} + u \cdot \nabla \alpha - \alpha \cdot \nabla u - \left(\alpha \cdot \nabla u\right)^{T}\right) = \left(\frac{b}{b+2}\right)\delta, \tag{A.28}$$

$$\tau_{p} = \frac{b+5}{b}\left(\frac{\alpha}{1 - tr\left(\alpha\right)/b} - \left(1 - \frac{2}{b+2}\right)\delta\right). \tag{A.29}$$

The pressure and velocity are again decomposed into the sum of a base profile and fluctuating component. The decomposed variables are substituted and the simplifying notation is then given by:

$$\mathbf{N} \equiv \mathbf{u} \cdot \nabla \mathbf{u}, \tag{A.30}$$

$$\mathbf{Lu}' \equiv \frac{\beta}{Re}\nabla^{2}\mathbf{u}', \tag{A.31}$$

$$\mathbf{C} \equiv \left(\frac{\beta}{Re}\frac{\partial^{2}U}{\partial y^{2}} - \Pi\right)\mathbf{e}_{x}, \tag{A.32}$$

$$\mathbf{S} \equiv \frac{2\left(1 - \beta\right)}{ReWi}\nabla \cdot \tau_{p}. \tag{A.33}$$

where $\mathbf{N}$ is the nonlinear inertia term, $\mathbf{Lu}'$ is the linear viscosity term, $\mathbf{C}$ is the constant term, and S is the nonlinear contribution of the divergence of polymer stress. Equation A.26 can then be rewritten as

$$\frac{\partial \mathbf{u}'}{\partial t} = -\mathbf{N} - \nabla p' + \mathbf{Lu}' + \mathbf{C} + \mathbf{S} \tag{A.34}$$

and Fourier-transformed in the x and z directions to obtain

$$\frac{\partial \tilde{\mathbf{u}}'}{\partial t} = -\tilde{\mathbf{N}} - \nabla \tilde{p}' + \tilde{\mathbf{L}}\tilde{\mathbf{u}}' + \tilde{\mathbf{C}} + \tilde{\mathbf{S}} \tag{A.35}$$

where $\sim$ signifies variable in the Fourier space in the x and z directions, and in physical space in the y direction. The Fourier-transformed differential operators in

the x and z directions are

$$\tilde{\nabla} \equiv 2\pi i \frac{k_x}{L_x}\mathbf{e}_x + \frac{\partial}{\partial y}\mathbf{e}_y + 2\pi i \frac{k_z}{L_z}\mathbf{e}_z, \tag{A.36}$$

$$\tilde{\nabla}^2 \equiv \frac{\partial^2}{\partial y^2} - 4\pi^2\left(\frac{k_x^2}{L_x^2} + \frac{k_z^2}{L_z^2}\right), \tag{A.37}$$

$$\tilde{\mathbf{L}} \equiv \frac{\beta}{Re}\tilde{\nabla}^2 \tag{A.38}$$

Again, the 3rd order Adams-Bashforth scheme is used for temporal discretization, with the linear terms discretized implicitly and nonlinear terms discretized explicitly. The time-stepping equation is given by:

$$\frac{1}{\Delta t}\left(\eta\tilde{\mathbf{u}}'^{,n+1} + \sum_{j=0}^{k-1} a_j\tilde{\mathbf{u}}'^{,n-j}\right) = \sum_{j=0}^{k-1} b_j\left(-\tilde{\mathbf{N}}^{n-j} + \tilde{\mathbf{S}}^{n-j}\right) + \tilde{\mathbf{L}}\tilde{\mathbf{u}}'^{,n+1} + \tilde{\mathbf{C}} - \tilde{\nabla}\tilde{p}'^{,n+1}$$

$$\tag{A.39}$$

We can rearrange A.39 to have the current time step values on the LHS and the $n+1$ time step on the RHS:

$$\frac{\eta}{\Delta t}\tilde{\mathbf{u}}'^{,n+1} - \tilde{\mathbf{L}}\tilde{\mathbf{u}}'^{,n+1} + \tilde{\nabla}\tilde{p}'^{,n+1} = \sum_{j=0}^{k-1}\left(-\frac{a_j}{\Delta t}\tilde{\mathbf{u}}'^{,n-j} - b_j\left(\tilde{\mathbf{N}}^{n-j} - \tilde{\mathbf{S}}^{n-j}\right)\right) + \tilde{\mathbf{C}}$$

$$\equiv \tilde{\mathbf{R}}^n \tag{A.40}$$

where n is the index for the current time step and $n+1$ is the index of the following time step to be solved. The previous k time steps are necessary to iterate the equation to the $n+1$ time step. The above equation can be expanded using the linear operator $\tilde{\mathbf{L}}$ to get a function of wave number with a wave number pair (k_x, k_z). For each pair, A.40 is a differential equation with y-derivatives, only. It may be further simplified to what is known as a *tau-equation* and, along with the Fourier-transformed continuity

equation and boundary condition, is given by:

$$\nu \frac{\partial^2 \tilde{\mathbf{u}}'}{\partial y^2} - \lambda \tilde{\mathbf{u}}' - \tilde{\nabla} \tilde{p}' = -\tilde{\mathbf{R}}, \tag{A.41}$$

$$\tilde{\nabla} \cdot \tilde{\mathbf{u}}' = 0, \tag{A.42}$$

$$\tilde{\mathbf{u}}'|_{y\pm 1} = 0. \tag{A.43}$$

The parameters ν and λ are constants given by:

$$\nu \equiv \frac{\beta}{\Re} \tag{A.44}$$

$$\lambda \equiv 4\pi^2 \nu \left(\frac{k_x^2}{L_x^2} + \frac{k_z^2}{L_z^2} \right) + \frac{\eta}{\Delta t}. \tag{A.45}$$

The tau-equation is solved for wavenumber pair at each time step, where $\tilde{\mathbf{u}}'$ and $\tilde{p}'$ are unknown and $\tilde{\mathbf{R}}$ is known from previous time steps. Using what is known as the influence matrix, the tau-equation can be solved with both divergence-free and boundary conditions satisfied [26]. The tau-equation is split into two sub-problems: the *A-problem* and the *B-problem*. The *A-problem* cannot be solved directly because there are no boundary conditions for the pressure term $\tilde{p}'$. To obtain these boundary conditions, the *B-problem* is constructed by assuming the boundary conditions for velocity are replaced by Dirichlet boundary conditions for pressure. The *B-problem* is solved by constructing the *B'-problem* which is solved for a particular solution from the inhomogeneous version of the *B-problem* with homogeneous boundary conditions and basis solutions from two corresponding homogeneous problems: the $B_+ - problem$ and the $B_- - problem$. These two problems need only be solved once per simulation, as they do not vary with time. These problems are readily solvable with standard numerical schemes, like the Chebyshev-tau method [26], which is included in Chan-

nelFlow.

The FENE-P equation for polymer conformation tensor is easier to solve than the modified Navier-Stokes equations. By including an artificial diffusivity term, $1/(ScRe)\nabla^2\alpha$, for increased stability, the FENE-P constitutive model is given by:

$$\frac{\partial \alpha}{\partial t} = -\mathbf{u}\cdot\nabla\alpha + \alpha\cdot\nabla\mathbf{u} + (\alpha\cdot\nabla\mathbf{u})^T - \frac{2}{Wi}\frac{\alpha}{1 - tr(\alpha)/b} + \frac{2}{Wi}\frac{b}{b+2}\delta + \frac{1}{ScRe}\nabla^2\alpha. \quad (A.46)$$

Terms on the RHS are again grouped into nonlinear, linear, and constant terms to simplify the system:

$$\mathbf{N}_p \equiv -\mathbf{u}\cdot\nabla\alpha + \alpha\cdot\nabla\mathbf{u} + (\alpha\cdot\nabla\mathbf{u})^T - \frac{2}{Wi}\frac{\alpha}{1 - tr(\alpha)/b}, \quad (A.47)$$

$$\mathbf{C}_p \equiv \frac{2}{Wi}\frac{b}{b+2}\delta, \quad (A.48)$$

$$\mathbf{L}_p\alpha \equiv \frac{1}{ScRe}\nabla^2\alpha. \quad (A.49)$$

Substituting the new notation and taking the Fourier transform in the x and z directions, a simplified convection-diffusion equation is given by:

$$\frac{\partial \tilde{\alpha}}{\partial t} = \tilde{\mathbf{N}}_p + \tilde{\mathbf{C}}_p + \tilde{\mathbf{L}}_p\tilde{\alpha}. \quad (A.50)$$

This equation is solved using the semi-implicit temporal discretization scheme, with the nonlinear terms discretized explicitly with 3rd order Adams-Bashforth and linear terms discretized implicitly with backward-differentiation. The time-stepping equation is given by:

$$\frac{1}{\Delta t}\left(\eta\tilde{\alpha}^{n+1} + \sum_{j=0}^{k-1}\right) = \sum_{j=0}^{k-1} b_j \tilde{\mathbf{N}}_p^{n-j} + \tilde{\mathbf{L}}_p\tilde{\alpha}^{n+1} + \tilde{\mathbf{C}}_p \quad (A.51)$$

which becomes

$$\frac{\eta}{\Delta t}\tilde{\alpha}^{n+1} - \tilde{\mathbf{L}}_p\tilde{\alpha}^{n+1} = \sum_{j=0}^{k-1}\left(-\frac{a_j}{\Delta t}\tilde{\alpha}^{n-j} + b_j\tilde{\mathbf{N}}_p^{n-j}\right) + \tilde{\mathbf{C}}_p$$
$$= \tilde{\mathbf{R}}_p^n \qquad (A.52)$$

when rearranged. Again, $\tilde{\mathbf{R}}_p$ corresponds to the terms that are calculated with information from previous time steps. The coefficients for the numerical scheme are the same given in Table A.1. Boundary conditions for $\tilde{\alpha}^{n+1}$ are obtained by updating Equation A.52 without the linear term, which gives the equation

$$\tilde{\alpha}^{n+1} = \frac{\Delta t}{\eta}\left(\sum_{j=0}^{k-1}\left(-\frac{a_j}{\Delta t}\tilde{\alpha}^{n-j} + b_j\tilde{\mathbf{N}}_p^{n-j}\right) + \tilde{\mathbf{C}}_p\right) \qquad (A.53)$$

which can be solved explicitly.

The pseudo-algorithm is given here. At each time step, the inverse Fourier transform is performed on all fields, and nonlinear terms $\mathbf{N}$, $\mathbf{S}$, and $\mathbf{N}_p$ are computed on the grid directly. As before, the alternating form of the nonlinear term $\mathbf{N}$ is used, which alternates between divergence for and convection form at each successive time step. Fourier transforms are then performed on all fields, including the resulting nonlinear terms that were computed directly. A loop over every wavenumber pair (k_x, k_z) is performed. During each step, $\tilde{\mathbf{R}}^n$, $\tilde{\mathbf{R}}_p^n$, and the boundary conditions for $\tilde{\alpha}^{n+1}$ are computed and used to solve the tau-equation for velocity and pressure, and the Helmholtz equations for the polymer conformation tensor. For each wavenumber pair at each time step, 10 complex Helmholtz equations are solved, including four for the velocity and pressure and six for the FENE-P equation. Due to the symmetry of the conformation tensor, only three of the six off-diagonal components are solved for. For complete details of the methods used here in simulating viscoelastic flows,

readers are directed to the work of Xi [253].

A.4 Computation of nonlinear traveling wave solutions

The computation of the nonlinear traveling wave solutions is performed using a Newton-Krylov-hookstep algorithm developed by Viswanath [228], and is included in the ChannelFlow package [69]. A grid system is generated on $N_x \times N_y \times N_z$ using Fourier-Chebyshev-Fourier spectral spatial discretization. Traveling wave solutions of the Navier-Stokes equations are of the form:

$$\mathbf{u}(x, y, z, t) = \mathbf{u}(x - c_x t, y, z), \tag{A.54}$$

where c_x is a constant streamwise wave speed. ChannelFlow, however, looks to solve a more general case using a symmetric subspace, or a subspace of the state space which is invariant under imposed symmetries:

$$\sigma f^{t_1}(u) - u = 0, \tag{A.55}$$

where f^{t_1} is the time-t_1 forward integration in time of the Navier-Stokes equations, computed by direct numerical simulation. The symbol σ is a symmetry operator acting on the flow field, such that

$$\sigma [u, v, w] (x, y, z) = [s_x u, s_y v, s_z w] (s_x x + a_x L_x, s_y y, s_z z + a_z L_z). \tag{A.56}$$

The present notation for flow symmetries is taken from [71]. The symmetry operator σ used here consists of two sets of parameters that describe the rotation-reflection symmetries, s_x, s_y, s_z, and the streamwise and spanwise translations, a_x, a_z. From

Equation A.56, the symmetry operator σ corresponds to the translation symmetry of the traveling wave solution after time t_1. Computing these solutions as they propagate in the streamwise direction requires solving for the unknown symmetry parameter corresponding to the streamwise shift, $a_x = c_x t_1 / L_x$. The spanwise shift, a_z, is set to zero for the current study, and the other symmetry parameters are inherent to the solution. The time shift, t_1, is chosen *a priori*. Streamwise shift parameter is then determined as part of the solution.

The Navier-Stokes equations, along with the imposed periodic boundary conditions, are equivalent under certain reflections and translations in the streamwise and spanwise directions. With the symmetries imposed on the system, the flow and its evolution in time, and subsequent solutions, are then confined to this symmetric subspace. These symmetries of the resulting flow states can be expressed using Equation A.56 – $\mathbf{u} = \sigma \mathbf{u}$ – for certain values of σ. This symmetry parameter can then be expressed using distinct parameters for the various imposed symmetries: τ represents the spatial phase shifts, σ represents the reflections, and s represents the shift-reflection or shift-rotation. The four symmetries present for the P3 and P4 traveling wave solutions are those found in Park and Graham [182]:

$$\sigma_y [u, v, w] (x, y, z) = [u, -v, w] (x, -y, z), \tag{A.57}$$

$$\sigma_z [u, v, w] (x, y, z) = [u, v, -w] (x, y, -z), \tag{A.58}$$

$$\tau_{xz} [u, v, w] (x, y, z) = [u, v, w] (x + L_x/2, y, z + L_z/2), \tag{A.59}$$

$$s_1 [u, v, w] (x, y, z) = [u, v, -w] (x + L_x/2, y, -z). \tag{A.60}$$

Symmetries associated with reflections about the midplanes in the y and z directions are denoted by σ_y and σ_z, respectively. The τ_{xz} and s_1 parameters corresponds to

half-domain translations in the x and z directions and a shift-reflection symmetry, respectively. The s_1 symmetry is particularly relevant and corresponds to sinusoidal instability of the streamwise streaks of the self-sustaining process [231]. Pertinent symmetries help to reduce the complexity of the flow while preserving the characteristics of turbulence.

Bibliography

[1] H. A. Abdulbari, R. M. Yunus, N. H. Abdurahman, and A. Charles. Going against the flow-A review of non-additive means of drag reduction. *J. Ind. Eng. Chem.*, 19:27–36, 2013. ISSN 1226086X. doi: 10.1016/j.jiec.2012.07.023.

[2] R. J. Adrian. Hairpin vortex organization in wall turbulence. *Physics of Fluids*, 19(4), 2007. ISSN 10706631. doi: 10.1063/1.2717527. URL https://doi.org/10.1063/1.2717527.

[3] R. Agrawal, H. C. Ng, E. A. Davis, J. S. Park, M. D. Graham, D. J. C. Dennis, and R. J. Poole. Low- and High-Drag Intermittencies in Turbulent Channel Flows. *Entropy*, 22(1126):1–28, 2020. doi: 10.3390/e22101126.

[4] R. Agrawal, H. C.-H. Ng, E. A. Davis, J. S. Park, M. D. Graham, D. J. Dennis, and R. J. Poole. Low-and high-drag intermittencies in turbulent channel flows. *Entropy*, 22(10):1126, 2020.

[5] R. Akhavan, W. J. Jung, and N. Mangiavacchi. Turbulence control in wall-bounded flows by spanwise oscillations. *Applied Scientific Research*, 51(1-2): 299–303, 1993. ISSN 00036994. doi: 10.1007/BF01082552.

[6] K. T. Allhoff and B. Eckhardt. Directed percolation model for turbulence transition in shear flows. *Fluid Dyn. Res.*, 44(3):031201, 2012.

211

[7]   R. Antonia. Conditional sampling in turbulence measurement. *Annual Review of Fluid Mechanics*, 13(1):131–156, 1981.

[8]   F. Auteri, M. Carini, M. Fournié, D. Fratantonio, and F. Giannetti. Global Linear Stability Analysis of the Flow Around a Superhydrophobic Circular Cylinder. *Springer Proceedings in Physics*, 185:181–187, 2016. ISSN 18674941. doi: 10.1007/978-3-319-30602-5.

[9]   K. Avila, D. Moxey, A. de Lozar, M. Avila, D. Barkley, and B. Hof. The onset of turbulence in pipe flow. *Science*, 333(6039):192–196, 2011.

[10] K. Avila, D. Moxey, A. de Lozar, M. Avila, D. Barkley, and B. Hof. The Onset of Turbulence in Pipe Flow. *Science*, 333(6039):192–196, 2011. ISSN 0036-8075. doi: 10.1126/science.1203223.

[11] M. Avila, F. Mellibovsky, N. Roland, and B. Hof. Streamwise-localized solutions at the onset of turbulence in pipe flow. *Phys. Rev. Lett.*, 110(22):224502, 2013.

[12] D. Barkley. Simplifying the complexity of pipe flow. *Phys. Rev. E*, 84(1):016309, 2011.

[13] D. Barkley. Theoretical perspective on the route to turbulence in a pipe. *J. Fluid Mech.*, 803:P1, 2016.

[14] D. Barkley, B. Song, V. Mukund, G. Lemoult, M. Avila, and B. Hof. The rise of fully turbulent flow. *Nature*, 526(7574):550, 2015.

[15] A. Baron and M. Quadrio. Turbulent drag reduction by spanwise wall oscillations. *Applied Scientific Research*, 55(4):311–326, dec 1995. ISSN 15731987. doi: 10.1007/BF00856638.

[16] C. Barraud, B. Cross, C. Picard, F. Restagno, L. Léger, and E. Charlaix. Large slippage and depletion layer at the polyelectrolyte/solid interface. *Soft Matter*, 15:6308–6317, 2019. doi: 10.1039/C9SM00910H. URL `http://dx.doi.org/10.1039/C9SM00910H`.

[17] G. K. Batchelor. *An Introduction to Fluid Dynamics*. Cambridge University Press, Cambridge, 1967.

[18] T. W. Berger, J. Kim, C. Lee, and J. Lim. Turbulent boundary layer control utilizing the lorentz force. *Physics of Fluids*, 12(3):631–649, 2000. doi: 10.1063/1.870270. URL `https://doi.org/10.1063/1.870270`.

[19] T. R. Bewley, P. Moin, and R. Temam. DNS-based predictive control of turbulence: An optimal benchmark for feedback algorithms. *Journal of Fluid Mechanics*, 447:179–225, 2001. ISSN 00221120. doi: 10.1017/S0022112001005821. URL `https://doi.org/10.1017/S0022112001005821`.

[20] R. Bird, C. Curtiss, R. Armstrong, and O. Hassager. *Dynamics of Polymeric Liquids, Volume 2: Kinetic Theory, 2nd Edition*. Wiley, 2nd edition, 1987. ISBN 978-0-471-80244-0.

[21] L. Bocquet and E. Lauga. A smooth future? *Nature Mat.*, 10(5):334–337, 2011. ISSN 14764660. doi: 10.1038/nmat2994.

[22] S. Bottin and H. Chaté. Statistical analysis of the transition to turbulence in plane Couette flow. *Eur. Phys. J. B*, 6(1):143–155, 1998. ISSN 14346028. doi: 10.1007/s100510050536.

[23] E. Brand and J. F. Gibson. A doubly localized equilibrium solution of plane couette flow. *J. Fluid Mech.*, 750:R3, 2014.

[24] K. S. Breuer, J. Park, and C. Henoch. Actuation and control of a turbulent channel flow using Lorentz forces. *Physics of Fluids*, 16(4):897–907, 2004. ISSN 10706631. doi: 10.1063/1.1647142. URL `https://doi.org/10.1063/1.1647142`.

[25] N. B. Budanur, K. Y. Short, M. Farazmand, A. P. Willis, and P. Cvitanović. Relative periodic orbits form the backbone of turbulent pipe flow. *Journal of Fluid Mechanics*, 833:274–301, 2017. ISSN 14697645. doi: 10.1017/jfm.2017.699. URL `https://doi.org/10.1017/jfm.2017.699`.

[26] C. Canuto, M. Hussaini, A. Quateroni, and T. Zhang. *Spectral Methods in Fluid Dynamics*. Springer-Verlag, 1988.

[27] D. R. Carlson, S. E. Widnall, and M. F. Peeters. A flow-visualization study of transition in plane poiseuille flow. *J. Fluid Mech.*, 121:487–505, 1982.

[28] H. A. Carlson and J. L. Lumley. Active control in the turbulent wall layer of a minimal flow unit. *Journal of Fluid Mechanics*, 329:341–371, 1996. doi: 10.1017/S0022112096008944.

[29] A. B. Cassie and S. Baxter. Wettability of porous surfaces. *Transactions of the Faraday Society*, 40(0):546–551, jan 1944. ISSN 00147672. doi: 10.1039/tf9444000546.

[30] M. Castagna, N. Mazellier, and A. Kourta. Wake of super-hydrophobic falling spheres: influence of the air layer deformation. *J. Fluid Mech.*, 850:646–673, 2018.

[31] C. Chai and B. Song. Stability of slip channel flow revisited. *Physics of Fluids*,

31(8), 2019. ISSN 10897666. doi: 10.1063/1.5108804. URL `https://doi.org/10.1063/1.5108804`.

[32] G. J. Chandler and R. R. Kerswell. Invariant recurrent solutions embedded in a turbulent two-dimensional Kolmogorov flow. *J Fluid Mech*, 722:554–595, mar 2013.

[33] J. Chang, T. Jung, H. Choi, and J. Kim. Predictions of the effective slip length and drag reduction with a lubricated micro-groove surface in a turbulent channel flow. *J. Fluid Mech.*, 874:797–820, 2019.

[34] C. H. Choi and C. J. Kim. Large slip of aqueous liquid flow over a nanoengineered superhydrophobic surface. *Phys. Rev. Lett.*, 96(6):066001, 2006. ISSN 10797114. doi: 10.1103/PhysRevLett.96.066001.

[35] H. Choi, P. Moin, and J. Kim. Direct numerical simulation of turbulent flow over riblets. *Journal of Fluid Mechanics*, 255:503–539, 1993. ISSN 14697645. doi: 10.1017/S0022112093002575.

[36] H. Choi, P. Moin, and J. Kim. Active turbulence control for drag reduction in wall-bounded flows. *Journal of Fluid Mechanics*, 262(A):75–110, oct 1994. ISSN 14697645. doi: 10.1017/S0022112094000431.

[37] K. S. Choi. Near-wall structure of turbulent boundary layer with spanwise-wall oscillation. *Physics of Fluids*, 14(7):2530–2542, 2002. ISSN 10706631. doi: 10.1063/1.1477922. URL `https://doi.org/10.1063/1.1477922`.

[38] K. S. Choi, J. R. DeBisschop, and B. R. Clayton. Turbulent boundary-layer control by means of spanwise-wall oscillation. *AIAA Journal*, 36(7):1157–1163,

jul 1998. ISSN 00011452. doi: 10.2514/2.526. URL `https://arc.aiaa.org/doi/10.2514/2.526`.

[39] A. K. H. Chu. Instability of Navier slip flow of liquids. *Comptes Rendus - Mecanique*, 332(11):895–900, 2004. ISSN 16310721. doi: 10.1016/j.crme.2004.06.010.

[40] K. H. Chu, R. Xiao, and E. N. Wang. Uni-directional liquid spreading on asymmetric nanostructured surfaces. *Nature Materials*, 9(5):413–417, 2010. ISSN 14764660. doi: 10.1038/nmat2726. URL `www.nature.com/naturematerials`.

[41] Y. M. Chung and T. Talha. Effectiveness of active flow control for turbulent skin friction drag reduction. *Physics of Fluids*, 23(2):25102, 2011. ISSN 10706631. doi: 10.1063/1.3553278. URL `https://doi.org/10.1063/1.3553278`.

[42] B. Cross, C. Barraud, C. Picard, L. Léger, F. Restagno, and E. Charlaix. Wall slip of complex fluids: Interfacial friction versus slip length. *Phys. Rev. Fluids*, 3:062001, Jun 2018. doi: 10.1103/PhysRevFluids.3.062001. URL `https://link.aps.org/doi/10.1103/PhysRevFluids.3.062001`.

[43] P. Cvitanović and J. F. Gibson. Geometry of the turbulence in wall-bounded shear flows: Periodic orbits. *Physica Scripta T*, T142:47, 2010. ISSN 02811847. doi: 10.1088/0031-8949/2010/T142/014007.

[44] J. Davies, D. Maynes, B. W. Webb, and B. Woolford. Laminar flow in a microchannel with superhydrophobic walls exhibiting transverse ribs. *Phys. Fluids*, 18(8):087110, 2006. doi: 10.1063/1.2336453.

[45] E. A. Davis and J. S. Park. Dynamics of laminar and transitional flows over

slip surfaces: effects on the laminar-turbulent separatrix. *arXiv*, 2020. URL `http://arxiv.org/abs/2004.01051`.

[46] E. A. Davis and J. S. Park. Dynamics of laminar and transitional flows over slip surfaces: effects on the laminar-turbulent separatrix. *Journal of Fluid Mechanics*, 894(A16), 2020. doi: 10.1017/jfm.2020.282. URL `http://arxiv.org/abs/2004.01051`.

[47] P.-G. de Gennes. On fluid/wall slippage. *Langmuir*, 18(9):3413–3414, 2002.

[48] P.-G. de Gennes, F. Brochard-Wyart, and D. Quere. *Capilarity and Wetting Phenomena: Drops, Bubbles, Pearls, Waves.* Springer, 2004. ISBN 9780387216560. doi: 10.1007/978-0-387-21656-0.

[49] D. De Souza, T. Bergier, and R. Monchaux. Transient states in plane Couette flow. *J. Fluid Mech*, 903:33–34, 2020. doi: 10.1017/jfm.2020.635. URL `https://doi.org/10.1017/jfm.2020.635`.

[50] P. Doohan, A. P. Willis, and Y. Hwang. Shear stress-driven flow: the state space of near-wall turbulence as $Re_\tau \to \infty$. *J. Fluid Mech*, 874:606–638, 2019. doi: 10.1017/jfm.2019.472. URL `https://doi.org/10.1017/jfm.2019.472`.

[51] J. Drelich, J. L. Wilbur, J. D. Miller, and G. M. Whitesides. Contact angles for liquid drops at a model heterogeneous surface consisting of alternating and parallel hydrophobic/hydrophilic strips. *Langmuir*, 12(7):1913–1922, 1996. ISSN 07437463. doi: 10.1021/la9509763. URL `https://pubs.acs.org/sharingguidelines`.

[52] Y. Du, V. Symeonidis, and G. E. Karniadakis. Drag reduction in wall-bounded turbulence via a transverse travelling wave. *Journal of Fluid Mechanics*, 457:

1–34, 2002. ISSN 00221120. doi: 10.1017/S0022112001007613. URL `https://doi.org/10.1017/S0022112001007613`.

[53] Y. Duguet, A. P. Willis, and R. R. Kerswell. Transition in pipe flow: the saddle structure on the boundary of turbulence. *J. Fluid Mech.*, 613:255–274, 2008.

[54] Y. Duguet, A. P. Willis, and R. R. Kerswell. Transition in pipe flow: the saddle structure on the boundary of turbulence. *J Fluid Mech*, 613:255–274, 2008.

[55] D. Dylewsky, E. Kaiser, S. L. Brunton, and J. N. Kutz. Principal Component Trajectories (PCT): Nonlinear dynamics as a superposition of time-delayed periodic orbits. Technical report, 2020.

[56] B. Eckhardt, H. Faisst, A. Schmiegel, and T. M. Schneider. Dynamical systems and the transition to turbulence in linearly stable shear flows. *Phil. Trans. R. Soc. Lond. A*, 366(1868):1297–1315, 2007.

[57] B. Eckhardt, T. M. Schneider, B. Hof, and J. Westerweel. Turbulence transition in pipe flow. *Annu. Rev. Fluid Mech.*, 39(1):447–468, 2007. doi: 10.1146/annurev.fluid.39.050905.110308.

[58] T. Endo and N. Kasagi. Active control of wall turbulence with wall deformation. *Nihon Kikai Gakkai Ronbunshu, B Hen/Transactions of the Japan Society of Mechanical Engineers, Part B*, 66(641):113–119, 2000. ISSN 03875016. doi: 10.1299/kikaib.66.113.

[59] C. Fairhall, N. Abderrahaman-Elena, and R. García-Mayoral. The effect of slip and surface texture on turbulence over superhydrophobic surfaces. *J. Fluid Mech.*, 861:88–118, 2019.

[60] X. Feng and L. Jiang. Design and creation of superwetting/antiwetting surfaces. *Advanced Materials*, 18(23):3063–3078, 2006. ISSN 09359648. doi: 10.1002/adma.200501961.

[61] O. Flores and J. Jiménez. Hierarchy of minimal flow units in the logarithmic layer. *Citation: Physics of Fluids*, 22, 2010. URL `https://doi.org/10.1063/1.3464157http://aip.scitation.org/toc/phf/22/7`.

[62] O. Flores and J. Jiménez. Hierarchy of minimal flow units in the logarithmic layer. *Citation: Physics of Fluids*, 22, 2010. URL `https://doi.org/10.1063/1.3464157http://aip.scitation.org/toc/phf/22/7`.

[63] Y. Fu, C. Yuan, and X. Bai. Marine drag reduction of shark skin inspired riblet surfaces. *Biosurface and Biotribology*, 3(1):11–24, 2017. ISSN 24054518. doi: 10.1016/j.bsbt.2017.02.001.

[64] K. Fukagata, N. Kasagi, and P. Koumoutsakos. A theoretical prediction of friction drag reduction in turbulent flow by superhydrophobic surfaces. *Physics of Fluids*, 18(5):051703, 2006. doi: 10.1063/1.2205307. URL `https://doi.org/10.1063/1.2205307`.

[65] L. Gao and T. J. McCarthy. Contact angle hysteresis explained. *Langmuir*, 22 (14):6234–6237, 2006. ISSN 07437463. doi: 10.1021/la060254j. URL `https://pubs.acs.org/sharingguidelines`.

[66] R. García-Mayoral and J. Jiménez. Drag reduction by riblets. *Philosophical Transactions of the Royal Society A: Mathematical, Physical and Engineering Sciences*, 369(1940):1412–1427, 2011. ISSN 1364503X. doi: 10.1098/rsta.2010.0359.

[67] R. García-Mayoral, G. Gómez-De-Segura, and C. T. Fairhall. The control of near-wall turbulence through surface texturing. *Fluid Dynamics Research*, 51 (1), 2019. ISSN 01695983. doi: 10.1088/1873-7005/aadfcc. URL `https://doi.org/10.1088/1873-7005/aadfcc`.

[68] H. D. Gesser and D. R. Lafreniere. A drag-reducing water insoluble hydrophilic marine coating. *Progress in Organic Coatings*, 49(4):372–374, may 2004. ISSN 03009440. doi: 10.1016/j.porgcoat.2003.12.003.

[69] J. F. Gibson. Channelflow: A spectral Navier-Stokes simulator in C++. Technical report, U. New Hampshire, 2012. Channelflow.org.

[70] J. F. Gibson and E. Brand. Spanwise-localized solutions of planar shear flows. *J. Fluid Mech.*, 745:25–61, 2014.

[71] J. F. Gibson, J. Halcrow, and P. Cvitanović. Visualizing the geometry of state space in plane couette flow. *J. Fluid Mech.*, 611:107–130, 2008.

[72] J. F. Gibson, J. Halcrow, and P. Cvitanović. Visualizing the geometry of state space in plane Couette flow. *Journal of Fluid Mechanics*, 611:107–130, 2008. ISSN 00221120. doi: 10.1017/S002211200800267X.

[73] J. F. Gibson, J. Halcrow, and P. Cvitanović. Equilibrium and travelling-wave solutions of plane couette flow. *J. Fluid Mech.*, 638:243–266, 2009.

[74] K. B. Golovin, J. Gose, M. Perlin, S. L. Ceccio, and A. Tuteja. Bioinspired surfaces for turbulent drag reduction. *Philosophical Transactions of the Royal Society A: Mathematical, Physical and Engineering Sciences*, 374(2073), 2016. ISSN 1364503X. doi: 10.1098/rsta.2016.0189.

[75] K. B. Golovin, J. W. Gose, M. Perlin, S. L. Ceccio, and A. Tuteja. Bioinspired surfaces for turbulent drag reduction. 374, 2016. doi: 10.1098/rsta.2016.0189.

[76] S. Gomé, L. S. Tuckerman, and D. Barkley. Statistical transition to turbulence in plane channel flow. *Physical Review Fluids*, 5(083905), 2020. ISSN 2469990X. doi: 10.1103/PhysRevFluids.5.083905.

[77] G. Gómez-De-Segura and R. García-Mayoral. Turbulent drag reduction by anisotropic permeable substrates-analysis and direct numerical simulations. *Journal of Fluid Mechanics*, 875:124–172, 2019. ISSN 14697645. doi: 10.1017/ jfm.2019.482. URL `https://doi.org/10.1017/jfm.2019.482`.

[78] J. W. Gose, K. Golovin, M. Boban, J. M. Mabry, A. Tuteja, M. Perlin, and S. L. Ceccio. Characterization of superhydrophobic surfaces for drag reduction in turbulent flow. *J. Fluid Mech.*, 845:560–580, 2018.

[79] M. D. Graham. Drag Reduction in Turbulent Flow of Polymer Solutions. *The British Society of Rheology*, 2004:143–170, 2004. URL `http://www.bsr.org.uk`.

[80] M. D. Graham. Drag reduction and the dynamics of turbulence in simple and complex fluids. *Physics of Fluids*, 26(10), 2014. ISSN 10897666. doi: 10.1063/1.4895780. URL `https://doi.org/10.1063/1.4895780http://aip.scitation.org/toc/phf/26/10http://dx.doi.org/10.1063/1.4895780`.

[81] M. D. Graham. *Microhydrodynamics, Brownian Motion, and Complex Fluids*. Cambridge Texts in Applied Mathematics. Cambridge University Press, 2018. doi: 10.1017/9781139175876.

[82] M. D. Graham and D. Floryan. Exact Coherent States and the Nonlinear Dynamics of Wall-Bounded Turbulent Flows. *Annual Review of Fluid Mechanics*, 15:17, 2020. doi: 10.1146/annurev-fluid-051820. URL `https://doi.org/10.1146/annurev-fluid-051820-`.

[83] S. Granick, Y. Zhu, and H. Lee. Slippery questions about complex fluids flowing past solids. *Nature Mat.*, 2(4):221, 2003.

[84] B. R. Gruncell, N. D. Sandham, and G. McHale. Simulations of laminar flow past a superhydrophobic sphere with drag reduction and separation delay. *Physics of Fluids*, 25(4), 2013. ISSN 10706631. doi: 10.1063/1.4801450.

[85] G. Guyard, A. Vilquin, N. Sanson, S. Jouenne, F. Restagno, and J. D. Mc-Graw. Near-surface rheology and hydrodynamic boundary condition of semi-dilute polymer solutions. *Soft Matter*, 17:3765–3774, 2021. doi: 10.1039/D0SM02116D. URL `http://dx.doi.org/10.1039/D0SM02116D`.

[86] J. M. Hamilton, J. Kim, and F. Waleffe. Regeneration mechanisms of near-wall turbulence structures. *Journal of Fluid Mechanics*, 287:317–348, 1995. doi: 10.1017/S0022112095000978.

[87] E. P. Hammond, T. R. Bewley, and P. Moin. Observed mechanisms for turbulence attenuation and enhancement in opposition-controlled wall-bounded flows. *Physics of Fluids*, 10(9):2421–2423, 1998. ISSN 10706631. doi: 10.1063/1.869759.

[88] D. Han, C. Farino, C. Yang, T. Scott, D. Browe, W. Choi, J. W. Freeman, and H. Lee. Soft Robotic Manipulation and Locomotion with a 3D Printed Electroactive Hydrogel. *ACS Applied Materials and Interfaces*, 10(21):17512–

17518, 2018. ISSN 19448252. doi: 10.1021/acsami.8b04250. URL `www.acsami.org`.

[89] D. Han, Z. Lu, S. A. Chester, and H. Lee. Micro 3D Printing of a Temperature-Responsive Hydrogel Using Projection Micro-Stereolithography. *Scientific Reports*, 8(1), 2018. ISSN 20452322. doi: 10.1038/s41598-018-20385-2. URL `www.nature.com/scientificreports/`.

[90] X. He, M. Aizenberg, O. Kuksenok, L. D. Zarzar, A. Shastri, A. C. Balazs, and J. Aizenberg. Synthetic homeostatic materials with chemo-mechano-chemical self-regulation. *Nature*, 487(7406):214–218, 2012. ISSN 00280836. doi: 10.1038/nature11223.

[91] J. Hoepffner and K. Fukagata. Pumping or drag reduction? *Journal of Fluid Mechanics*, 635:171–187, 2009. ISSN 00221120. doi: 10.1017/S0022112009007629. URL `https://doi.org/10.1017/S0022112009007629`.

[92] B. Hof, C. W. H. van Doorne, J. Westerweel, F. T. M. Nieuwstadt, H. Faisst, B. Eckhardt, H. Wedin, R. R. Kerswell, and F. Waleffe. Experimental observation of nonlinear traveling waves in turbulent pipe flow. *Science*, 305(5690): 1594–1598, 2004.

[93] B. Hof, J. Westerweel, T. M. Schneider, and B. Eckhardt. Finite lifetime of turbulence in shear flows. *Nature*, 443(7107):59–62, 2006. ISSN 14764687. doi: 10.1038/nature05089.

[94] S. Hoyas and J. Jiménez. Scaling of the velocity fluctuations in turbulent channels up to $re_\tau = 2003$. *Physics of Fluids*, 18(1):011702, 2006.

[95] H. Hu, J. Wen, L. Bao, L. Jia, D. Song, B. Song, G. Pan, M. Scaraggi, D. Dini, Q. Xue, and F. Zhou. Significant and stable drag reduction with air rings confined by alternated superhydrophobic and hydrophilic strips. *Science Advances*, 3(9), 2017. ISSN 23752548. doi: 10.1126/sciadv.1603288. URL `http://advances.sciencemag.org/`.

[96] L. Huang, B. Fan, and G. Dong. Turbulent drag reduction via a transverse wave traveling along streamwise direction induced by lorentz force. *Physics of Fluids*, 22(1):015103, 2010. doi: 10.1063/1.3291071. URL `https://doi.org/10.1063/1.3291071`.

[97] L. Huang, B. Fan, and D. Mei. Mechanism of drag reduction by spanwise oscillating Lorentz force in turbulent channel flow. *Theoretical and Applied Mechanics Letters*, 2(1):012005, 2012. ISSN 20950349. doi: 10.1063/2.1201205.

[98] Y. Hwang. Near-wall turbulent fluctuations in the absence of wide outer motions. *Journal of Fluid Mechanics*, 723:264–288, 2013.

[99] Y. Hwang and Y. Bengana. Self-sustaining process of minimal attached eddies in turbulent channel flow. *Journal of Fluid Mechanics*, 795:708–738, 2016.

[100] J. I. Ibrahim, Q. Yang, P. Doohan, and Y. Hwang. Phase-space dynamics of opposition control in wall-bounded turbulent flows. *J. Fluid Mech.*, 861:29–54, 2018. doi: 10.1017/jfm.2018.905.

[101] T. Itano and S. Toh. The dynamics of bursting process in wall turbulence. *J. Phys. Soc. Jpn.*, 70(3):703–716, 2001.

[102] J. Jimenez. Coherent Structures and Dynamical Systems. *Center for Turbulence Research Proceeding of the Summer Program*, pages 323–324, 1987.

[103] J. Jiménez. The Minimal Channel Flow Unit in Near-Wall Turbulence. *Journal of Fluid Mechanics*, 225:213–240, 1990. URL `https://torroja.dmt.upm.es/pubs/1990s/jim{_}moin{_}91.pdf`.

[104] J. Jiménez. How linear is wall-bounded turbulence? *Phys. Fluids*, 25:110814, 2013. doi: 10.1063/1.4819081. URL `https://doi.org/10.1063/1.4819081`.

[105] J. Jiménez and P. Moin. The minimal flow unit in near-wall turbulence. *J. Fluid Mech.*, 225:213–240, 1991.

[106] J. Jiménez and P. Moin. The minimal flow unit in near-wall turbulence. *J. Fluid Mech.*, 225:213–240, 1991.

[107] J. Jiménez and A. Pinelli. The autonomous cycle of near-wall turbulence. *Journal of Fluid Mechanics*, 389:335–359, 1999. ISSN 00221120. doi: 10.1017/S0022112099005066. URL `https://doi.org/10.1017/S0022112099005066`.

[108] J. Jiménez and A. Pinelli. The autonomous cycle of near-wall turbulence. *Journal of Fluid Mechanics*, 389:335–359, 1999. doi: 10.1017/S0022112099005066.

[109] J. Jiménez, S. Hoyas, M. P. Simens, and Y. Mizuno. Turbulent boundary layers and channels at moderate reynolds numbers. *Journal of Fluid Mechanics*, 657: 335, 2010.

[110] J. Jiménez, S. Hoyas, M. P. Simens, and Y. Mizuno. Turbulent boundary layers and channels at moderate reynolds numbers. *Journal of Fluid Mechanics*, 657: 335–360, 2010. doi: 10.1017/S0022112010001370.

[111] T. Jung, H. Choi, and J. Kim. Effects of the air layer of an idealized super-hydrophobic surface on the slip length and skin-friction drag. *J. Fluid Mech.*, 790:R1, 2016.

[112] W. J. Jung, N. Mangiavacchi, and R. Akhavan. Suppression of turbulence in wall-bounded flows by high-frequency spanwise oscillations. *Physics of Fluids A*, 4(8):1605–1607, 1992. ISSN 08998213. doi: 10.1063/1.858381. URL `https://doi.org/10.1063/1.858381`.

[113] Y. C. Jung and B. Bhushan. Biomimetic structures for fluid drag reduction in laminar and turbulent flows. *J. Phys. Cond. Matt.*, 22(3):35104, 2010. ISSN 09538984. doi: 10.1088/0953-8984/22/3/035104.

[114] Y. S. Kachanov. Physical mechanisms of laminar-boundary-layer transition. *Annu. Rev. Fluid Mech.*, 26(1):411–482, 1994.

[115] A. J. Kaithakkal, Y. Kametani, and Y. Hasegawa. Dissimilarity between turbulent heat and momentum transfer induced by a streamwise travelling wave of wall blowing and suction. *Journal of Fluid Mechanics*, 886, 2020. ISSN 14697645. doi: 10.1017/jfm.2019.1045.

[116] S. Kang and H. Choi. Active wall motions for skin-friction drag reduction. *Physics of Fluids*, 12(12):3301–3304, 2000. ISSN 10706631. doi: 10.1063/1.1320833. URL `https://doi.org/10.1063/1.1320833`.

[117] G. Karniadakis and K.-S. Choi. Mechanisms on transverse motions in turbulent wall flows. *Annual Review of Fluid Mechanics*, 35(1):45–62, 2003. ISSN 0066-4189. doi: 10.1146/annurev.fluid.35.101101.161213. URL `www.annualreviews.org`.

[118] G. Kawahara. Laminarization of minimal plane couette flow: Going beyond the basin of attraction of turbulence. *Phys. Fluids*, 17(4):041702, 2005.

[119] G. Kawahara, M. Uhlmann, and L. Van Veen. The significance of simple invariant solutions in turbulent flows. *Annu. Rev. Fluid Mech.*, 44:203–225, 2012.

[120] R. R. Kerswell. Recent progress in understanding the transition to turbulence in a pipe. *Nonlinearity*, 18(6):R17, 2005.

[121] T. Khapko, T. Kreilos, P. Schlatter, Y. Duguet, B. Eckhardt, and D. S. Henningson. Edge states as mediators of bypass transition in boundary-layer flows. *Journal of Fluid Mechanics*, 801:1–12, 2016. ISSN 14697645. doi: 10.1017/jfm.2016.434.

[122] J. Kim. Physics and control of wall turbulence for drag reduction. *Philosophical Transactions of the Royal Society A: Mathematical, Physical and Engineering Sciences*, 369(1940):1396–1411, 2011. ISSN 1364-503X. doi: 10.1098/rsta.2010. 0360. URL `http://rsta.royalsocietypublishing.org/content/roypta/369/1940/1396.full.pdfhttp://rsta.royalsocietypublishing.org/cgi/doi/10.1098/rsta.2010.0360`.

[123] P. Kim, L. D. Zarzar, X. He, A. Grinthal, and J. Aizenberg. Hydrogel-actuated integrated responsive systems (HAIRS): Moving towards adaptive materials. *Current Opinion in Solid State and Materials Science*, 15(6):236–245, 2011. ISSN 13590286. doi: 10.1016/j.cossms.2011.05.004.

[124] P. S. Klebanoff, K. D. Tidstrom, and L. M. Sargent. The three-dimensional nature of boundary-layer instability. *Journal of Fluid Mechanics*, 12(1):1–34, 1962. doi: 10.1017/S0022112062000014.

[125] S. J. Kline, W. C. Reynolds, F. A. Schraub, and P. W. Runstadler. The structure of turbulent boundary layers. *Journal of Fluid Mechanics*, 30(4):741–773, 1967.

[126] F. Kramer, R. Grueneberger, F. Thiele, E. Wassen, W. Hage, and R. Meyer. Wavy riblets for turbulent drag reduction. In *5th Flow Control Conference*, Reston, Virigina, jun 2010. American Institute of Aeronautics and Astronautics. ISBN 978-1-62410-140-3. doi: 10.2514/6.2010-4583. URL `http://arc.aiaa.org/doi/10.2514/6.2010-4583`.

[127] A. Kushwaha, J. S. Park, and M. D. Graham. Temporal and spatial intermittencies within channel flow turbulence near transition. *Physical Review Fluids*, 2(2):24603, 2017. ISSN 2469990X. doi: 10.1103/PhysRevFluids.2.024603.

[128] A. Kushwaha, J. S. Park, and M. D. Graham. Temporal and spatial intermittencies within channel flow turbulence near transition. *Physical Review Fluids*, 2, 2017. ISSN 2469990X. doi: 10.1103/PhysRevFluids.2.024603.

[129] E. Lauga and C. Cossu. A note on the stability of slip channel flows. *Physics of Fluids*, 17(8):1–4, 2005. ISSN 10706631. doi: 10.1063/1.2032267. URL `https://doi.org/10.1063/1.2032267`.

[130] C. Lee, J. Kim, D. Babcock, and R. Goodman. Application of neural networks to turbulence control for drag reduction. *Physics of Fluids*, 9(6):1740–1747, 1997. ISSN 10706631. doi: 10.1063/1.869290. URL `https://doi.org/10.1063/1.869290`.

[131] C. Lee, J. Kim, and H. Choi. Suboptimal control of turbulent channel flow for drag reduction. *Journal of Fluid Mechanics*, 358:245–258, mar 1998. ISSN 00221120. doi: 10.1017/S002211209700815X.

[132] C. Lee, C. H. Choi, and C. J. Kim. Structured surfaces for a giant liquid slip. *Phys. Rev. Lett.*, 101(6):064501, 2008. ISSN 00319007. doi: 10.1103/PhysRevLett.101.064501.

[133] C. Lee, C. H. Choi, and C. J. Kim. Superhydrophobic drag reduction in laminar flows: a critical review. *Exp. in Fluids*, 57(12):176, 2016. ISSN 07234864. doi: 10.1007/s00348-016-2264-z.

[134] J. Lee, T. O. Jelly, and T. A. Zaki. Effect of reynolds number on turbulent drag reduction by superhydrophobic surface textures. *Flow Turb. Combust.*, 95 (2-3):277–300, 2015.

[135] M. Lee and R. D. Moser. Direct numerical simulation of turbulent channel flow up to $Re_\tau \approx 5200$. *J. Fluid Mech.*, 774:395–415, 2015. ISSN 1469-7645. doi: 10.1017/jfm.2015.268. URL http://journals.cambridge.org/article_S0022112015002682.

[136] M. Lee and R. D. Moser. Extreme-scale motions in turbulent plane couette flows. *Journal of Fluid Mechanics*, 842:128–145, 2018.

[137] M. Lee and R. D. Moser. Spectral analysis of the budget equation in turbulent channel flows at high reynolds number. *Journal of Fluid Mechanics*, 860:886–938, 2019.

[138] G. Lemoult, L. Shi, K. Avila, S. V. Jalikop, M. Avila, and B. Hof. Directed percolation phase transition to sustained turbulence in couette flow. *Nature Phys.*, 12(3):254, 2016.

[139] G. Lemoult, L. Shi, K. Avila, S. V. Jalikop, M. Avila, and B. Hof. Directed percolation phase transition to sustained turbulence in Couette flow. *Nature Phys.*, 12(3):254–258, 2016. ISSN 17452481. doi: 10.1038/nphys3675.

[140] C. Li, Y. Jiao, X. Lv, S. Wu, C. Chen, Y. Zhang, J. Li, Y. Hu, D. Wu, and J. Chu. In Situ Reversible Tuning from Pinned to Roll-Down Superhy-

drophobic States on a Thermal-Responsive Shape Memory Polymer by a Silver Nanowire Film. *ACS Applied Materials and Interfaces*, 12:13464–13472, 2020. ISSN 19448252. doi: 10.1021/acsami.9b20223. URL `https://dx.doi.org/10.1021/acsami.9b20223`.

[141] C. Li, Y. Jiao, X. Lv, S. Wu, C. Chen, Y. Zhang, J. Li, Y. Hu, D. Wu, and J. Chu. In Situ Reversible Tuning from Pinned to Roll-Down Superhydrophobic States on a Thermal-Responsive Shape Memory Polymer by a Silver Nanowire Film. *ACS Applied Materials and Interfaces*, 12:13464–13472, 2020. ISSN 19448252. doi: 10.1021/acsami.9b20223. URL `https://dx.doi.org/10.1021/acsami.9b20223`.

[142] C. Li, H. Xiao, R. Jiang, and X. Ye. Effect of wall slip on vertical film drainage in presence of soluble surfactants. *Physics of Fluids*, 33(4):042113, 2021. doi: 10.1063/5.0045877. URL `https://doi.org/10.1063/5.0045877`.

[143] J. Li, Q. Sun, S. Han, J. Wang, Z. Wang, and C. Jin. Reversibly light-switchable wettability between superhydrophobicity and superhydrophilicity of hybrid ZnO/bamboo surfaces via alternation of UV irradiation and dark storage. *Progress in Organic Coatings*, 87:155–160, 2015. ISSN 03009440. doi: 10.1016/j.porgcoat.2015.05.028. URL `http://dx.doi.org/10.1016/j.porgcoat.2015.05.028`.

[144] W. Li and M. D. Graham. Polymer induced drag reduction in exact coherent structures of plane Poiseuille flow. *Physics of Fluids*, 19(8), 2007. ISSN 10706631. doi: 10.1063/1.2748443. URL `https://doi.org/10.1063/1.2748443http://aip.scitation.org/toc/phf/19/8`.

[145] W. Li, L. Xi, and M. D. Graham. Nonlinear travelling waves as a framework for understanding turbulent drag reduction. *Journal of Fluid Mechanics*, 565: 353–362, 2006. ISSN 00221120. doi: 10.1017/S0022112006002138.

[146] H. Ling, S. Srinivasan, K. Golovin, G. H. McKinley, A. Tuteja, and J. Katz. High-resolution velocity measurement in the inner part of turbulent boundary layers over super-hydrophobic surfaces. *J. Fluid Mech.*, 801:670–703, 2016.

[147] M. Liu, S. Wang, and L. Jiang. Nature-inspired superwettability systems, 2017. ISSN 20588437. URL `www.nature.com/natrevmats`.

[148] T. Liu, B. Semin, L. Klotz, R. Godoy-Diana, J. Wesfreid, and T. Mullin. Decay of streaks and rolls in plane couette–poiseuille flow. *Journal of Fluid Mechanics*, 915:A65, 2021. doi: 10.1017/jfm.2021.89.

[149] A. Lozano-Durán and J. Jiménez. Effect of the computational domain on direct simulations of turbulent channels up to Reτ = 4200. *Physics of Fluids*, 26(1), 2014. ISSN 10897666. doi: 10.1063/1.4862918.

[150] S. S. Lu and W. W. Willmarth. Measurements of the structure of the reynolds stress in a turbulent boundary layer. *Journal of Fluid Mechanics*, 60(3):481–511, 1973. doi: 10.1017/S0022112073000315.

[151] S. S. Lu and W. W. Willmarth. Measurement of the mean period between bursts. *Physics of Fluids*, 16(11):2012–2013, 1973. doi: 10.1063/1.1694249. URL `https://aip.scitation.org/doi/abs/10.1063/1.1694249`.

[152] P. Luchini, F. Manzo, and A. Pozzi. Resistance of a grooved surface to parallel flow and cross-flow. *J. Fluid Mech.*, 228:87–109, 1991.

[153] J. Lumley and P. Blossey. CONTROL OF TURBULENCE. *Annual Review of Fluid Mechanics*, 30(1):311–327, jan 1998. ISSN 0066-4189. doi: 10.1146/annurev.fluid.30.1.311.

[154] J. R. T. Lustro, G. Kawahara, L. van Veen, M. Shimizu, and H. Kokubu. The onset of transient turbulence in minimal plane couette flow. *J. Fluid Mech.*, 862:R2, 2019.

[155] S. A. Mäkiharju, M. Perlin, and S. L. Ceccio. On the energy economics of air lubrication drag reduction. *International Journal of Naval Architecture and Ocean Engineering*, 4(4):412–422, 2012. ISSN 2092-6782. doi: https://doi.org/10.2478/IJNAOE-2013-0107. URL https://www.sciencedirect.com/science/article/pii/S2092678216303594.

[156] H. Mamori, K. Fukagata, and J. Hoepffner. Phase relationship in laminar channel flow controlled by traveling-wave-like blowing or suction. *Physical Review E - Statistical, Nonlinear, and Soft Matter Physics*, 81(4), 2010. ISSN 15393755. doi: 10.1103/PhysRevE.81.046304.

[157] M. B. Martell, J. P. Rothstein, and J. B. Perot. An analysis of superhydrophobic turbulent drag reduction mechanisms using direct numerical simulation. *Physics of Fluids*, 22(6):1–13, 2010. ISSN 10706631. doi: 10.1063/1.3432514.

[158] I. Marusic, B. J. McKeon, P. A. Monkewitz, H. M. Nagib, A. J. Smits, and K. R. Sreenivasan. Wall-bounded turbulent flows at high reynolds numbers: Recent advances and key issues. *Physics of Fluids*, 22(6):065103, 2010. doi: 10.1063/1.3453711. URL https://doi.org/10.1063/1.3453711.

[159] J. C. Maxwell. On stresses in rarified gases arising from inequalities of temperature. *Phil. Trans. R. Soc.*, 170:231–256, 1879.

[160] D. Maynes, K. Jeffs, B. Woolford, and B. W. Webb. Laminar flow in a microchannel with hydrophobic surface patterned microribs oriented parallel to the flow direction. *Phys. Fluids*, 19(9):93603, 2007. ISSN 10706631. doi: 10.1063/1.2772880.

[161] B. J. McKeon. The engine behind (wall) turbulence: Perspectives on scale interactions. *Journal of Fluid Mechanics*, 817(P1), 2017. ISSN 14697645. doi: 10.1017/jfm.2017.115. URL https://doi.org/10.1017/jfm.2017.115.

[162] B. J. McKeon, A. S. Sharma, and I. Jacobi. Experimental manipulation of wall turbulence: A systems approach. *Physics of Fluids*, 25(3):31301, 2013. ISSN 10706631. doi: 10.1063/1.4793444. URL https://doi.org/10.1063/1.4793444.

[163] T. Min and J. Kim. Effects of hydrophobic surface on skin-friction drag. *Phys. Fluids*, 16(7):55, 2004. ISSN 10706631. doi: 10.1063/1.1755723.

[164] T. Min and J. Kim. Effects of hydrophobic surface on stability and transition. *Phys. Fluids*, 17(10):108106, 2005. ISSN 10706631. doi: 10.1063/1.2126569.

[165] T. Min, S. M. Kang, J. L. Speyer, and J. Kim. Sustained sub-laminar drag in a fully developed channel flow. *Journal of Fluid Mechanics*, 558:309–318, 2006. ISSN 00221120. doi: 10.1017/S0022112006000206. URL https://doi.org/10.1017/S0022112006000206.

[166] Y. Mito and N. Kasagi. DNS study of turbulence modification with streamwise-uniform sinusoidal wall-oscillation. *International Journal of Heat and Fluid Flow*, 19(5):470–481, 1998. ISSN 0142727X. doi: 10.1016/S0142-727X(98)10025-5.

[167] M. V. Morkovin. Bypass Transition To Turbulence and Research Desiderata. *NASA Conference Publication*, pages 161–211, 1985. ISSN 01917811.

[168] M. Nagata. 3-Dimensional Finite-Amplitude Solutions in Plane Couette-Flow - Bifurcation From Infinity. *J. Fluid Mech.*, 217:519–527, aug 1990.

[169] M. Nagata and K. Deguchi. Mirror-symmetric exact coherent states in plane poiseuille flow. *J. Fluid Mech.*, 735, 2013.

[170] R. Nakanishi, H. Mamori, and K. Fukagata. Relaminarization of turbulent channel flow using traveling wave-like wall deformation. *International Journal of Heat and Fluid Flow*, 35:152–159, 2012. ISSN 0142727X. doi: 10.1016/j.ijheatfluidflow.2012.01.007. URL `http://dx.doi.org/10.1016/j.ijheatfluidflow.2012.01.007`.

[171] C. L. M. H. Navier. Mémoire sur les lois du mouvement des fluides. *Mémoires de l'Académie Royale des Sciences de l'Institut de France*, 6(1823):389–440, 1823.

[172] C. Neto, D. R. Evans, E. Bonaccurso, H.-J. Butt, and V. S. J. Craig. Boundary slip in newtonian liquids: a review of experimental studies. *Rep. Prog. in Phys.*, 68(12):2859, 2005.

[173] M. Nishi, B. Ünsal, F. Durst, and G. Biswas. Laminar-to-turbulent transition of pipe flows through puffs and slugs. *J. Fluid Mech.*, 614:425–446, 2008.

[174] P. Orlandi, S. Pirozzoli, M. Bernardini, and G. F. Carnevale. A minimal flow unit for the study of turbulence with passive scalars. *Journal of Turbulence*, 15 (11):731–751, 2014. doi: 10.1080/14685248.2014.927066. URL `https://doi.org/10.1080/14685248.2014.927066`.

[175] J. Ou and J. P. Rothstein. Direct velocity measurements of the flow past drag-reducing ultrahydrophobic surfaces. *Phys. Fluids*, 17(10):103606, 2005. ISSN 10706631. doi: 10.1063/1.2109867.

[176] J. Ou, B. Perot, and J. P. Rothstein. Laminar drag reduction in microchannels using ultrahydrophobic surfaces. *Phys. Fluids*, 16(12):4635–4643, 2004. ISSN 10706631. doi: 10.1063/1.1812011.

[177] J. Page, M. P. Brenner, and R. R. Kerswell. Revealing the state space of turbulence using machine learning. *arXiv*, 2020.

[178] M. Pamiès, É. Garnier, A. Merlen, and P. Sagaut. Opposition control with arrayed actuators in the near-wall region of a spatially developing turbulent boundary layer. *International Journal of Heat and Fluid Flow*, 32(3):621–630, 2011. ISSN 0142727X. doi: 10.1016/j.ijheatfluidflow.2011.03.005.

[179] C. S. Paranjape. *Onset of turbulence in plane Poiseuille flow*. PhD thesis, IST Austria, Klosterneuburg, oct 2019.

[180] H. Park, H. Park, and J. Kim. A numerical study of the effects of superhydrophobic surface on skin-friction drag in turbulent channel flow. *Phys. Fluids*, 25(11):110815, 2013. ISSN 10706631. doi: 10.1063/1.4819144.

[181] H. Park, G. Sun, and C. J. Kim. Superhydrophobic turbulent drag reduction as a function of surface grating parameters. *J. Fluid Mech.*, 747:722–734, 2014.

[182] J. S. Park and M. D. Graham. Exact coherent states and connections to turbulent dynamics in minimal channel flow. *J. Fluid Mech.*, 782:430–454, 2015.

[183] J. S. Park, A. Shekar, and M. D. Graham. Bursting and critical layer frequencies in minimal turbulent dynamics and connections to exact coherent states. *Phys. Rev. Fluids*, 3(1):014611, 2018.

[184] F. Picella, J.-C. Robinet, and S. Cherubini. Laminar-turbulent transition in channel flow with superhydrophobic surfaces modelled as a partial slip wall. *J. Fluid Mech*, 881:462–497, 2019. doi: 10.1017/jfm.2019.740.

[185] B. Podvin and J. Lumley. A low-dimensional approach for the minimal flow unit. *Journal of Fluid Mechanics*, 362:121–155, 1998. doi: 10.1017/S0022112098008854.

[186] Y. Pomeau. Front motion, metastability and subcritical bifurcations in hydrodynamics. *Physica D*, 23(1-3):3–11, 1986.

[187] S. B. Pope. *Turbulent flows*. Cambridge university Press, 2000.

[188] A. Prigent and O. Dauchot. Transition to versus from turbulence in subcritical couette flows. In T. Mullin and R. Kerswell, editors, *IUTAM Symposium on Laminar-Turbulent Transition and Finite Amplitude Solutions*, pages 195–219, Dordrecht, 2005. Springer Netherlands. ISBN 978-1-4020-4049-8.

[189] D. Quéré. Non-sticking drops. *Rep. Prog. in Phys.*, 68(11):2495, 2005.

[190] D. Quéré. Wetting and Roughness. *Annual Review of Materials Research*, 38(1):71–99, 2008. ISSN 1531-7331. doi: 10.1146/annurev.matsci.38.060407.132434. URL www.annualreviews.org.

[191] A. Rajappan and G. H. McKinley. Polymers and Plastrons in Parallel Yield Enhanced Turbulent Drag Reduction. *Fluids*, 5(4):197, 2020. ISSN 2311-5521. doi: 10.3390/fluids5040197.

[192] A. Rajappan and G. H. Mckinley. Cooperative drag reduction in turbulent flows using polymer additives and superhydrophobic walls. *Phys. Rev. Fluids*, 5(114601):1–18, 2020. doi: 10.1103/PhysRevFluids.5.114601.

[193] A. Rajappan, K. Golovin, B. Tobelmann, V. Pillutla, Abhijeet, W. Choi, A. Tuteja, and G. H. McKinley. Influence of textural statistics on drag reduction by scalable, randomly rough superhydrophobic surfaces in turbulent flow. *Physics of Fluids*, 31(4):042107, 2019. doi: 10.1063/1.5090514. URL `https://doi.org/10.1063/1.5090514`.

[194] O. Reynolds. Xxix. an experimental investigation of the circumstances which determine whether the motion of water shall be direct or sinuous, and of the law of resistance in parallel channels. *Phil. Trans. Roy. Soc. Lond.*, (174):935–982, 1883.

[195] J. P. Rothstein. Slip on superhydrophobic surfaces. *Annu. Rev. Fluid Mech.*, 42(1):89–109, 2010. doi: 10.1146/annurev-fluid-121108-145558.

[196] M. Sano and K. Tamai. A universal transition to turbulence in channel flow. *Nature Phys.*, 12(3):249, 2016.

[197] W. S. Saric, H. L. Reed, and E. J. Kerschen. Boundary-layer receptivity to freestream disturbances. *Annu. Rev. Fluid Mech.*, (1996):291–319, 2002.

[198] T. Sayadi, C. W. Hamman, and P. Moin. Direct numerical simulation of complete H-type and K-type transitions with implications for the dynamics of turbulent boundary layers. *J. Fluid Mech.*, 724:480, 2013. doi: 10.1017/jfm.2013.142.

[199] P. J. Schmid and D. S. Henningson. *Stability and transition in shear flows*. Springer Science & Business Media, 2012.

[200] A. Schmiegel and B. Eckhardt. Fractal stability border in plane couette flow. *Phys. Rev. Lett.*, 79:5250–5253, Dec 1997. doi: 10.1103/PhysRevLett.79.5250. URL `https://link.aps.org/doi/10.1103/PhysRevLett.79.5250`.

[201] T. M. Schneider and B. Eckhardt. Lifetime statistics in transitional pipe flow. *Phys. Rev. E*, 78(4):1–10, 2008. ISSN 15393755. doi: 10.1103/PhysRevE.78. 046310.

[202] T. M. Schneider, B. Eckhardt, and J. A. Yorke. Turbulence transition and the edge of chaos in pipe flow. *Phys. Rev. Lett.*, 99(3):034502, 2007.

[203] D. Seki and M. Matsubara. Experimental investigation of relaminarizing and transitional channel flows. *Physics of Fluids*, 24(12):124102, 2012. doi: 10. 1063/1.4772065. URL `https://doi.org/10.1063/1.4772065`.

[204] J. Seo and A. Mani. On the scaling of the slip velocity in turbulent flows over superhydrophobic surfaces. *Phys. Fluids*, 28(2):25110, 2016. ISSN 10897666. doi: 10.1063/1.4941769. URL `https://doi.org/10.1063/1.4941769`.

[205] J. Seo and A. Mani. Effect of texture randomization on the slip and interfacial robustness in turbulent flows over superhydrophobic surfaces. *Phys. Rev. Fluids*, 3(4):44601, 2018. ISSN 2469990X. doi: 10.1103/PhysRevFluids.3.044601.

[206] J. Seo, R. García-Mayoral, and A. Mani. Turbulent flows over superhydrophobic surfaces: Flow-induced capillary waves, and robustness of air-water interfaces. *Journal of Fluid Mechanics*, 835:45–85, 2018. ISSN 14697645. doi: 10.1017/ jfm.2017.733. URL `https://doi.org/10.1017/jfm.2017.733`.

[207] A. Shekar and M. D. Graham. Exact coherent states with hairpin-like vortex structure in channel flow. *J. Fluid Mech.*, 849:76–89, 2018.

[208] H.-Y. Shih, T.-L. Hsieh, and N. Goldenfeld. Ecological collapse and the emergence of travelling waves at the onset of shear turbulence. *Nature Phys.*, 12(3): 245, 2016.

[209] M. Shimizu and P. Manneville. Bifurcations to turbulence in transitional channel flow. *Physical Review Fluids*, 4:113903, 2019. doi: 10.1103/PhysRevFluids. 4.113903.

[210] A. Sidorenko, T. Krupenkin, A. Taylor, P. Fratzl, and J. Aizenberg. Reversible switching of hydrogel-actuated nanostructures into complex micropatterns. *Science*, 315(5811):487–490, 2007. ISSN 00368075. doi: 10.1126/science.1135516. URL `www.sciencemag.orgSCIENCEVOL`.

[211] M. Sipos and N. Goldenfeld. Directed percolation describes lifetime and growth of turbulent puffs and slugs. *Phys. Rev. E*, 84(3):035304, 2011.

[212] J. D. Skufca, J. A. Yorke, and B. Eckhardt. Edge of chaos in a parallel shear flow. *Phys. Rev. Lett.*, 96(17):174101, 2006.

[213] A. J. Smits, B. J. McKeon, and I. Marusic. High-Reynolds number wall turbulence. *Annual Review of Fluid Mechanics*, 43:353–375, 2011.

[214] A. Spille, A. Rauh, and H. Buehring. Critical curves of plane Poiseuille flow with slip boundary conditions. 2001. URL `http://arxiv.org/abs/physics/0101018`.

[215] T. M. Squires and S. R. Quake. Microfluidics: Fluid physics at the nanoliter scale. *Rev. Modern Phys.*, 77(3):977, 2005.

[216] T. Sun, G. Wang, L. Feng, B. Liu, Y. Ma, L. Jiang, and D. Zhu. Reversible Switching between Superhydrophilicity and Superhydrophobicity. *Angewandte*

Chemie - International Edition, 43(3):357–360, 2004. ISSN 14337851. doi: 10.1002/anie.200352565.

[217] B. Suri, J. Tithof, R. O. Grigoriev, and M. F. Schatz. Forecasting fluid flows using the geometry of turbulence. *Phy. Rev. Lett.*, 118(11):114501, 2017.

[218] L. Tang, Z. Zeng, G. Wang, E. Liu, L. Li, and Q. Xue. Investigation on super-hydrophilic surface with porous structure: Drag reduction or drag increasing. *Surface and Coatings Technology*, 317:54–63, may 2017. ISSN 02578972. doi: 10.1016/j.surfcoat.2017.03.048.

[219] Y. H. Tee, D. C. Barros, and E. K. Longmire. Motion of finite-size spheres released in a turbulent boundary layer. *International Journal of Multiphase Flow*, 133:103462, 2020. ISSN 0301-9322. doi: https://doi.org/10.1016/j.ijmultiphaseflow.2020.103462. URL `https://www.sciencedirect.com/science/article/pii/S0301932220305735`.

[220] H. Tian, J. Zhang, E. Wang, Z. Yao, and N. Jiang. Experimental investigation on drag reduction in turbulent boundary layer over superhydrophobic surface by TRPIV. *Theoretical and Applied Mechanics Letters*, 5(1):45–49, 2015. ISSN 20950349. doi: 10.1016/j.taml.2015.01.003.

[221] J. Tithof, B. Suri, R. K. Pallantla, R. O. Grigoriev, and M. F. Schatz. Bifurcations in a quasi-two-dimensional kolmogorov-like flow. *J. Fluid Mech.*, 828: 837–866, 2017.

[222] B. Toms. Some observations on the flow of linear polymer solutions through straight tubes at large reynolds numbers. 1948.

[223] B. A. Toms. On the early experiments on drag reduction by polymers. *The Physics of Fluids*, 20(10):S3–S5, 1977. doi: 10.1063/1.861757. URL `https://aip.scitation.org/doi/abs/10.1063/1.861757`.

[224] R. Truesdell, A. Mammoli, P. Vorobieff, F. van Swol, and C. J. Brinker. Drag reduction on a patterned superhydrophobic surface. *Phys. Rev. Lett.*, 97:044504, Jul 2006. doi: 10.1103/PhysRevLett.97.044504.

[225] L. S. Tuckerman, T. Kreilos, H. Schrobsdorff, T. M. Schneider, and J. F. Gibson. Turbulent-laminar patterns in plane poiseuille flow. *Phys. Fluids*, 26(11): 114103, 2014.

[226] P. S. Virk. Drag reduction fundamentals. *AIChE Journal*, 21(4):625–656, 1975. doi: https://doi.org/10.1002/aic.690210402. URL `https://aiche.onlinelibrary.wiley.com/doi/abs/10.1002/aic.690210402`.

[227] P. S. Virk. Drag reduction fundamentals. *AIChE J.*, 21(4):625–656, 1975. ISSN 1547-5905. doi: 10.1002/aic.690210402. URL `http://dx.doi.org/10.1002/aic.690210402`.

[228] D. Viswanath. Recurrent motions within plane couette turbulence. *Journal of Fluid Mechanics*, 580:339–358, 2007. doi: 10.1017/S0022112007005459.

[229] D. Viswanath and P. Cvitanović. Stable manifolds and the transition to turbulence in pipe flow. *Journal of Fluid Mechanics*, 627:215–233, 2009. ISSN 00221120. doi: 10.1017/S0022112009006041. URL `https://doi.org/10.1017/S0022112009006041`.

[230] F. Waleffe. Hydrodynamic stability and turbulence: beyond transients to a self-sustaining process. *Studies in applied mathematics*, 95(3):319–343, 1995.

[231] F. Waleffe. On a self-sustaining process in shear flows. *Physics of Fluids*, 9(4): 883–900, 1997. ISSN 10706631. doi: 10.1063/1.869185. URL `http://dx.doi.org/10.1063/1.869185http://pof.aip.org/resource/1/PHFLE6/v9/i4`.

[232] F. Waleffe. On a self-sustaining process in shear flows. *Physics of Fluids*, 9(4): 883–900, 1997. ISSN 10706631. doi: 10.1063/1.869185. URL `http://dx.doi.org/10.1063/1.869185http://pof.aip.org/resource/1/PHFLE6/v9/i4`.

[233] F. Waleffe. Exact coherent structures in channel flow. *J. Fluid Mech.*, 435: 93–102, 2001.

[234] F. Waleffe. Homotopy of exact coherent structures in plane shear flows. *Phys. Fluids*, 15:1517, 2003.

[235] J. M. Wallace. Quadrant analysis in turbulence research: history and evolution. *Annu. Rev. Fluid Mech.*, 48:131–158, 2016.

[236] B. Wang, J. Wang, G. Zhou, and D. Chen. Drag Reduction by Microvortexes in Transverse Microgrooves. *Advances in Mechanical Engineering*, 2014, 2014. ISSN 16878140. doi: 10.1155/2014/734012. URL `http://dx.doi.org/10.1155/2014/734012`.

[237] J. Wang, J. Gibson, and F. Waleffe. Lower branch coherent states in shear flows: transition and control. *Phys. Rev. Lett.*, 98(20):204501, 2007.

[238] S. Wang, H. Liu, D. Liu, X. Ma, X. Fang, and L. Jiang. Enthalpy-driven three-state switching of a superhydrophilic/ superhydrophobic surface. *Angewandte Chemie - International Edition*, 46(21):3915–3917, 2007. ISSN 14337851. doi: 10.1002/anie.200700439.

[239] S.-N. Wang, M. D. Graham, F. J. Hahn, and L. Xi. Time-Series and Extended Karhunen–Loe've Analysis of Turbulent Drag Reduction in Polymer Solutions. *AICHE Journal*, 60(4):1460–1475, 2014. ISSN 0001-1541. doi: 10.1002/aic.

[240] S.-N. Wang, M. D. Graham, F. J. Hahn, and L. Xi. Time-series and extended karhunen–loève analysis of turbulent drag reduction in polymer solutions. *AIChE Journal*, 60(4):1460–1475, 2014.

[241] S. N. Wang, A. Shekar, and M. D. Graham. Spatiotemporal dynamics of viscoelastic turbulence in transitional channel flow. *Journal of Non-Newtonian Fluid Mechanics*, 244:104–122, 2017. ISSN 03770257. doi: 10.1016/j.jnnfm. 2017.04.008. URL `http://dx.doi.org/10.1016/j.jnnfm.2017.04.008`.

[242] K. Watanabe, K. Okido, and H. Mizunuma. Drag reduction in flow through square and rectangular ducts with highly water-repellent walls. *Trans. Jpn. Soc. Mech. Eng. B*, 62:3330–3334, Sep 1996.

[243] T. Wei and W. W. Willmarth. Reynolds-number effects on the structure of a turbulent channel flow. *Journal of Fluid Mechanics*, 204:57–95, 1989. doi: 10.1017/S0022112089001667.

[244] R. N. Wenzel. Resistance of solid surfaces to wetting by water. *Industrial and Engineering Chemistry*, 28(8):988–994, aug 1936. ISSN 00197866. doi: 10.1021/ie50320a024.

[245] J. Westerweel and F. Scarano. Universal outlier detection for piv data. *Experiments in fluids*, 39(6):1096–1100, 2005.

[246] R. D. Whalley, J. S. Park, A. Kushwaha, D. J. C. Dennis, M. D. Graham, and R. J. Poole. Low-drag events in transitional wall-bounded tur-

bulence. *Physical Review Fluids*, 2(3):034602, mar 2017. ISSN 2469-990X. doi: 10.1103/PhysRevFluids.2.034602. URL `https://link.aps.org/doi/10.1103/PhysRevFluids.2.034602`.

[247] R. D. Whalley, D. J. Dennis, M. D. Graham, and R. J. Poole. An experimental investigation into spatiotemporal intermittencies in turbulent channel flow close to transition. *Experiments in Fluids*, 60(6):102, 2019. ISSN 14321114. doi: 10.1007/s00348-019-2739-9. URL `https://doi.org/10.1007/s00348-019-2739-9`.

[248] W. Willmarth and S. Lu. Structure of the reynolds stress and the occurrence of bursts in the turbulent boundary layer. In F. Frenkiel and R. Munn, editors, *Turbulent Diffusion in Environmental Pollution*, volume 18 of *Advances in Geophysics*, pages 287–314. Elsevier, 1975. doi: https://doi.org/10.1016/S0065-2687(08)60467-7. URL `https://www.sciencedirect.com/science/article/pii/S0065268708604677`.

[249] W. W. Willmarth and S. S. Lu. Structure of the reynolds stress near the wall. *Journal of Fluid Mechanics*, 55(1):65–92, 1972. ISSN 14697645. doi: 10.1017/S002211207200165X.

[250] J. D. Woodcock, J. E. Sader, and I. Marusic. Induced flow due to blowing and suction flow control: An analysis of transpiration. *Journal of Fluid Mechanics*, 690:366–398, 2012. ISSN 00221120. doi: 10.1017/jfm.2011.441. URL `https://doi.org/10.1017/jfm.2011.441`.

[251] X. Wu and P. Moin. Direct numerical simulation of turbulence in a nominally zero-pressure-gradient flat-plate boundary layer. *J. Fluid Mech.*, 630:5–41, 2009.

[252] I. J. Wygnanski and F. H. Champagne. On transition in a pipe. part 1. the origin of puffs and slugs and the flow in a turbulent slug. *J. Fluid Mech.*, 59 (2):281–335, 1973.

[253] L. Xi. *Nonlinear dynamics and instabilities of viscoelastic fluid flows.* PhD thesis, University of Wisconsin-Madison, 2009.

[254] L. Xi. Turbulent drag reduction by polymer additives: Fundamentals and recent advances. *Physics of Fluids*, 31(12):121302, 2019. doi: 10.1063/1.5129619. URL `https://doi.org/10.1063/1.5129619`.

[255] L. Xi and M. D Graham. Turbulent drag reduction and multistage transitions in viscoelastic minimal flow units. *Journal of Fluid Mechanics*, 647:421, 2010.

[256] L. Xi and M. D. Graham. Active and hibernating turbulence in minimal channel flow of newtonian and polymeric fluids. *Physical Review Letters*, 104(21), apr 2010. ISSN 00319007. doi: 10.1103/PhysRevLett.104. 218301. URL `http://arxiv.org/abs/1004.5159http://dx.doi.org/10.1103/PhysRevLett.104.218301`.

[257] L. Xi and M. D. Graham. Intermittent dynamics of turbulence hibernation in Newtonian and viscoelastic minimal channel flows. *Journal of Fluid Mechanics*, 693:433–472, feb 2012. ISSN 0022-1120. doi: 10.1017/jfm.2011.541. URL `http://www.journals.cambridge.org/abstract_S0022112011005416`.

[258] C. X. Xu, J. I. Choi, and H. J. Sung. Suboptimal control for drag reduction in turbulent pipe flow. *Fluid Dynamics Research*, 30(4):217–231, 2002. ISSN 01695983. doi: 10.1016/S0169-5983(02)00041-2. URL `http://www.iop.org/journals/FDR`.

[259] Q. Yang, A. P. Willis, and Y. Hwang. Energy production and self-sustained turbulence at the Kolmogorov scale in Couette flow. *Journal of Fluid Mechanics*, 834:531–554, 2018. ISSN 14697645. doi: 10.1017/jfm.2017.704.

[260] Z. Yang, J. K. Park, and S. Kim. Magnetically Responsive Elastomer–Silicon Hybrid Surfaces for Fluid and Light Manipulation. *Small*, 14(2):1–9, 2018. ISSN 16136829. doi: 10.1002/smll.201702839.

[261] J. Yao, X. Chen, and F. Hussain. Composite active drag control in turbulent channel flows. *Physical Review Fluids*, 6(5), 2021. ISSN 2469990X. doi: 10.1103/PhysRevFluids.6.054605.

[262] C. Ybert, C. Barentin, C. Cottin-Bizonne, P. Joseph, and L. Bocquet. Achieving large slip with superhydrophobic surfaces: Scaling laws for generic geometries. *Phys. Fluids*, 19(12):123601, 2007.

[263] G. Yin, W.-X. Huang, and C.-X. Xu. Prediction of near-wall turbulence using minimal flow unit. *Journal of Fluid Mechanics*, 841:654–673, 2018. doi: 10.1017/jfm.2018.55.

[264] X. Y. You, J. R. Zheng, and Q. Jing. Effects of boundary slip and apparent viscosity on the stability of microchannel flow. *Forschung im Ingenieurwesen/Engineering Research*, 71(2):99–106, 2007. ISSN 00157899. doi: 10.1007/s10010-007-0048-6.

[265] T. Young. III. An essay on the cohesion of fluids. *Philosophical Transactions of the Royal Society of London*, 95:65–87, 1805. ISSN 0261-0523. doi: 10.1098/rstl.1805.0005.

[266] K. H. Yu, C. J. Teo, and B. C. Khoo. Linear stability of pressure-driven flow over longitudinal superhydrophobic grooves. *Phys. Fluids*, 28:22001, 2016. doi: 10.1063/1.4940336. URL `https://doi.org/10.1063/1.4940336`.

[267] S. Zammert and B. Eckhardt. Streamwise and doubly-localised periodic orbits in plane poiseuille flow. *J. Fluid Mech.*, 761:348–359, 2014.

[268] T. A. Zang. On the rotation and skew-symmetric forms for incompressible flow simulations. *Applied Numerical Mathematics*, 7(1):27–40, 1991. ISSN 0168-9274. doi: https://doi.org/10.1016/0168-9274(91)90102-6. URL `https://www.sciencedirect.com/science/article/pii/0168927491901026`.

[269] J. Zhang, X. Lu, W. Huang, and Y. Han. Reversible superhydrophobicity to superhydrophilicity transition by extending and unloading an elastic polyamide film. *Macromolecular Rapid Communications*, 26(6):477–480, 2005. ISSN 10221336. doi: 10.1002/marc.200400512.

[270] J. Zhang, H. Tian, Z. Yao, P. Hao, and N. Jiang. Mechanisms of drag reduction of superhydrophobic surfaces in a turbulent boundary layer flow. *Exp. in Fluids*, 56(9):179, 2015. ISSN 07234864. doi: 10.1007/s00348-015-2047-y.

[271] J. Zhou, R. J. Adrian, S. Balachandar, and T. M. Kendall. Mechanisms for generating coherent packets of hairpin vortices in channel flow. *J. Fluid Mech.*, 387:353–396, 1999. doi: 10.1017/S002211209900467X.